In-Depth Temperature Profiles in Pyrolyzing Wood

Pedro Reszka

A thesis submitted for the degree of Doctor of Philosophy.
The University of Edinburgh.
June 2008

In-Depth Temperature Profiles in Pyrolyzing Wood

by

Pedro Reszka

This thesis has been supervised by

Prof Jose Luis Torero

Dr Stephen Welch

The examining committee was integrated by

Prof Arvind Atreya

Dr Guillermo Rein

To Elena Pedrasa Guzmán.

Without you, nothing would have been possible.

Declaration

I declare that this thesis was composed by myself and that the work contained therein is my own, except where explicitly stated otherwise in the text.

(*Pedro Reszka*)

Abstract

The move towards performance-based design of the fire resistance of structures requires more accurate design methods. An important variable in the fire performance of timber structures is the in-depth temperature distribution, as wood is weakened by an increase of temperature, caused by exposure to high heat fluxes. New construction techniques of timber structures use new types of metallic connectors that have poor fire performance, and present evidence of low temperature failure. The temperature distribution is also an important variable in the performance of these connections. Thus, a proper prediction of temperature profiles in wood structural elements has become an essential part of timber structural design. Current design methods use empirically determined equations for the temperature distribution of the uncharred section of the wood member, but these assume constant charring rates (i.e. steady-state conditions), do not account for changes in the heating conditions, and were obtained under poorly defined boundary conditions in fire resistance furnaces.

Another approach consists of calculating the temperature profiles by modelling wood pyrolysis. The energy conservation equation for the timber element is solved numerically, and several models have been created in the past. However, there has been no clear indication whether each term included in the different models adds enough accuracy to justify the increased computational cost to solve a more complicated model. Finally, comparisons of predicted and measured results show good initial agreement, but greater inaccuracy as the pyrolysis process progresses and the temperatures rise.

As part of this research project, a series of experimental in-depth temperature measurements were done in wood samples exposed to various intensities of radiant heat fluxes, with clearly defined boundary conditions that allow a proper input for pyrolysis models. The imposed heat fluxes range from 10 $kW \cdot m^{-2}$, which generates an almost inert behaviour, to 60 $kW \cdot m^{-2}$, where spontaneous flaming is almost immediately observed. Mass loss measurements for all

the imposed heat fluxes were also performed.

The initial behaviour of wood is inert, as has been proven by comparing the experimental data with an inert, one-dimensional heating model. It has also been shown that pyrolysis reactions will commence at a radiation intensity close to $10\,\mathrm{kW{\cdot}m^{-2}}$. Moisture evaporation can be treated as a heat sink, as has been shown by a scaling of the times for the different thermocouples to reach 100°C.

The second part of this project dealt with the modelling of the pyrolysis process, with an emphasis placed on temperature prediction. The main objective was to identify the simplest model that can accurately predict temperature distributions in wood elements exposed to fires. For this, an analysis of the different terms which have been included by several models in the energy equation has been done, by quantifying its magnitude. Four models with different degrees of simplification have been developed, that group the main approaches of the previous models. A fifth model was also developed, which constitutes a different numerical approach to the rest of the four models. This model solves the energy equation by using a moving boundary approach, which assumes that all reactions occur in the boundary, while the rest of the models solve volumetric reactions for the entire solid.

The analysis of the magnitude of terms and a comparison of the results of the different models has shown that, for the purpose of in-depth temperature predictions, no gas phase processes need to be considered. This includes the gas phase sensible heats, the modelling of the pressure build up and the heat losses by convection of pyrolysis gases and vapour. Also, it has been shown that a simple one-step reaction scheme is sufficient for temperature predictions. Comparison with the experimental data has shown that moisture evaporation must be included. An increase in the heating rate at later heating times was not predicted by the models. This is probably caused by the exothermic effect of char oxidation, which was not included in the models. It has been concluded that this effect must also be considered in a temperature prediction model.

Thus, a model for an accurate and simple prediction of temperature profiles in wood exposed to high intensity heat fluxes must include the rise in the solid sensible heat, the heat transferred by conduction, the heat of moisture evaporation, the heat of pyrolysis reaction and the exothermic effect which was not accounted for in this work.

Acknowledgments

It is amusing to see how life takes you through unexpected paths. What seemed like a harmless meeting to discuss my MSc thesis with a young "American" lecturer (he apparently spoke Spanish) that was visiting the Mechanical Engineering Department in my university in Chile changed my life. In the year following that meeting I was not only to visit Edinburgh to work for him, but I was also going to decide that my PhD was going to be on "Fire", and that I was going to do it under his supervision. Even though the subject of that MSc thesis had to do with Fire Safety Engineering, it was really thanks to my coming to Edinburgh and being under his orders that I got to know what this discipline is like. For this and for all the support and opportunities that I have received from him during all these years in Edinburgh I am deeply grateful to Professor José Luis Torero.

I must also thank Professor Juan de Dios Rivera, for introducing me to this discipline and for giving me the opportunity to visit Edinburgh in the first place. Dr Andrés Fuentes has become a very important friend during these years, and his great experience and knowledge have always been present when I have needed them. He also gave me the opportunity to fulfil one of my childhood dreams and experience zero gravity. I will never forget it!

In more down to earth matters, I must thank all the people in the fire group which have helped me and suffered from my sometimes excessive extroversion, in particular my friends Hubert Biteau and Thomas Steinhaus, which have helped me solve innumerable problems and have provided the much needed family figures far away from home. My rusty mathematical knowledge was constantly polished by Wolfram Jahn, thank you very much! The great conversations on every possible subject with Francesco Colella are greatly appreciated.

The students that have worked with me on their final year projects and internships have been crucial on the outcome of this thesis, and have also allowed me to learn a lot. They are Graeme

Wells, Robbie Templeton, Darren McClure, Arnaud Demange, Esther Yoo, Osman Hussein and Cristián Maluk. Also, and on another of the greatest adventures of my life (undertaken while I was doing this thesis), I want to thank my friends Felipe Recart, Juan Rodillo, Felipe Oettinger and Santiago Valdés for getting all of us out of the Ice Fields safely.

Financial support was provided by Programme Alβan, the European Union Programme of High Level Scholarships for Latin America, thank you for the opportunity.

I feel that this project is not only a fruit of my work, but also the fruit of the efforts and love of all my family. My mother has dedicated her life to us, making sure that nothing was missing from our lives and giving us the best gift one can possibly receive: education. Everything is thanks to her. My father has inspired me with his hard work and great values, and has really been a role model in terms of my professional and personal life. And my sister, she has been there for me, always.

Thanks to all. You make me feel that I am too lucky.

Contents

List of Figures

List of Tables

Nomenclature

A	Pre-exponential factor (s^{-1})
E	Energy (J) ; Activation Energy ($J \cdot mol^{-1}$)
F	View Factor
G_{wat}	Moisture Evaporation Rate ($kg \cdot m^{-3} \cdot s^{-1}$)
H	Volumetric Enthalpy ($J \cdot m^{-3}$)
K	Reaction Rate Coefficient (s^{-1}); Permeability (m^2)
L	Thermal Penetration Depth (m); Length (m)
MC	Moisture Content ($kg_{water} \cdot kg_{wood}^{-1}$)
Q	Heat (J)
R	Universal Gas Constant ($J \cdot mol^{-1} \cdot K^{-1}$)
T	Temperature, (K; °C)
V	Volume (m^3)
W	Work (J)
X_{CI}	Confidence Interval
Δh_{fg}	Latent Heat of Moisture Evaporation ($J \cdot kg^{-1}$)
Δh_i	Heat of Reaction ($J \cdot kg^{-1}$)
$\dot{q}''$	Heat Flux ($W \cdot m^{-2}$)

$c; c_p$ Specific Heat (J·kg^{-1}·K^{-1})

e Thickness (m)

g Acceleration of Gravity, 9.81 m·s^{-2}

h Convective Heat Transfer Coefficient (W· m^{-2}· K $^{-1}$); Specific Enthalpy (J·kg^{-1})

k Thermal Conductivity (W·m^{-1}·K^{-1})

m Mass (kg)

p Pressure (N·m^{-2})

s Position of Moving Boundary (m)

t Time, (s)

u Speed (m·s^{-1})

v Speed (m·s^{-1})

x depth (m)

z Height (m)

Greek Symbols

α Thermal Diffusivity (m^2·s^{-1}); Surface Absorptivity

$\dot{\omega}$ Reaction Rate (kg·m^{-3}·s^{-1})

ϵ Surface Emissivity

μ Dynamic Viscosity (kg·m^{-1}·s^{-1}]

ν_c Char Mass Fraction

ρ Density, Mass Concentration (kg·m^{-3})

σ Stefan-Boltzmann Constant, 5,67×10^{-8} W·m^{-2}·K^{-4}]

φ Porosity (m^3·m^{-3})

Subscripts

∞	Ambient
a	Active Fraction
c	Char; Characteristic
CV	Control Volume
e	External
g	Gas
s	Solid
vap	Vapour
wat	Moisture

Superscripts

$*$	Non-dimensional
sat	Saturation

Chapter 1

Introduction

The modelling of the thermal degradation of cellulosic materials has applications in different areas of combustion. From biomass energy conversion to fire safety problems, and also including waste disposal, a need exists to properly model the physical and chemical phenomena that occur during the heating up, pyrolysis and subsequent combustion of cellulosic elements exposed to either high temperatures or external heat fluxes. These applications are becoming more widespread because of the abundance of these materials and because of the environmental benefits that arise from their use, such as requiring relatively low energy to process and manufacture and being renewable (Antal & Varhegyi 1995, Foliente 2000). In the area of fire safety, the process of wood pyrolysis is of fundamental importance in structural fires, where structural timber members undergo pyrolysis and subsequent combustion.

Over 70% of the population in the developed world lives in homes built in timber frames. The number of dwellings built using this method grew faster in the UK than other forms of construction in recent years, according to statistics of the UK Timber Frame Association. Above 90% of the residential buildings in North America are constructed with light timber frames, while in Australia this figure is of 75%. In Japan and the USA, the majority of the sawn wood has structural usage (Foliente 2000). The fire performance of these types of structures therefore plays an important role in the further development of this industry and in the safety of the population using these types of construction.

1.1 Timber Structures

Wood is an abundant, renewable and recyclable material, which has been used by humans for thousands of years. Its use in construction is still widespread, ranging from structural frames to floors, panelling, doors, interior and exterior woodwork, and furniture, among its multiple uses in an average dwelling (FPL 1999). Three polymeric materials make up the wood cells: cellulose, hemicellulose and lignin (Kollmann & Cote 1968). Cellulose makes up the cell walls, and provides the tensile strength of the wood matrix. Hemicellulose is similar to cellulose, and grows around the cellulose fibres. Lignin gives rigidity to the wood, allowing trees to grow upright; it cements the cells together, thus accounting for the compressive and shear strengths of wood (Kollmann & Cote 1968, Moraes 2003).

These three polymers form an inhomogeneous and anisotropic material, which exhibits great variability among different species, but in general tree species can be divided into two major groups, hardwoods and softwoods. Hardwoods are porous, and present greater hardness than softwoods (although some exceptions exist) (FPL 1999). The most commonly used types of wood by the timber construction industry are softwoods.

Timber structures have traditionally been built using heavy timber frames, with the walls being constructed of various materials such as interwoven branches and split logs in the very early versions of these types of structures (as early as 6500 BC), and later using plastered panels and bricks (Foliente 2000). Other forms of timber structures are palisade-type buildings and log-cabin constructions. Roof structures, an integral part of the building, have also traditionally been made in wood, and are still popular to this day. Timber roof structures have two basic forms: simple horizontal beams, or more complicated rafters being supported by the frame. Combinations of these two types have developed into hammer-beam roofs, which were used with great skill during the Renaissance, and into trusses, where originally the struts were also under flexion, unlike modern trusses where all the joints are assumed to be pinned (Foliente 2000).

The coming of the industrial revolution marked the appearance of industrially built planks, boards and nails which spawned the appearance of new construction techniques, especially in the USA, where new framing methods reduced labour costs, increased the flexibility in construction and allowed for prefabrication (Foliente 2000). These light frame construction methods are nowadays the predominant form of construction in residential and low-rise buildings.

Other technological advances developed in this period are the glued laminated timber (first used in Bavaria in 1809) and improvements in wood trusses (Foliente 2000). Glued laminated timber in its present form was developed in the twentieth century, as well as another important innovation, plywood (Foliente 2000).

1.1.1 Fire Behaviour

But wood is also a combustible material. Its safe use in construction will therefore depend on a proper design, which involves a correct knowledge of the phenomena that affect the performance of timber structures in fires. Great amounts of research have been destined for this purpose, since the late years of the nineteenth century up to present times (Babrauskas & Williamson 1978, Ingberg & Mitchell 1941, Bamford, Crank & Malan 1946, Drysdale 1998, Buchanan 2000, White 2002). Good reviews covering the performance of timber structures in fires and their design are those by Schaffer (Schaffer 1984), Buchanan (Buchanan 2000), Benichou and Sultan (Benichou & Sultan 2000) and Poon (Poon 2003), while Lau and Barrett make an assessment of the design process (Lau & Barrett 1994).

Structural failure of timber elements can occur due to two mechanisms. Mechanical resistance can decrease due to changes in wood properties caused by the temperature rise (Kollmann & Cote 1968, Gerhards 1982, Schaffer 1984, Moraes 2003). In particular, metallic connectors can fail at low temperatures because of a decrease in the embedding strength of wood (Moraes, Rogaume, Bocquet & Triboulot 2005). At higher temperatures and longer times, timber structures can fail because of the reduction of the cross section of the timber elements due to charring (CEN 2004).

When subjected to high temperatures or radiant heat fluxes of the magnitude of those encountered in fires, wood undergoes physical, chemical and structural changes. Initially, wood heats up and the moisture contained in its voids will begin to evaporate. This will generate a pressure build up, which causes a flow of vapour and liquid water in some cases to the outside of the wood matrix and also to the inner, colder regions, thus increasing the moisture content in those areas (White & Schaffer 1981).

Timber is weakened by temperature and moisture content increments (Kollmann & Cote 1968). This can cause structural failure even at temperatures below the charring temperature. Gerhards (Gerhards 1982) provides an excellent review of the particular changes of properties such as

the modulus of elasticity, shear modulus, and tensile, compressive and shear strengths with variations in temperature and moisture content. In general, wood is weakened by the increase of moisture and temperature, with the modulus of elasticity parallel to the grain decreasing to 80% of its value at equilibrium moisture conditions when it reaches the fibre saturation point (30% moisture content), and falling to 70% of its value when it reaches 473 K (200°C). The decrease in strength can reach values of more than 30% for shear and compressive strengths at temperatures of only 323 K (50°C) (Gerhards 1982), with respect to the values at 293 K. Ostman studied the wood tensile strength in high temperatures and increasing moisture contents (Ostman 1985), reporting a drop close to 40% in the tensile strength at a temperature of 473 K, and a drop of 30% in the modulus of elasticity when the moisture content reaches a value of 30% (for wood parallel to grain).

Moraes (Moraes 2003) measured a decrease of about 20% in the embedding strength at a similar temperature rise (Figure 1.1). Embedding strength is a critical property in connector performance, since resistance to shear stresses is directly related to the embedding strength (Moraes et al. 2005) (and, as will be mentioned later, some connectors transfer the loads from one timber element to the other by means of shear stresses). Moraes detected an initial drop in the embedding strength to about 70% when temperature reaches 353 K (80°C), both for loading parallel and perpendicular to grain. After 373 K, the embedding strength increases, reaching a relative maximum at 413 K (140°C), which is 10% lower than the initial value at ambient temperature. The strength then decreases, to reach a value close to 60% of the initial strength for a temperature of 473 K. This conduct is explained by the behaviour of the lignin matrix. Lignin will attain glass transition between 333 K and 353 K (60°C to 80°C) (Schaffer 1973, Irvine 1984, Moraes 2003) for moisture contents between 3 and 10%, which leads to a loss of binding strength between the fibres and to a consequent loss of embedding and compressive strengths of the timber element (Figure 1.2). For dry conditions, the glass transition temperature increases, and Moraes states that the increase in the embedding strength at the temperatures mentioned above occurs because at those temperatures the samples are practically oven dry (Moraes et al. 2005). Earlier, Noren reported that although there was no data on the evolution of embedding strength with temperature available at the time, it was expected that it would follow a similar behaviour to the compressive strength, because both are related (Noren 1996).

However, the dominant mechanical property in the behaviour of timber structures in fires is the compressive strength (Young & Clancy 2001*a*). Young and Clancy (Young & Clancy 2001*a*)

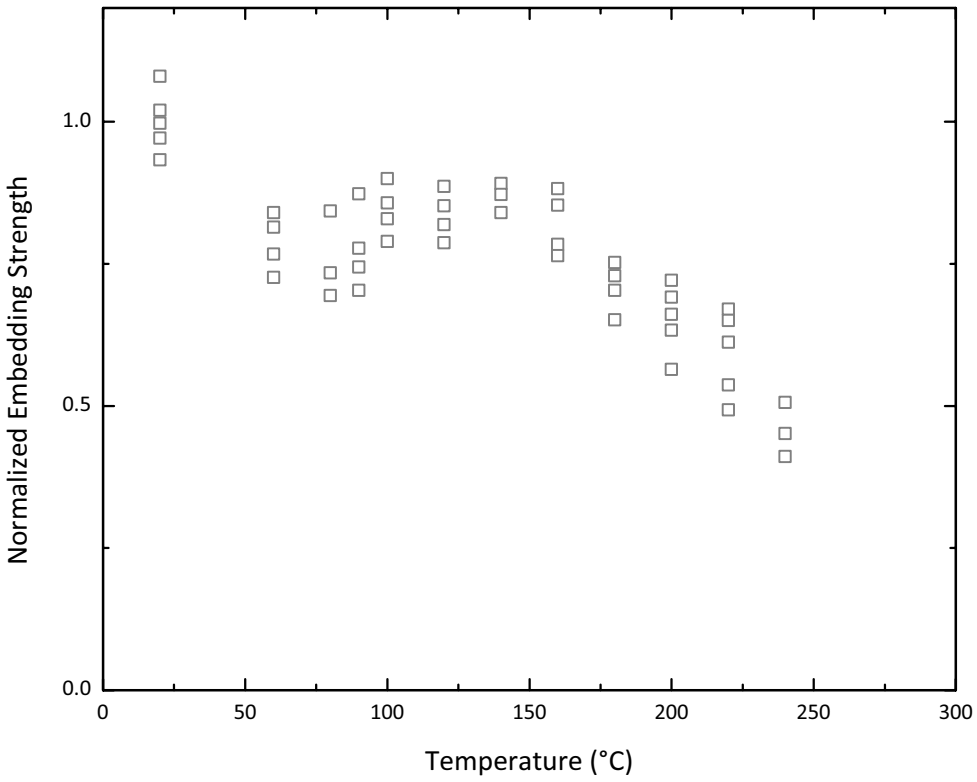

Figure 1.1: Normalized embedding strength parallel to grain (Moraes et al. 2005). The initial loss of strength is caused by the glass transition of the lignin matrix.

report reductions on the compressive strength of dry samples loaded parallel to grain of about 20% at a temperature of 473 K. They state that the magnitude of the change with temperature of compression properties differs to that of tensile properties, which can thus be related to the lignin matrix (see the description of the different polymers that constitute wood at the beginning of this section). Finally, these researchers also expect an increase of the compressive strength between 433 K and 483 K (160°C to 210°C). Since fires will increase both the temperature and moisture content, it is certain that these strength reductions will be faced by every timber element exposed to a fire.

White and Schaffer (White & Schaffer 1981) have measured peak moisture contents of about 20% in wood samples heated following standard furnace testing curves (ISO 1999), and observed that the front of peak moisture content consistently moves ahead of the charring front. The peak moisture content occurs at 373 K, and is 1.3 to 2.0 times the initial moisture content. Fredlund (Fredlund 1988), using a pressure model, calculated slightly higher values for the moisture content, of up to 25%, in wood exposed to a fixed incident heat flux. The measured

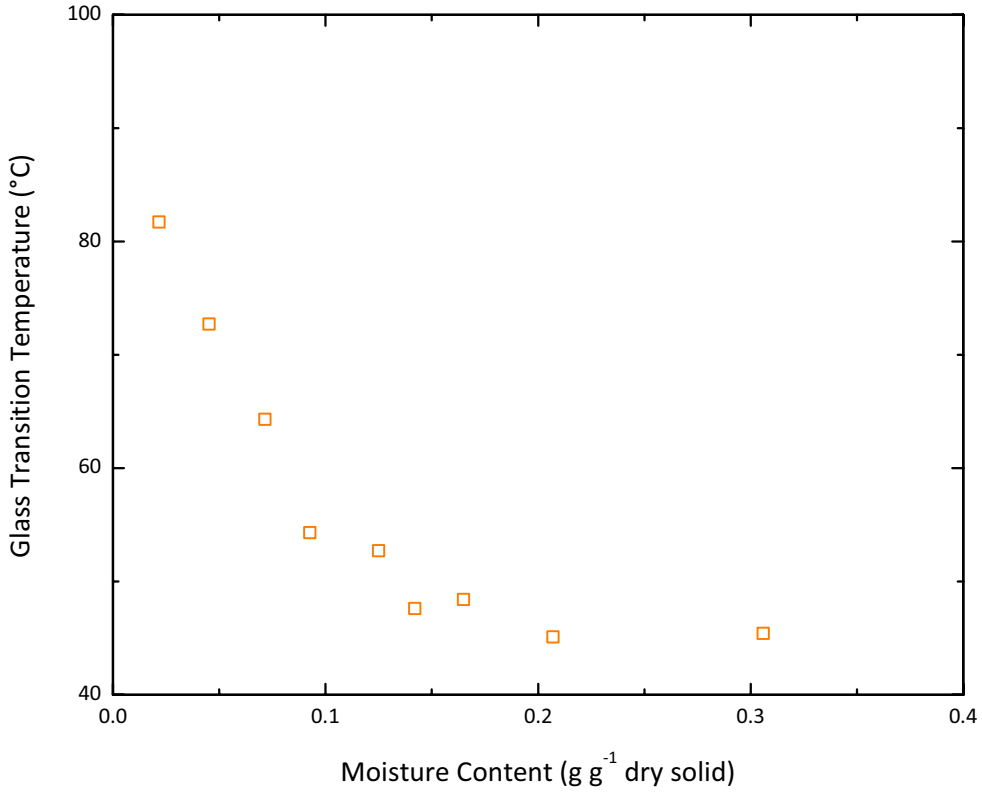

Figure 1.2: Evolution of the glass transition temperature of lignin with the moisture content (Irvine 1984). The loss of embedding strength suffered by wood at low temperatures can be attributed to this phenomenon. As wood is heated, part of its moisture will migrate to deeper regions, increasing the moisture content (up to values close to 20% (White & Schaffer 1981)) and thus decreasing the glass transition temperature.

peak pressure rise is of the order of 100 kPa (Fredlund 1988).

As the temperature continues to rise, devolatilization of the wood polymers will commence. The loss of tensile strength in wood is attributed to the depolymerisation of cellulose, which begins at around 473 K (200°C), while hemicellulose suffers a rapid mass loss at around 453 K that is partly responsible for changes in compressive strength (Schaffer 1973, Young & Clancy 2001*a*). Lignin, after a series of physical changes, will begin to lose mass at about 553 K (280°C). The products of this chemical transformation are pyrolysis gases which are mainly released to the exterior, and a char layer, which has insulating properties but also has a greater porosity. The pressure rise generated by the release of pyrolysis gases is lower than that associated with the vaporization of water (Fredlund 1988), and is of the order of 20 kPa (Tinney 1965, Lee, Chaiken & Singer 1976). Char is more brittle than virgin wood, and due to shrink-

ing or pressure build up, cracks will appear on its surface. Subsequent heating will increase the thickness of the char layer and eventually combustion, either flaming or surface combustion, will take place.

It is the char layer that causes the most known mode of failure of timber structures under fire. As heating of the timber element continues for an extended period of time, the pyrolysis front will move into the virgin sections of wood located at deeper positions. The brittle layer of char is not able to support any loads, causing an increase in the stress of the reduced cross section of virgin wood. In addition, the virgin wood will heat up, which will cause a decrease in the strength as has already been described. A series of methodologies have been developed to account for the speed at which the char layer progresses into the virgin wood and the loss of strength of the timber member (CEN 2004, Schaffer 1984, White 2002, Poon 2003). They consider a reduction in the cross section caused by charring, and normally the charring rate is taken as a constant. Thus, knowing the time of exposure of the timber element to a fire allows calculating the remaining cross section which is still load bearing. These methods also consider the loss of strength of the virgin wood due to the temperature rise.

1.1.2 Connectors

Connectors constitute an essential feature of the structure. The earliest form of connector is the joint, where timber members are interlocked together and can use wooden or iron dowels and pegs, or iron ties, to add stability (Foliente 2000, Schober 2000) (see Figure 1.3). Examples of this type of connection are notches and lap-joints. The transfer of stress in joints is thus made from member to member by compression or flexion (Schober 2000). Fasteners constitute another popular and early way of making timber connections, where elements such as nails, screws, bolts and dowels appeared when the use of iron and later of steel became widespread. Fasteners transfer stresses from one element to another usually by shear through the fastener itself (Schober 2000). One advantage of nails over bolts and dowels is that they can carry more load (Herzog, Natterer, Schweitzer, Volz & Winter 2004). Recently developed connections are glued connections, where the adhesive bonding makes them behave like solid wood, and steel connectors. The latter connectors are normally steel plates with fasteners, and the load is transferred through the connector and the fastener to the wood elements (Schober 2000). Since the steel plate is attached to the timber element by fasteners, the stresses are transferred by shear. Examples of these are the now popular truss plates (Figure 1.3) and especially-shaped

steel supports such as joist hangers, column bases and framing anchors (Herzog et al. 2004). Thus, shear stress plays a more important role in the performance of timber structures using modern construction techniques.

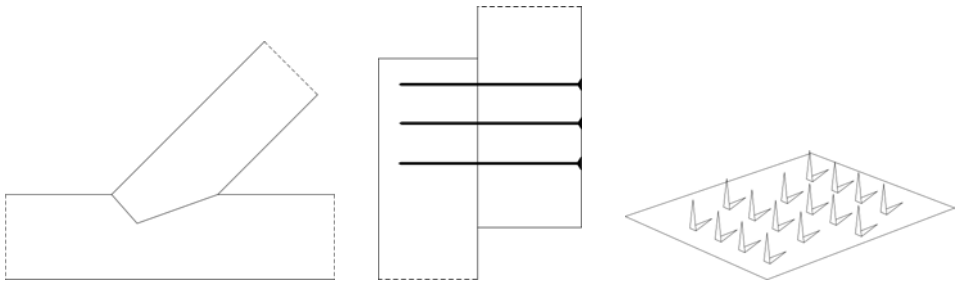

(a) *Traditional Timber Joint* (b) *Nailed Fastener* (c) *Truss Plate*

Figure 1.3: Schematic drawings of different connection types.

The performance in fires of metallic connectors will depend on the mechanical properties of wood, the geometry and type of connector, and the nature of the forces acting on the connection. It is recommended that connectors are protected by extra layers of wood or plaster board covering the whole connection, or by glued-in plugs made of wood that are inserted into the hole where the connector is located (Buchanan 2002, CEN 2004). Unprotected joints are accepted by the codes, but are deemed to have less fire resistance (CEN 2004). Timber structures have normally been regarded as having a good fire resistance, withstanding fires without presenting great structural damage (Buchanan 2002). But the introduction of new types of connectors, especially metallic connectors, has caused a general feeling of insecurity in the fire services when facing fires involving timber structures (Schaffer 1988). Metallic connectors are cost-effective and easy to erect, and have good structural properties when correctly installed (Schaffer 1988). Schaffer states that truss plates are used in 90% of the residential dwellings of the USA.

Joints have a good fire performance because the timber elements are connected between themselves, so there are no shear forces acting on the wood (as was previously discussed). There are examples of traditionally built timber structures suffering fires and withstanding them even though important sections of the structural elements have been charred (Poon 2003). The work of Noren, which included testing and modelling, showed that the behaviour of nails will depend both on the charring of the surface portions of the timber element and on the strength reduction of the remaining non-charred central section, where embedding strength plays an important role (Noren 1996). No comprehensive studies had been published on the behaviour of other types of fasteners, like bolts and dowels, in fires (Buchanan 2002), until the work of Moraes

(Moraes 2003). As discussed previously, this work was focused on the embedding strength of wood at fire conditions. Tests were done on dowels embedded in timber samples, and showed a similar behaviour to that of nails. It is then expected that the behaviour of bolts is similar, given that the mechanism of load transfer is the same for all fasteners. Finally, the influence of moisture content has also been researched, and it has been found that an increase in moisture content is detrimental for the performance of nail dowel fasteners (Rammer 2001, Rammer & Winistorfer 2001).

Metal plates, as mentioned above, have become very popular after their introduction. It has been proven that their behaviour in fires is not good. Truss plates have been reported to fail after 5 minutes of exposure in the standard furnace test (Buchanan 2002). This same work reported that even at lower temperature exposures the plates would still fail at earlier times than bolted or nailed fasteners. Plates can fail either by tooth withdrawal or by failure of the plate itself, the former being the mode of failure at elevated temperatures (White & Cramer 1994). Other types of modern connections, like shear plates and split rings, have poor performance, according to the study by Leicester et al (Buchanan 2002), while Schaffer (Schaffer 1984) reports failure of unprotected split rings in less than 5 minutes. Glued connections, finally, are deemed to behave in the same way as solid wood (Buchanan 2002), so their behaviour will be similar to that of joints.

There is a beneficial effect caused by the presence of a metallic connector in the wood member, the thermal bridge generated by the greater thermal conductivity which helps to carry heat away from the surface of wood into the colder, inner regions, reducing the speed of charring. This effect has been reported by several authors (Carling 1989, White, Cramer & Shrestha 1993, Noren 1996, Moraes 2003).

Two methods can be used for the determination of the fire endurance of connectors (and of timber structures in general), that of the reduced cross section and analytical methods (Buchanan 2002, CEN 2004), that apply heat transfer models to calculate the temperature fields in the timber elements and with that information use structural response models that determine the distribution of mechanical properties in the element under consideration and thus calculate deformation, strength and ultimately, failure (Noren 1996, Buchanan 2002, Young & Clancy 2001*b*, Clancy & Young 2004, Moraes 2003). Reduced cross section methods are more associated with heavy timber structures, while for light timber frames the analytical design methods should be applied (Buchanan 2002, Moraes 2003). But analytical methods are not restricted to

light timber structures, and as performance based design becomes accepted in more countries and structures are not only required to behave well in fires, but at the same time to be cost effective, these methods will begin to be used for a greater range of applications.

Analytical methods require a better knowledge of the physical, chemical and mechanical processes that affect the behaviour of wood when exposed to high heat fluxes. In particular, a good knowledge of the temperature profiles inside the exposed wood elements is needed (White et al. 1993, Noren 1996, Young & Clancy 2001*b*, Moraes 2003). Other phenomena that must be understood are the variation with temperature of the mechanical and thermophysical properties of wood, the rates of charring, wood surface recession, identification of structural failure mechanisms, radiation in wall cavities and sloughing of gypsum board (Noren 1996, Clancy 2001, Clancy & Young 2004, Moraes 2003). But due to the complex process of wood pyrolysis, in order to properly predict temperature profiles in timber elements exposed to fires, it is necessary to model wood pyrolysis itself.

1.2 Previous Experimental Work

The prediction of the fire resistance of timber structures has been limited to the characterization of charring rates and average in-depth temperatures. Indeed, the reduced cross section design methods being used today assume temperature profiles in the virgin wood which have been obtained from charring experiments in standard fire resistance furnaces (Schaffer 1984, Klingsch, Tavakkol-Khah, Wesche & Kersken-Bradley 1993, Janssens & White 1994, Frangi & Fontana 2003). In a different approach, and more related to the study of the phenomena of wood pyrolysis and combustion both for energy conversion and fire safety, temperature profiles have been measured for samples exposed to constant imposed heat fluxes. Between these two approaches, pyrolysis and combustion studies have been carried out in furnaces. This section will detail the work done under these three types of heating, and will discuss the advantages and disadvantages of each approach.

1.2.1 Standard Fire Resistance Furnaces

The temperature profile equations used in the design guidelines are equations that give the temperature distribution as a function of depth but only for the non-charred part of the timber

element. They assume that the temperature at the char front is constant, and that there will be ambient temperature in the core of the wood member; the only section affected by the temperature is that given by the thermal penetration depth which is taken usually as a fixed value or at least independent of the external heat flux (Klingsch et al. 1993, Janssens & White 1994, Frangi & Fontana 2003). It is interesting to note that the Eurocode temperature profiles are mentioned throughout the literature, but in fact they are not published in the drafts or the final version of the standard that the author has been able to read, and as a matter of fact there are divergences between the equation in the literature itself, for instance see Janssens and White (Janssens & White 1994) as opposed to Frangi and Fontana (Frangi & Fontana 2003). The equation appearing in the latter reference as being the one used in the Eurocode is presented next:

$$T(x) = 20 + 180\left(1 - \frac{x}{25}\right)^2. \tag{1.1}$$

In this particular case, the charring temperature has been taken as 473 K (hence the value of 180, which corresponds to the charring temperature minus the ambient temperature, in degrees Celsius), the thermal penetration depth is assumed to be 25 mm and the charring rate is considered to have a value of 0.7 mm·min^{-1} for laminated timber and 0.8 mm·min^{-1} for solid wood. These expressions can vary by having an exponential term instead of the power term, or can have the power term raised to a function of time instead of a fixed value (Schaffer 1984, Klingsch et al. 1993, Frangi & Fontana 2003).

The advantage of these expressions is that they are simple, and they are the result of correlations with experimental data measured in fire resistance furnaces. As a matter of fact, they agree reasonably well with other test data under similar conditions, as has been shown by Janssens and White (Janssens & White 1994). It is even reasonable to assume constant charring rates, but only once the pyrolysis has reached steady state conditions, as can be seen from the mass loss experiments in this present research (see Chapter 2).

The problems with standard fire resistance furnaces have been well identified for the past 30 years. First, the standard curve prescribed in 1917 was developed without the knowledge of the actual temperatures encountered in real fires (Babrauskas & Williamson 1978). Then, the issue of the imposed heat flux being variable in time and dependent on the type of lining used in the furnace and its geometry make it likely that no two furnaces give the same results (Drysdale

1998). Finally, the actual imposed heat flux to the specimen and the velocity field around it are difficult to quantify.

The fact that the temperature curves themselves only account for the virgin wood, that they are independent of the imposed heat flux (this is a consequence of doing the tests in a fire resistance furnace) and that they are valid only when a char layer has been established (as they quantify the temperatures from the char front into the virgin wood) are potential sources of inaccuracy. Schaffer and others (Schaffer 1984, FPL 1999) mention that these curves are valid only when a quasi steady state has been attained. Thus, initial heating is completely neglected when using these equations, which can potentially cause design problems in the event of low temperature failure of structures, particularly in the connections. This is reinforced by evidence of low temperature collapse of timber structures, even before charring has significantly affected the timber members (Clancy 2001). Finally, the use of constant properties, such as the thermal penetration depth, or the absence of the moisture content could yield erroneous results.

In terms of experimental work, Schaffer carried out experiments with the aim of calculating charring rates (Schaffer 1967), and did in-depth temperature measurements using furnaces, exposing samples to the standard curve and to constant temperatures. He observed that charring of the surface occurred simultaneously to the ignition of the samples. He determined that the charring rates are direct functions of the furnace temperature, and developed equations for charring depth as a function of time.

Other works with the same objective are those by White and Schaffer (White & Schaffer 1981), who also exposed samples to standard furnace temperature - time curves and to constant temperatures. As discussed before, they performed measurements of moisture content vs. time curves. Hadvig (Hadvig 1981) performed an extensive series of tests on laminated and solid wood beams and blocks exposed to standard fire heating. He observed that laminated wood presented less cracks than solid wood, and found good agreement between the measured and predicted results. Frangi and Fontana (Frangi & Fontana 2003) studied the fire behaviour of timber beams and slabs, and obtained mean charring rates between 0.67 and 0.7 $mm \cdot min^{-1}$. Noren (Noren 1996) studied nailed connections under fire conditions, namely under ISO standard fire exposure, and performed 8 tests where temperature measurements were carried out. He determined that heat would flow one-dimensionally for the first 20 minutes of exposure. Takeda and Mehaffey (Takeda & Mehaffey 1998) did measurements and compared their results with a two dimensional model, showing close agreement, although the thermal boundary

conditions are not clearly defined. They conducted 4 small scale and 2 full scale tests on wood stud walls protected by gypsum board. White (White 1988), Shrestha et al (Shrestha, Cramer & White 1994) as well as Clancy and Young (Clancy & Young 2004) have conducted temperature measurements as part of efforts to validate analytical models that predict the pyrolysis of wood and the structural behaviour of walls in fires. White developed empirical models in terms of fundamental properties, and showed the importance of surface recession and the initial moisture content in the fire behaviour of wood. Shrestha et al have validated their model only to a temperature of 573 K. Clancy and Young observed that the thermal properties of wood vary little from test to test and mention that the temperature distribution in 90 x 45 mm wood studs is uniform until all moisture evaporates. They present no definition of the thermal boundary conditions.

In general, the number of tests carried out in each investigation is low, because of the greater scale of the samples. Also, the thermal boundary conditions are not clearly defined, a direct consequence of the utilization of fire resistance furnaces.

1.2.2 Furnaces

Roberts and Clough measured temperature profiles and mass loss rates in an inert atmosphere, as part of studies of wood pyrolysis (Roberts & Clough 1963). They concluded that wood pyrolysis can be represented in terms of a global one-step reaction, but using the final weight of the leftover char. Weatherford and Sheppard did ignition criteria studies of cellulosic materials in a furnace, where they measured surface temperatures (Weatherford & Sheppard 1965). They used convective heating from a non-radiant source, and they proved the concept of a fixed ignition temperature for the piloted ignition phenomenon. Tinney measured temperatures, mass loss rates and pressure inside wooden dowels heated in a furnace kept at a constant temperature (Tinney 1965). These studies used samples of smaller sizes, and, due to the nature of the research carried out, the thermal boundary conditions are more defined than in the previously exposed studies.

1.2.3 Fixed Heat Fluxes

The method used to measure temperature profiles in wood using a fixed imposed heat flux consists of heating timber samples -of a smaller scale than those used in the full sized fire

resistance furnaces- in devices that produce constant and quantifiable heat fluxes, normally radiative fluxes. Examples of these machines are the popular Cone Calorimeter (ISO 1993), the OSU calorimeter (Filipczak, Crowley & Lyon 2005) and custom made equipment.

The advantages of using this technique lie in the well defined boundary conditions, where the convective and radiative losses at the surface can be better quantified than at a furnace, while the imposed heat flux is easily measured by the use of a radiometer. Lee, Chaiken and Singer mention the importance of using constant incident heat fluxes (Lee et al. 1976). Also, the range of fire "severities" can be broadened, by testing the samples at different imposed heat fluxes. In terms of repeatability, the design of these machines is standardized in a much better way than the fire resistance furnaces, so in general the results are more reproducible between separate devices. Finally, the possibility of conducting not only temperature measurements but also measuring mass loss rates, heat release rates and ignition times and performing gas analyses and the fact that the experimental conditions as a whole can be controlled in a better way make these devices superior means to achieve a good understanding of the process of wood pyrolysis. In terms of disadvantages, as mentioned before, the scale of the samples is normally much smaller than the scale that can potentially be achieved in a furnace but this is offset by performing experiments in well defined environments whose results can easily be compared with those from other experiments and models.

Even though the data generated in the previous experimental studies can be used for the purposes of the present research project, it is not readily available in most of the cases, and the imposed heat fluxes and thermocouple depths in each individual study do not cover the whole range of exposures that can be generated in a fire.

The first work of this type was that of Bamford, Crank and Malan in 1945. They measured the temperature at the centre of the sample, which was irradiated on both sides by a luminous flame or by radiant heaters (Bamford et al. 1946). They determined a pyrolysis temperature of 570 K, and measured a minimum mass flux for spontaneous ignition. They also defined a concept of a "critically hot surface", which is the minimum surface temperature at which piloted ignition occurs, and is analogous to the constant ignition surface temperature used nowadays. They deduced an exothermic heat of pyrolysis based on the temperature measurements and the use of an Arrhenius expression. In addition, Crank and Nicolson developed a numerical method to solve the energy conservation equation that has proved a popular scheme, and in fact it was used in this work (Crank & Nicolson 1947).

Others carried on with this pioneering work, but focusing on the damage caused by nuclear explosions, like Williams (part of Hottel's group in MIT, which also included Gardon), who measured temperature profiles in two species of oven dried and moist wood under high radiative fluxes (Williams 1953). He concluded that wood is opaque to the radiation generated by a 2000 K body, and observed evidence of moisture migration away from the irradiated surface. He also observed that charring at any depth was coincident with a fixed temperature.

Martin (Martin 1965) subjected cellulose samples to intense radiation and measured surface and in-depth temperatures, as well as an analysis of the volatile products. He concluded that the transient temperature profiles are well represented by an empirical expression derived from parameter groupings, and stated that the pyrolysis reaction must be exothermic. He determined that sustained flaming depends on the mass flow of volatiles and not on a particular composition of the fuel-air mixture, and that spontaneous flaming ignition occurs at a constant surface temperature of 873 - 923 K. He finally concluded that cellulose decomposes in two ways, one producing volatile fuels and the other generating chars and water vapour, and that secondary reactions of the volatiles are produced in the surface of wood.

Blackshear and Kanury also measured temperature profiles inside cellulose cylinders using a complicated system to heat the samples and maintain a constant surface temperature (Blackshear & Kanury 1965). They observed that endothermic pyrolysis occurs at 593 K, and that exothermic devolatilization takes place at about 773 K. This secondary pyrolysis reaction augments the heat flux at the surface of the wood (this is the same observation as Roberts and Clough (Roberts & Clough 1963)). They finally observed that smaller samples exhibit a greater burning rate than larger samples, and concluded that diffusion and convection of mass will affect the internal heat transfer and heat source and sink strengths of the process.

Lee, Chaiken and Singer used laser radiation to heat wood samples and measured mass loss, densities, pressures and temperature profiles (Lee et al. 1976). They concluded that the thermal decomposition process is dependent on the heating rate and the heating time. For high heating rates, the pyrolysis reaction was estimated as being exothermic, while for low heating rates it is endothermic. This explains the discrepancies in the literature regarding the heat of pyrolysis, and implies that wood pyrolysis cannot be modelled with a one-step global reaction. They proposed a two step reaction, which involves the decomposition of tar into char and gas by an exothermic reaction. Kanury provides a review of the work carried out until the early 1970s, focusing on the ignition characteristics of cellulosic solids (Kanury 1972).

Following the initial years, several studies were done, focusing on pyrolysis of wood, burning rates, ignition and flame spread. Yoshizawa and Kubota studied cellulose ignition and measured temperature profiles to estimate the imposed heat flux on the samples (Yoshizawa & Kubota 1982). They observed that initial endothermic pyrolysis generates CO and CO_2, and that later exothermic reactions generate small amounts of hydrocarbons. Vovelle, Akrich and Delfau measured temperature profiles and mass loss rates for particle board (Vovelle, Akrich & Delfau 1984), and found that the mass loss rate is directly proportional to the instantaneous value of the heat flux absorbed during the transient pyrolysis stage. Chan, Kelbon and Krieger heated cylinders of wood, sawdust, cellulose and lignin with a xenon arc lamp and measured density profiles with X-rays, surface and in-depth temperatures, and performed devolatilization gases analyses (Chan, Kelbon & Krieger 1985). They concluded that pyrolysis must be an endothermic process, according to the comparison of experimental temperatures and model predictions, and that the effect of moisture evaporation cannot be neglected. They proposed three competing reactions for the decomposition of wood and one secondary reaction for tar. Comparison with experimental temperature profiles indicates that there are only few consistent values for the kinetic parameters of the reaction of wood transforming into char, but that the approach is fundamentally correct.

Kashiwagi, Ohlemiller and Werner measured mass fluxes, in-depth temperatures and evolved products in three different atmospheres on White Pine samples (Kashiwagi, Ohlemiller & Werner 1987). They determined that ambient oxygen concentrations increase the gas mass flux, inner temperatures, char depth and change the gaseous products distribution, as opposed to results from inert atmosphere tests. Char oxidation will increase the surface temperature as much as 200°C with respect to inert atmosphere results. Thus, great care must be applied when extrapolating results from inert atmosphere testing to air conditions. Fredlund conducted complete experiments where he measured heat release and mass loss rates, densities, temperature profiles and pressures within the samples for different wood species and chipboard (Fredlund 1988, Fredlund 1993). He observed that the pressure build-up is very sensitive to cracking. Comparison of modelling results with experiments showed good agreement between the measured and calculated densities, proving that the use of a one-step global reaction is valid.

Mikkola measured temperatures within wooden samples to obtain charring rates (Mikkola 1990, Mikkola 1992), observing that ISO standard furnace tests present a lower mass flux than tests conducted at other machines (i.e. Cone Calorimeter) because of a lower oxygen concentrations, as shown by Kashiwagi et al (Kashiwagi et al. 1987). He also determined that mass loss

rates decrease rapidly after the initial maximum value and attain a practically constant value. The derived charring rates assume that the mass loss rate is constant, and they are directly dependent on the external heat flux and decrease as the moisture content increases. Motevalli et al used a modified version of the LIFT apparatus to study flame spread, and measured in-depth temperature profiles but only at 3 mm below the surface (Motevalli, Chen, Gallagher & Sheppard 1992). They measured a surface ignition temperature of 645 K. Tran and White conducted experiments in an OSU calorimeter, and measured mass losses, heat release rates and charring rates for various wood species (Tran & White 1992). They concluded that char oxidation is a significant mechanism at low heat fluxes.

Suuberg, Milosavljevic and Lilly performed a complete study on the behaviour of charring materials in fires, working with cellulose samples (Suuberg, Milosavljevic & Lilly 1994). They mention that the pyrolysis process under fire conditions can be either heat transfer controlled or kinetic controlled, depending on the incident heat flux. At high heat fluxes, the charring front propagates with a constant velocity, but at low heat fluxes, charring does not progress at a constant rate because of the decrease in the heat flux at deeper positions. They mention the importance of having an accurate knowledge of the thermophysical properties of wood and conclude that no single set of kinetic parameters was able to fit all the mass loss data.

Bilbao et al made in-depth temperature measurements on laterally heated samples of pine in an inert atmosphere, for different moisture contents (Bilbao, Mastral, Ceamanos & Aldea 1996). They observed that the temperature gradients inside the solid increase with the incident heat flux and with the sample moisture content, while mass loss rates decrease when the moisture content increases. Tsantaridis and Ostman measured temperature distributions as part of a study of the charring of timber studs (Tsantaridis & Ostman 1998). The charring depths measured in Cone Calorimeter tests at 50 $kW \cdot m^2$ agree well with tests carried out in standard furnaces after 30 - 40 minutes of exposure.

Spearpoint and Quintiere measured temperature profiles, mass and heat release rates, smoke extinction and times to ignition of four species of wood, for burning rate calculations (Spearpoint 1999, Spearpoint & Quintiere 2000, Spearpoint & Quintiere 2001). They observed that burning rates depend on wood species, grain orientation, moisture content and exposure conditions. They mention that there is an apparently different ignition mechanism for wood at low and high heat fluxes, where at low heat fluxes glowing may play an important part.

Yang et al also have measured temperature profiles (Yang, Chen, Zhou & Fan 2002), and

Moraes measured temperature profiles in irradiated samples as part of her research on the failure of timber joints (Moraes 2003). Finally, Shen et al conducted experiments of pyrolysis of wet wood, and measured mass loss rates and temperature profiles (Shen, Fang, Luo & Cen 2006).

1.3 Prediction of Temperature Profiles

Several mathematical models have been proposed which can generate the temperature profiles of interest with various degrees of complexity and accuracy. The problem-solving approach ranges from simple empirical formulae to obtain in-depth temperature distributions (Schaffer 1967, Janssens & White 1994, Mikkola 1990, Klingsch et al. 1993) to the analytical or numerical solution of the energy, mass and momentum conservation equations with various degrees of assumptions and simplifications (Di Blasi 1993*a*, Fredlund 1993, Luikov 1975, Kung 1972, Bamford et al. 1946, Atreya 1983, Baum & Atreya 2007). The last set of models can be subdivided into those that consider a volumetric reaction for the pyrolysis of wood (Di Blasi 1993*a*, Fredlund 1993, Kung 1972, Bamford et al. 1946, Atreya 1983) or those that solve Stefan-like problems where pyrolysis and moisture evaporation take place in the moving boundaries (Luikov 1975, Spearpoint & Quintiere 2000, Baum & Atreya 2007, Galgano & Di Blasi 2004, Kocaefe, Younsi, Poncsak & Kocaefe 2006). A more complete description of these models will be presented in Chapter 4.

It is not clear whether these various degrees of complexity add improved degrees of accuracy in the prediction of temperature profiles. Some of the processes described need accurately measured parameters, like reaction schemes. There is no agreement whether the use of a single one-step reaction is valid or not (see the description of the previous experimental work). Even kinetic parameters present great spread (Di Blasi 2007). Models that include the pressure build up in the solid matrix should include structural changes, because the pressure build up will depend on the formation of cracks (Fredlund 1988), but this phenomenon is not well understood. Moreover, if the goal of the fire safety engineering community is to perform structural design using analytical methods, then the models that predict the temperature evolution of the timber elements must be simple to implement and cheap in terms of computational time, given that the design process is iterative and that the amount of calculations that must be carried out is large. Thus, the need to identify models that are accurate but as simple as possible is important

for the design process.

Several of these models have been compared with experimental data (Bamford et al. 1946, Kansa, Perlee & Chaiken 1977, Chan et al. 1985, Fredlund 1988, Suuberg et al. 1994, Do & Springer 1983, Bilbao et al. 1996, Kuo & Hsi 2005, Shen et al. 2006, Yang, Chen, Zhou & Fan 2003), but in general the agreement is good only for the initial heating stages, and the comparisons are not presented for varied conditions, for example for different heat fluxes and different depths from the exposed surface, although some exceptions exist (Fredlund 1988, Suuberg et al. 1994, Do & Springer 1983). Some of the models present the results only for short exposure times, but from a structural design point of view the behaviour should be modelled for a long period, in order to assure safe evacuation and fire fighting. Some models do not include the presence of water, and as will be shown in this work, it is important for the results. Finally, and as will also be shown in this thesis, most models show greater disagreements at later heating times, meaning that at higher temperatures and depths the process of wood pyrolysis is not well represented.

1.4 Present Work

A series of experiments were carried out with the main aim of developing a dependable procedure to obtain well characterized temperature distributions inside wood specimens subjected to radiant energy within magnitudes typical of fires. The methodology then allowed building up a set of reliable measurements in order to compare them against the results of the computational modelling of the pyrolysis process. Mass loss measurements were also performed, and the important variables that affect the models were linked to these results.

Since the pyrolysis and burning of wood has been rigorously and frequently studied experimentally over the past 60 years (see the previous section), the focus of the experimental study was not getting as much information as possible from each test but to only measure what was needed for this particular project. For this reason, no calorimetry measurements were done. The experiments were performed in two stages. The initial stage consisted of measuring the temperature profiles of wood samples exposed to various heat fluxes, while during the next step mass loss measurements were carried out using the same heat fluxes as in the previous phase. No temperature measurements were conducted in this latter stage to avoid interference of the thermocouples in the mass loss rate measurements.

The numerical study in this work consisted of an analysis of several representative models that predict the pyrolysis of wood, with a special emphasis on the prediction of in-depth temperature profiles. The aim of this part of the work was to identify the simplest model that accurately predicts the temperature profiles in wood elements exposed to high heat fluxes. The reason for this is the need to count with a simple and accurate model for the design process of timber structures, and also the fact that the previously presented results of temperature predictions do not seem to be accurate enough for these design purposes.

Different ways in which the energy conservation equation is represented by different authors, including terms that account for phenomena such as the convective transport of heat by volatile gases, the rise in sensible energy of the pyrolysis gases and the heat sink generated by the moisture evaporation, have been modelled. Also, different kinetic schemes have been studied, some of which include multiple competing reactions and others that assume a prescribed final solid density. Five models with various degrees of simplifications were constructed and their results were compared. This permitted to identify the terms which have a significant impact on the prediction of temperature profiles. Once the model that includes only the most important terms was identified, a comparison with the temperature measurements was performed.

This thesis is divided into six chapters. Chapter 2 details the experimental design and procedure, while Chapter 3 presents the main experimental observations and conclusions of the experimental process. Following that, Chapter 4 gives an analysis of the different numerical models for the pyrolysis of wood, and details the different models that were developed in this project, each one incorporating various simplifications. Chapter 5 compares the results of the different models, and then shows the prediction of temperature profiles of the simplest model and compares these predictions with the experimental measurements. Finally, Chapter 6 summarizes the main conclusions and gives some recommendations.

Part of the work presented in this thesis has been already published (Reszka & Torero 2008), and the reproduction of some of the written paragraphs has been done with the consent of the co-author, Professor José Luis Torero.

Chapter 2

Experimental Work

2.1 Instrument Description

The tests were carried out in a Cone Calorimeter (ISO 1993). This was simply for practical reasons, because for the purpose of this study only the load cell and the cone heater were used, thus the standard procedure for the operation of the machine was not followed. The cone heater was used in a vertical configuration (i.e. the exposed face is in a vertical position), with no piloted ignition source and under normal air conditions (cf. Figure 2.1). Even though no calorimetry was performed (therefore rendering the calibration of the gas analyzers unnecessary), the load cell and the incident heat flux were calibrated according to the normal procedures. The flow rate in the Cone Calorimeter exhaust duct was set to 24 $l \cdot s^{-1}$, according to the standard operating practice. The heat flux was measured with a Schmidt-Boelter gauge (Kidd & Nelson 1995).

The sample holder utilised during the experiments was not the standard Cone Calorimeter (ISO 1993), because the dimensions of the samples exceeded those of the sample holder. A steel plate of roughly the same dimensions of the specimen was bolted to the load cell, it was covered by ceramic fibre insulating board, and on top of it the samples were placed.

The thermocouples utilised were N-type with fibreglass insulation of a 0.2 mm strand diameter and a 2 mm sheath diameter. This type of thermocouple was developed to address the inherent instabilities of K-type thermocouples which are caused by long term exposures to high temperatures or by hysteresis between 573 K and 873 K (Childs, Greenwood & Long 2000, Majesko, Brady & Burley 1985). The fibreglass insulation allows the thermocouple to reach tempera-

tures as high as 813 K without sustaining considerable damage. The tip of the thermocouples was cut off after each test and a new junction was welded in order to ensure the total integrity of the device.

The thermocouples were connected to a data logger, which relayed the data directly into a computer where they were immediately recorded. During the first set of tests the data logger used was a Pico TC 08, while later in the project this was upgraded to an Agilent Technologies 34980 A. Images of the evolution of the samples were taken with an Axis network camera directly connected to a computer.

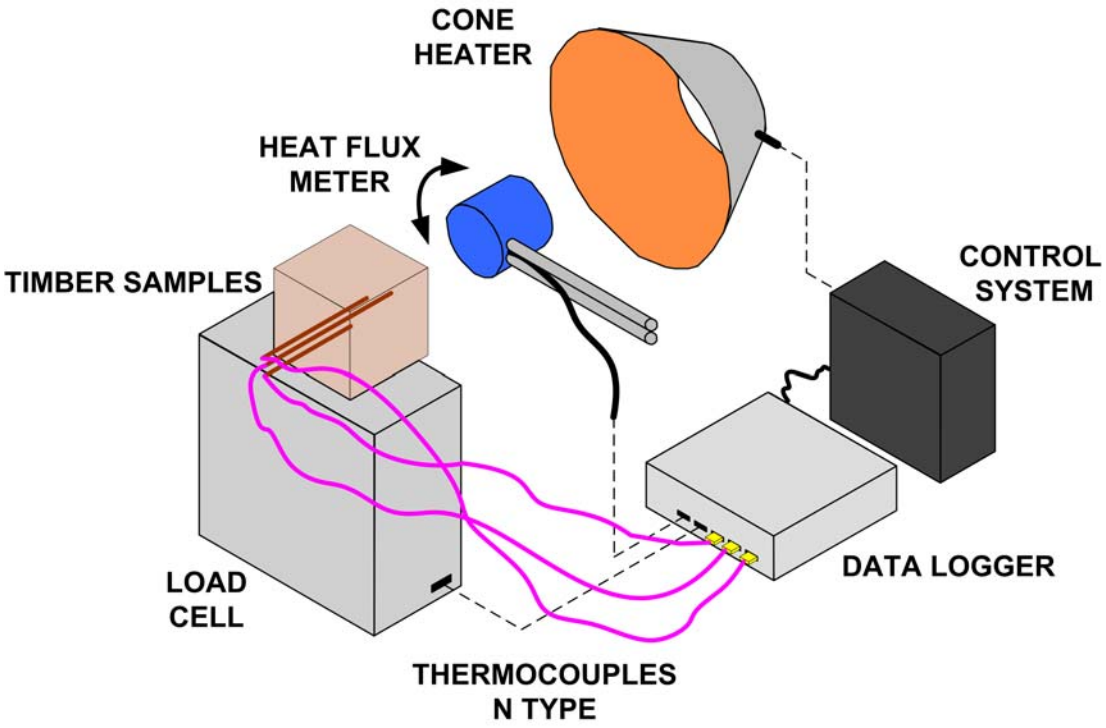

Figure 2.1: Schematic drawing of the experimental set-up, with the cone heater in vertical configuration.

2.2 Experimental Design

The design of the experiments involved the selection of the type of wood, the range of heat fluxes to be used, the number of thermocouples to be inserted in the specimen and their placement, heater orientation, the number of samples to be tested and finally the order in which the tests were going to be performed.

2.2.1 Wood Characteristics

The choice of the type of wood was to use a commercially available species which was commonly used in the timber construction industry. The species selected is Redwood Pine (Pinus sylvestris). Given the amount of tests to be performed and the limited time span of the project, it was decided to circumscribe the experiments to a single wood species. However, the tests were conducted for two different sample orientations (i.e. the incoming heat flux was parallel and perpendicular to the grain), which in effect constitutes two types of wood, due to the differences in the thermophysical properties of wood in both directions.

2.2.2 Test Conditions

The selected imposed heat fluxes for heating perpendicular to the wood grain were 10, 18, 25, 40 and 60 kW·m^{-2}. For the heating parallel to the grain, the selected heat fluxes were the extremes in the range: 10 and 60 kW·m^{-2}. These heat fluxes represent a wide set of exposures that is unusual for structural type analyses. Nevertheless, given the low temperature at which the physical changes start to take place in wood, it was deemed necessary to study exposures typical of the early stages of fire growth.

2.2.3 Temperature Measurements

Since the main outcome of the experimental process was to be a set of dependable in-depth temperature measurements of timber exposed to various heat fluxes, the choice of the number of thermocouples to be inserted in the samples was not a minor one. An obvious way to proceed was to place the thermocouples close to the centre of the specimen face, as there the effects of the heat losses through the sides of the sample are minimized and the assumption of a unidimensional transport of heat to the back of the wooden block is more certain.

Several researchers have performed in-depth temperature measurements of wood samples, and there is agreement on the way the thermocouples are placed: the junction and the wire leading to it are placed perpendicular to the direction of the incident heat flux (Bamford et al. 1946, Lee et al. 1976, Kashiwagi et al. 1987, Fredlund 1988, Tran & White 1992, Spearpoint 1999). The problem with placing the thermocouple parallel to the gradient of the temperature field (i.e. inserting the thermocouple from the back of the sample) when the surrounding medium

has a significantly lower thermal conductivity than the thermocouple wires is that a thermal disturbance is created by the presence of the thermocouple, which leads to a local descent in the temperature of the solid in the vicinity of the thermocouple junction (Beck 1962).

This thermal bridge is caused by the cold end of the thermocouple, and is reduced when the thermocouple is embedded from the side, as there is going to be an important portion of wire at a similar temperature, which reduces the heat losses and thus minimizes the temperature disturbance. However, when placing the thermocouple from the side the thermal bridge is not eliminated, and the problem generated is that the boundary conditions at the colder end of the wire are not well known: the temperature of the wire is not quantified and it will be affected by the incoming heat flux, which under certain conditions can even make the temperature of the exposed wire higher than the junction and cause a contrary disturbance (higher temperatures than the real ones). This is not the case with the thermocouples inserted from the back, where the exposed end of the wire is at ambient temperature.

Thus, two scenarios are encountered: one with lower disturbances but with undefined boundary conditions and another with greater disturbances but with boundary conditions that allow for a correction to be conducted. Other problems include an enhanced moisture vapour migration from the side holes, as opposed to the back holes, where moisture will recondense ahead of the evaporation front because of the temperature gradient.

Finally, a geometrical issue can also have influence on the results. If there is a misalignment when the thermocouple hole is drilled, an error in the depth of the thermocouple is generated (Figure 2.2). The error, δ, is expressed as a function of the misalignment angle, β:

$$\delta_{back} = r_{back} \left(1 - \cos \beta\right), \tag{2.1}$$

$$\delta_{side} = r_{side} \sin \beta. \tag{2.2}$$

The error is greater for the side thermocouples. Taking the shallowest thermocouple, the calculated errors are presented in Table 2.1.

It was decided to insert the thermocouples from the back of the samples and to carry out the appropriate correction. Tests with thermocouples inserted from the side were also performed,

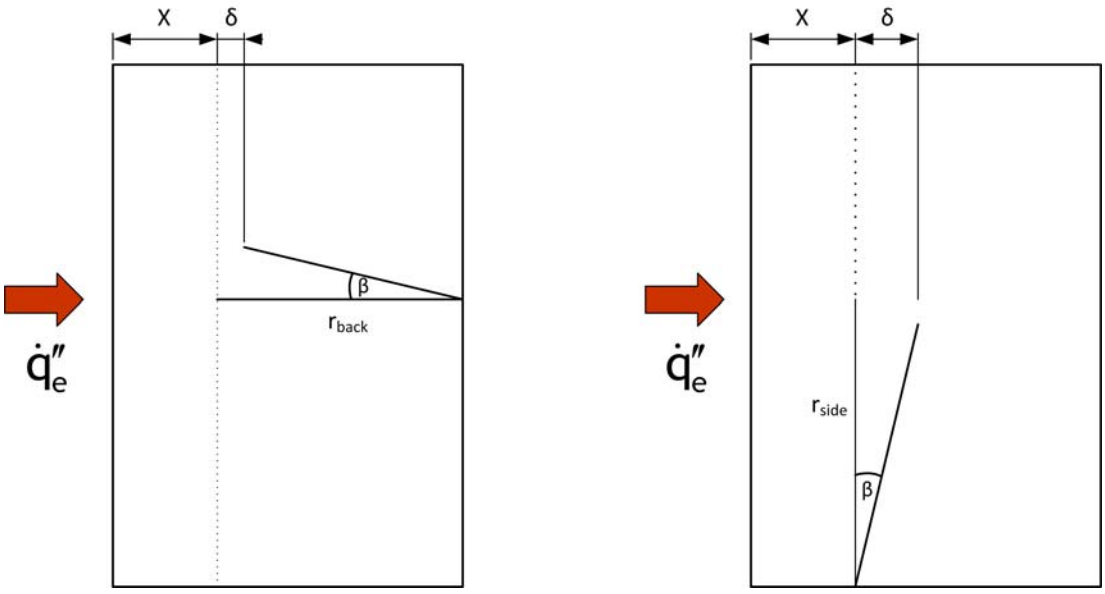

Figure 2.2: Error in the thermocouple depth generated by a misalignment of the drilled hole for thermocouples placed from the back and the side of the sample. Even though the drilled depth is lower when making the holes from the side of the sample, the error is greater, see Table 2.1

Misalignment Angle	**1°**	**5°**
δ_{back} **(mm)**	0.01	0.24
δ_{side} **(mm)**	0.87	4.4

Table 2.1: Calculated geometric errors for two misalignment angles. r_{back} = 62 mm; r_{side} = 50 mm.

and these have been used to establish the consistency of the measurements.

In conclusion, five thermocouples were inserted from the back of the sample, one at the centre of the exposed face and the rest on the intersections of the diagonals and a circle of 20 mm radius whose centre coincides with the centre of the sample face. The radius of the circle was chosen taking into account the distribution of the incident radiation provided by the heater (cf. Section 2.4 ahead) and by an estimation of the thermal penetration depth (by making the Fourier number equal to 1). The thermal penetration depth will give an idea of how deeply the material is thermally perturbed when subjected to a unit of heat in a given (characteristic) time (Incropera & DeWitt 2002):

$$L = 4 \cdot \sqrt{\alpha \cdot t_c}. \tag{2.3}$$

With t_c, the characteristic time, being defined as (Long, Torero, Quintiere & Fernandez-Pello

2000, Reszka & Torero 2008):

$$t_c = \frac{k\,\rho\,c_p}{{h_{tot}}^2}. \tag{2.4}$$

And α being the thermal diffusivity of wood. The choice of this characteristic time effectively makes the thermal penetration depth dependent only on the thermal conductivity and the total heat transfer coefficient (which includes the effects of convection and radiation), thus rendering it valid for zones close to the sample surface. With a value of h_{tot} of 35 W·m^{-2}·K^{-1} (for a more detailed explanation on how it was calculated see Appendix A), and using the ranges for the thermophysical properties of wood shown in Table 2.2 (the values were taken from (FPL 1999)), a maximum value for the thermal penetration depth of 17.2 mm is thus obtained.

Parameter	**Units**	**Range of Values**
k	W · m^{-1}· K^{-1}	0.10 – 0.15
ρ	kg· m^{-3}	450 – 550
c	J· kg^{-1}· K^{-1}	1700 – 2600

Table 2.2: Range of thermophysical properties used to estimate the thermal penetration depth.

It must be noted that the values for the thermal conductivity are for the heat flowing perpendicular to the grain. For heat flowing parallel to the grain, conductivity is on average 1.8 times greater (FPL 1999). So, placing the thermocouples at a minimum horizontal distance of 20 mm ensures that there will be no disturbance of the temperature field by the presence of a thermocouple nearby.

The thermal penetration depth can also be used to estimate the minimum depth interval at which the thermocouples should be embedded in the wood sample. Using the same reasoning as above, the distance of 17.2 mm should be increased at least two times to account for experiments with heating parallel to the grain. But here a clash of interests is encountered, because the idea is to produce measurements as closely spaced along the depth of the wood as possible. So a compromise has been done, and it has been chosen to place the thermocouples at 5 mm intervals.

It was decided to perform the tests using a vertical heater configuration because of greater simplicity in the determination of the boundary conditions, see Section 2.4. A disadvantage of the horizontal configuration is that the convective flows are not unidimensional (Incropera & DeWitt 2002), therefore affecting the assumption of heat flowing in only one dimension. Also,

the back end of the sample could be heated rather than cooled by the contact with the sample holder and its structure (Atreya 1983, Boonmee & Quintiere 2005).

It was decided that each sample would have 5 embedded thermocouples, all placed at the same depth. The number of replicate measurements (that is, the number of samples with the same thermocouple depth and same incident energy) was determined by estimating the confidence interval (Montgomery 2001). A given confidence interval is specified and, by having an estimate of the sample variance the number of replicates can be obtained, assuming that the random variables follow a normal distribution. The accuracy of the confidence interval is obtained by Equation 2.5, assuming that the experiment is a single factor experiment (taken to be the incident heat flux intensity):

$$X_{CI} = \pm t_{\alpha/2,N-a}\sqrt{\frac{2 \cdot S_E}{n}}. \tag{2.5}$$

With $t_{\alpha/2,N-a}$ being a random variable following the t distribution, 1-α = 0.95 the confidence coefficient, S_E =15 K the sample standard deviation, $N = n \cdot a$ the total number of observations, a the number of levels of the factor and finally n being the number of replicate measurements. These values give a minimum number of replications of 2 (n =10, 5 thermocouples per replication), but in order to account for possible failures in the temperature readings it was decided to perform 3 replications (n =15). With 15 measurements, the accuracy of the confidence interval is smaller than the standard deviation, indicating a greater accuracy.

2.2.4 Sequence of Tests

The order in which the samples are tested is also relevant to the outcome of the experiments. Systematic errors could be involuntarily introduced, and if the samples were all tested following a given order, the results could be severely affected by them. Thus the order in which the experiments were carried out was randomized to minimize this type of error.

2.3 Experimental Procedure

Four sets of tests can be identified: temperature profile tests with the imposed heat flux perpendicular to the wood grain, temperature profile tests with the imposed heat flux parallel to

the grain, mass loss tests with the imposed heat flux perpendicular to the grain and finally mass loss tests with the imposed heat flux parallel to the wood grain. More emphasis was nevertheless placed on the cases of the imposed heat flux being perpendicular to the grain, as this is the most common case in timber structures (due to the way trees grow, the longest dimension is in the direction of the grain, therefore beams and columns are heated perpendicular to the grain for most of their surface). The cases for heating parallel to the grain are thus coarser in terms of the values of the imposed heat fluxes and thermocouple depths. They were carried out for comparison with the perpendicular heating case.

In each temperature profile test, five thermocouples were placed at the same depth in 2 mm diameter holes drilled perpendicular to the exposed surface. The holes were drilled from the back (unexposed) side of the specimen. The perpendicular heating tests comprised samples with thermocouple junctions placed at depths of 5, 10, 15, 20, 25, 30, 35 and 40 mm from the exposed surface. For the parallel heating temperature profile tests the thermocouples were placed only at depths of 5, 10, 15, 20, 25 and 30 mm from the specimen surface.

As was stated before, the incident heat fluxes ranged from 10 to 60 kW·m^{-2} (10, 18, 25, 40 and 60 kW·m^{-2}), with the parallel tests only being done at the extremes of this range, while the perpendicular heating ones were conducted for a greater amount of heating intensities. Each experimental condition (i.e. heat flux and thermocouple depth, or only heat flux for the mass loss tests) was repeated three times, which means that there are 15 temperature-time measurements for every thermocouple depth - imposed heat flux value. This allows for enough data to be collected and thus unreliable data can be discarded with entire confidence that it will not greatly affect the confidence interval of the measurements (as was discussed in Section 2.2). A total of 120 perpendicular heating temperature tests and 36 parallel heating temperature tests were carried out. For the mass loss tests, 15 were conducted for perpendicular heating while 6 were done for heating parallel to the wood grain.

During the first series of tests only temperatures were recorded, with no mass loss measurements or gas analysis performed. Measurement of the ambient temperature in the test chamber of the Cone Calorimeter was carried out. The results were averaged, discarding evident faulty readings and truncating the temperatures at the point where the different repetitions started to show a divergent or erratic behaviour. In the mass loss tests only data from the load cell was recorded. The results were also averaged, discarding bad results, but no truncation was performed, averaging the data for the duration of the particular test.

2.3.1 Sample Preparation

The sample dimensions were ~ 100 x 98 mm on the exposed surface and a 67 mm depth for the perpendicular heating experiments and of ~ 93 x 93 mm with a depth of 81 mm for the parallel heating tests. This divergence was due to stock problems in the timber suppliers. The blocks of wood were cut from dressed, kiln dried planks. The samples were stored for 40 days before the beginning of the tests in a room with quiescent air in order for them to attain an equilibrium moisture content. The temperature and relative humidity in the room were recorded daily.

Even though the wood was not conditioned as other researchers have done it, storing the samples for longer periods of time (of the order of months) in controlled atmosphere environments (Atreya 1983, Fredlund 1988, Spearpoint 1999), the storage conditions are adequate for the samples to attain equilibrium conditions and are closer to what would be encountered in real dwellings, where wood in service is exposed to daily and longer term changes in relative humidity and temperature (FPL 1999).

The sample moisture content was measured in two ways: before a weekly set of tests was carried out, two representative specimens were oven dried and then discarded; and prior to each experiment, the moisture content of the sample to be tested was measured using an electrical moisture meter.

The testing was conducted in two separate periods of time, namely during the summer and fall of the year 2005 and during the summer of 2007. The average moisture content of the samples tested during 2005, calculated with both methods, was of 10.3% (based on the oven dry weight), while the average for those tested in 2007 was of 9.6%. These results are in agreement with published values of equilibrium moisture content of wood at ambient conditions similar to those recorded in the storage room (FPL 1999). For all modelling purposes, the moisture content in the samples has been taken to be 10%.

As stated before, specimens for the temperature profile tests were fitted with 5 thermocouples, inserted in 2 mm holes drilled from their unexposed face. In each test, all the thermocouples were placed at the same depth from the exposed surface of the sample. The depth of the 2 mm holes corresponded to the depth the thermocouples should be placed at. The holes were drilled in a standard workshop drill. One hole was drilled on the centre of the sample face, while the remaining four holes were drilled on a 20 mm radius circle around the first hole, on the diagonals of the sample face (see Figure 2.3).

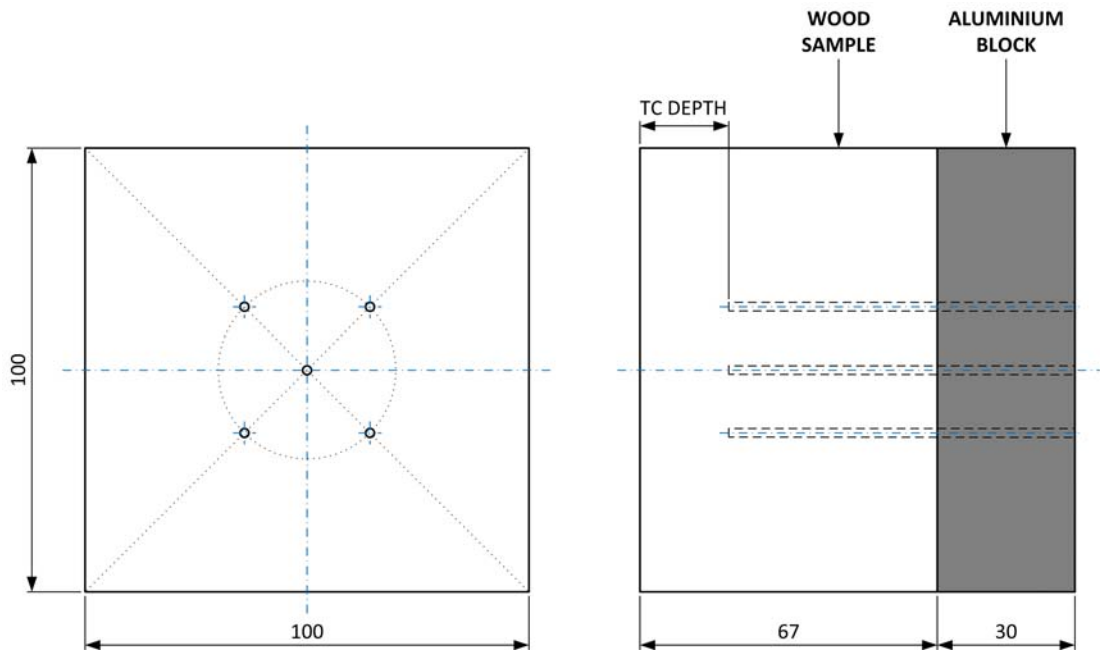

Figure 2.3: Dimensions and layout of the sample, aluminium block and thermocouples. In each particular temperature profile test, all the thermocouples were placed at the same depth. For mass loss rates, the samples had a slightly smaller cross-sectional area and a greater depth, but the aluminium block was still attached to their back.

An aluminium block (100 x 100 x 31 mm) was attached to the back of the sample as a means of providing a well defined back-end boundary condition (see Figure 2.3). For all tests an extra thermocouple was fitted at the interface between the sample and the aluminium block to track the evolution of its temperature (Measurements showed that the aluminium block had a constant temperature along its depth during the test, and the calculated Biot number for the block is 2.1 $\times 10^{-3}$).

The sample preparation for the mass loss tests did not involve any positioning of thermocouples, but the aluminium block was fitted, to count with the same boundary conditions as in the temperature experiments. Prior to each experiment (mass loss and temperature), the specimen was weighed and its dimensions measured. The sample density was then calculated.

2.3.2 Testing

Before the beginning of each test, the incident heat flux was measured. This was done because the order of the tests was determined randomly, so in general two consecutive tests would have different required heat fluxes. This was done even for two consecutive tests having the same heat flux.

The load cell was calibrated on a daily basis. No studies were done to determine the influence of temperature on the output readings, although the load cell was wrapped in aluminium foil during the mass loss tests. It must be said, however, that even for the higher heat fluxes the ambient temperature never rose to more than 10 K (see Section 2.4 ahead). It was observed in the preliminary testing that as the tests were done the temperature in the testing compartment rose, and therefore the heat flux read by the gauge would increase for a fixed heater temperature. It was decided that after each test the heater temperature would be brought down, and the doors of the compartment left open so that it would cool down.

Once the sample was ready and the Cone Calorimeter was calibrated and set to the required heat flux, the specimen was mounted on the sample holder and its position was carefully checked so that the exposed face was placed right on the centre of the cone heater. The distance from the heater was set to be 1 inch, following the standard Cone Calorimeter procedure (ISO 1993).

A shield was placed on the cone heater prior to the mounting of the wooden block, so that the sample was exposed to the imposed heat flux only when the test begun. The removal of the shield marked the beginning of the tests. The experiments would continue until the temperature readings reached 800 K, but in the cases of the lowest heat fluxes with the deepest thermocouples the tests were stopped before this condition was attained because the tests had to be finished at the end of the day as they could not be left running overnight. Mass loss tests, on the other hand, would continue as long as possible, ideally until the whole wood had pyrolyzed and charred. Again, some tests had to be stopped at the end of the day.

After the end of the test the specimen was removed from the sample holder and left to cool down for some instants in the Cone Calorimeter compartment. Then the aluminium block and the thermocouples were retired at the same time, with care taken so as not to move the thermocouples from their fixing in the aluminium block. This was done because the length of the thermocouples was then measured; this indicated whether they had been placed at the proper depth and gave some light on the reason for some potential spurious readings (that is, the thermocouple could have not been placed at the correct depth). The thermocouple junctions were re-welded prior to each test, and they were tested for electrical continuity to ensure that the welding was not faulty.

2.4 Quantification of Thermal Boundary Conditions

The thermal boundary condition at the exposed face of the specimen is made up of three components: the imposed incident heat flux, and heat losses due to convection and radiation. The first of these can be easily quantified, using the Schmidt-Boelter radiometer in the Cone Calorimeter, but relies on the assumption that the radiant energy is constant throughout the whole exposed surface of the wooden block. The other two components of the boundary condition depend on assumptions made about the flow conditions around the sample and about the temperature of the surrounding air and enclosure.

While the bottom face of the specimen is in contact with the insulating board, the rest of the lateral faces are in contact with the surrounding air and the back face is attached to the aluminium block (See Figure 2.4). The modelling work undertaken as part of this research project assumes that the heat flow through the wood block, when exposed to heat fluxes in the Cone Calorimeter, is unidimensional (the validity of this assumption will be discussed in the Chapter 3). So if that assumption is followed, then the heat losses through all the lateral faces of the sample can be neglected. Thus only the thermal boundary conditions of the back face need to be quantified.

There are two ways to treat the boundary condition at the back of the sample. Since the presence of the aluminium block is for improving the heat exchange of the back of the specimen with the surroundings, in order to avoid the back end temperature from rising above the ambient temperature and thus having a well defined boundary condition, it can be assumed that the back temperature will be ambient (thus considering a semi-infinite solid) or that the heat losses through the back are enhanced basically because of an increase of the surface area. It must be noted that the thermal contact resistance between the wood and the aluminium has been neglected in this analysis.

2.4.1 Incident Heat Flux

The incident heat flux in the Cone Calorimeter is measured by placing a radiometer 1 inch away from the base of the heater, in the centre of the base plane. Janssens (Janssens 1991) reports that the heat flux over a 50 mm side square in the centre of the base plane is within 5% of the reading obtained using the radiometer. Measurements were carried out in the Cone Calorimeter

Figure 2.4: Photograph of a specimen during a test. The cone heater is located at the left of the photograph. The aluminium block is seen at the right of the sample, while the white object underneath the wood specimen is the ceramic fibre insulating board.

used in the testing, and the results are satisfactory (see Figure 2.5): the heat flux varies less than 10% in the region within 40 mm from the centre. Thus, in the region of interest, i.e. where the thermocouples are placed (a 20 mm radius circle around the centre of the sample), and given the fact that a one-dimensional heat transfer is assumed, it can be confidently said that the incident heat flux on the specimen is uniform and that its value is that measured by the radiometer.

2.4.2 Convective Losses

The calculations to obtain the convective coefficient are detailed in Appendix A. The results show that the Rayleigh number reaches a maximum value of ~ 3 x 10^6 (at 400 K), therefore the flow is always laminar for the temperature range studied. So, using a correlation for a flat vertical plate (Incropera & DeWitt 2002), a convective coefficient of around 10 $W{\cdot}m^{-2}{\cdot}K^{-1}$ has been calculated for the exposed face.

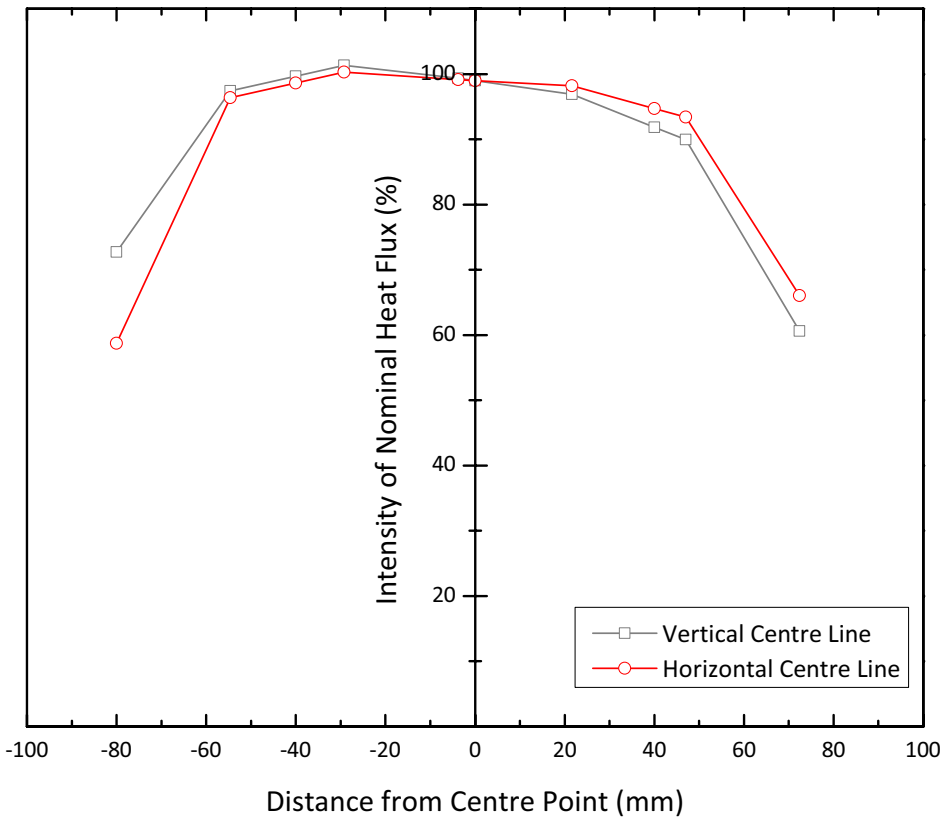

Figure 2.5: Intensity of the incident heat flux as a percentage of the measured heat flux in the centre of the heater base plane. In the case of the horizontal centre line, negative values in the abscissa are positions to the left of the centre point, looking into the heater. For the vertical centre line, negative values in the abscissa are positions above the centre point. It can be seen that the area where the thermocouples were located (a 20 mm radius circle around the centre of the specimen) is close to the nominal heat flux.

The back face presents the complexity of the aluminium block. Since the philosophy of the pyrolysis modelling carried out in this project is to be as simple as possible, it was chosen not to model it. So an estimation of an equivalent boundary condition had to be performed. As stated before, the presence of the aluminium block was aimed at keeping the back surface temperature as close as possible to the initial temperature for the longest possible time. Figure 2.6 presents the measured temperatures at the back of the specimen, and it shows a 50 K increase after 3000 s of exposure to the highest heat flux in the test range, as opposed to an increase of 20 K for an intensity of the radiant flux of 25 kW·m^{-2} at the same time.

Thus, for all practical purposes a temperature increase of 50 K is the maximum to be expected for the back of the wooden block. An estimation of the energy dissipated by the aluminium

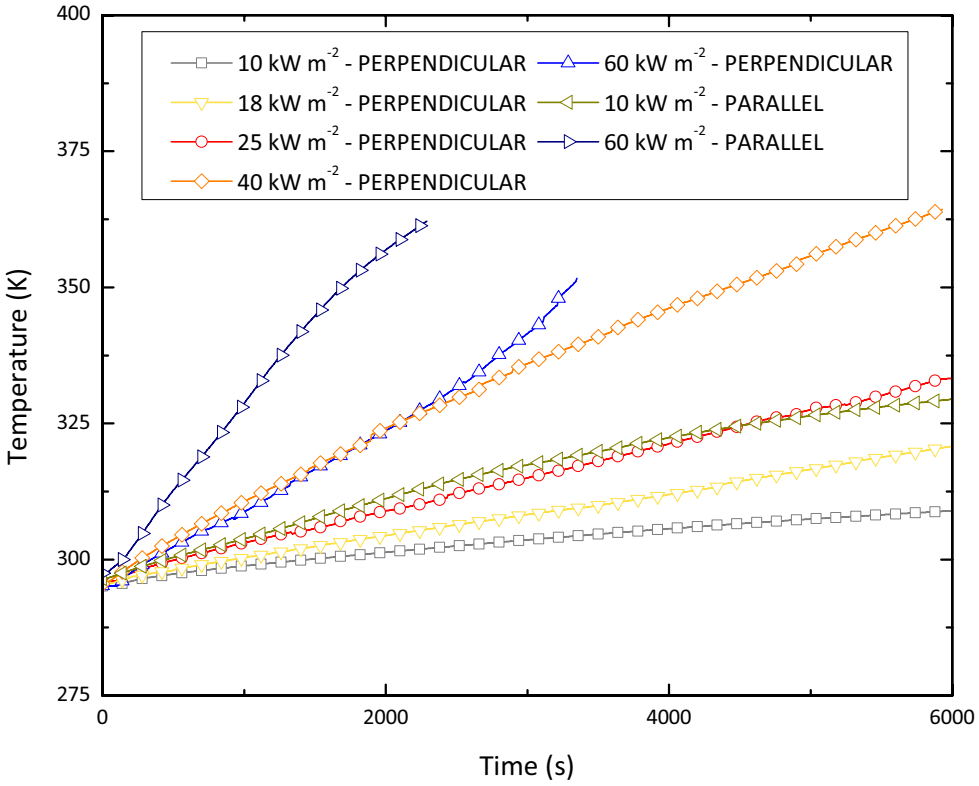

Figure 2.6: Evolution of the back surface temperature for various tests at various heat fluxes. Parallel heating tests show higher temperatures because of the higher thermal conductivity parallel to the wood grain. Measured temperatures at the back of the aluminium block showed that both temperatures are the same.

block has been conducted supposing the block to behave like a fin. The energy dissipated by the block is estimated, and then an equivalent convective heat transfer coefficient is calculated by assuming that the previously calculated energy is lost at the back end of the sample without the presence of the aluminium block. A more detailed description of the calculation is given in Appendix A. The calculated value for the convective coefficient at the back of the sample is 11.87 $W{\cdot}m^{-2}{\cdot}K^{-1}$. As it can be seen, the estimated convective coefficients for the front and back surfaces are similar, so it has been decided to use a value of 12 $W{\cdot}m^{-2}{\cdot}K^{-1}$ for the convective coefficient on both surfaces.

This value is similar to that estimated by Janssens for the Cone Calorimeter (13.5 $W{\cdot}m^{-2}{\cdot}K^{-1}$, (Janssens 1991)), although he states that this value is valid only for the heat flux range of 20 - 40 $kW{\cdot}m^{-2}$, and that at higher heat fluxes the convective coefficient should rise. He obtained that value carrying out surface and back temperature measurements on samples of various

materials and then applying an inverse technique to estimate the amount of heat conducted through the specimen. The best fit values of the conductive coefficient and surface emissivity were estimated using an optimization program by using the heat balance equation at the surface of the sample (i.e. incoming heat flux minus radiative and convective losses must be equal to the conducted heat through the sample). Thus, the value of the convective coefficient calculated for this study is deemed correct.

2.4.3 Radiative Losses

The magnitude of the radiative losses will depend on the temperature of the surrounding enclosure. No temperature measurements of the surrounding surfaces were performed; however, the surrounding air temperature was measured. Figure 2.7 shows the air temperature evolution for different perpendicular heating tests. The higher heat fluxes show a faster temperature rise, except for the 25 kW·m^{-2} test, which heats up slower than the 18 kW·m^{-2} case. This difference is attributed to colder initial ambient conditions at the start of that particular test. Even so, the graph gives an idea of the magnitude of the temperature rise in the Cone Calorimeter chamber, where for most of the tests it reaches a maximum value of 10 K. This justifies the use of a constant ambient temperature, which in the models has been set to be 295 K, the average initial temperature for all the tests.

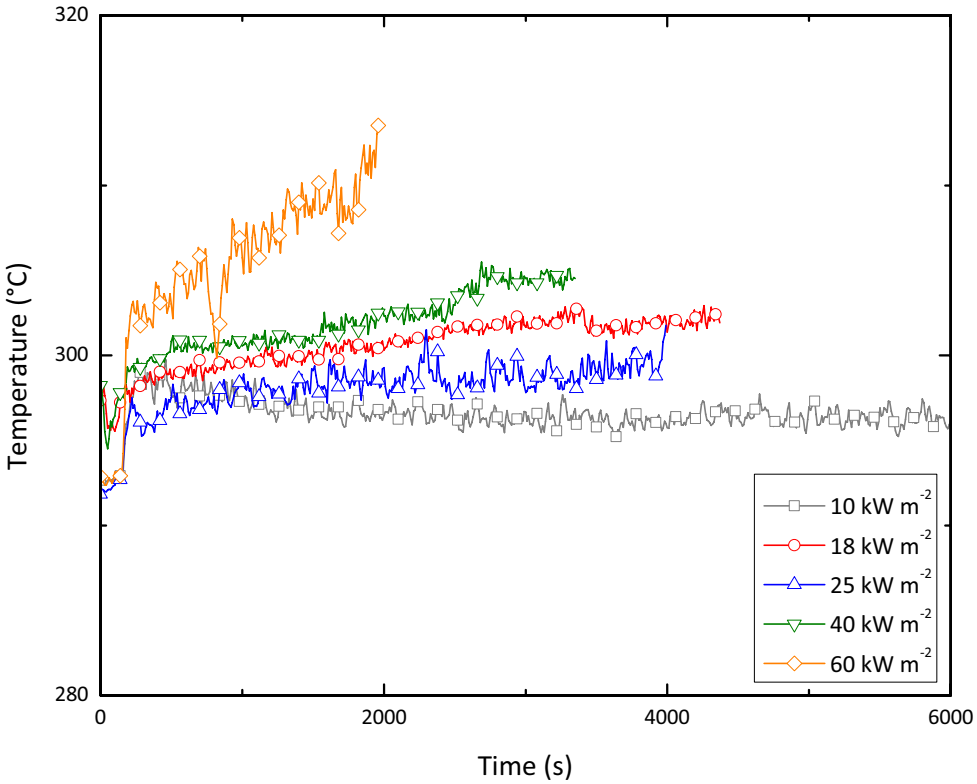

Figure 2.7: Temperature rise in the Cone Calorimeter chamber for various heat fluxes. These temperatures correspond to ambient air temperatures; the thermocouple was placed behind the specimen in order to prevent any errors caused by the radiative heat flux from the cone heater on the thermocouple junction.

Chapter 3

Experimental Results

3.1 Visual Observations

3.1.1 A Sample Case

In order to illustrate the behaviour of the wood samples during the tests, the case corresponding to an incident heat flux of 40 kW·m^{-2} will be presented as an example. When a vertical sample of wood is just exposed to a high intensity heat flux, the only noticeable changes in its surface are the release of vapours and pyrolysis gases. After 50 s of exposure, the front surface becomes completely black. The mass loss rate shows an increasing trend in the initial heating stages (see Figure 3.1), until 140 s, when it reaches its maximum value. At this time, the thickness of the char layer has grown to about 1 mm (cf. Figure 3.3), while the measured temperature in the shallowest thermocouple is of 369 K (96°C; Figure 3.2). An advancing front of liquid water is observed to flow out of the sample as early as 20 s after the beginning of the test. At 140 s, the front is at a deeper position than that of the shallowest thermocouple, namely between 7 and 8 mm from the exposed surface. The speed of the moisture front shows its maximum value closest to the surface, and then decreases as the test progresses and reaches an asymptotic value of approximately 0.005 mm·s^{-1} (refer to Figure 3.31 later in this chapter).

The recorded temperatures at the time the moisture front passes the position of the thermocouples are on average 359 K (85°C) and do not increase as the moisture front penetrates deeper into the sample (cf. Figure 3.32). In the vicinity of 373 K (100°C) there is a slowing down in the heating rate which is caused by the heat sink generated by moisture evaporation. This change in gradient becomes less marked as the depth increases, but at deeper positions its

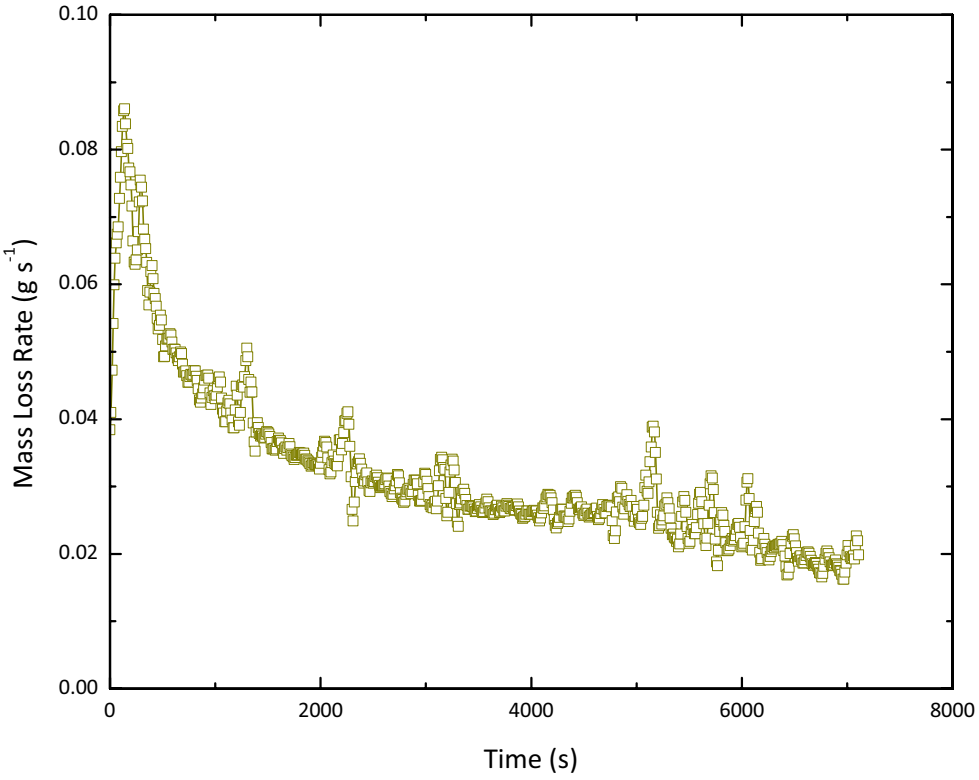

Figure 3.1: Average mass loss rates for an external heat flux of 40 kW·m^{-2}, perpendicular heating. The maximum value is attained at 140 s. The steady decrease in the mass loss rate after the peak value is caused by the increase in depth of the char layer. Surface glowing starts at 150 s of exposure, while flaming combustion begins at 3800 s.

effects are noticed until higher temperatures (see Figure 3.9).

As the moisture front progresses away from the heat source, the char layer keeps growing, establishing a second front. In this period, the propagation of both fronts is controlled by the heat transfer from the heater into the wood sample. Once the moisture has migrated away from the zone where the thermocouple is located, the heating rate suffers another inflexion, increasing its gradient, and the temperature rises, exceeding the accepted pyrolysis temperature in the vicinity of 573 K (300°C, (Schaffer 1967, White & Schaffer 1981, Frangi & Fontana 2003)). No clear change in the heating rate can be observed at these temperatures, indicating the weak nature of the pyrolysis reactions ((Atreya 1983, Di Blasi 1993*b*, Chan et al. 1985); Figure 3.9). Once this temperature has been surpassed, it can be assumed that wood has already begun to pyrolyze, thus an estimation of the progression of the charring front can be made (Schaffer 1967, White & Schaffer 1981).

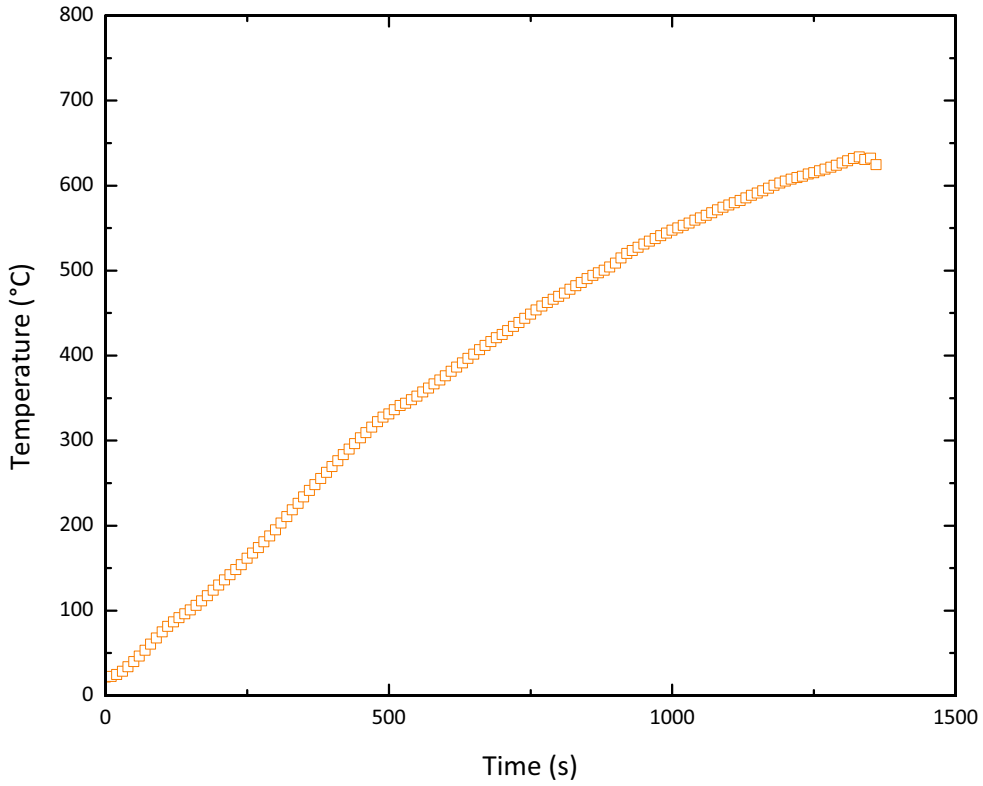

Figure 3.2: Average temperature history for an external heat flux of 40 kW·m^{-2}, perpendicular heating, and a thermocouple depth of 5 mm. A weak effect of moisture evaporation is noticed at a temperature of 100°C. The maximum mass loss rate is attained at 140 s, while surface glowing starts at 150 s of exposure.

The mass loss rate, after reaching its maximum value early in the test, decreases steadily, to converge to an asymptotic value close to 0.02 g·s^{-1}. This decline is caused by an increase in thickness of the char layer, which has greater insulating properties than virgin wood (Kung 1972, Atreya 1983), which in turn slows down the heat transfer into the virgin wood. Also, as the surface temperature increases, heat losses, mainly by reradiation, become important and decrease the net heat flux entering the solid (Atreya 1983).

Observation of the movement of the fronts indicates that the heating process is one-dimensional, because they move parallel to the exposed surface most of the time. Figures 3.3 to 3.8, which show the evolution of the sample as it is heated, also depict the movement of the moisture and charring fronts. The fronts move in a relatively parallel manner for almost two-thirds of the duration of the test, or about 3600 s. Although the speed of the charring front was not measured, visual observation indicates that its movement is slower than the moisture evaporation front, as

the separation between the two fronts increases with time; cf. Figures 3.3 to 3.8.

Another way of estimating the one-dimensional nature of the movement of the fronts is by inspection of the individual thermocouple readings. Since all thermocouples in a test are placed at a same depth on a plane bounded by a 20 mm radius circle, their readings are an indication of how parallel the heating wave is (and therefore the moisture and pyrolysis fronts) with respect to the vertical plane. The readings show, for an incident heat flux of 40 kW·m^{-2}, that for an average temperature of 373 K (corresponding to the moisture evaporation front), the spread in the thermocouple readings (including the deepest thermocouples) is ±10 K, and for an average temperature of 573 K (corresponding to the pyrolysis front) the spread increases to ±50 K. These figures confirm that the moisture front moves in a parallel manner up to the deepest positions, while the charring front moves in a less uniform manner. The results for other heat fluxes are shown graphically in Appendix B.

A final way of assessing the movement of the fronts is by inspection of the samples once the tests have finished. Figure 3.19, presented later in this chapter, depicts a sample exposed to a 40 kW·m^{-2} heat flux with thermocouples placed at a depth of 10 mm. The cross section reveals that the charring front is relatively parallel to the exposed surface at the time the test was stopped.

Another aspect to note from Figures 3.3 to 3.8is the effect of the insulation properties of the ceramic fibre board placed on the sample holder. It has been observed that the speed of the fronts is faster at the bottom part of the specimen, which occurs due to a reduction of the heat losses that makes the temperatures in that zone of the sample be higher than in the rest of it, therefore speeding up the degradation reactions.

Once the temperature has become high enough to allow for the oxidation of char, glowing, or smouldering ignition, commences. It is first observed on the exposed surface of the sample at 150 s after the beginning of the test. Though initially weak, later in the test glowing becomes more generalized, thus increasing the heat flowing into the sample. This extra heat flux into the sample was not measured, but is believed to be important for the evolution of the in-depth temperatures, as will be shown in Chapter 5. At this stage, a recession of the char surface begins, leaving ash residues (Figure 3.4). Structural changes, namely the appearance of cracks on the surface of the wood, begin to appear at similar times (Figure 3.4). The presence of cracks enhances the radiative transfer into the wood matrix (Roberts 1971). This increase in the heat flux reaching the virgin wood is not noticed either in the mass loss rates or in the moisture front

Figure 3.3: 140 s: maximum mass loss rate is attained at this time. The moisture evaporation front corresponds to a lighter coloured line on the left side of the sample. At this instant the front is parallel to the exposed surface. Sample is exposed to an incident heat flux of 40 $kW \cdot m^{-2}$, perpendicular heating.

speeds, which, as was previously mentioned, are both decreasing in time.

In some of the tests, transition to flaming combustion occurs. A pulsating flame first appears at the top of the sample (cf. Figure 3.5). This occurs at about 3800 s. At this time, the moisture front has almost reached the back of the sample, and it has ceased to move parallel to the exposed face, therefore giving less validity to the assumption of one-dimensional heating. No increment is observed in the mass loss rates at this time (see Figure 3.1), while the surface has receded about 20 mm, thus showing that the recession front will reach the position of the thermocouple roughly when it reads a temperature of 820 K (see Figure 3.9).

The flame then propagates to the charred surface of the sample, and surface charring rapidly advances to cover the remaining virgin wood in flames, as can be seen in Figures 3.6 and 3.7. Because this is a surface process, a new charring front will be created from the sides of the sample advancing to its interior, thus rendering the assumption of one-dimensional heating

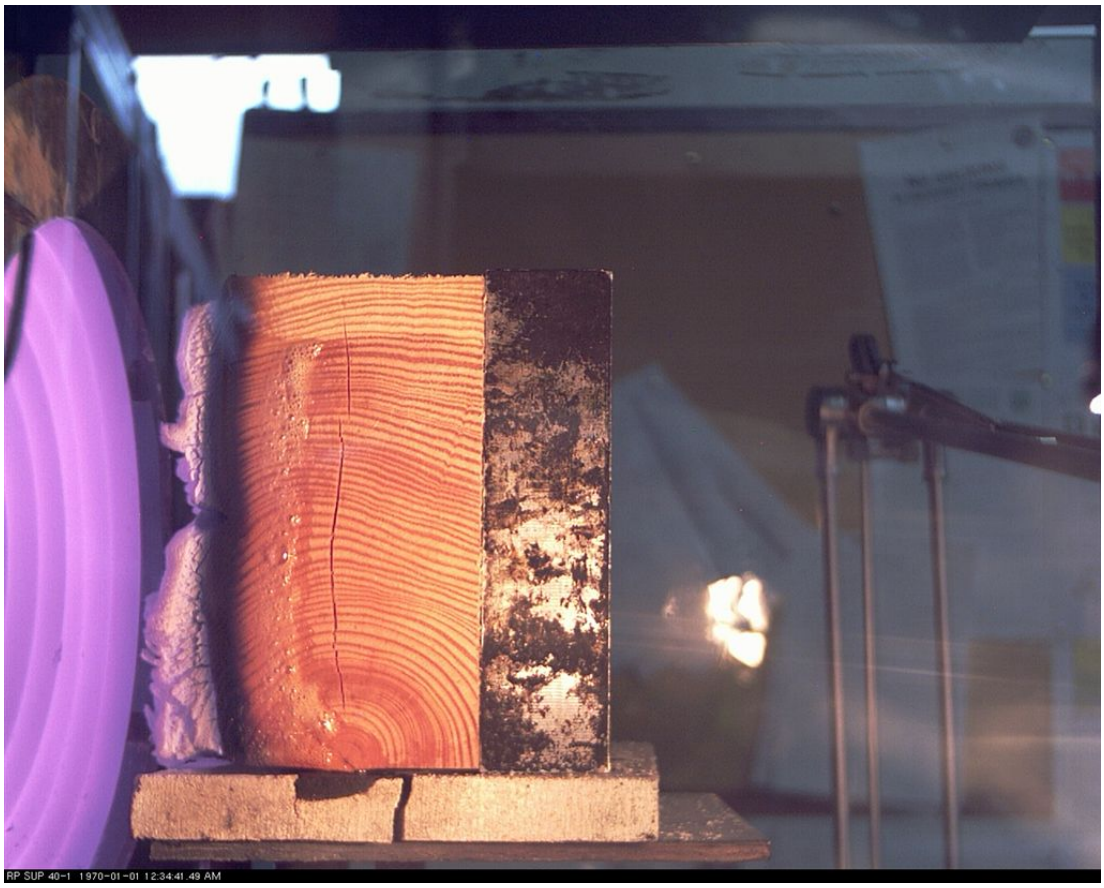

Figure 3.4: 1460 s: surface oxidation and cracking have become important. Cracking is also observed on the sides of the sample. Note the charring front moving in parallel to the moisture evaporation front. Sample is exposed to an incident heat flux of 40 kW·m^{-2}, perpendicular heating.

invalid. More pyrolyzed material is observed in the edges than in the central sections of the sample, where the thermocouples are located (Figure 3.19). After the sample has been burning for a considerable time (about one-third of the duration of the test), flaming will reduce its intensity and the pulsating flame returns to the top of the sample, until it dies out (cf. Figure 3.8).

3.1.2 Summary

The duration of the tests was in the order of tens of minutes for the higher heat fluxes and in the order of hundreds of minutes for the lower fluxes. Flaming ignition was observed after minutes of exposure for the higher heat fluxes (i.e. > 40 kW·m^{-2}), while at 10 kW·m^{-2} the charring process occurred slowly and glowing was observed only after hours of exposure for some of the samples, while for others it was not observed at all. This erratic behaviour separated the tests at

Figure 3.5: 3950 s: transition to flaming. Pulsating flame is first observed on the top portion of the sample. Note the how the moisture evaporation front is now at an angle with respect to the exposed surface. This is caused by the insulating effect of the ceramic fibre board on the bottom of the sample. Sample is exposed to an incident heat flux of 40 $kW \cdot m^{-2}$, perpendicular heating.

this energy intensity from the rest. This phenomenon is explained by the onset of the pyrolysis reactions close to this heat flux, as will be detailed subsequently. Parallel heating samples had a different behaviour, with for example some cases not presenting flaming ignition at all (at 60 $kW \cdot m^{-2}$), as opposed to the perpendicular case where flaming was always observed.

In most of the temperature measurements, a change in the heating gradient is identified in the vicinity of 100°C, showing the effect of the evaporation of the moisture contained within the wood. In the deeper positions, this effect is weakened, because the heating rate is slower than the loss of moisture, but still there is an increase in the heating rate above that temperature (i.e. once the moisture has been removed).

Tables 3.1 and 3.2 summarize the approximate times for the most important observations occurring at the surface of the specimen. Note that these values are intended to serve only as

Figure 3.6: 3965 s: flame descends to the sides of the sample. Pulsating flame now is located over the pyrolyzed parts of the wood. Sample is exposed to an incident heat flux of 40 $\mathrm{kW{\cdot}m^{-2}}$, perpendicular heating.

reference, as there is scatter between each test repetition and they depend on the criterion of the person making the observations. This is especially true for events that occur at longer times, because the experimenters did not stay at the Cone Calorimeter for the whole duration of the tests. Retaking the previous example, glowing ignition was observed for some samples at 10 $\mathrm{kW{\cdot}m^{-2}}$ exposed to perpendicular heating, but in others it was not observed, so it was chosen not to present a time for that event. Finally, observations were not performed for all the tests.

Heat Flux	**Surface Blackened**	**Glowing Ignition**	**Flaming Ignition**
$10\,\mathrm{kW/m^2}$	$\sim 2000\,\mathrm{s}$	Not observed	Not observed
$18\,\mathrm{kW/m^2}$	$\sim 350\,\mathrm{s}$	$\sim 1400\,\mathrm{s}$	Not observed
$25\,\mathrm{kW/m^2}$	$\sim 120\,\mathrm{s}$	$\sim 150\,\mathrm{s}$	Not observed
$40\,\mathrm{kW/m^2}$	$\sim 50\,\mathrm{s}$	$\sim 150\,\mathrm{s}$	$\sim 3800\,\mathrm{s}$
$60\,\mathrm{kW/m^2}$	$\sim 30\,\mathrm{s}$	$\sim 30\,\mathrm{s}$	$\sim 35\,\mathrm{s}$

Table 3.1: Times of occurrence of various events observed at the sample surface, perpendicular heating.

The maximum mass loss rate is directly proportional to the intensity of the incident heat flux,

Figure 3.7: 4070 s: whole sample is involved in flaming. The charring front has advanced until the back end of the sample, and the moisture evaporation front is not noticeable. Sample is exposed to an incident heat flux of 40 kW·m^{-2}, perpendicular heating.

Heat Flux	**Surface Blackened**	**Glowing Ignition**	**Flaming Ignition**
$10\,\mathrm{kW/m^2}$	$\sim 1600\,\mathrm{s}$	$\sim 3400\,\mathrm{s}$	Not observed
$60\,\mathrm{kW/m^2}$	$\sim 30\,\mathrm{s}$	$\sim 40\,\mathrm{s}$	$\sim 50\,\mathrm{s}$

Table 3.2: Times of occurrence of various events observed at the sample surface, parallel heating.

as can be seen in Figure 3.30. As can be seen in Tables 3.3 and 3.4, the heating rate is also directly proportional to the incident heat flux, while the times for attaining the maximum mass loss rate decrease as the external radiation increases. In all cases the phenomena that led to assume a one-dimensional heating process were observed. The moisture front however, was less clear in the parallel heating tests, where grain orientation prevents the transport of moisture to the sides of the specimen. Photographs of a parallel heating test are presented in Appendix B.

Figure 3.8: 6395 s: flaming about to end. The char oxidation is more important at the base of the sample, due to the insulating effect of the ceramic fibre board. The test is about to end. Normally the temperature profile tests are stopped when the thermocouples read temperatures above 873 K. Sample is exposed to an incident heat flux of 40 $kW{\cdot}m^{-2}$, perpendicular heating.

Heat Flux	**5 mm Thermocouple Reaches 373 K**	**Maximum Mass Loss Rate**
$10\,kW/m^2$	470 s	280 s
$18\,kW/m^2$	280 s	1320 s
$25\,kW/m^2$	185 s	670 s
$40\,kW/m^2$	150 s	140 s
$60\,kW/m^2$	115 s	60 s

Table 3.3: Times of occurrence of various measured events, perpendicular heating.

Heat Flux	**5 mm Thermocouple Reaches 373 K**	**Maximum Mass Loss Rate**
$10\,kW/m^2$	510 s	4520 s
$60\,kW/m^2$	105 s	60 s

Table 3.4: Times of occurrence of various measured events, parallel heating.

3.1.3 The 10 $kW{\cdot}m^{-2}$ Tests

The external heat flux of 10 $kW{\cdot}m^{-2}$ is close to a critical value above which the pyrolysis and combustion reactions begin to take place (Drysdale 1998, Boonmee & Quintiere 2005).

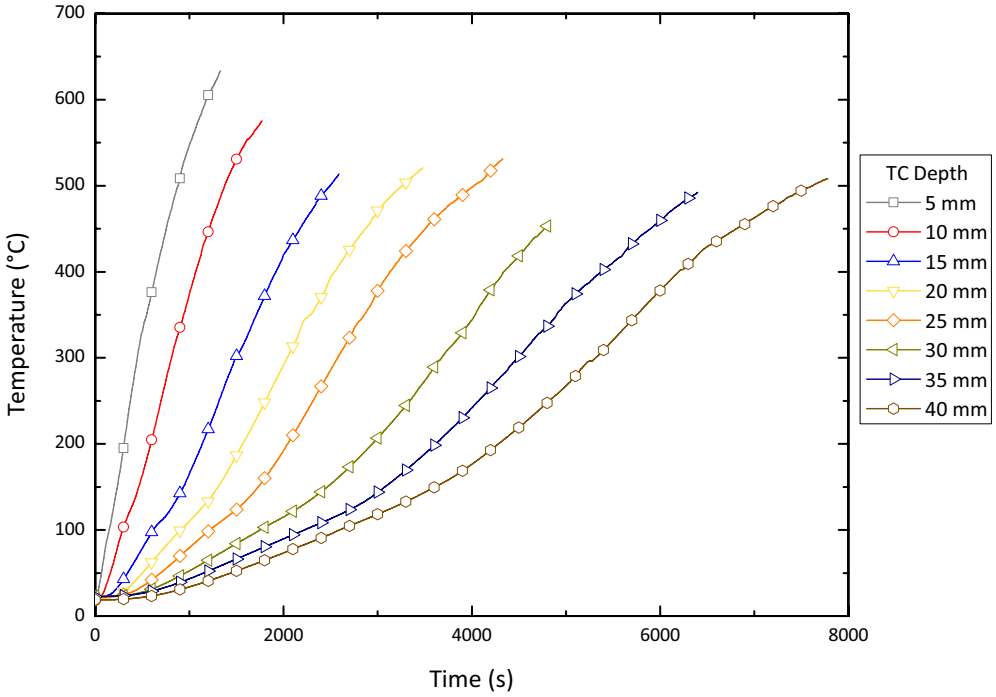

Figure 3.9: Average temperature histories for an external heat flux of 40 kW·m^{-2}, perpendicular heating, and various thermocouple depths. The effect of moisture evaporation on the heating rates is weakened as depth increases but it lasts up to higher temperatures. The steady decrease in the mass loss rate after the peak value is caused by the increase in depth of the char layer. Surface glowing starts at 150 s of exposure, while flaming combustion begins at 3800 s.

Boonmee and Quintiere detected that the lowest incident heat flux for the glowing ignition of wood to occur was 10 kW·m^{-2}, while the critical heat flux for pilot ignition, as reported by Drysdale is 12 kW·m^{-2}. What would be expected in terms of behaviour when heating samples with this energy intensity are non-consistent results, due to the fact that some imposed heat fluxes might actually fall closer to that mark than others and thus show heating and mass loss rates which are closer to the inert heating case. This has proven to be the case, as is illustrated by the Figures 3.10 and 3.11.

The first of these figures (Figure 3.10) shows the temperature histories for a thermocouple depth of 15 mm, under perpendicular heating. Three distinct trends can be observed for the three replications. Indeed, the heater temperatures for tests numbers 1, 2 and 3 were 683, 672 and 678 K respectively. Not surprisingly, the curve showing the slowest heating rate corresponds to the lowest temperature while the fastest heating corresponds to the highest one. As a matter of fact, those tests which show a closer agreement between the heater temperatures for the

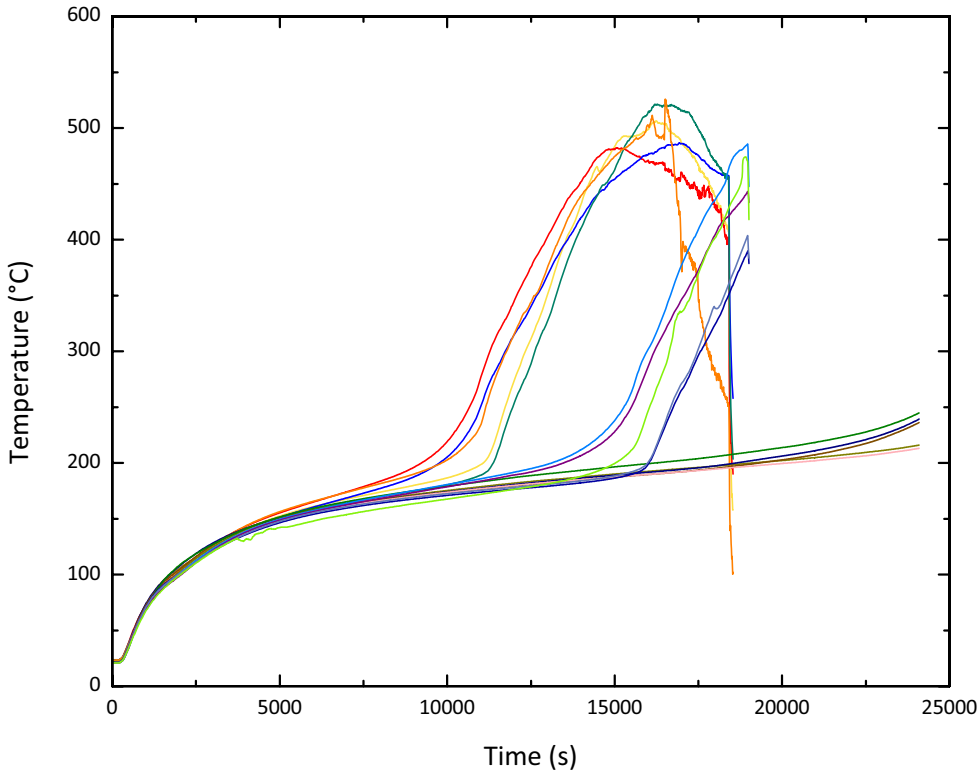

Figure 3.10: Individual thermocouple measurements for a heat flux of 10 kW·m^{-2} and a depth of 15 mm. The three trends correspond to the three different replications for this partcular heat flux and thermocouple depth. The average was done only until the first point of departure (i.e. 10000 s). The sharp increase in the heating rate can be attributed to the onset of exothermic oxidation reactions.

different replications show a much better agreement in their results.

Figure 3.11 on the other hand shows the mass loss rates for the three replications made under parallel heating. Again, there was a maximum difference of 12 K in the heater temperatures. The two curves which are closer only presented a 2 K heater temperature difference between themselves.

An interesting behaviour at this heat flux is the temperature "jump" reported in (Boonmee & Quintiere 2005). The authors claim that the beginning of this sharp increase in temperature is the point where glowing ignition starts. This jump is observed in the positions closer to the surface in the temperature-time plots, starting at around 250°C (see Figures 3.10 and 3.23). The performance of the shallow thermocouples agrees well with the predicted behaviour for the surface, indicating that at the time when the jump occurs in the tests the regression front is

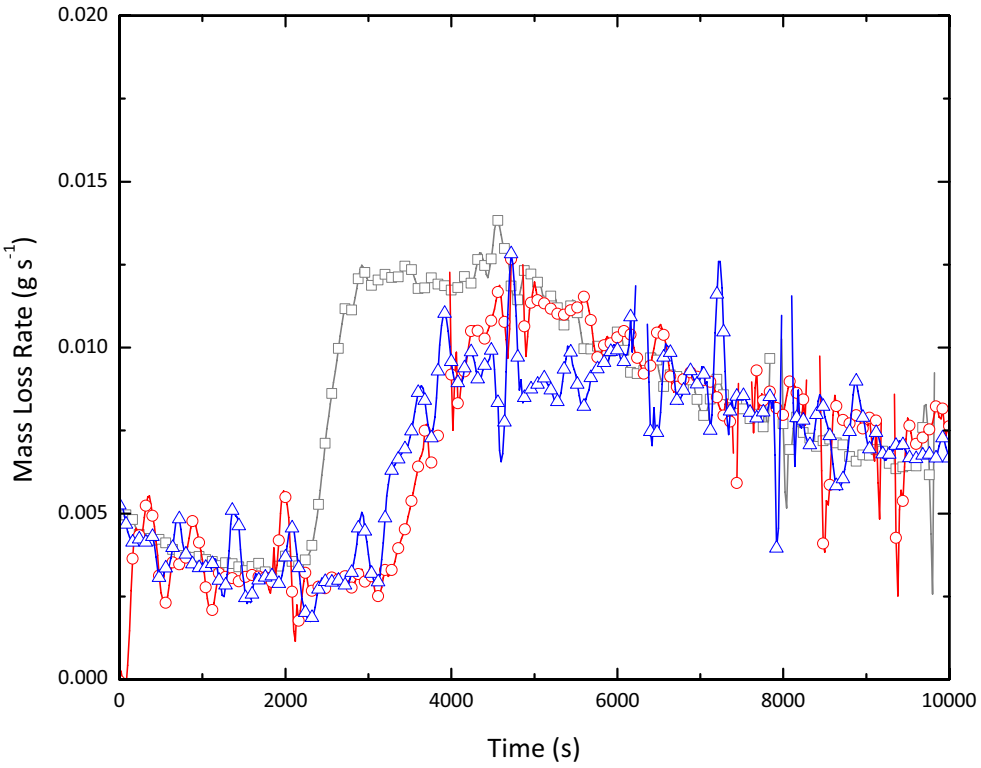

Figure 3.11: Individual mass loss measurements for a heat flux of 10 kW·m^{-2}. The average was done until the end of the tests, because the agreement is closer than for some thermocouple measurements, for example see Figure 3.10.

close to the position of the thermocouples.

3.1.4 Parallel Heating

An important difference observed between parallel and perpendicular heating tests was the appearance of liquid water flowing out through the sides of the samples, marking the movement of the moisture evaporation front. This phenomenon was more noticeable in the perpendicular than in the parallel heating case, something explained by the differences in the moisture diffusion coefficients between the longitudinal (parallel to the grain) and transverse directions (Siau 1984): the longitudinal diffusion coefficient is almost 2 orders of magnitude greater than the transversal coefficient for a temperature of 373 K and a moisture content of 10%.

Wood conductivity is about 2 times greater on the direction parallel to the grain than perpendicular to it (See the Section 2.2 in the previous chapter). Thus it is logical to expect a faster

heating in the parallel case, with a greater proportion of the incoming heat flux being transmitted into the deeper regions. In terms of temperature profiles, the 10 kW·m^{-2} case behaves as expected, with the parallel heated samples showing a faster heating rate, as can be seen in Figure 3.12.

Mass loss rates for parallel 10 kW·m^{-2} heating show an initial peak which coincides with the perpendicular heating experiments and then a second, larger one. Glowing ignition, as shown in Table 3.2, was observed at about 3400 s for the parallel heated tests, whereas it was not observed for the perpendicular case. The acceleration of the heating rate and the increase in the mass loss rate occur at approximately the same time (Figures 3.12 and 3.13).

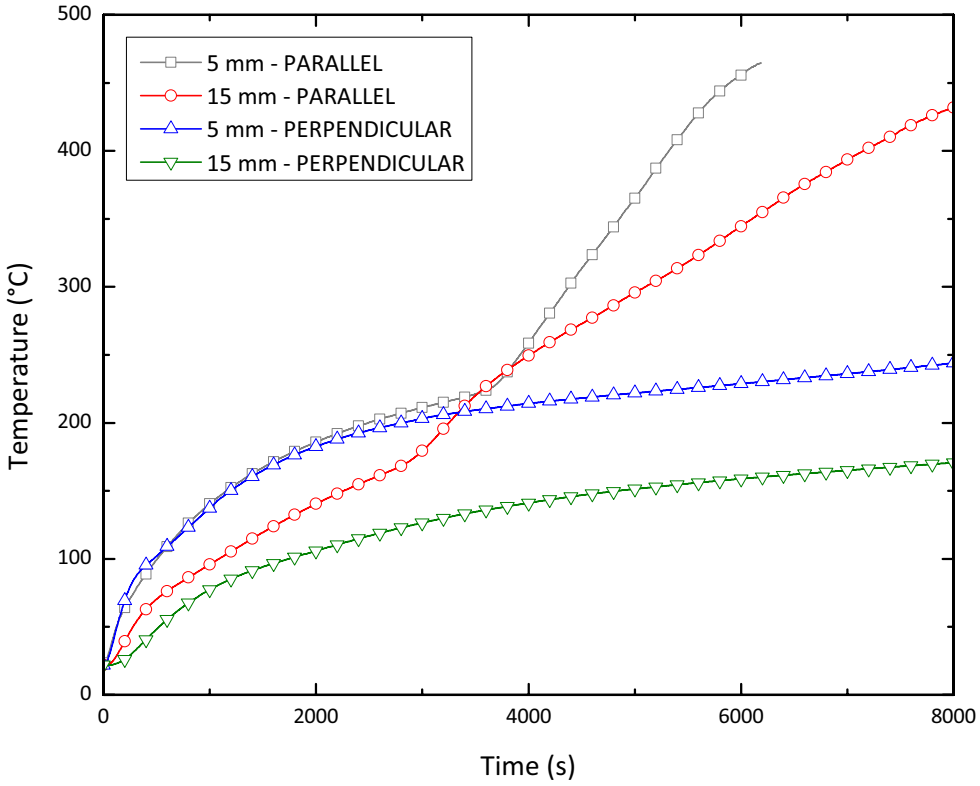

Figure 3.12: Comparison of parallel vs. perpendicular heating. Temperature histories for an imposed heat flux of 10 kW·m^{-2}. Parallel heating samples show a faster heating rate. The sharp increase in the heating rate of the shallower thermocouples is attributed to the onset of exothermic reactions.

On the other hand, for the 60 kW·m^{-2} tests the behaviour was inversed, with the parallel samples heating up more slowly than the perpendicular ones (Figure 3.14). This difference is attributed to the intensity of the burning rate, as expressed in the mass loss rates (Figure 3.15).

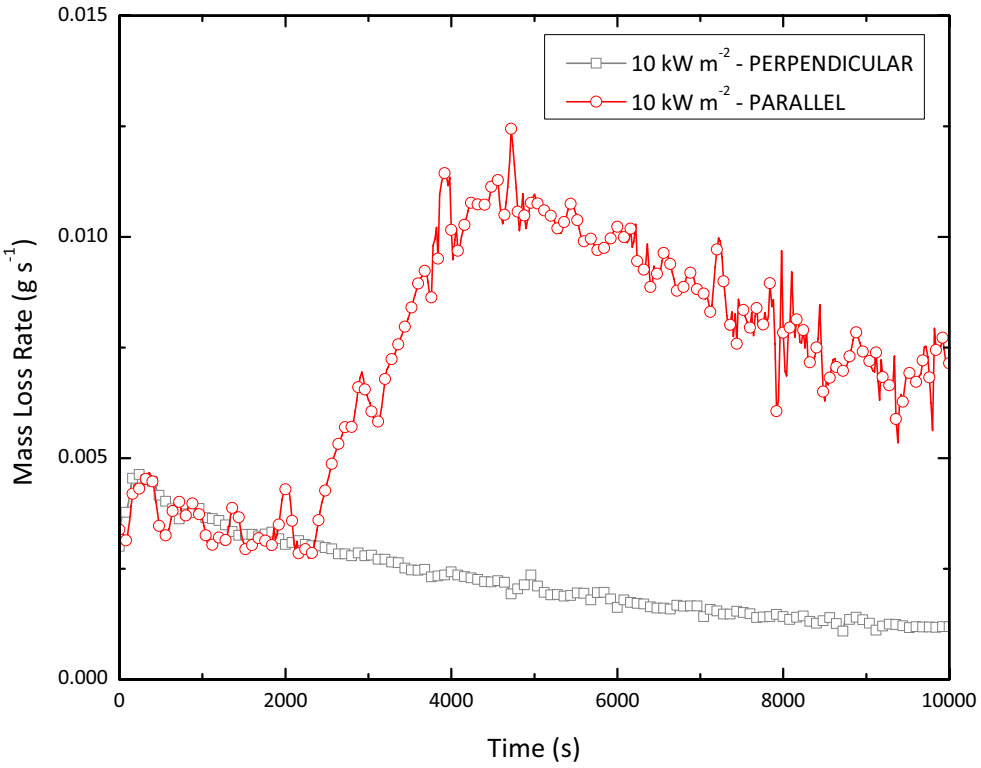

Figure 3.13: Comparison of parallel vs. perpendicular heating. Mass loss rates for an imposed heat flux of 10 kW·m^{-2}. The large differences in behaviour are attributed to glowing reactions, which were more frequent in the parallel heating cases.

The mass loss rates show close agreement during the initial heating stages, only to diverge later. This might indicate that the char layer begins to form at almost the same time (following Roberts's analysis, see Section 3.3) in both cases. The mass loss rates for parallel and perpendicular heating separate at about 200 s, at approximately the same time when the temperature histories for a depth of 5 mm begin to show different trends. Perpendicular heating tests show greater mass loss rates, indicating that burning is more intense, thus accounting for the greater measured temperatures.

These examples provide evidence of the magnitude of the additional heat flux provided by both glowing and flaming, which can generate noticeable differences in the in-depth temperature histories.

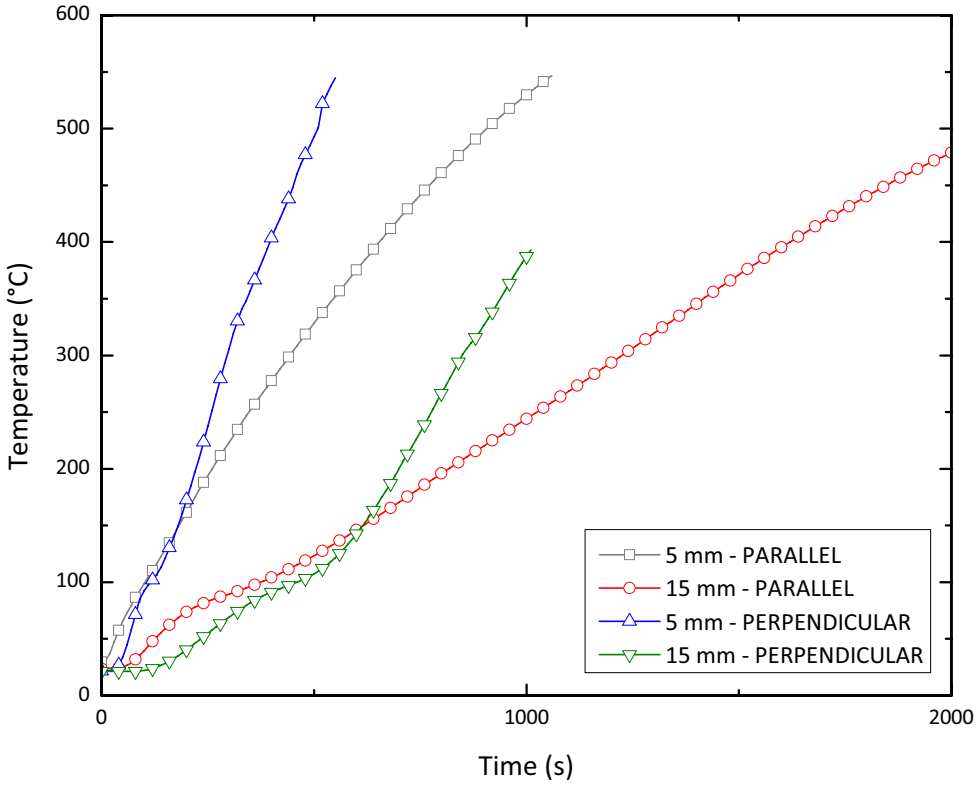

Figure 3.14: Comparison of parallel vs. perpendicular heating. Temperature histories for an imposed heat flux of 60 kW·m^{-2}. As opposed to the 10 kW·m^{-2} case, at this level of irradiance the perpendicular tests show faster heating rates than the parallel tests. This is caused by flaming combustion, which was observed more frequently in the former tests.

3.1.5 Sample Degradation

Another observation highlighting the differences between samples heated at high and low heat fluxes is the state of the specimens after the end of the tests (Rein 2007). While the samples at higher heat fluxes -and particularly those that presented flaming- show more significant degradation on their sides, specimens exposed to lower heat fluxes present less charring and deformation (see Figures 3.16 to 3.20). This is caused by the heat that is lost through the sides of the sample, which in the higher fluxes is not able to overcome the external heat imposed on it (and any heat generated in the interior of the wood matrix), but at lower intensities losses become significant, making the pyrolysis less important.

Except for the samples that flamed, the edges of the samples present less degradation than the centres, due to the aforementioned heat losses and also because the intensity of the imposed

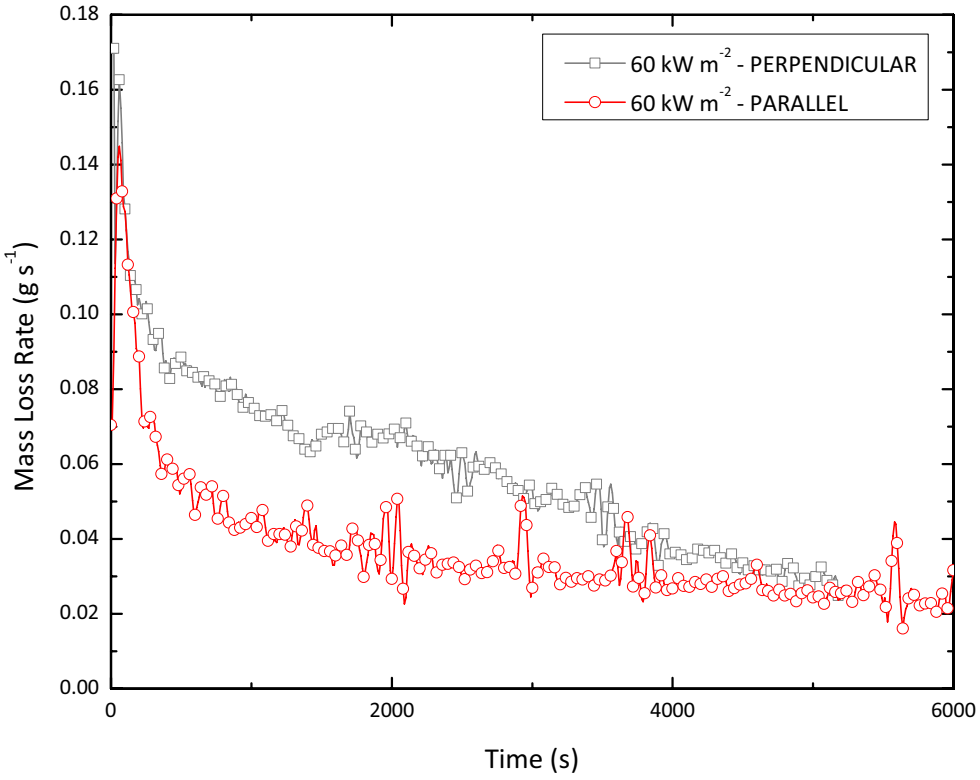

Figure 3.15: Comparison of parallel vs. perpendicular heating. Mass loss rates for an imposed heat flux of 60 kW·m^{-2}. As opposed to the 10 kW·m^{-2} case, at this level of irradiance the perpendicular tests show faster mass loss rates than the parallel tests. This is caused by flaming combustion, which was observed more frequently in the former tests.

heat flux decreases at increasing distances from the centre of the cone heater. Specimens heated parallel to the grain show greater decomposition in the centre than those heated perpendicular to the grain.

3.2 Temperature Profiles

Figures 3.21 and 3.22 show typical raw thermocouple readings for a given heat flux and thermocouple depth. Note the defective thermocouples, which were eliminated from the final results. The sudden dip in the temperatures at the end of some of the tests was caused when the sample was removed from the test chamber when the test was finished. Thermocouples showing this behaviour probably were already exposed (i.e. were not embedded in the wood). After reaching temperatures of about 500°C, the thermocouple measurements became unstable: it

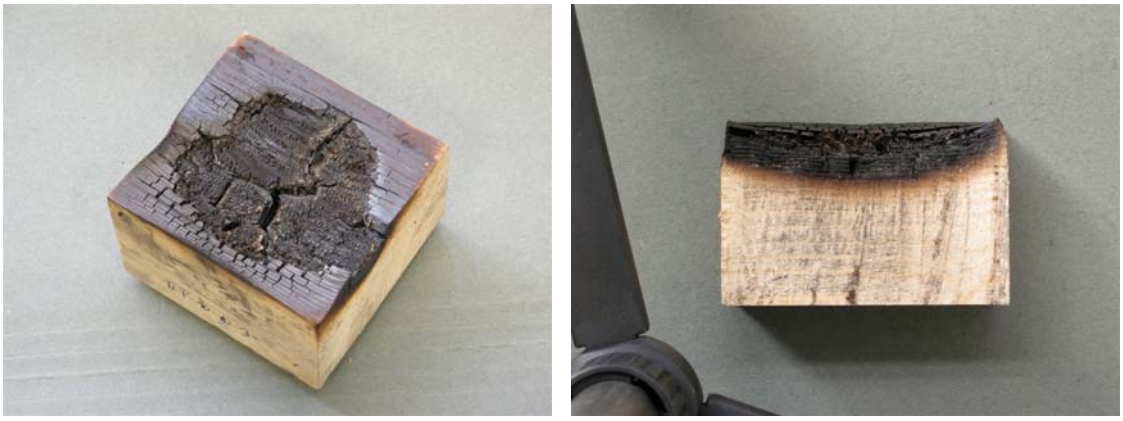

(a) *Complete Specimen* (b) *Specimen Cross Section*

Figure 3.16: 10 kW·m^{-2}, 10 mm deep thermocouple, perpendicular heating. Test duration: 19680 s. Most of the degradation occurs in the centre of the sample. Note that the pyrolysis front is not parallel to the exposed surface because of lower degradation on the outer sections of the sample, and that its top edges are sharp.

(a) *Complete Specimen* (b) *Specimen Cross Section*

Figure 3.17: 18 kW·m^{-2}, 10 mm deep thermocouple, perpendicular heating. Test duration: 6120 s. Degradation becomes more uniform across the sample surface. The degradation of the outer sections is greater, but still the pyrolysis front is not parallel to the exposed surface. The top edges of the sample are still sharp.

was considered that the regression front had reached the thermocouple at that point. The data obtained beyond that temperature was deemed to be unusable. Note that these figures show data for the three replications of a particular test, and that not necessarily the three experiments had the same duration. Even though it seems that with increased depth the standard deviation of the measurements increases, it was found that the standard error is independent of the depth (see Section 3.5).

The results were averaged for each thermocouple depth and heat flux. Some averages were

(a) *Complete Specimen* (b) *Specimen Cross Section*

Figure 3.18: 25 kW·m^{-2}, 10 mm deep thermocouple, perpendicular heating. Test duration: 1250 s. Degradation uniform across the entire sample surface. The degradation is equal for the inner and outer sections of the sample, making the pyrolysis front parallel to the exposed surface. The top edges of the sample are now rounded.

(a) *Complete Specimen* (b) *Specimen Cross Section*

Figure 3.19: 40 kW·m^{-2}, 10 mm deep thermocouple, perpendicular heating. Test duration: 2340 s. Degradation is still uniform across the entire sample surface. Note that the pyrolysis front is parallel to the exposed surface, but the top edges of the sample are now rounded, indicating greater degradation on the outer parts of the specimen. No flaming was observed in this test.

truncated when the divergences between the different replications become important. Some averaged results are presented in Figures 3.23, 3.24 and 3.9, while the remaining results are shown in Appendix B. As it can be seen, the figures show the average temperature histories for the 8 different depths and different heat fluxes.

The behaviour of the 10 kW·m^{-2} tests is different from that of the rest of the external heat fluxes (compare Figures 3.23 and 3.24). The change in the heating rate caused by the moisture evaporation is barely noticeable, except in the shallower thermocouples, and the heating

(a) *Complete Specimen* (b) *Specimen Cross Section*

Figure 3.20: 60 kW·m^{-2}, 10 mm deep thermocouple, perpendicular heating. Test duration: 780 s. Degradation is now greater on the outer portions of the sample. The pyrolysis front is still parallel to the exposed surface in the central section, but it is also advancing into the virgin part of the wood from the sides of the sample.

after that seems to be slower than the rest, where a steep gradient is observed after 373 K (100°C). When the thermocouples reach temperatures of approximately 523 to 573 K, a sharp increase in the heating rate is observed. Finally, some thermocouple positions appear as having greater temperatures than shallower positions. All these effects will be discussed in the coming sections.

The temperature profiles for some heat fluxes are presented in the Figures 3.25, 3.26 and 3.27. Like the temperature history plots, the behaviour of the 10 kW·m^{-2} temperature profiles differs from the rest. The maximum temperatures are lower, about half of the values for the other heat fluxes presented (40 and 60 kW·m^{-2}, although some of these curves have been truncated), and the curves show a lower gradient. As previously mentioned, an increase in the gradient is observed for the 40 and 60 kW·m^{-2} cases after the temperatures have gone above 373 K. The temperature rise at the back of the sample, for all three heat fluxes, is of the same order of magnitude.

3.2.1 Determination of the Characteristic Parameters

The behaviour for all the heat fluxes is similar, except for the 10 kW·m^{-2} tests. Their heating histories seem "stretched" in time, but nevertheless shallower thermocouples sometimes present slower heating rates than deeper ones. In order to compare the results between themselves, and to prove whether the 10 kW·m^{-2} experiments are actually different from the rest,

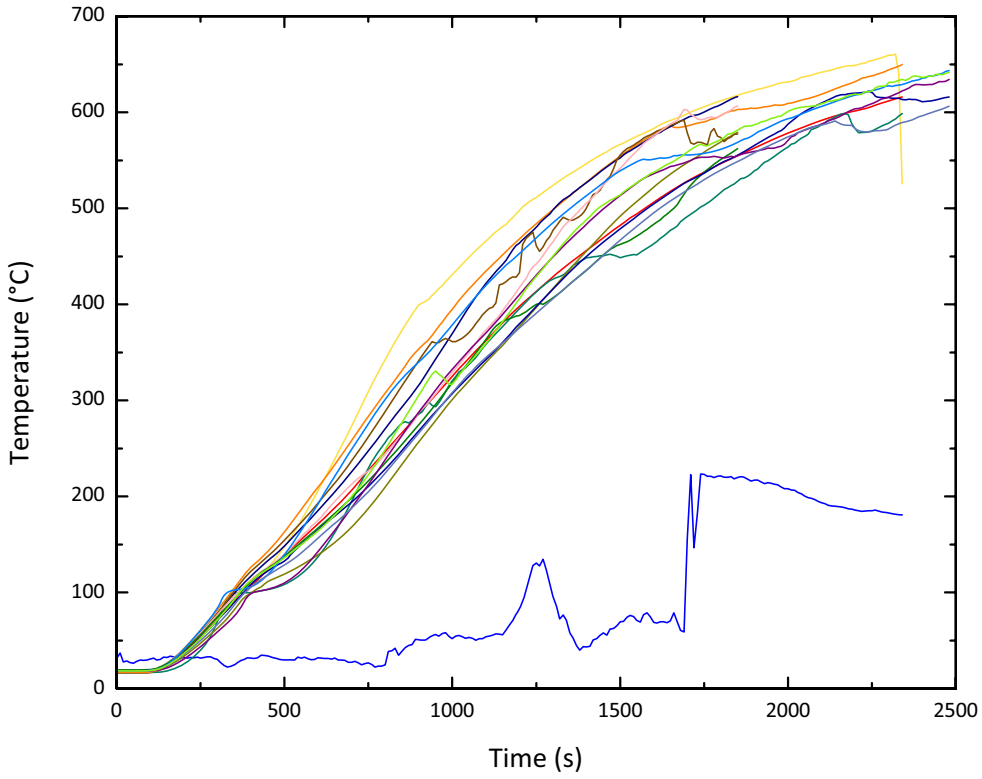

Figure 3.21: Raw thermocouple data for 40 kW·m^{-2} and a depth of 10 mm, perpendicular heating. Note the faulty thermocouple, in blue. Tests would continue until the thermocouples reached a temperature of 800 K. The sudden dip in some thermocouple readings near the end of the tests was caused when the sample was removed from the heat source, and surface regression had already caused the exposure of the particular thermocouple.

the results were non-dimensionalized and compared against an analytical solution of the heating of a semi-infinite solid. This was done only for the perpendicular heating, as it is assumed that the parallel heating will present a similar performance.

Consequently, a semi-infinite heat transfer model that treats the material as a non-reacting solid was used to establish characteristic values for the different parameters of the problem (Long et al. 2000, Incropera & DeWitt 2002). These characteristic values were used to non-dimensionalize time, depth and temperatures. The non-dimensional variables are the following:

$$t^* = \frac{t}{t_c}, \tag{3.1}$$

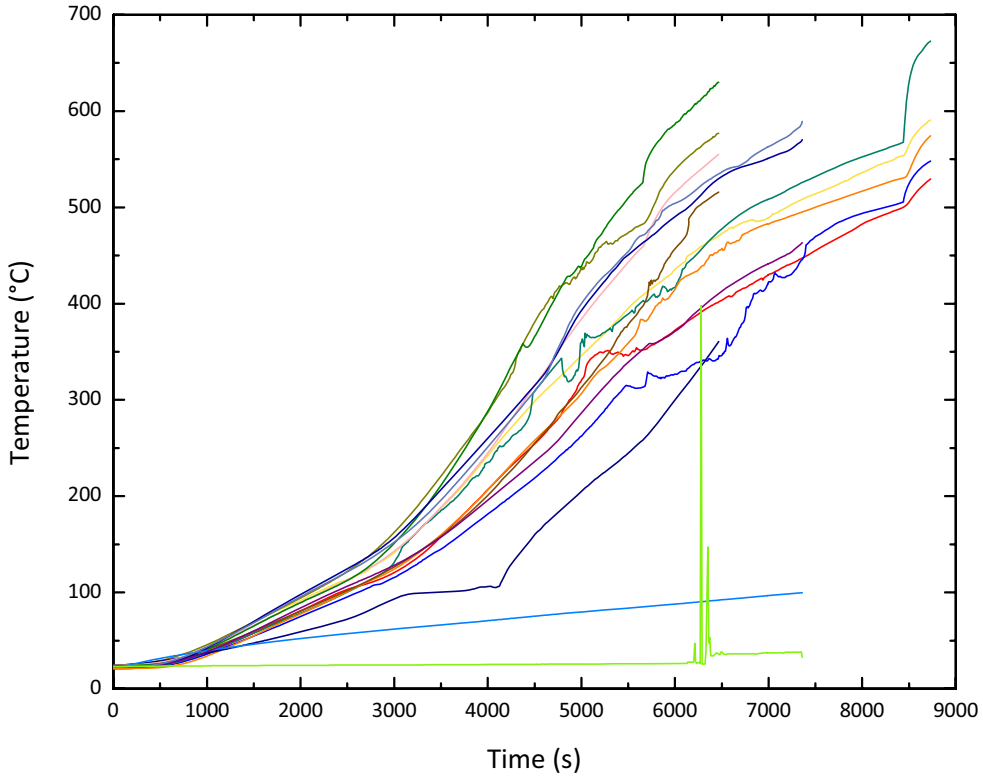

Figure 3.22: Raw thermocouple data for 40 kW·m^{-2} and a depth of 35 mm, perpendicular heating. Note the faulty thermocouples, in light blue and green. Tests would continue until the thermocouples reached a temperature of 800 K. Even though there seems to be a greater variability in the readings at deeper positions than at shallower ones (cf. Figure 3.21, the standard error for both measurements is similar.)

$$x^* = \frac{x}{x_c}, \tag{3.2}$$

$$\theta^* = \frac{T - T_\infty}{T_c - T_\infty}. \tag{3.3}$$

The characteristic variables, denoted by the subscript c, are defined by the following equations (t_c is written again for convenience).

$$T_c = \frac{a \cdot \dot{q}''}{h_{tot}}, \tag{3.4}$$

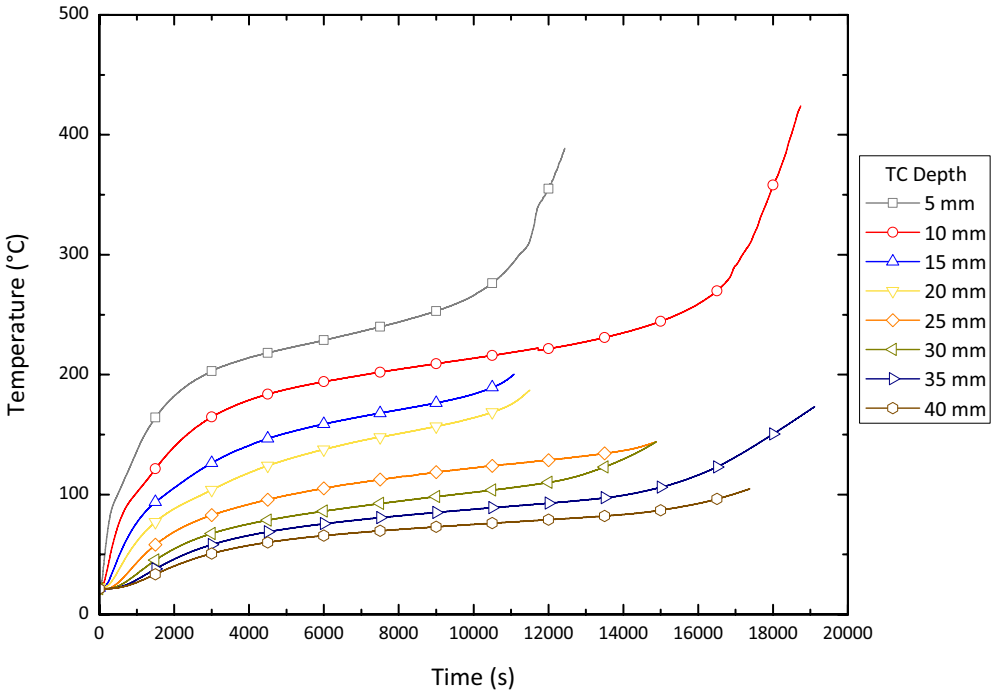

Figure 3.23: Averaged temperature histories for 10 kW·m^{-2}, perpendicular heating. The shallower thermocouples show the temperature "jump" as reported in (Boonmee & Quintiere 2005), although other thermocouples show this behaviour but it was not repeated in all the tests, thus the average was not done until that point (cf. Figure 3.10). The effect of moisture evaporation is weak, and the general behaviour of the samples seems more erratic.

$$x_c = \frac{k}{h_{tot}}, \tag{3.5}$$

$$t_c = \frac{k \cdot \rho \cdot c}{{h_{tot}}^2}. \tag{3.6}$$

The temperature distribution for the heating of an inert solid with constant heat flux and heat losses at the surface by radiation and convection, represented by h_{tot}, is given by the following expression:

$$\theta(x,t) = T_c \cdot \left[erfc\left(\frac{n}{\sqrt{4t}}\right) - e^{(mn+m^2t)} \cdot erfc\left(m\sqrt{t} + \frac{n}{\sqrt{4t}}\right)\right], \tag{3.7}$$

with

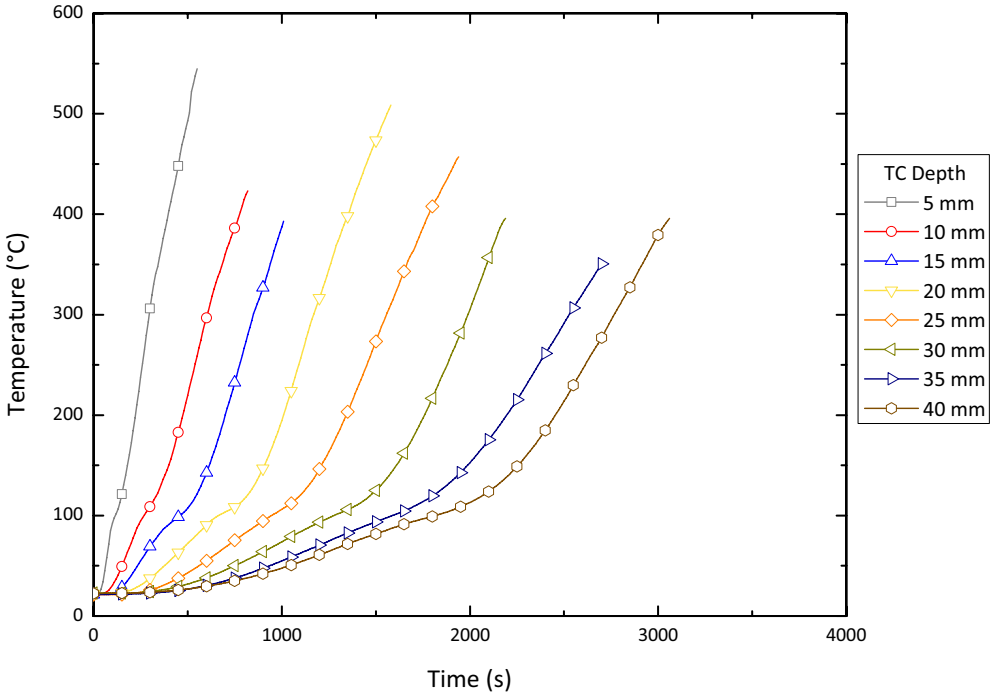

Figure 3.24: Averaged temperature histories for 60 kW·m^{-2}, perpendicular heating. The behaviour is more systematic than for the 10 kW·m^{-2} case (Figure 3.23).The moisture evaporation effect becomes weakened as depth increases, and it finishes at higher temperatures.

$$\theta = T - T_{\infty}, \tag{3.8}$$

$$n = \frac{x}{\sqrt{\alpha}}, \tag{3.9}$$

$$m = \frac{h_{tot}}{\sqrt{k \cdot \rho \cdot c}}, \tag{3.10}$$

Figure 3.28 represents the non-dimensional temperature distribution for thermocouples placed at 5 mm from the surface for heat fluxes of 10, 25 and 60 kW·m^{-2}. Also included is the inert heating temperature history per equation (3.7). A comparison of this curve with the experimental temperature histories establishes how much they depart from the inert behaviour.

It can be seen in Figure 3.28 that for all heat fluxes the initial behaviour of wood is inert, with the samples subjected to higher heat fluxes departing in the first place from the non-burning

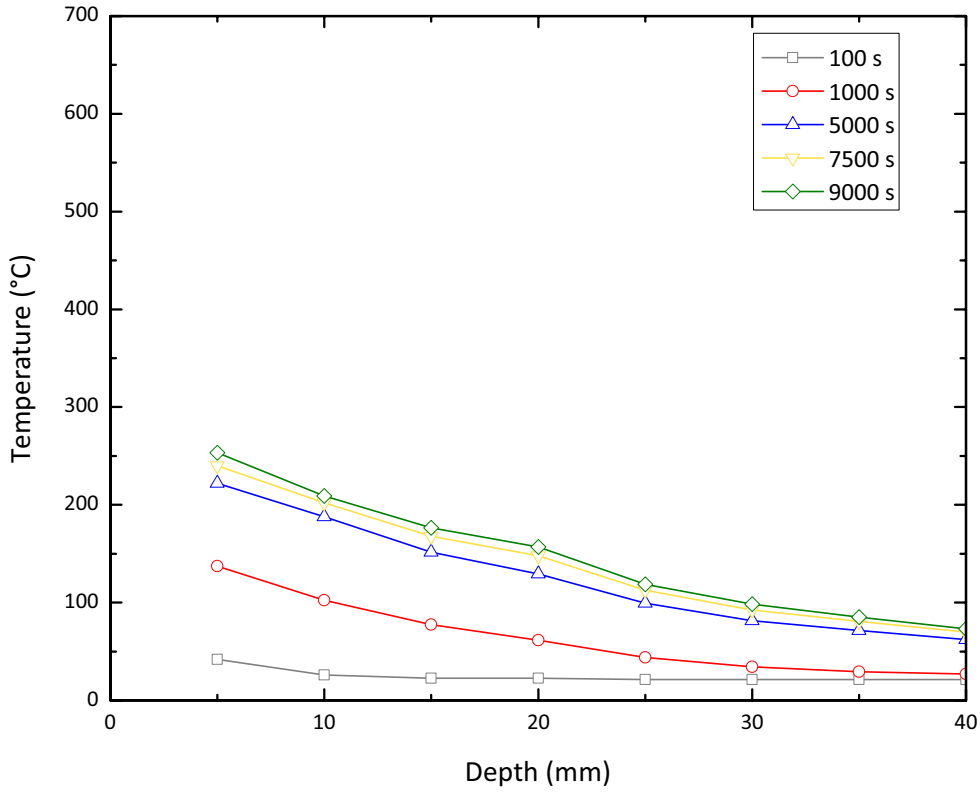

Figure 3.25: Averaged temperature profiles for 10 kW·m^{-2}, perpendicular heating. As time progresses, the curves become less spaced, indicating that heating is reaching a steady state. The small disturbance at a depth of 20 mm is attributed to experimental errors.

behaviour. This observation confirms what was stated by Martin and Blackshear and Kanury (Martin 1965, Blackshear & Kanury 1965). Moreover, following these authors, it was decided to make an estimation of the thermophysical properties of virgin wood by fitting the inert heating curve to the non-dimensional results. The only parameter that was left fixed was the sample density, taken to be that of the average of all the perpendicular heating temperature profile tests (530.8 kg·m^{-3}, this includes the moisture). This results in a thermal conductivity of 0.1 W·m^{-1}·K^{-1} (for the full porous sample, which includes the moisture content), a specific heat of 2600 J·kg^{-1}·K^{-1}, and combining these three values, a thermal diffusivity of 7.25 $\times 10^{-8}$ m^{2}· s^{-1}. The values are close to those reported in the literature (FPL 1999), although the specific heat is higher than the reported values. At deeper positions, the agreement between the analytical solution and the experimental behaviour is poorer, with both the low and high heat fluxes showing temperatures above the inert solution.

The departure from the inert heating is originated by the beginning of the process of moisture

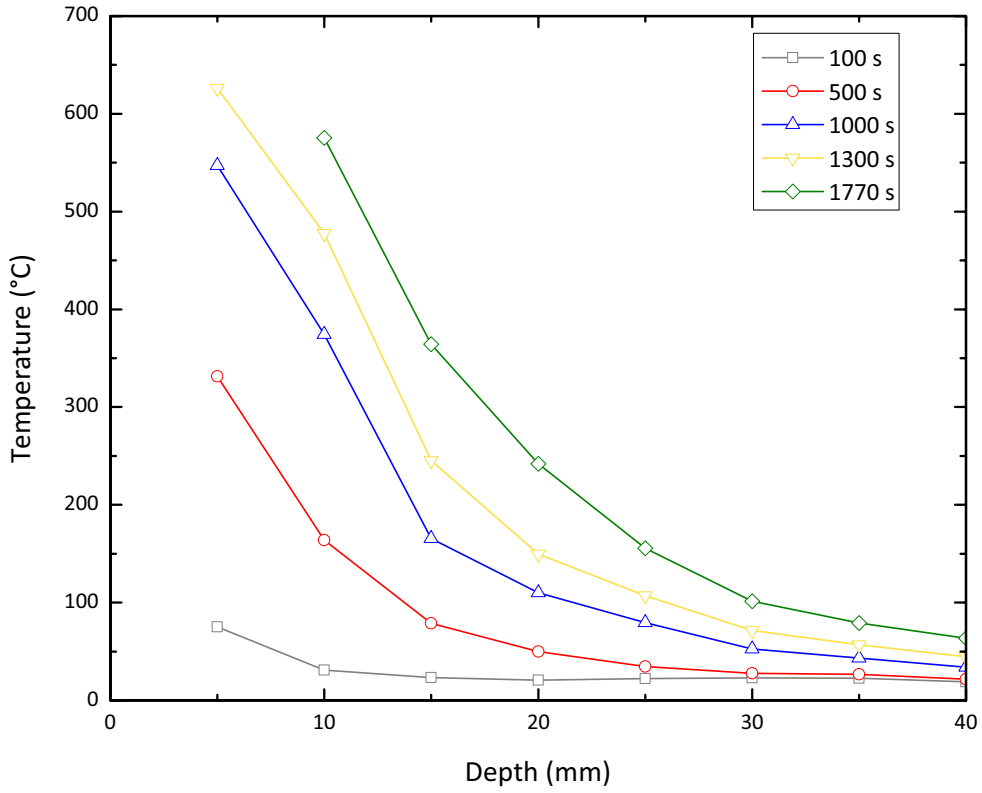

Figure 3.26: Averaged temperature profiles for 40 kW·m^{-2}, perpendicular heating. The gradient of the temperature profile is steeper than for the 10 kW·m^{-2} case, and unlike the results presented for these tests in Figure 3.25, no steady state heating conditions are observed in this case, although the times are shorter.

loss, which acts as a heat sink, slowing down the heating, and by the fact that closer to the surface the wood has already started to char, creating an insulating layer. It is important to note that at 10 kW·m^{-2} wood virtually behaves as an inert material, departing from this non-reacting behaviour at the point where the temperature reaches the vicinity of 100°C. After that instant the temperature-time curve continues to grow closely following the inert solution. This indicates that the process does not depart strongly from the inert behaviour, confirming the observations of Boonmee and Quintiere (Boonmee & Quintiere 2005).

When the non-dimensional temperature profiles (temperature vs. depth curves) are analyzed (Figure 3.29), similar conclusions can be observed. Initially, the experimental profiles have a lower temperature than the inert solution, caused, as previously mentioned, by the loss of moisture and the growth of the char layer. At a non-dimensional time of 1 for example, the 60 kW·m^{-2} tests already have a char layer of significant thickness (the maximum mass loss

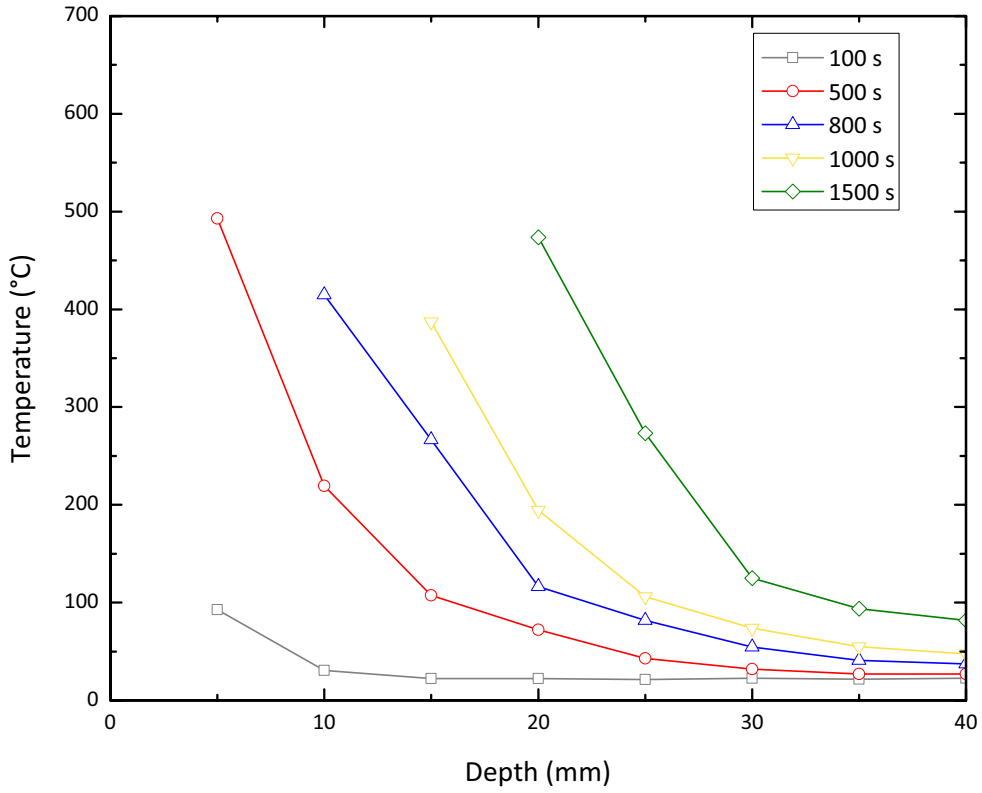

Figure 3.27: Averaged temperature profiles for 60 kW·m^{-2}, perpendicular heating. Steeper gradients than for the 40 kW·m^{-2} tests (Figure 3.26). Although at a similar time, 1500 s, both heat flux intensities show a similar position for the moisture evaporation front (100°C), the temperatures at positions closer to the exposed surface are higher for 60 kW·m^{-2}.

rate occurs at 60s, see Table 3.3) and the shallowest thermocouple (5 mm deep) is reading a temperature close to 373 K (see Table 3.5. The experiments carried out at an incident heat flux of 10 kW·m^{-2} present the closest agreement with the inert heating solution.

Heat Flux	**373 K**	**573 K**
10 kW/m^2	0.342	1.21
25 kW/m^2	0.130	0.459
60 kW/m^2	0.053	0.188

Table 3.5: Corresponding non-dimensional temperatures for 373 K (100°C) and 573 K (300°C)

Non-dimensional Time	**1**	**5**	**10**	**20**
Time (s)	110	550	1100	2200

Table 3.6: Corresponding times for the non-dimensional times used in the temperature profiles plot (Figure 3.15).

For greater times, the agreement is poorer, especially for the 25 and 60 kW·m^{-2} cases, where

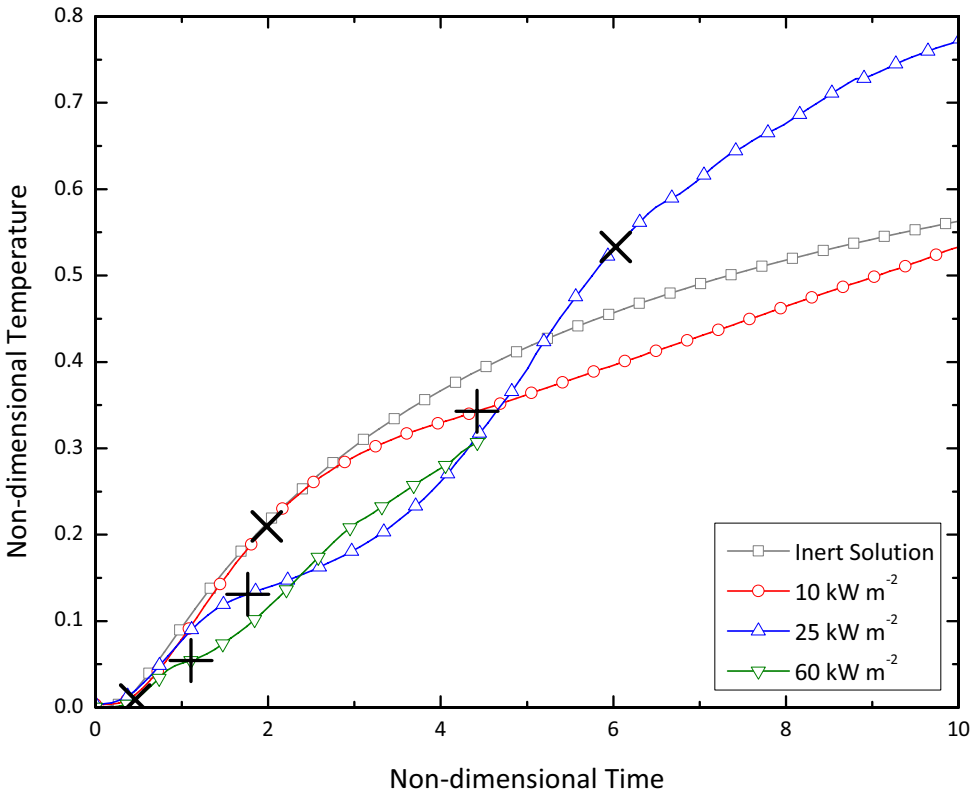

Figure 3.28: Non-dimensional temperature vs. time curves for various heat fluxes at a thermocouple depth of 5mm. The maximum mass loss rate is marked by the symbols "×", while the symbols "+" mark the instant when the solid has reached a temperature of 100°C at the specified depth.

the glowing and flaming ignition reactions add to the imposed heat flux and thus make the temperatures higher than the almost inert 10 kW·m^{-2} tests. In deeper positions however, there is agreement between the different imposed heat fluxes analyzed even at longer times, as can be seen for the curves at a non-dimensional time of 20. Deeper thermocouples remain close to the inert behaviour until a time of 5, when they begin to depart from it in a similar manner for all the external heat fluxes.

The inert heating analytical solution makes good predictions of the heating of wood only at the early stages of this process, and is more accurate for lower heat fluxes. However, the semi-infinite solid solution is a good starting point for the comparison and the assessment of different pyrolysis models, as it can also establish how much they depart from the inert heating behaviour, by comparing this solution with those given by the models. In conclusion, this method represents a good way of scaling only at short times or low temperatures, where the

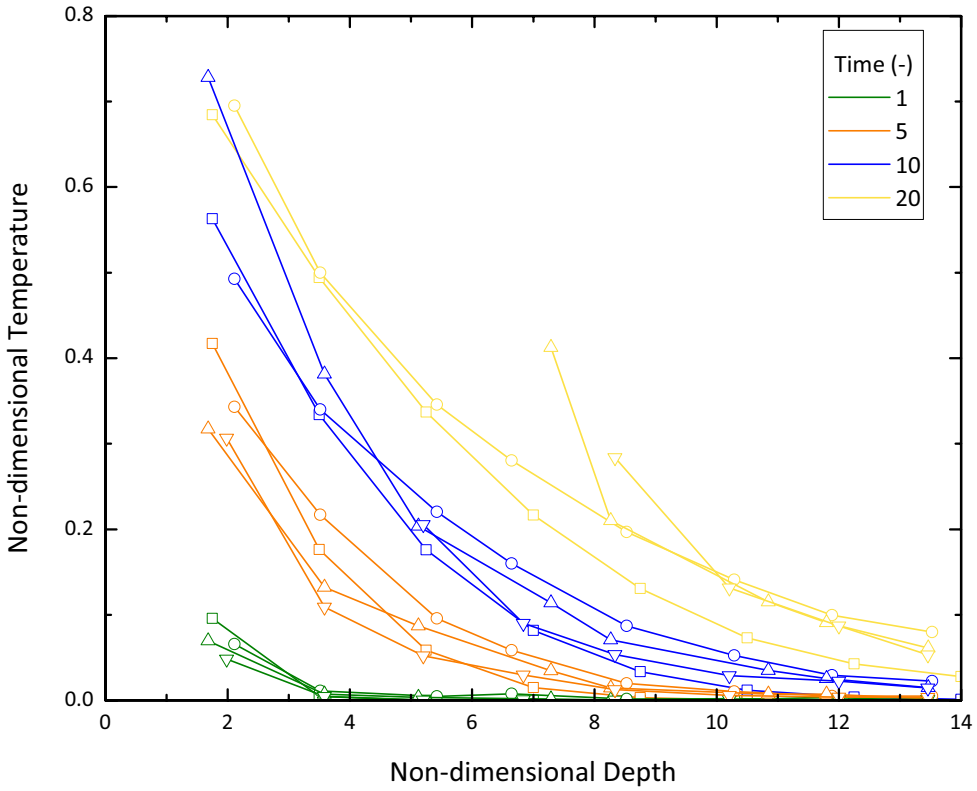

Figure 3.29: Non-dimensional temperature vs. depth curves at various non-dimensional times. The symbols "□" correspond to the inert solution, "◯" to a heat flux of 10 kW·m^{-2}, "△" to 25 kW·m^{-2} and "▽" to 60 kW·m^{-2}. Note that the non-dimensional depths are different for each heat flux because the measured thermocouple depths, not the nominal ones, were used. The depths used for the inert solution correspond to the nominal thermocouple depths.

effects of the moisture evaporation and the pyrolysis and combustion reactions are not strong.

3.3 Mass Loss Rates

The mass loss results follow the expected trends, with the higher heat fluxes presenting greater maximum values and shorter times to reach them. For all heat fluxes except 10 kW·m^{-2} perpendicular heating (and including the parallel heating cases), the mass loss rates converge to a slightly decreasing value (see Figure 3.30). This is an indication that once the char layer reaches a minimum thickness the quantity of wood being pyrolyzed, and thus the amount of heat passing through it into the virgin zones of the wood specimen, becomes independent of the external heat flux being imposed on the sample. This could serve as a validation for the con-

stant charring rate models used particularly in building design (as seen in Chapter 1). However, this is only at longer times, close to steady state conditions. So, steady state conditions seem to be independent of the imposed heat flux, while transient conditions are clearly dependent on the boundary conditions of the specimen.

The 60 kW·m^{-2} perpendicular heating curve shows convergence at a later time than the rest of the samples. This is attributed to flaming combustion, present in all the samples at these heating conditions (unlike the parallel case, where at the same imposed heat flux, some samples did not burn), which increases the incident energy on the sample thus incrementing the mass loss rate. Another important observation is the lack of a final peak in the mass loss rates, which has been previously reported (Boonmee & Quintiere 2005). This phenomenon occurs due to the heating of the back of the sample when it is insulated (Atreya 1983) and constitutes a nuisance in the modelling process that was effectively eliminated by the inclusion of the aluminium block and by performing the tests using a vertical configuration.

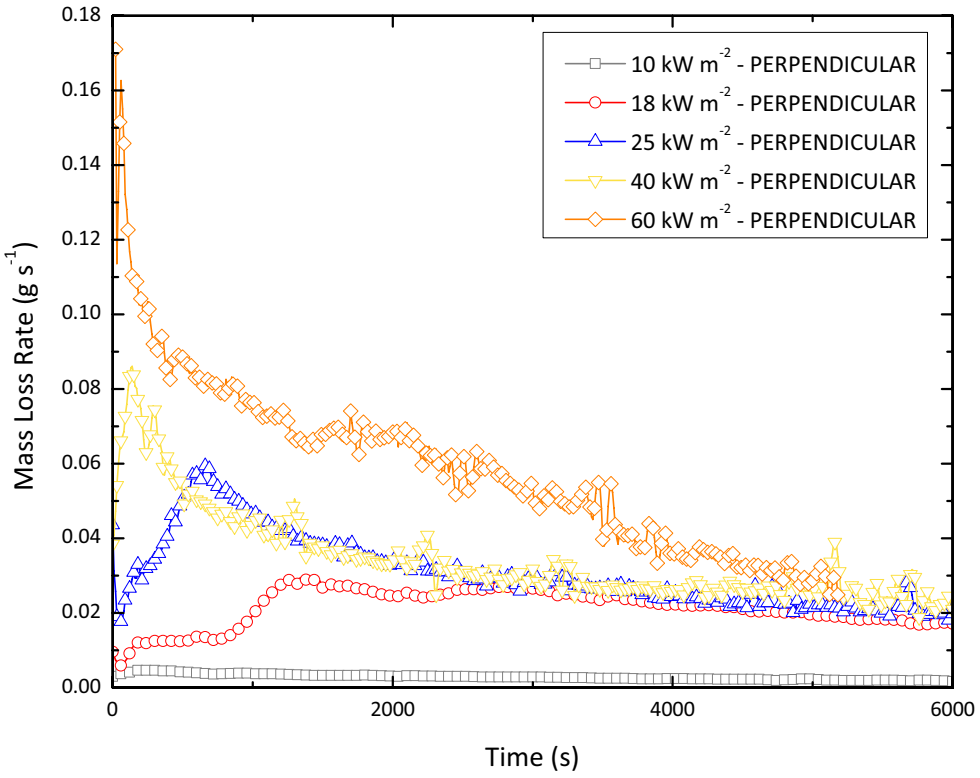

Figure 3.30: Mass loss rates for all the heat fluxes tested, perpendicular heating. The 10 kW·m^{-2} case presents a distinct behaviour from the rest of the tests, which converge to a final value.

Roberts (Roberts 1971) states that the peak in the mass loss rates will correspond to the maximum time when the char residue will still have no thickness, and thus after that, when the insulating properties of the char layer reduce the amount of heat reaching the virgin material, the mass loss rate will begin to decrease. Indeed, at a heat flux of 25 $kW{\cdot}m^{-2}$, the time for the maximum value of the mass loss rate corresponds to a reduction in the gradient of the non-dimensional temperature vs. time curve as shown in Figure 3.28.

3.4 Moisture Front

The position of the moisture front was measured using a video camera, and with this information the moisture front velocities were calculated. As with the mass loss rates, the moisture front speeds for different external heat fluxes converge to a slightly decreasing value (Figure 3.31). The peak speeds, as was mentioned before, are attained at the shallowest positions (i.e. the shortest times). This is not unexpected, and occurs due to reasons previously explained: less amount of heat will reach the virgin wood as the char layer builds up, as more energy is used in the moisture loss heat sink and as depth increases. This reinforces the observation that steady state conditions seem to be independent of the external heat flux imposed on the wood sample.

Two patterns are observed in Figure 3.31, with the speed for the 40 $kW{\cdot}m^{-2}$ tests being higher, while the remaining heat fluxes, all of which are of lower intensity, have a similar peak speed and in general present a similar behaviour throughout the whole duration of the tests. A similar behaviour is observed in Figure 3.32, which shows the temperature recorded by the thermocouple at the time the moisture front passes through its position. Again, the 40 $kW{\cdot}m^{-2}$ thermocouples show a different behaviour than the rest. What this image indicates, for heat fluxes lower than 40 $kW{\cdot}m^{-2}$, is that by the time the moisture reaches the exterior of the sample the temperature at the central part of the block of wood is already past the moisture evaporation temperature. In other words, for lower heat fluxes, water has enough time to migrate to the sides of the specimen where it recondenses. For higher heat fluxes (and probably the changing point is near the critical heat flux for spontaneous ignition of wood, 28 $kW{\cdot}m^{-2}$ (Drysdale 1998)), the heating is faster than the migration rate for moisture, which forces it to advance to deeper positions, where it recondenses ahead of the front, thus accounting for the lower temperatures.

This can also imply that heating is not one-dimensional for the lower heat fluxes, because of

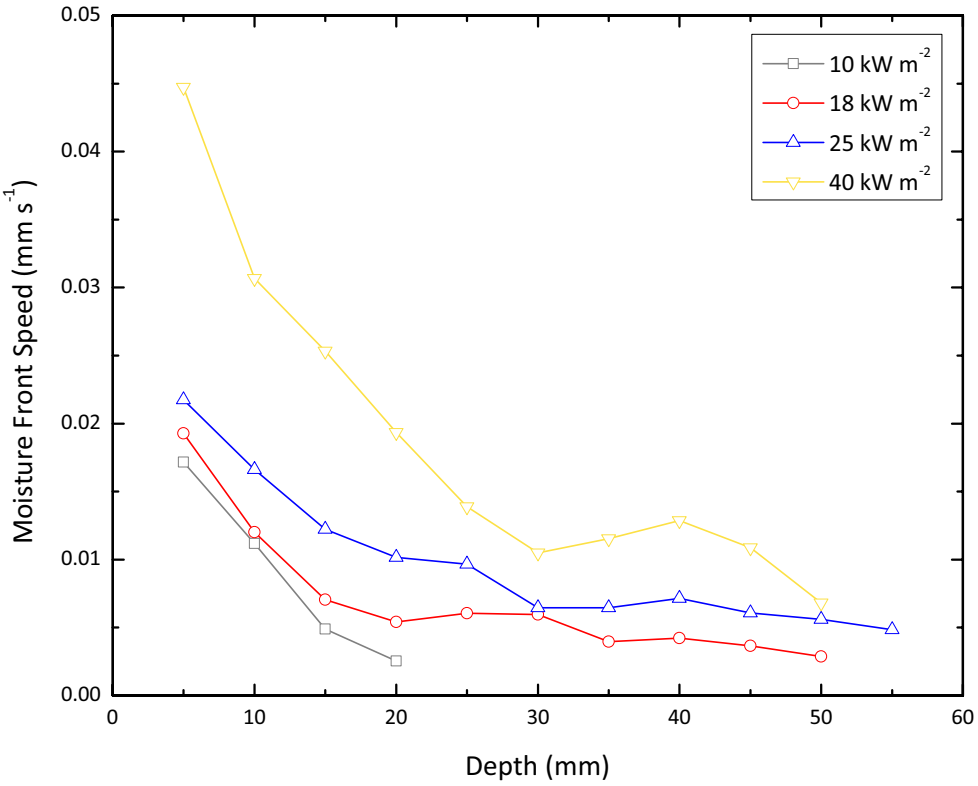

Figure 3.31: Measured moisture front speeds for various heat fluxes as a function of depth. No moisture front speeds were measured for 60 kW·m^{-2} because the front could not be seen once the flames covered the sides of the samples.

the presence of liquid water at the sides of the samples when the recorded temperatures at its centre are higher. But evidence from the specimens after being tested (cf. Section 3.1, Sample Degradation) shows uniform charring on the cross section of samples heated at 25 kW·m^{-2}, and the thermocouple records for a temperature of 373 K show little scattering for all the heat fluxes.

By observing the behaviour of the samples exposed at different heat fluxes, the following analysis was carried out to test if the times for the solid to reach the moisture evaporation temperature could be scaled. For this, the time was non-dimensionalized by a different term than the one employed in Section 3.2, Determination of the Characteristic Parameters. The reason for this is that the characteristic time shown in Equation 3.6 does not include the depth, and because there is variability not only in time but also in depth, a term which includes both variables is needed. Following Martin (Martin 1965), the non-dimensional time is:

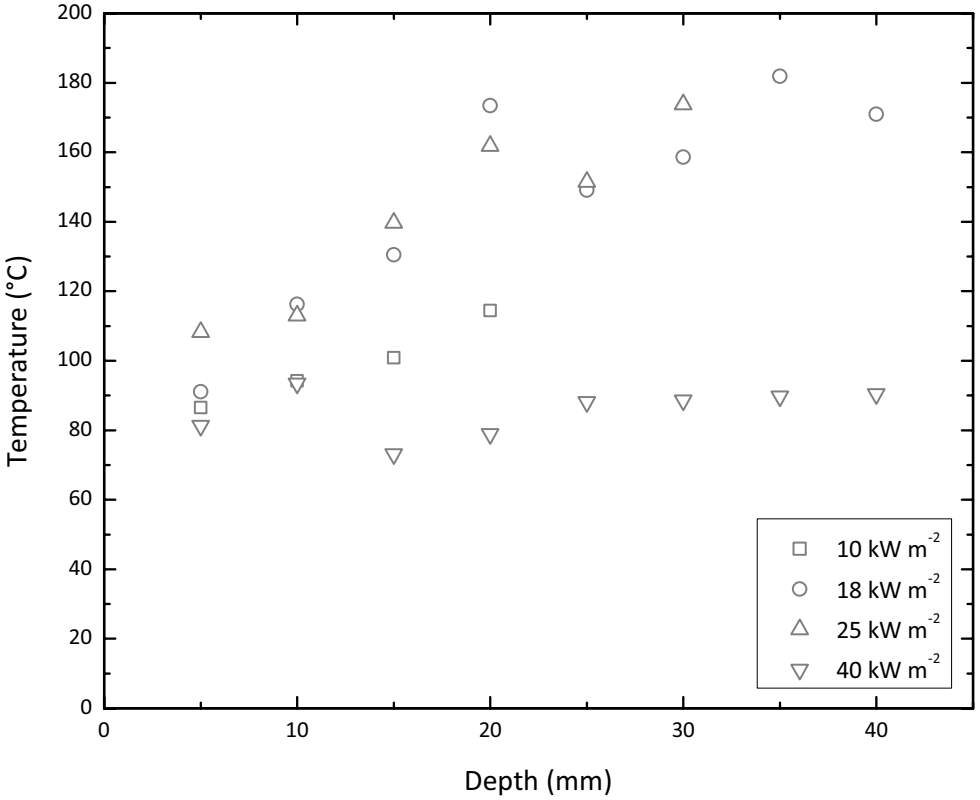

Figure 3.32: Measured temperature when the moisture front reaches a given depth for various heat fluxes. The position of the moisture front as a function of time is used to obtain the corresponding temperature from the tables of average temperatures.

$$t^* = \frac{\alpha\, t}{x^2}. \tag{3.11}$$

Note that this expression was not used for the other analyses precisely because it incorporates two variables, which is undesirable when the effect of each individual variable is being studied. Figure 3.33 shows what has been termed Moisture Delay Time. The figure shows good agreement for every depth except for 5 mm, where a consistent disagreement is observed in every imposed heat flux. It is inferred that because of its proximity to the surface, other phenomena affect the drying of wood, like diffusion and migration not only ahead of the front, but also to the surface of the sample. Greater spread is seen in the heat fluxes lower than 40 kW·m^{-2}, which confirms the previous observations of two different behaviours. It seems that above an intensity located between 25 and 40 kW·m^{-2}, the Moisture Delay Time becomes weakly dependent on the imposed heat flux. This would indicate that the moisture front speed is also

weakly dependent on the imposed heat flux for intensities above that mark.

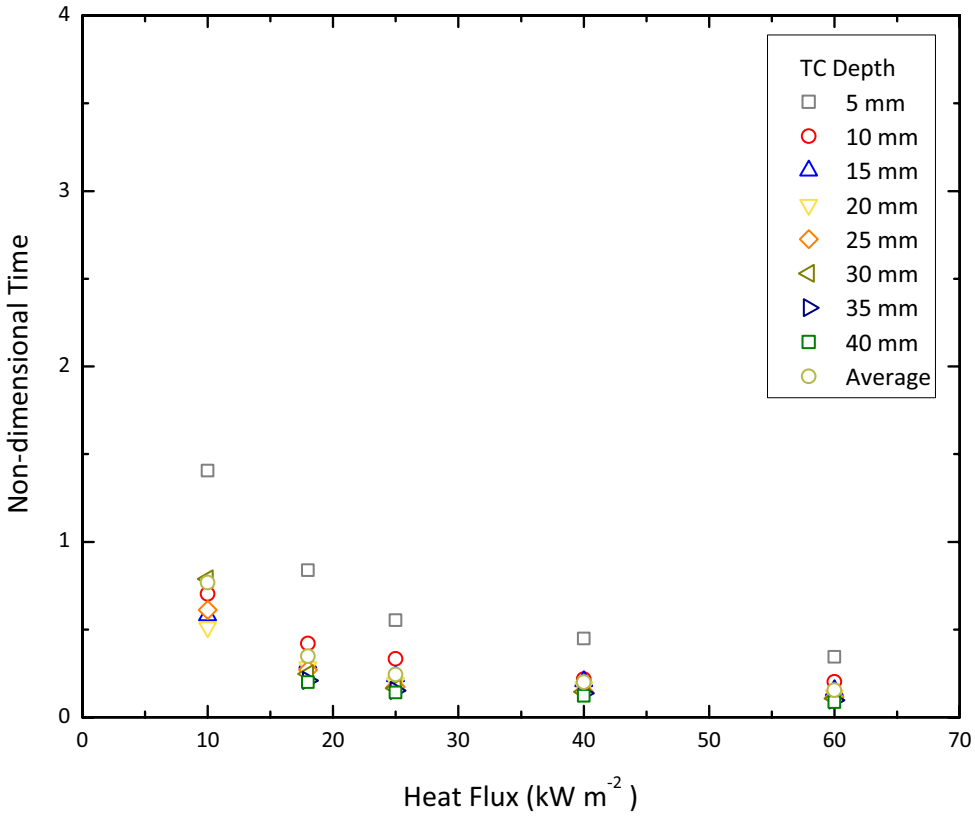

Figure 3.33: Moisture delay time: non-dimensional time for a thermocouple to reach a temperature of 373 K, considered to mark the base of the moisture front. The non-dimensional time is calculated using the Equation 3.11

Figure 3.33 also proves that moisture truly behaves like a heat sink, because it shows that the delay time is only dependent on the imposed heat flux, which means that no other phenomenon is significantly affecting the process. This scaling shows that the non-dimensional time to reach the end of the inert heating phase is virtually independent on depth, and can potentially give information similar in scope to the temperature profile equations currently utilized in the design guidelines (Klingsch et al. 1993, Janssens & White 1994), but obviously being more limited due to the fact that the aforementioned equations predict the behaviour of wood until the pyrolysis temperature instead of only the moisture evaporation temperature. It would be interesting, however, to study this scaling for other values of moisture content (a parameter that is not included in the scaling) and wood species (i.e. thermal diffusivity), as it could give some insight into the phenomenon of moisture migration and drying of timber in fire conditions. Further research is needed in this direction, in order to quantify the heat flux that separates the

two behaviours, and to establish the reason for the higher time measured for the shallowest thermocouples.

3.5 Error Analysis

A weaker repeatability was found in the lower heat fluxes, with some tests showing a different heating behaviour than others. However, the calculated random error is of the same order of magnitude in all the cases. Table 3.7 shows the maximum errors for the averaged temperatures for all the heat fluxes, expressed in kelvins and as percentage (note that these maximum values occurred at different times and depths). The error was calculated by dividing the standard deviation by the square root of the number of measurements (Taylor 1997).

3.5.1 Temperature Tests

The errors shown in Table 3.7 are not only thermocouple errors, but they represent the whole ensemble of propagated uncertainties. They are the final result of any errors that could have been produced during the experimental procedure, and they comprise only the random errors (Taylor 1997) (as was said before, systematic errors can be minimized by randomizing the order in which the experiments are carried out). Random errors that can be encountered during the temperature profile tests are errors in the measurement of the imposed heat flux (which will be discussed in the following paragraphs), in the correct placement of the thermocouples (especially the depth from the exposed face of the sample), the thermocouple inherent accuracy, the data logger accuracy and response time, wood inhomogeneity (i.e. presence of knots), and finally daily and seasonal fluctuations in the ambient conditions (namely ambient temperature and relative humidity).

Heat Flux	**Heating**	δT	$\delta T / \lvert\overline{T}\rvert$
$10\,\mathrm{kW/m^2}$	Perpendicular	$31.6\,\mathrm{K}$	$8.79\,\%$
$18\,\mathrm{kW/m^2}$	Perpendicular	$30.5\,\mathrm{K}$	$10.76\,\%$
$25\,\mathrm{kW/m^2}$	Perpendicular	$19.1\,\mathrm{K}$	$6.95\,\%$
$40\,\mathrm{kW/m^2}$	Perpendicular	$23.8\,\mathrm{K}$	$12.59\,\%$
$60\,\mathrm{kW/m^2}$	Perpendicular	$29.3\,\mathrm{K}$	$7.63\,\%$
$10\,\mathrm{kW/m^2}$	Parallel	$30.8\,\mathrm{K}$	$10.12\,\%$
$60\,\mathrm{kW/m^2}$	Parallel	$23.0\,\mathrm{K}$	$6.47\,\%$

Table 3.7: Temperature profile tests. Maximum calculated random errors for different heat fluxes.

The times for the thermocouples in the different replications to reach 100°, 250° and 500°C were used to calculate the error in time. The maximum values are presented in Table 3.8. Temperature history curves with error bars in temperature and time are presented in Figure 3.34.

Heat Flux	**Heating**	δt	$\delta t / \bar{t}$
$10\,\mathrm{kW/m^2}$	Perpendicular	$565.5\,\mathrm{s}$	$5.9\,\%$
$18\,\mathrm{kW/m^2}$	Perpendicular	$254.5\,\mathrm{s}$	$10.0\,\%$
$25\,\mathrm{kW/m^2}$	Perpendicular	$72.6\,\mathrm{s}$	$2.4\,\%$
$40\,\mathrm{kW/m^2}$	Perpendicular	$140.7\,\mathrm{s}$	$5.3\,\%$
$60\,\mathrm{kW/m^2}$	Perpendicular	$34.5\,\mathrm{s}$	$1.7\,\%$
$10\,\mathrm{kW/m^2}$	Parallel	$598.1\,\mathrm{s}$	$6.2\,\%$
$60\,\mathrm{kW/m^2}$	Parallel	$99.9\,\mathrm{s}$	$5.4\,\%$

Table 3.8: Temperature profile tests. Maximum calculated random errors in time for different heat fluxes.

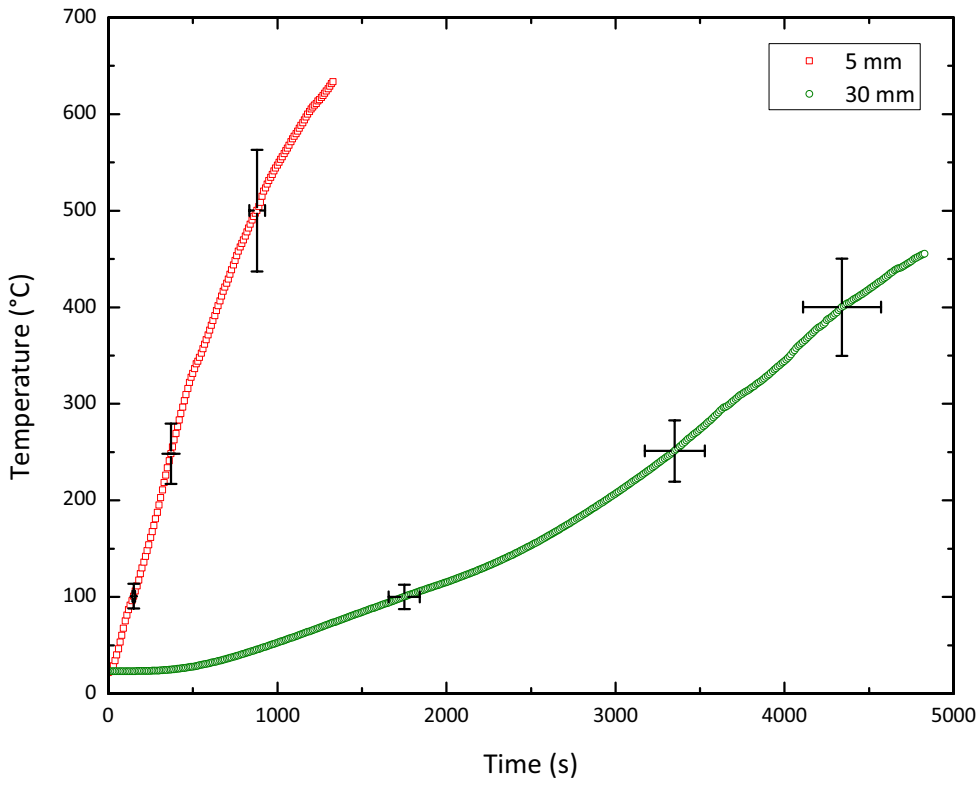

Figure 3.34: Error bars for the two thermocouple readings, at depths of 5 and 30 mm, 40 $\mathrm{kW{\cdot}m^{-2}}$. The error caused by the placement of the thermocouples parallel to the incident heat flux has not been included. Note that the error introduced by the placement of the thermocouples from the back side of the sample was not included (see Section 3.5.4)

3.5.2 Mass Loss Tests

The measured uncertainties in the mass loss tests showed a similar behaviour to the temperature tests, although in general the average errors were lower. The same weaker repeatability was observed in the lower heat fluxes, where even though the statistical mode of the error was low, peaks were observed due to the different behaviour at some instants during the tests, as can be seen in Figure 3.35 for the perpendicular heating at 18 kW·m^{-2}. Table 3.9 shows the maximum errors for all the heating cases.

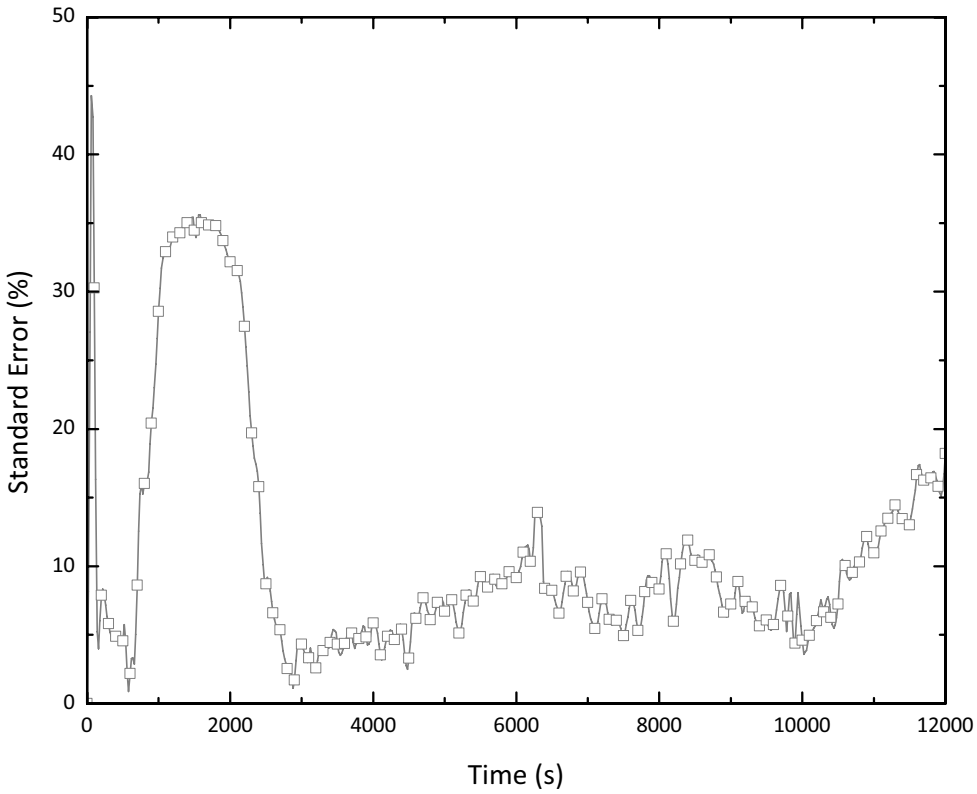

Figure 3.35: Standard error for 18 kW·m^{-2}, perpendicular heating. Although the replications clearly showed a different behaviour at about 2000 s, they all converged to the final mass loss rate (like all the tests except for 10 kW·m^{-2}), thus showing a smaller error at longer times.

3.5.3 Systematic Errors

On the other hand, systematic errors can occur and go unnoticed. They are hard to treat statistically and it is difficult to identify them (Taylor 1997). These occur mainly with defective equipment (that has not been properly calibrated, for example) or with a flawed experimental

Heat Flux	**Heating**	$\delta\dot{m}$	$\delta\dot{m}/\lvert\overline{\dot{m}}\rvert$
$10\,\mathrm{kW/m^2}$	Perpendicular	$3.46\times10^{-4}\,\mathrm{g\cdot s^{-1}}$	$19.2\,\%$
$18\,\mathrm{kW/m^2}$	Perpendicular	$1.03\times10^{-2}\,\mathrm{g\cdot s^{-1}}$	$35.6\,\%$
$25\,\mathrm{kW/m^2}$	Perpendicular	$6.25\times10^{-3}\,\mathrm{g\cdot s^{-1}}$	$14.1\,\%$
$40\,\mathrm{kW/m^2}$	Perpendicular	$1.28\times10^{-2}\,\mathrm{g\cdot s^{-1}}$	$16.1\,\%$
$60\,\mathrm{kW/m^2}$	Perpendicular	$5.52\times10^{-2}\,\mathrm{g\cdot s^{-1}}$	$26.2\,\%$
$10\,\mathrm{kW/m^2}$	Parallel	$3.11\times10^{-3}\,\mathrm{g\cdot s^{-1}}$	$48.3\,\%$
$60\,\mathrm{kW/m^2}$	Parallel	$2.11\times10^{-2}\,\mathrm{g\cdot s^{-1}}$	$23.6\,\%$

Table 3.9: Mass loss tests. Maximum calculated random errors for different heat fluxes. Note that the noise in the mass loss measurements in some cases makes these maximum values to be non-representative of the general trend.

method. During the testing campaigns conducted for this project, one source of systematic error was identified. The Cone Calorimeter at the University of Edinburgh has been in service for over 10 years and some of its components have not been replaced in that time span. During the tests carried out in the summer of 2007, it was noticed that the required heater temperature to obtain the desired heat flux levels was consistently lower than those required for the experiments in the previous times. It was decided to continue following the readings given by the computer, and no correction was performed. This led to those series of tests which were done in both 2005 and 2007 to present a greater uncertainty than those only carried out in just one campaign. This is exemplified in Table 3.10 showing the error in the heater temperature for temperature profile tests under perpendicular heating conditions.

Heat Flux	δT	$\delta T/\lvert\overline{T}\rvert$
$10\,\mathrm{kW/m^2}$	$0.65\,\mathrm{K}$	$0.16\,\%$
$18\,\mathrm{kW/m^2}$	$3.45\,\mathrm{K}$	$0.68\,\%$
$25\,\mathrm{kW/m^2}$	$0.43\,\mathrm{K}$	$0.07\,\%$
$40\,\mathrm{kW/m^2}$	$5.73\,\mathrm{K}$	$0.82\,\%$
$60\,\mathrm{kW/m^2}$	$0.66\,\mathrm{K}$	$0.08\,\%$

Table 3.10: Heater temperature errors for temperature profile tests, perpendicular heating. Note that the 18 and 40 $\mathrm{kW\cdot m^{-2}}$ sets of tests were performed in two different periods of time, showing an increased uncertainty.

Another possible source of systematic error was the load cell. It was observed that the more recent tests showed greater noise in the mass loss rate results, but in general they are consistent. These errors have not been thoroughly studied, and it must be pointed out that in fact the values presented in Tables 3.7 and 3.9 include these systematic errors. In terms of the actual influence of variations in the heater temperature on the measured heat flux, it will be analyzed in the coming paragraphs.

Concerns have been raised about the influence of the correct placement of the heat flux meter in

the actual incident radiant energy on the sample because the mounting system is not completely fail proof, so it is not uncommon to observe a badly fitted radiometer. After the variations in the heater temperature noticed during the last period of testing, it was decided to analyze the sensitivity of the measured heat flux not only to variations in the positioning of the sensor but also to changes in the heater temperature (Fuentes 2007). For this, a brief exercise was conducted, starting from the view factor calculations performed by Janssens during his doctoral research (Janssens 1991). The incident heat flux, as measured by the radiometer, was defined by Janssens as,

$$\dot{q}_e'' = \epsilon_h \cdot F \cdot \sigma \left(T_h^4 - T_\infty^4 \right), \tag{3.12}$$

expression which is obtained assuming that the gauge surface emissivity is equal to 1 and that its temperature is close to ambient. F is a "view factor",

$$F = \frac{F_{m-h}}{1 - F_{h-h}\left(1 - \epsilon_h\right)}. \tag{3.13}$$

The definitions for each of the terms and a more detailed development are given in Appendix D. For the moment, it is pertinent only to know that the view factors F_{m-h} and F_{h-h} are a function of the normal distance between the meter surface and the base of the cone (which is termed L_2, following Janssens's notation) and the distance between the centre of the radiometer and the edge of the heater, r_r (in a correctly placed gauge, this distance is equal to the radius of the base of the conical heater; see Figure 3.36 for a schematic representation of the cone heater). The error in the incident heat flux can be expressed as (Atreya 1983):

$$d\dot{q}_e'' = \left| \frac{\partial \dot{q}_e''}{\partial L_2} \right| dL_2 + \left| \frac{\partial \dot{q}_e''}{\partial r_r} \right| dr_r + \left| \frac{\partial \dot{q}_e''}{\partial T_h} \right| dT_h, \tag{3.14}$$

and by some mathematical handling the total error in the measurement of the incident heat flux can finally be expressed as a function of the uncertainties of the relevant variables (which can be estimated or measured):

$$\frac{d\dot{q}_e''}{\dot{q}_e''} = f_1\left(L_2, r_r\right) \frac{dL_2}{L_2} + f_2\left(L_2, r_r\right) \frac{dr_r}{r_r} + f_3\left(T_h\right) \frac{dT_h}{T_h}. \tag{3.15}$$

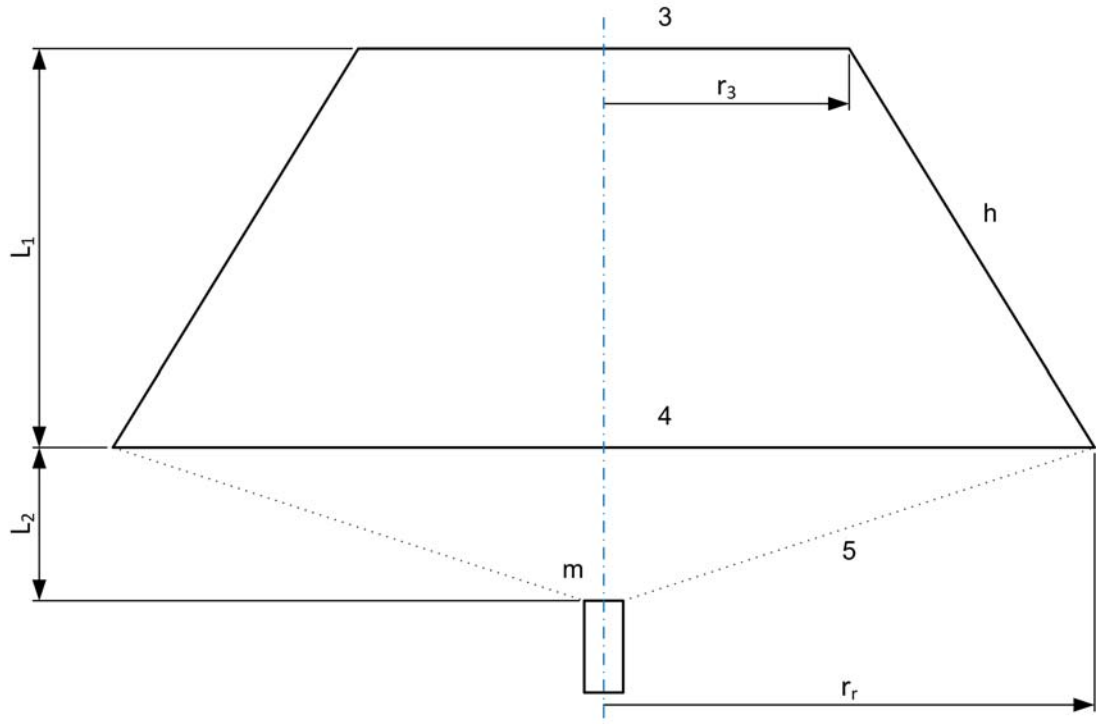

Figure 3.36: Cone Calorimeter heater dimensions. L_1 =65 mm; L_2 =25 mm; r_r =80 mm; r_3 =40 mm.

The error in the measurement of the incident heat flux on the specimen is thus dependent on the intensity of the radiation (heater temperature) and on the placement of the gauge. A 1.0% uncertainty of the heater temperature (cf. Table 3.10) yields a 1.0% error on the measured irradiance, but for lower heat fluxes the uncertainties are slightly larger (but given the fact that they are just estimations of random and unknown phenomena, uncertainties should not be written with too many decimal values, so they are basically the same). It was observed that irradiance uncertainties are directly proportional to heater temperature uncertainties.

The separation between the plane formed by the base of the heater and the surface of the meter does not seem to be much influential on the total uncertainty of the measured heat flux. A 10% error (this corresponds to roughly misplacing the radiometer by 2.5 mm, something very likely to happen during the normal Cone Calorimeter operation) will produce a measured radiant energy with an uncertainty of only 0.98%, thus showing that the results are robust to this type of error.

The measured heat flux uncertainty shows a greater sensitivity to the correct alignment of the heat flux gauge with the axis of the cone. Indeed, a misalignment of 8 mm (10% of the value of r_r, also something plausible to happen) will generate an error of 6.2%. Thus, it can be

concluded that the most influential sources of error when measuring the incident heat flux prior to an experiment are the heater temperature (showing a one to one proportionality) and the correct alignment of the meter to the axis of the cone. With this information, the estimated uncertainty for the incident heat flux on the sample is of 8.0%, independently of the intensity of the radiant energy.

3.5.4 Temperature Correction

The calculated disturbances generated by the thermal bridge caused when inserting the thermocouples parallel to the incident heat flux were calculated. The method is that described by Beck (Beck 1962), and is detailed in Appendix C. Disturbances for two solids, representing virgin wood and char, were calculated. The values obtained will constitute respectively the lower and upper bounds of the disturbances. The disturbances decrease in the deeper positions, but they are less dependent on the incident heat flux (see Figure 3.37).

These values are of the same order of magnitude as those reported by Schaffer (Schaffer 1967). Instead of placing the thermocouples from the sides of the samples, he inserted them from behind, but he bent the tip so as to place it perpendicular to the incident heat flux. He found differences of up to 32 K. He heated the samples using a furnace, so he provides no estimation of the incident heat flux.

3.6 Comparison with Other Experimental Results

In order to prove the correctness of the experimental results, they were compared with some previously published data. In general, mass loss data agrees well but the temperature measurements do not. The work by Kashiwagi et al (Kashiwagi et al. 1987) included mass loss and temperature profile measurements on White Pine at varying levels of ambient oxygen concentrations. The tests were done with parallel heating. The mass loss tests show similar shapes and converge to the same value as the tests conducted in this project (Figure 3.38). The temperature profiles show faster heating rates, when compared against measurements for the same heat flux but different grain orientation (Figure 3.39). The differences in the temperature measurements are caused by the orientation of the thermocouples. In this case, they were inserted perpendicular to the incident heat flux.

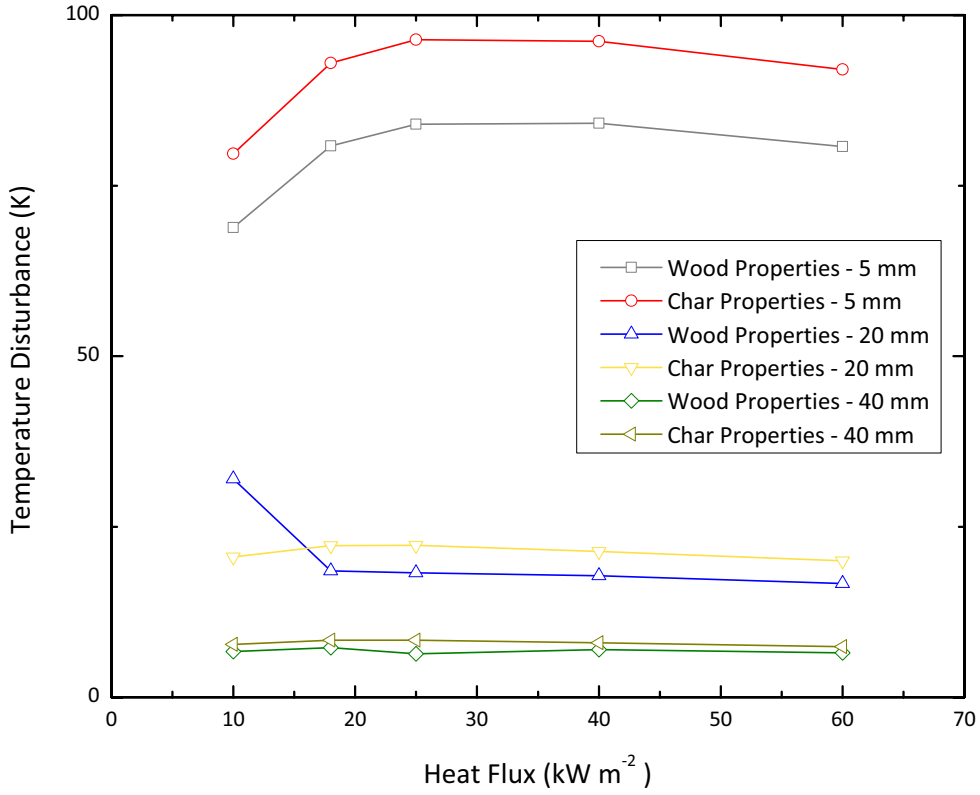

Figure 3.37: Maximum temperature disturbances caused by the presence of the thermocouples. The results for char are always greater, because it has greater insulation properties than virgin wood.

Roberts (Roberts 1971) plotted the maximum mass loss rate against the imposed heat flux. The results do not exactly compare, but are within the order of magnitude (Figure 3.40).

The measured temperature profiles were compared with those measured by Spearpoint (Spearpoint 1999) (Figure 3.41), with similar results as those obtained with the comparison with Kashiwagi et al. The reason for the discrepancy is again the orientation of the thermocouples. Finally, the calculated values for the speed of the moisture front are of the same order of magnitude as those calculated by White and Schaffer (White & Schaffer 1981).

3.7 Summary

The experiments yielded repeatable results, both in the temperature profile and mass loss tests, something difficult to achieve with wood. Lower heat fluxes, however, showed less repeata-

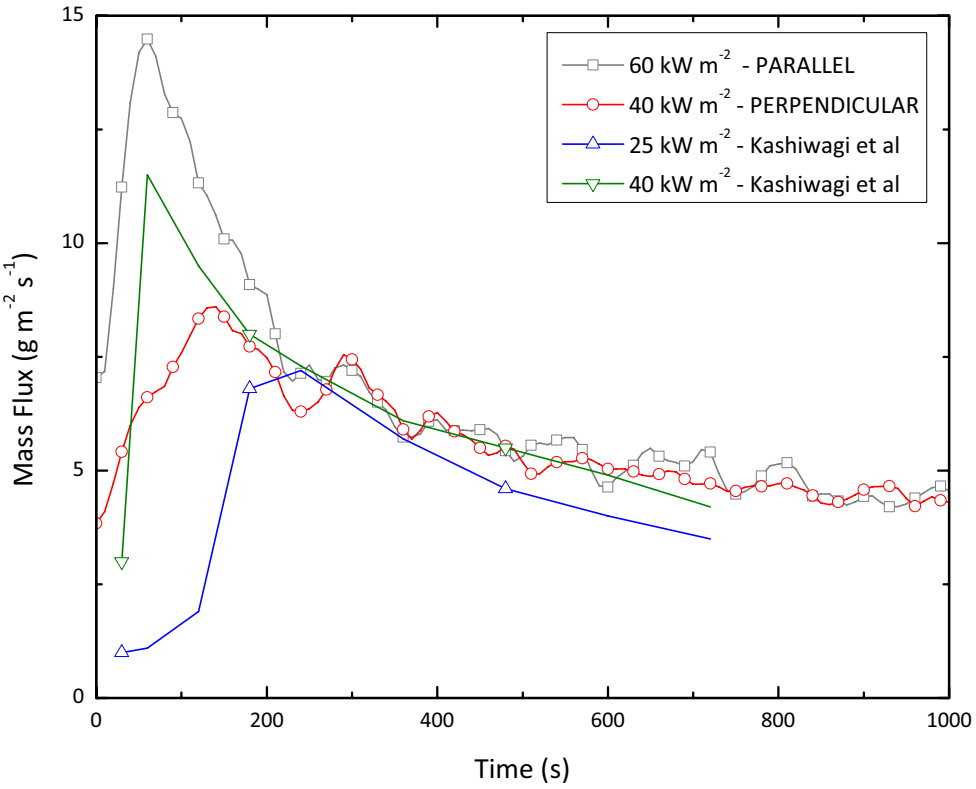

Figure 3.38: Comparison with mass flux measured by Kashiwagi et al. (Kashiwagi et al. 1987). Results show good agreement at later times, with the differences in the peak values being attributed to differences in the wood species and grain orientation (The samples of Kashiwagi et al. were heated parallel to the grain).

bility, especially at 10 kW·m^{-2}, where this intensity is close to the critical heat flux for pilot ignition, and marks the onset of the pyrolysis reactions. This behaviour has been confirmed by non-dimensioning the measured data using the results of an inert heating solution. It shows that the 10 kW·m^{-2} follows the inert behaviour more closely than the rest of the tests.

Wood initially presents an inert behaviour, and departs from it as moisture evaporation commences. This produces a marked front of liquid moisture flowing from the sides of the sample. The measured speed of the front indicates that at longer times the speeds for all heat fluxes converge to an asymptotic value. The measured temperatures at the time the moisture front reached the particular thermocouple position show two distinct behaviours for low and high heat fluxes, where the higher heat fluxes show a constant temperature close to 359 K, while for the lower heat fluxes the temperatures grow as depth increases. This conduct is reinforced by the Moisture Delay Time, which marks the time for a particular thermocouple to reach a

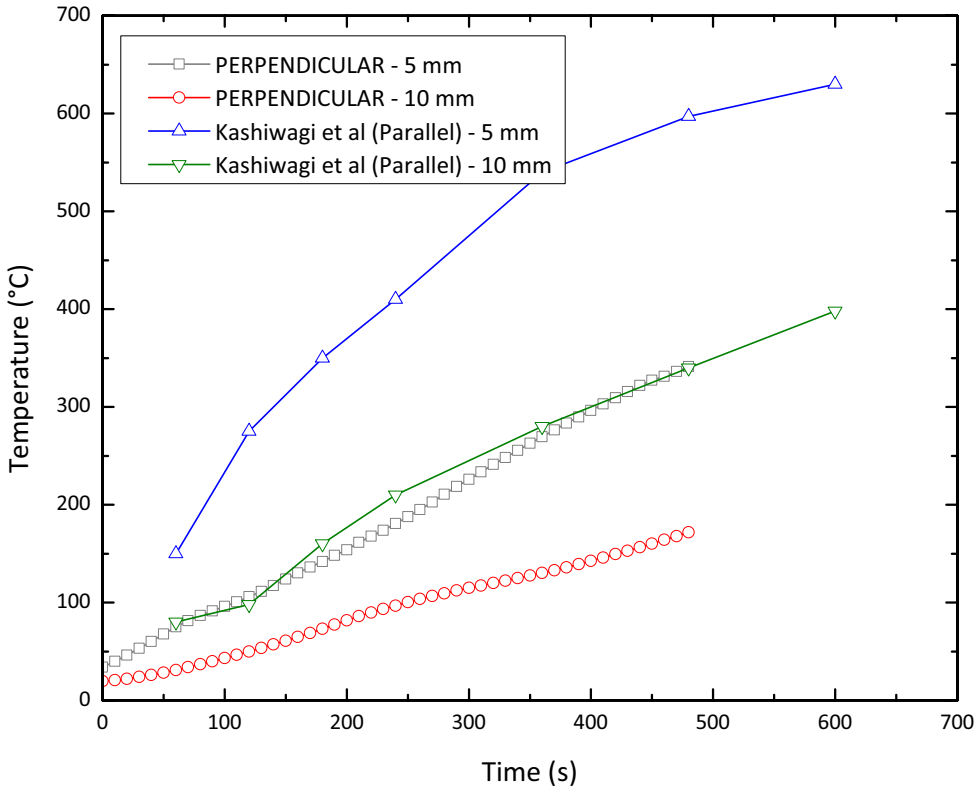

Figure 3.39: Comparison with temperature histories measured by Kashiwagi et al. (Kashiwagi et al. 1987), for an external heat flux of 40 kW·m^{-2}. The samples of Kashiwagi et al. are parallel heated samples, and the thermocouples were inserted from the sides of the samples, which explains the differences.

temperature of 373 K, and where the higher heat fluxes, namely above 40 kW·m^{-2}, show a constant time regardless of the depth, while the lower heat fluxes show increasing times and greater spread. The Moisture Delay Time also proves that the effect of the moisture evaporation can be modelled as a heat sink, as it depends only on the imposed heat flux.

The effect of the pyrolysis reactions is less marked in terms of the recorded temperature rise, and the charring front proceeds more slowly than the moisture evaporation front. It has been proven that both fronts proceed in a one-dimensional manner for a long period of exposure, confirming the one-dimensional heating assumption that will be used in the numerical modelling of the phenomenon.

Mass loss rates show a peak value early in the tests that is dependent on the incident heat flux. However, for longer times the mass loss rates reach an asymptotic value common for all levels

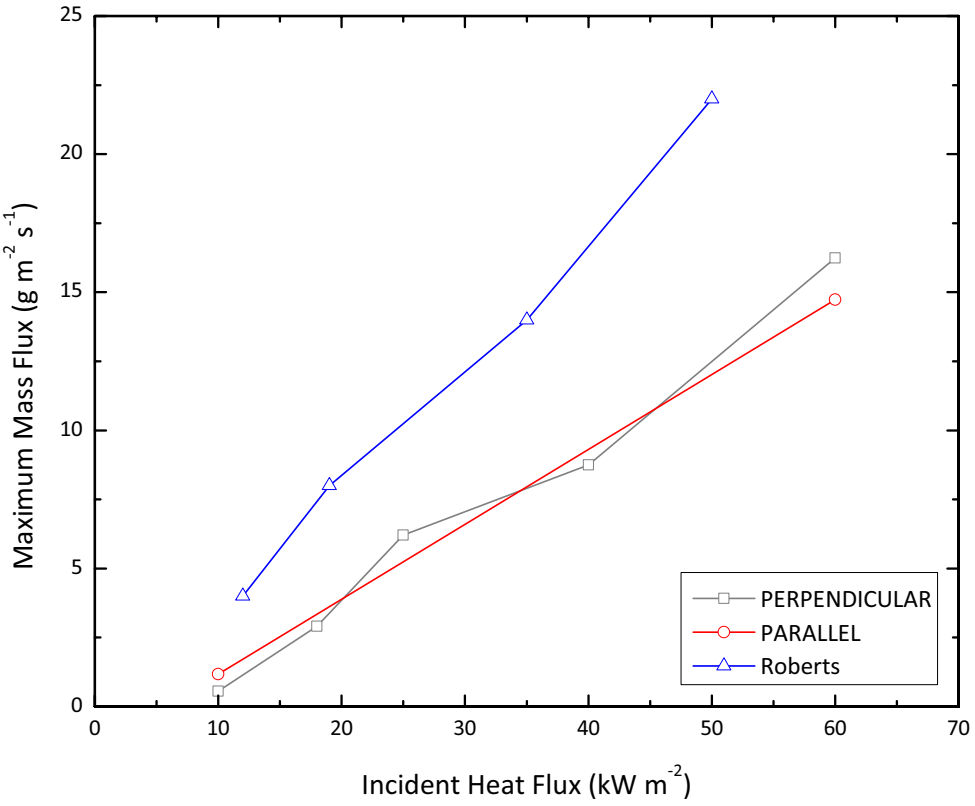

Figure 3.40: Comparison with maximum mass flux measured by Roberts (Roberts 1971).

of irradiance, something which was also observed for the speed of the moisture front. Thus, it can be concluded that steady state conditions are independent of the incident heat flux.

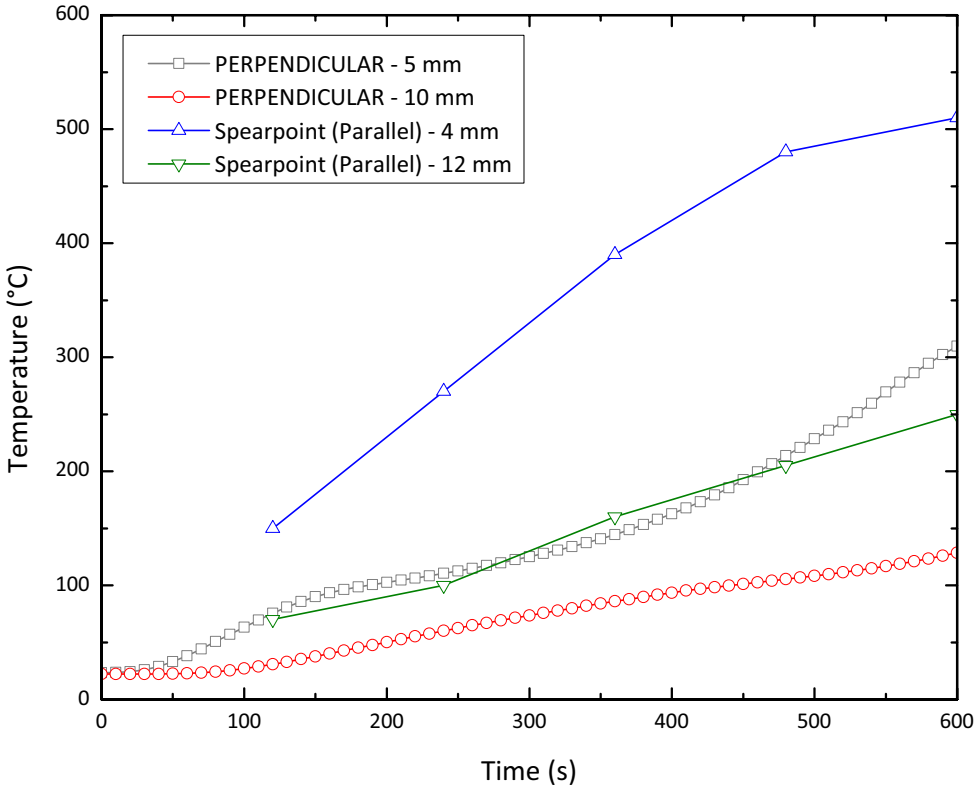

Figure 3.41: Comparison with temperature histories measured by Spearpoint (Spearpoint 1999). Spearpoint inserted the thermocouples from the sides of the samples, which explains the differences.

Chapter 4

Mathematical Modelling of Wood Pyrolysis

This chapter will present a brief description of the pyrolysis process, and then will deal with the modelling of the pyrolysis process itself. Roberts (Roberts 1971), Drysdale (Drysdale 1998), Atreya (Atreya 1983) and Fredlund (Fredlund 1988) provide good phenomenological analyses of the problem of wood pyrolysis and burning, while other reviews present more information on the modelling process itself (Kanury 1972, Di Blasi 1993*b*, Atreya 1998, Moghtaderi 2006, Di Blasi 2007). Several models have been developed during the course of this project, with the goal of obtaining the most simplified model which still yields accurate temperature predictions. The results of the modelling, with the comparison of the different models and a comparison with the experimental measurements will be presented in the next chapter.

4.1 Pyrolysis of Wood

When a thick timber member is subjected to a heat flux, initially, as was seen in the previous chapter, it heats up as an inert material, with the regions closest to the exposed surface heating faster than the deeper areas. The heating rate is going to be controlled, apart from the magnitude of the incident heat flux, by the thermal properties of wood itself. Wood is inhomogeneous, and its thermophysical properties vary not only with each species but also some of them vary with the direction of the heating, as is the case with its thermal conductivity (and therefore the thermal diffusivity) and permeability.

The first phenomenon that makes wood divert from the inert behaviour is the evaporation of the moisture contained in it. As pointed out by Siau (Siau 1984), moisture is present in wood in two forms, as bound water within the cell wall and as free liquid water in the voids of wood (water is also present as part of the molecules that make up wood (Atreya 1983), but this water is freed only when wood pyrolyzes). Normally, for moisture content values below the fibre saturation point, all the moisture present is in the form of bound water. When the shallower regions reach temperatures close to 373 K, moisture begins to evaporate, slowing down the heating rate. Some of the generated vapour will flow out of the wood matrix, but some of it will diffuse and flow into the deeper sections of the timber element, where it will re-condense (the importance of this process is not large (Atreya 1983)). As this process progresses into the interior, there will be an increase in the pressure generated, speeding up the flow of vapour. It is likely that at some point the moisture content will be higher than the fibre saturation point, so there will be a presence of free water. Some of this water will then flow in liquid form. Liquid water flowing out from the sides of the wood specimens has been observed experimentally (cf. Chapter 3).

Once the water has been evaporated in the surface regions, the temperature will continue rising until it is high enough to permit the pyrolysis reactions to start. Wood molecules will break up and produce volatile gases and char. Just before the char layer forms, the mass loss rate will reach its maximum value (Roberts 1971), and then the insulating properties of char, plus the fact that the raise in the surface temperature will increase the losses thus diminishing the net heat flux, will make the mass loss rate to decrease its value. There is agreement now about the endothermic nature of this process (Kanury 1972, Atreya 1983, Fredlund 1988, Koufopanos, Papayannakos, Maschio & Lucchesi 1991, Di Blasi 1993*b*). The gases will exit through the forming cracks on the surface and will also be forced inwards, due to an increase in the pressure (maximum measured values range from about 0.3 to 1 atm manometric (Tinney 1965, Lee et al. 1976, Fredlund 1988)). At higher temperatures, secondary reactions involving gases and char will begin to take place. There is also agreement that the nature of these reactions is exothermic (Atreya 1983, Koufopanos et al. 1991, Di Blasi 1993*b*), particularly for thick samples.

4.1.1 The Challenge of Modelling the Pyrolysis of Wood

Wood is an extremely inhomogeneous material, with a marked anisotropy. These and several other characteristics of wood make the modelling of its pyrolysis a difficult process. First of

all, the changes of the thermophysical properties of wood with both temperature and moisture content (Siau 1984), and once charring has begun, will affect the transport processes inside the wood (Roberts 1971, Di Blasi 2007). This is enhanced by the fact that there will be gradients of temperature, pressure, moisture content and degree of charring along the depth and sides of the pyrolyzing timber element. Char will have less density and thermal conductivity, about the same value of specific heat (Roberts 1971), and more porosity (Panton & Rittmann 1971) and permeability (it is expected to vary with porosity, (Di Blasi 1993*a*)). Data for partially pyrolyzed wood is not readily available (Atreya 1983), so their properties are taken as a linear combination of virgin wood and char.

Structural changes, namely shrinkage of the wood element and cracking are also an inconvenience for the modelling process. Wood shrinks when it loses moisture from the cell walls, and swells when it gains moisture (FPL 1999). These processes will certainly take place during the pyrolysis process, with the moisture being evaporated and part of it re-condensing. Shrinkage is also likely to be caused by the pyrolysis process itself.

Shrinkage in turn is the cause of mechanical forces that could cause cracking (Atreya 1983). Cracking reduces the residence time of the volatiles, which in turn affects the importance of the secondary reactions on the energetics of the pyrolysis process (Roberts 1971, Di Blasi 1993*b*). Cracking will also alter the heat transfer into the timber element (Roberts 1971).

Inhomogeneity in wood also is expressed in the differences in the kinetic parameters for different wood species (for example see Table 1, (Di Blasi 2007)). Kinetic modelling of wood will be further discussed in the coming sections. All these difficulties have led to various approaches followed by those who have undertaken the modelling of the pyrolysis of wood. Some of these will be discussed in the following section.

4.2 Pyrolysis Modelling

The aim of this section is to perform a concise review of the forms in which the thermal decomposition of wood has been modelled by various researchers. More emphasis will be placed on the energy conservation equation, but due to the coupling between the processes of heat, mass and momentum transfer, these final two modes of transport will also be analyzed. The idea is to examine every term in the energy equation and to present and analyze the different ways of

representing them available in the literature.

4.2.1 Foreword

The following review will show that there are two main numerical strategies in modelling the pyrolysis of wood. The most common one is to solve the conservation equations for the whole element in consideration, assuming, as it happens in reality, that the decomposition reactions and the process of moisture evaporation occur in the whole volume. In contrast, moving boundary problems assume that infinitely fast decomposition reactions occur in a plane which moves in time into deeper positions of the sample. Thus, the conservation equations are solved in as many different domains as are defined by the moving boundaries. In this case, three different domains were considered, the virgin wood, the dry wood and the char.

In terms of the physical strategies, which in theory can be implemented in both volumetric reaction and moving boundary models, many approaches can be found in the way the conservation equations are expressed. Summarizing the following sections, the main differences the models will exhibit lie in the reaction schemes, from multiple, competing reactions to one step reactions, some of which incorporate final char densities, to a single, infinitely fast reaction. Depending on the kinetic models employed, the number of species considered, particularly in the gas phase, will vary between the models. Water evaporation is another effect that is treated differently: Arrhenius one step schemes, evaporation rates calculated on the basis of expressions relating the saturation pressure with temperature, and finally infinitely fast changes of phase happening in a moving evaporation front. Convection can be treated by modelling the pressure build up and then calculating the gas velocities through the porous matrix, or the gases can simply be assumed to exit immediately once they are produced. Most of these variations in approach were modelled.

4.2.2 Energy Balance in Wood

In order to put the equations into context, the analysis will begin with the energy balance of a block of wood heated by an external heat flux. If an infinitely wide slab of wood of a finite thickness is heated by a uniform heat flux such that heat, mass and momentum transfer in the slab are one dimensional, the first law of thermodynamics applied to a control volume anywhere within the block of wood can be expressed in this form (Moran & Shapiro 1998, Bejan 1997):

$$\frac{d}{dt}\left(E_{cv}\right) = \dot{Q} - \dot{W}_{cv} + \sum_{in} \dot{m}\left(h + \frac{\vec{v}^2}{2} + g \cdot z\right) - \sum_{out} \dot{m}\left(h + \frac{\vec{v}^2}{2} + g \cdot z\right). \tag{4.1}$$

Note that the enthalpy terms of the flowing masses already include the work due to pressure. The total energy of the control volume, E_{cv}, is the sum of the internal, kinetic and potential energies. Assuming that the wood matrix is homogeneous, that the gases and the solid are in local thermal equilibrium (Kansa et al (Kansa et al. 1977) argue that for many pyrolysis situations the Peclet number, defined as $Pe = c_{p,g} \cdot \dot{m}''_g \cdot L / k_{sol}$, is large enough for this statement to be valid), that the kinetic and potential energies of the control volume and the gases can be neglected (Atreya 1983), and that there is no work done by the control volume. Neglecting the mass transfer of liquid water and the term pV in the equation $H = U + pV$ (Di Blasi 1993*a*), dividing by the total volume of the control volume, and applying lim $\Delta x \rightarrow 0$, the energy conservation equation can then be rewritten in a differential form as:

$$\frac{\partial}{\partial t}\left(\rho_{cv}^{app} \cdot h_{cv}\right) = \frac{1}{V_{tot}}\left(\dot{Q}\right) - \frac{\partial}{\partial x}\left(\sum_i \dot{m}''_{g_i} \cdot h_{g_i}\right). \tag{4.2}$$

The left hand side term represents the rate of change in the sensible energy over the entire control volume (now expressed in terms of enthalpy), the first term on the right accounts for the net heat transfer through the volume and the heat sources (or sinks), and finally the last term indicates the net transfer of enthalpy by unit area due to convection in the gas phase only. The following paragraphs will analyze each one of these terms and present the way they are modelled by various researchers.

4.2.3 Density vs. Mass Concentration

It is important at this stage of the analysis to refer to the significance of the proper representation of the mass concentrations which appear in the conservation equations. The use of density and mass concentration is somewhat loose in the literature, and in the specific case of dealing with porous media a clear definition must done between two similar properties, which will be termed

density and mass concentration. Density, as described by Van Wylen and Sonntag (Van Wylen & Sonntag 1978), is defined as the mass of species i per unit volume of the species. If we consider a small volume δV of species i, with a mass δm_i, then the density is

$$\rho_i = \lim_{\delta V \to \delta V'} \frac{\delta m_i}{\delta V}, \tag{4.3}$$

where $\delta V'$ is the smallest volume for which the species can be considered a continuum (Van Wylen & Sonntag 1978). Mass concentration of species i is defined as the amount of mass divided by the total volume of the control volume (analogous to the definition by Kuo (Kuo 2005)). To avoid the use of extra symbols, mass concentration will be denoted with the superscript app (meaning apparent) as:

$$\rho_i^{app} = \frac{m_i}{V_{tot}}, \tag{4.4}$$

The differences between density and mass concentration become clear when within the control volume there are gases and porous solids. These two representations are used indistinctively throughout the literature, and sometimes both of them are employed in the same model, so care must be taken to use a consistent representation throughout the whole analysis. In this case it has been chosen to use the densities for the gas-phase species and to use mass concentrations for the solid and liquid phases. There is really no important reason to do so, it is rather historical: the first model analyzed was that by Di Blasi (Di Blasi 1993*a*), which uses the same representation.

Gas-phase mass concentrations can be converted into apparent concentrations by multiplying them by the porosity of the solid matrix:

$$\rho_{g_i}^{app} = \varphi_{gas} \cdot \rho_{g_i}. \tag{4.5}$$

Note that in this particular problem three phases are present, so the porosity used corresponds to the volume of gases, not the volume of voids, divided by the total volume, because the pores are partially filled with free water. So, assuming that the pyrolysis gases will always be perfectly mixed in all the pores of the solid matrix, a single gas porosity can be defined:

$$\varphi_{gas} = \frac{V_{gas}}{V_{tot}}. \tag{4.6}$$

The water porosity is defined in a similar way (it is emphasized that the movement of liquid water through the porous matrix has not been considered).

$$\varphi_{liq} = \frac{V_{liq}}{V_{tot}}. \tag{4.7}$$

4.2.4 Sensible Heat

The first term of Eq. 4.2, represents the change in the enthalpy of the substances contained in the control volume. By representing the total enthalpy of the control volume as the sum of the different components and assuming that the only solid phase elements which are present are virgin wood and char, the term becomes

$$\rho_{cv}^{app} \cdot h_{cv} = \rho_{w}^{app} \cdot h_{w} + \rho_{c}^{app} \cdot h_{c} + \rho_{wat}^{app} \cdot h_{wat} + \varphi_{gas} \sum_{i} \rho_{g_i} \cdot h_{g_i}, \tag{4.8}$$

with i gas phase species and the terms with the subscript wat representing the liquid water contained within the pores. Now, the change in time of the sensible heat contained within the control volume can be written as (see, for example, (Di Blasi 1993*a*, Melaaen 1996)):

$$\frac{\partial}{\partial t}\left(\rho_{w}^{app} \cdot h_{w} + \rho_{c}^{app} \cdot h_{c} + \rho_{wat}^{app} \cdot h_{wat} + \varphi_{gas} \sum_{i} \rho_{g_i} \cdot h_{g_i}\right).$$

This would be the most complete representation. A common simplification made on this term is neglecting the contribution of the gas-phase species (Bamford et al. 1946, Kung 1972, Atreya 1983, Fredlund 1993, Benkoussas, Consalvi, Porterie, Sardoy & Loraud 2007), arising from the observation that (Atreya 1983)

$$\rho_g \cdot h_g \ll \rho_s \cdot h_s.$$

Note that changes of phase are not represented here: two phases of the same substance are treated as different species and the latent heats are accounted for elsewhere (as is the case

for liquid water and water vapour). For convenience the superscript will be dropped from the apparent mass concentrations in the coming equations, but the way of representing the mass concentrations for the solid, liquid and gas phases will remain intact.

Finally, using the definition of enthalpy (Bejan 1997),

$$\partial h = c_p \, \partial T, \tag{4.9}$$

the sensible heat term can be expanded into

$$\left[\rho_w \, c_{p_w} + \rho_c \, c_{p_c} + \rho_{wat} \, c_{p_{wat}} + \varphi_{gas} \left(\rho_{vap} \, c_{p_{vap}} + \sum_i \rho_{g_i} \, c_{p_{g_i}} \right) \right] \frac{\partial T}{\partial t}$$

$$+ h_w \frac{\partial \rho_w}{\partial t} + h_c \frac{\partial \rho_c}{\partial t} + h_{wat} \frac{\partial \rho_{wat}}{\partial t} + \varphi_{gas} \left(h_{vap} \frac{\partial \rho_{vap}}{\partial t} + \sum_i h_{g_i} \frac{\partial \rho_{g_i}}{\partial t} \right)$$

$$+ \left(\rho_{vap} \cdot h_{vap} + \sum_i \rho_{g_i} \cdot h_{g_i} \right) \frac{\partial \varphi_{gas}}{\partial t}.$$

4.2.5 Heat Transfer and Heat Sources

The first term at the right hand side of Equation 4.2 is divided into the heat that is conducted through the control volume and the heat sources (sinks) caused by chemical reactions or phase changes. Neglecting cross-diffusion both in the energy and mass conservation equations (Dufour and Soret effects) and convection due to the fact that local thermal equilibrium is assumed, the heat will be transferred only by conduction (although a radiative contribution can be incorporated, as will be shown shortly).

Heat transfer through the gas can be included by incorporating an overall thermal conductivity. Most researchers calculate this conductivity by doing an arithmetic mean of the fluid, liquid and solid conductivities, under the assumption that the heat is conducted in parallel through the gas, liquid and solid phases. This represents an upper bound, with the value of the overall conductivity being lower if the heat transfer is assumed to happen in series, using a harmonic mean (Nield & Bejan 1992, Staggs 2003):

$$k_{arith} = \left(1 - \varphi_{gas} - \varphi_{liq}\right) k_{sol} + \varphi_{gas} \cdot k_{gas} + \varphi_{liq} \cdot k_{liq},$$
$$\frac{1}{k_{harm}} = \frac{1 - \varphi_{gas} - \varphi_{liq}}{k_{sol}} + \frac{\varphi_{gas}}{k_{gas}} + \frac{\varphi_{liq}}{k_{liq}}. \tag{4.10}$$

The solid conductivity is generally expressed as a linear combination of the wood and char conductivities, weighed by the ratio of the solid material mass to the initial wood mass or final char density (Panton & Rittmann 1971, Kung 1972, Atreya 1983, Do & Springer 1983, Fredlund 1988, Di Blasi 1993*a*).

$$k_{sol} = \frac{\rho_w}{\rho_w^o} k_w + \frac{\rho_c}{\rho_w^o} k_c. \tag{4.11}$$

Another term is sometimes included in the overall conductivity to account for the radiative transfer inside the pore structure (Chan et al. 1985, Di Blasi 1993*a*). The original approximation is a function of the solid conductivity, its emissivity and the matrix porosity (Siegel & Howell 2002, Singh & Kaviany 1994),

$$k_{rad} = 4F \cdot \sigma \cdot d \cdot T^3; \quad F = f(k_{sol}, \varepsilon, \varphi). \tag{4.12}$$

With all, the net conductivity is then expressed as:

$$k_{net} = \left(1 - \varphi_{gas} - \varphi_{liq}\right) k_{sol} + \varphi_{gas} \cdot k_{gas} + \varphi_{liq} \cdot k_{liq} + k_{rad}. \tag{4.13}$$

Heat sinks due to chemical reactions are normally modelled as a heat of reaction multiplied by the reaction rate. The values of the heats of reaction and the reaction rates will depend on the kinetic schemes used. The reader is referred to the reviews by Di Blasi (Di Blasi 1993*b*, Di Blasi 2007), Antal and Varhegyi (Antal & Varhegyi 1995), and Moghtaderi (Moghtaderi 2006) for details on the state of the art of pyrolysis kinetics modelling. The heat sink is represented as

$$\dot{\omega}_i \cdot \Delta h_i,$$

with $\dot{\omega}_i$ being the reaction rate. In the present notation, the reaction rates for the solid phase will differ from those of the gas phase in that the latter ones must be multiplied by the porosity. Reactions are usually taken as first order (Bamford et al. 1946, Simms 1962, Weatherford & Sheppard 1965, Tinney 1965, Chan et al. 1985, Alves & Figueiredo 1989, Fredlund 1993, Di Blasi 1993*a*, Bryden, Ragland & Rutland 2002, Yuen, Yeoh, de Vahl Davis & Leonardi 2007).

$$\begin{aligned} \dot{\omega}_i &= \rho_i \cdot K_i \qquad \text{(solid phase)}, \\ \dot{\omega}_i &= \varphi_i \cdot \rho_i \cdot K_i \quad \text{(gas phase)}. \end{aligned} \tag{4.14}$$

Reaction rate coefficients are calculated using Arrhenius first order expressions, where the kinetic scheme used will determine the number of reactions taking place (Di Blasi 1993*b*, Di Blasi 2007, Antal & Varhegyi 1995):

$$K_i = A_i \cdot e^{-E_i/RT}. \tag{4.15}$$

Another way of representing the reaction rates for pyrolyzing wood has been widely used (Kung 1972, Kansa et al. 1977, Atreya 1983), and it relies on the assumption that the reacting solid is constituted by an active fraction and a final, inert fraction, which would correspond to char (but the value of the final mass concentration should take into account its shrinkage (Atreya 1983)). Thus, with ρ_a being the instantaneous density of the pyrolyzing wood (active material),

$$\dot{\omega}_a = -\left(\rho_a - \rho_c\right) \cdot K_a. \tag{4.16}$$

This scheme normally assumes a one-step global reaction for the pyrolysis process. Saastamoinen and Richard (Saastamoinen & Richard 1996) use a modified version of this equation, where the final char density is given by an empirically determined function of temperature, $e(T)$. K_e is also experimentally determined:

$$\dot{\omega}_a = -[\rho_a - \rho_0 \cdot e\,(T)] \cdot K_e. \tag{4.17}$$

They mention that constant final char yields may overestimate the generation of volatiles at high temperatures and underestimate it at low temperatures. A third way of expressing wood reaction rates is by using a char mass fraction (Benkoussas et al. 2007, Di Blasi 1996), where the decomposition of wood is modelled as in Equation 4.14 and the char and gas reaction rates are

$$\dot{\omega}_c = \nu_c \cdot \rho_a \cdot K_a, \tag{4.18}$$

$$\dot{\omega}_g = (1 - \nu_c) \cdot \rho_a \cdot K_a. \tag{4.19}$$

Some authors consider surface char oxidation and include it as a boundary condition in the energy conservation equation (Fredlund 1988, Benkoussas et al. 2007), but this phenomenon has not been considered in this work. A summary of the different kinetic schemes will be presented in the section that deals with the pyrolysis models used.

There is less agreement in the treatment of the water evaporation. First-order Arrhenius expressions are sometimes used to calculate the "reaction" rate, therefore treating water vapour like another pyrolysis gas (Chan et al. 1985, Bryden et al. 2002).

$$\begin{aligned} \dot{\omega}_{wat} &= \rho_{wat} \cdot K_{wat}, \\ K_{wat} &= A_{wat} \cdot e^{-E_{wat}/RT}. \end{aligned} \tag{4.20}$$

Benkoussas et al (Benkoussas et al. 2007) use a modified version of this equation:

$$K_{wat} = A_{wat} \cdot T^{-1/2} \cdot e^{-E_{wat}/RT}. \tag{4.21}$$

Another approach (Fredlund 1988, Yuen et al. 2007) is to suppose the vapour pressure to be

equal to the saturation pressure, and assume that it follows the relationship

$$p_{vap}^{sat} = A_1 \cdot e^{-A_2/T}, \tag{4.22}$$

where A_1 and A_2 are empirically obtained constants. If vapour is thought to behave like an ideal gas and after differentiating ρ_{vap} and p_{vap}^{sat} with respect to time and inserting these terms into the vapour mass conservation equation, an expression for the rate of evaporation is obtained

$$G_{wat} = \frac{M_{wat}}{R}\left(\frac{1}{T^3}A_1 \cdot A_2 \cdot e^{-A_2/T} - \frac{1}{T^2}A_1 \cdot e^{-A_2/T}\right)\frac{\partial T}{\partial t} - \frac{\partial}{\partial x}\left(\dot{m}''_{vap}\right). \tag{4.23}$$

With G_{wat} being equivalent to the term ω_{wat} in the Arrhenius type formulations. The solution procedure is recursive, because the mass flows must be known in order to obtain a value for G_{wat} and subsequently calculate the updated values for ρ_{wat} and ρ_{vap} from the conservation equations.

The heat transfer and heat source term then takes the form

$$\frac{1}{V_{tot}}\left(\dot{Q}\right) = \frac{\partial}{\partial x}\left(k_{net}\frac{\partial T}{\partial x}\right) + \dot{\omega}_{wat} \cdot \Delta h_{fg} + \sum_i \dot{\omega}_i \cdot \Delta h_i. \tag{4.24}$$

4.2.6 Heat Transfer by Convection

The final term in the energy conservation equation represents the net transfer of enthalpy originated by the convection of the pyrolysis gases. There is general agreement on the form of this expression, but there are variations in the way the mass fluxes are calculated. It is therefore convenient to continue the discussion with the analysis of mass transfer in the porous matrix. Note that in these conservation equations the presence of air in the porous medium, as well as the mass transfer by diffusion, have been neglected: Chan et al (Chan et al. 1985) estimated that the characteristic time for mass transfer by diffusion is 3 orders of magnitude greater than the mass transfer by hydrodynamic flow, a result corroborated by Moghtaderi (Moghtaderi 2006).

Since there is no mass flux for solid of liquid substance, the rate of change in time of the density of the substance will be equal to the sum of the reaction rates for the production or consumption

of that substance (or both). So, the mass balance equation for the solid phase becomes

$$\frac{\partial \rho_{sol}}{\partial t} = \sum \dot{\omega}_{sol}. \tag{4.25}$$

In the case of the gaseous phase, the convective term must be incorporated (Nield & Bejan 1992, Kuo 2005):

$$\frac{\partial}{\partial t}\left(\varphi_{gas} \cdot \rho_{g_i}\right) + \frac{\partial}{\partial x}\left(u \cdot \rho_{g_i}\right) = \sum \dot{\omega}_{g_i}. \tag{4.26}$$

Equation 4.26 replaces the mass flux term $\dot{m}''_{g_i}$ by $u \cdot \rho_{g_i}$ (Kuo 2005). The term u corresponds to the gas seepage velocity, and is defined as the fluid velocity averaged over V_{tot} (Nield & Bejan 1992). If pressure is considered in the model, the gas seepage velocity is given by Darcy's Law (instead of the momentum conservation equation):

$$u = -\frac{K}{\mu} \cdot \frac{\partial p}{\partial x}. \tag{4.27}$$

Another note must be made here regarding the correct use of the chosen mass concentrations and the porosity. The proper velocity to use in the gas mass conservation equation would be the intrinsic fluid velocity (averaged over V_g). In that term the porosity is also present, and combining both by the Dupuit - Forchheimer relationship (Nield & Bejan 1992) the seepage velocity is obtained and can be calculated by Darcy's Law.

$$u = \varphi_{gas} \cdot v. \tag{4.28}$$

When no pressure is considered, the mass flux can be calculated from the simplified conservation equation assuming that the devolatilization gases immediately flow out of the solid after they are generated (Kung 1972, Tamanini 1976*a*, Parker 1985, Benkoussas et al. 2007). This means that the gases do not accumulate in the pores, so the mass accumulation term in Equation 4.26 is zero. The mass conservation equation is reduced to:

$$\frac{\partial \dot{m}''_{g_i}}{\partial x} = \sum \dot{\omega}_{g_i}. \tag{4.29}$$

So finally the expression for the last term in Eq. 4.2, whatever the form used to calculate the gas mass fluxes, can be written as

$$\frac{\partial}{\partial x}\left(\sum_i \dot{m}''_{g_i} \cdot h_{g_i}\right) = \sum_i \left(h_{g_i}\frac{\partial}{\partial x}\left(u \cdot \rho_{g_i}\right) + u \cdot \rho_{g_i} \cdot c_{p_{g_i}}\frac{\partial T}{\partial x}\right). \tag{4.30}$$

4.2.7 Energy Equation

Now Equation 4.2 can be rewritten as:

$$\begin{aligned}
&\left[\rho_w\, c_{p_w} + \rho_c\, c_{p_c} + \rho_{wat}\, c_{p_{wat}} + \varphi_{gas}\left(\rho_{vap}\, c_{p_{vap}} + \sum_i \rho_{g_i}\, c_{p_{g_i}}\right)\right]\frac{\partial T}{\partial t} \\
&+ h_w\frac{\partial \rho_w}{\partial t} + h_c\frac{\partial \rho_c}{\partial t} + h_{wat}\frac{\partial \rho_{wat}}{\partial t} + h_{vap}\frac{\partial \varphi_{gas}\cdot\rho_{vap}}{\partial t} \\
&+ \sum_i h_{g_i}\frac{\partial \varphi_{gas}\cdot\rho_{g_i}}{\partial t} = \frac{\partial}{\partial x}\left(k_{net}\frac{\partial T}{\partial x}\right) + \dot{\omega}_{wat}\cdot\Delta h_{fg} \\
&+ \sum_i \dot{\omega}_i \cdot \Delta h_i - \sum_i \left(h_{g_i}\frac{\partial}{\partial x}\left(u\cdot\rho_{g_i}\right) + u\cdot\rho_{g_i}\cdot c_{p_{g_i}}\frac{\partial T}{\partial x}\right).
\end{aligned} \tag{4.31}$$

This equation is coupled to the mass conservation equations and the Darcy equation, becoming a stiff system of differential equations (Kansa et al. 1977). A very popular numerical scheme used to solve this system is that developed by Crank and Nicolson (Crank & Nicolson 1947, Tinney 1965, Kung 1972, Tamanini 1976*b*, Atreya 1983, Alves & Figueiredo 1989, Suuberg et al. 1994, Yang et al. 2002), although other methods have been used.

4.2.8 Moving Boundary Solution

The phenomenon of wood pyrolysis can be viewed as the progression of two moving fronts, where the first one corresponds to the evaporation of the moisture content and the second one to the pyrolysis process itself. This simplification is based on experimental observations (see Chapter 3) that show that these physical and chemical changes take place in sections of small

thickness. It thus seems appropriate to apply the approach of moving boundary or Stefan problems to this particular process.

First developed as problems to deal with changes of phase (Carslaw & Jaeger 1959, Crank 1984), they have been employed for the modelling of pyrolysis (and also for the drying of wood) in several occasions, with varying degrees of complexity and assumptions (Luikov 1975, Agarwal, Genetti & Lee 1986, Bilbao et al. 1996, Saastamoinen & Richard 1996, Spearpoint & Quintiere 2000, Atreya & Baum 2002, Staggs 2003, Galgano & Di Blasi 2004, Dietenberger 2006, Kocaefe et al. 2006, Kuo & Hsi 2005). In general, they are simpler than the models that treat volumetric decomposition, and analytical solutions have been found by several authors (Carslaw & Jaeger 1959, Crank 1984, Atreya & Baum 2002), but these are restricted to one-dimensional cases with infinite or semi-infinite regions (Crank 1984).

One of the main suppositions in these types of problems has been to assume a particular form for the variation of temperature with the space variable, the so called integral methods (Agarwal et al. 1986, Atreya & Wichman 1989, Spearpoint & Quintiere 2000, Atreya & Baum 2002). But because of this assumption and the fact that the goal of this investigation is to predict temperature profiles, it was decided not to work with them.

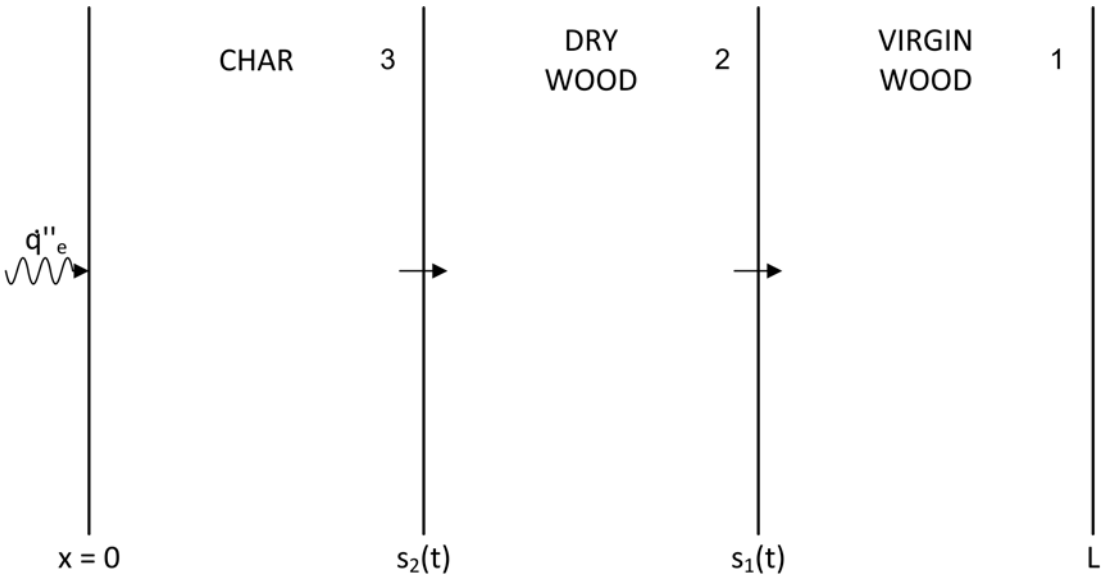

Figure 4.1: Schematic representation of the moving boundary domain. Moisture evaporation occurs in the first boundary (s_1), while the pyrolysis reactions take place in the second boundary (s_2).

The energy equation is treated as it was described in the previous sections, except that there is one equation for each of the phases, namely the virgin wood, the dry wood, and the char.

The boundary condition between each of the phases will incorporate the source terms for the moisture evaporation and the pyrolysis reactions, which, in this case, are infinitely fast one-step reactions and are assumed to take place only in the moving front (Di Blasi 2007) (see Figure 4.1). Convective heat transfer, pressure driven flow and various kinetic schemes have been modelled (Saastamoinen & Richard 1996, Staggs 2003, Galgano & Di Blasi 2004, Kuo 2005, Di Blasi 2007). Following similar assumptions as in the previous section, the energy balance equations are expressed in the following general form:

$$s_1(t) < x < L:$$

$$(\rho\, c_p)_1 \frac{\partial T}{\partial t} = \frac{\partial}{\partial x}\left(k_1 \frac{\partial T}{\partial x}\right); \tag{4.32}$$

$$s_2(t) < x < s_1(t):$$

$$(\rho\, c_p)_2 \frac{\partial T}{\partial t} = \frac{\partial}{\partial x}\left(k_2 \frac{\partial T}{\partial x}\right) + \frac{\partial}{\partial x}\left(\sum_i \dot{m}''_{g_i}\, h_{g_i}\right); \tag{4.33}$$

$$0 < x < s_2(t):$$

$$(\rho\, c_p)_2 \frac{\partial T}{\partial t} = \frac{\partial}{\partial x}\left(k_2 \frac{\partial T}{\partial x}\right) + \frac{\partial}{\partial x}\left(\sum_i \dot{m}''_{g_i}\, h_{g_i}\right). \tag{4.34}$$

Note that for region 1 there is no convective term because it corresponds to virgin wood, where no gases are assumed to be present. The following boundary conditions are set between the phases:

$$-k_2\frac{\partial T}{\partial x} = -k_1\frac{\partial T}{\partial x} + \Delta h_{fg}\,\rho_1\frac{ds_1(t)}{dt}, \tag{4.35}$$

$$T|_{x=s_1^+} = T|_{x=s_1^-} = T_{evap}\,;$$

$$-k_3\frac{\partial T}{\partial x} = -k_2\frac{\partial T}{\partial x} + \Delta h_{pyr}\,\rho_2\frac{ds_2(t)}{dt}, \tag{4.36}$$

$$T|_{x=s_2^+} = T|_{x=s_2^-} = T_{pyr}\,.$$

4.3 Implementation of the Model

With the information from the previous sections, a model describing the pyrolysis process was developed, incorporating most of the terms discussed. The idea is to identify the terms with the greatest relevance on the results, particularly the in-depth temperature profiles, in order to produce a simplified model that accurately predicts these temperature histories. As a way of testing the relevance of each of the terms, five models were developed, each incorporating different degrees of simplification and modelling approaches. Four treated pyrolysis as a volumetric decomposition process, while the last one was a moving boundary type solution. The relative magnitude of each of the terms included in the energy equation was obtained, thus allowing to identify the importance of each of the terms in the final temperature results. Also, the results yielded by each of the models were compared with each other, in order to assess their performance. Even though it was decided to make a "complete" model that accounted for all the processes that take place during the devolatilization process, some simplifications were indeed made.

4.3.1 Summary of Simplifications

As was previously discussed when developing the energy conservation equation, several assumptions were done about the wood element and the heating process itself. A one dimensional heating situation was assumed, which greatly simplifies the equations. This assumption is not far from reality, at least where the thermocouples were placed in the temperature profiles

experiments, as was shown in Chapter 3.

Main assumptions regarding the pyrolysis gases are that the work done by the gases is not considered. This term comes from the differentiation of the pressure term contained in the definition of the enthalpy of the control volume, and has been incorporated by Kansa et al. (Kansa et al. 1977). The presence of air in the wood voids was discarded, although it has been considered by some researchers (Yuen et al. 2007). Finally, the kinetic energy of the gases was not considered. Following with the transfer of mass, the movement of liquid water has been neglected, as well as the diffusive mass transfer. These effects are however deemed to be of little importance to the results (Atreya 1983, Di Blasi 1993*a*).

More important could be the structural changes that occur during the pyrolysis process and which were completely neglected. Apart from the shrinking of wood, which could be a direct cause of the cracking, surface ablation was not modelled. All these phenomena have an influence in the heat transfer from the surroundings to the interior of the wood matrix and in the way the gases leave the charred solid. They have been studied elsewhere (Parker 1985, Di Blasi 2007).

Also affecting the heat transferred into the wood are the temperature variations of the thermophysical properties. Even though the overall thermal conductivity and density do vary with time, the intrinsic wood, char, gases, and moisture properties are taken as constant values. Finally, combustion processes were not studied, specifically char oxidation and flaming, because it was felt that the problem needed to be simplified as much as possible, but nevertheless these phenomena will be present in many cases and as will be seen in the next chapter, are important.

4.3.2 Complete Model

The complete model (Model 1) considers volumetric reactions, and incorporates the following phenomena in the energy conservation equation: solid and gaseous phase rise of enthalpy; heat transfer by conduction and energy generated by the pyrolysis reactions and moisture evaporation; and finally energy convected by the gases.

The model is essentially that formulated by Di Blasi (Di Blasi 1993*a*), but with the incorporation of the moisture evaporation terms. The energy equation becomes (see Equation 4.31 for an expanded version of this equation):

$$\frac{\partial}{\partial t}\left[\rho_w\, h_w + \rho_c\, h_c + \rho_{wat}\, h_{wat} + \varphi_{gas}\left(\rho_{vap}\, h_{vap} + \sum_i \rho_{g_i}\, h_{g_i}\right)\right] = \tag{4.37}$$

$$\frac{\partial}{\partial x}\left(k_{net}\frac{\partial T}{\partial x}\right) + \dot{\omega}_{wat}\cdot\Delta h_{fg} + \sum_{i=1}^{5}\dot{\omega}_i\cdot\Delta h_i - \frac{\partial}{\partial x}\left(\sum_i \dot{m}''_{g_i}\cdot h_{g_i}\right).$$

Six species were considered: virgin wood, char, pyrolysis gas, tar, liquid water and water vapour. Five competing first order reactions describe the pyrolysis process, with three primary, endothermic reactions and two weakly exothermic secondary reactions accounting for tar decomposition (Di Blasi 1993*a*). Water evaporation is described by another first order Arrhenius expression (Figure 4.2).

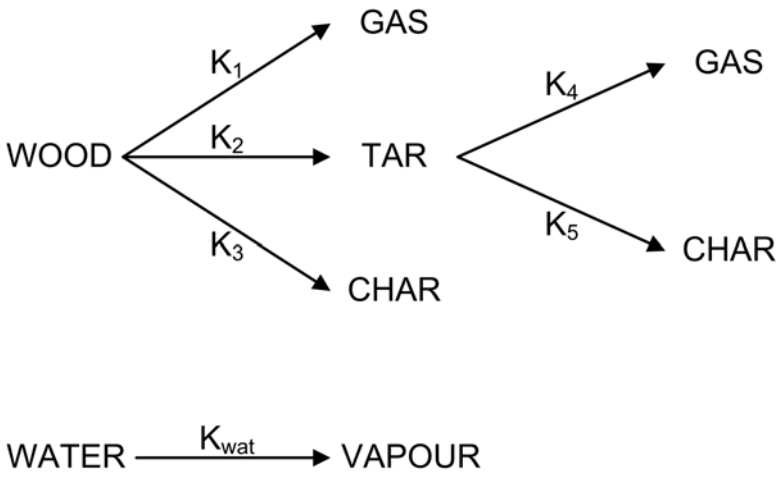

Figure 4.2: Kinetic scheme used in Model 1. The other models use simplified versions of this scheme.

Mass conservation equations are formulated for each of the species as per Equation 4.38:

$$
\begin{aligned}
\frac{\partial \rho_w}{\partial t} &= -\left(K_1 + K_2 + K_3\right)\, \rho_w, \\
\frac{\partial \rho_c}{\partial t} &= K_3\, \rho_w + \varphi_{gas}\, K_5\, \rho_t, \\
\frac{\partial \rho_{wat}}{\partial t} &= -K_{wat}\, \rho_w, \\
\frac{\partial}{\partial t}\left(\varphi_{gas} \cdot \rho_t\right) + \frac{\partial}{\partial x}\left(u \cdot \rho_t\right) &= K_2\, \rho_w - \varphi_{gas}\, \left(K_4 + K_5\right)\, \rho_t, \\
\frac{\partial}{\partial t}\left(\varphi_{gas} \cdot \rho_g\right) + \frac{\partial}{\partial x}\left(u \cdot \rho_g\right) &= K_1\, \rho_w + \varphi_{gas}\, K_4\, \rho_t, \\
\frac{\partial}{\partial t}\left(\varphi_{gas} \cdot \rho_{vap}\right) + \frac{\partial}{\partial x}\left(u \cdot \rho_{vap}\right) &= K_{wat}\, \rho_{wat}.
\end{aligned}
\tag{4.38}
$$

Pressure is calculated by doing a mass conservation equation for all the gaseous species and, by assuming ideal gas behaviour, getting an expression for the pressure in terms of the total gas mass concentration. The following simplified equation was used, instead of that used by Di Blasi (Di Blasi 1993*a*). In this case, as opposed to the work by Di Blasi, the velocity was not expressed in terms of the pressure gradient, but both expressions are equivalent.

$$
\begin{aligned}
\frac{\partial}{\partial t}\left(\frac{\varphi_{gas} \cdot p}{T}\right) + \frac{\partial}{\partial x}\left(u \cdot \frac{p}{T}\right) = \frac{R}{M_g}\Big[&\left(K_1 + K_2\right) \rho_w \\
&+ K_{wat}\, \rho_{wat} - \varphi_{gas}\, K_5\, \rho_t \Big]
\end{aligned}
\tag{4.39}
$$

A simplification was done in Equation 4.39: the total molecular mass of the gas phase was simply taken as the sum of the molecular masses of the different gases, instead of weighing them by their particular mass concentrations.

The initial and boundary conditions are the same as those used by Di Blasi:

$$t = 0: \quad T = T_\infty; \quad p = 0; \quad u = 0; \quad \rho_w = \rho_{w_0}. \tag{4.40}$$

$$\begin{aligned} x = 0: \; -k_{net}\frac{\partial T}{\partial x} &= \alpha\, \dot{q}_e'' - h_c\,(T - T_\infty) - \varepsilon\,\sigma\left(T^4 - T_\infty^4\right);\; p = p_\infty. \\ x = L: \; -k_{net}\frac{\partial T}{\partial x} &= h_c\,(T - T_\infty) + \varepsilon\,\sigma\left(T^4 - T_\infty^4\right); \quad \frac{\partial p}{\partial x} = 0. \end{aligned} \tag{4.41}$$

The model was solved using the method developed by Crank, Nicolson, Bamford and Malan (Crank & Nicolson 1947, Bamford et al. 1946), as formulated by Kung (Kung 1972). The temperature for the next time step is assumed to be equal to the temperature at the present time, and with that, new values for densities, solid and gas phase volumes, porosities, permeability, pressure, velocity, effective thermal conductivity, mass fluxes, enthalpies and boundary conditions are calculated. The energy equation is then solved using the updated parameters. With the new temperatures, the previous parameters are calculated again, and after that the energy equation is solved. This loop is repeated until the temperatures converge to a given tolerance value.

This is a model considered to be of a high level of detail, incorporating all of the phenomena discussed in the previous section. If simplifications to this model are to be made, the actual algorithm has to be modified, in order to account for some critical changes that will affect the solving process. Three simplified models of the same type were done apart from the original, complex one.

4.3.3 Simplified Models

The modelling of a given phenomenon should faithfully represent the reality, ideally including every aspect of it. It results difficult and not practical, however, to solve a comprehensive model, due to ignorance of some of the phenomena involved and also due to limitations in computing power and mathematical tools. Satisfactory solutions can be obtained by simplifying the problem, but only if the simplification process has eliminated the neglected terms (Kanury 1987). In this study, three models have been developed starting from the complete model just described. Two main features have been simplified from the models, the pressure build up,

which drives the gases flowing out of the porous matrix has been completely neglected, and the kinetic model which, instead of having multiple and competing reactions accounting for the devolatilization of wood, just counts with one global reaction with a specified final char density. The last model incorporates these two approximations.

The first of these simplified models (Model 2) is fundamentally the same as the detailed model, except that it does not take pressure into account. Not accounting for the pressure build up means that there will be no mass accumulation in the control volume, and also means that the gas velocities can no longer be calculated using the Darcy equation. Therefore Equation 4.29 is used for the gas phases (repeated here for convenience).

$$\frac{\partial \dot{m}''_{g_i}}{\partial x} = \sum \dot{\omega}_{g_i}.$$

When using this equation, the gas phase mass concentrations are not calculated (Bamford et al. 1946, Weatherford & Sheppard 1965, Benkoussas et al. 2007, Panton & Rittmann 1971, Simms 1962). Others, however, do include the full mass conservation equation for the gases but still calculate the mass fluxes as per Equation 4.29 (Di Blasi 1996). In this case, no gas densities were calculated. The gas sensible heat is also discarded in this model, as well as all the secondary reactions (because the gas mass concentrations are not calculated). So, in terms of the kinetic modelling, 3 primary pyrolysis reactions are considered (the same as for Model 1) plus the moisture evaporation term, which means that the same 6 species are considered, but only the solid phase species are calculated using the mass conservation equations.

The second simplified model (Model 3) considers only one global pyrolysis reaction and defines a final density for the charred material, as stated in Equation 4.16. Rather than presenting differences in the physical aspect of the model, the differences in this case are in the chemical modelling of the problem. In this case the chemistry is simplified, not accounting for the competing and secondary reactions. However, the kinetic parameters used for this reaction were obtained considering a single reaction, so all the effects of the reactions that were not taken into account are lumped into one (see the following section for a further discussion on this). This model accounts for only four species (reacting solid, liquid water, pyrolysis gas and water vapour), with no secondary reactions. Pressures are obtained in the same way as in the original model, but this time only two gas phase species are considered.

The final simplified model (Model 4) uses the same one-step global scheme as described above,

but without the pressure calculations, being a combination of Models 2 and 3. Mass concentrations for only two species are calculated, the reacting solid and liquid water. Mass fluxes for the pyrolysis gas and water vapour are calculated with Eq. 4.29.

4.3.4 Moving Boundary Model

Moving boundary problems pose a problem when applying numerical methods to solve them. Since the boundary condition must be satisfied at all times and there will be two or more domains with different differential equations (see Equations 4.32 to 4.36), the position of the moving boundary must be known at all times. This raises the need of numerical techniques to modify the grid according to the movement of the boundary. A simple method overcomes these difficulties and by reformulating the problem, only one equation applies to the whole of the domain. The enthalpy method (Crank 1984) modifies the formulation of the problem by introducing a total enthalpy function which includes the sensible heat of the species included and the latent heat for the phase change.

The method was modified by treating the pyrolysis reaction as a phase change phenomenon and therefore including an extra phase (i.e. virgin, moist wood, dry wood and char; see again Equations 4.32 to 4.36). So, if the function $H(T)$ is defined as the enthalpy of the solid,

$T < T_{evap}$:

$$H(T) = \rho_w \, c_{p_w} \, T \, ; \quad (4.42)$$

$T = T_{evap}$:

$$\rho_w \, c_{p_w} \, T_{evap} \leq H(T) \leq \rho_{dry} \, c_{p_{dry}} \, T_{evap} + \rho_{wat} \, \Delta h_{fg} \, ; \quad (4.43)$$

$T_{evap} < T < T_{pyr}$:

$$H(T) = \rho_{dry}\, c_{p_{dry}}\, T + \rho_{wat}\, \Delta h_{fg}\,; \quad (4.44)$$

$T = T_{pyr}$:

$$\rho_{dry}\, c_{p_{dry}}\, T_{pyr} + \rho_{wat}\, \Delta h_{fg} \leq H(T) \leq \rho_c\, c_{p_c}\, T_{pyr} + \rho_{dry}\, \Delta h_{pyr} + \rho_{wat}\, \Delta h_{fg}\,; \quad (4.45)$$

$T_{pyr} < T$:

$$H(T) = \rho_c\, c_{p_c}\, T + \rho_{dry}\, \Delta h_{pyr} + \rho_{wat}\, \Delta h_{fg}\,. \quad (4.46)$$

The problem presented in Equations 4.32 to 4.34 can be reformulated as (without considering the convective term in Equations 4.33 and 4.34):

$$\frac{\partial H(T)}{\partial t} = \frac{\partial}{\partial x}\left(k \frac{\partial T}{\partial x}\right). \quad (4.47)$$

This equation is valid for the whole domain. Then, by expressing T in terms of the enthalpy H, the problem can be solved using standard finite differences. This model is labelled as Model 5.

4.3.5 Model Parameters

Most of the parameters used in Model 1 are those employed by Di Blasi (Di Blasi 1993*a*). The same values were used in the rest of the models when applicable. Kinetic parameters are those obtained by Thurner and Mann (Thurner & Mann 1981) for wood primary devolatilization, by Liden et al (Liden, Berruti & Scott 1988) for the tar degradation into gas and an estimated value by Di Blasi for tar converting into char. Values by Chan et al (Chan et al. 1985) were used for moisture evaporation (note that Di Blasi did not model moisture evaporation in that particular

publication).

Thurner and Mann (Thurner & Mann 1981) not only present values of kinetic parameters for the primary reactions in the kinetic scheme used in the complex model, but they also present the parameters for a global reaction and for a lumped gasification reaction (both without considering secondary reactions). As the purpose of this exercise is to evaluate the importance of each of the terms included in the pyrolysis models, it was opted to use these parameters in the different models, even though they were obtained for oak sawdust and the experimental study of this project was carried out using thick samples of redwood pine. The following tables present the principal parameters used in each of the models.

The wood density that was used was the measured one, which included the moisture, and from that a dry wood density was calculated. The wood thermal conductivity and specific heat were obtained by fitting the inert heating solution to the non dimensional results, as shown in Chapter 3. The thermal conductivity obtained in Chapter 2 corresponds to the total conductivity of the sample, including the effects of the moisture content and the porosity, and from that value, the wood thermal conductivity was obtained. Table 4.1 presents these and other parameters common to the models used in this study. Table 4.2 presents the kinetic parameters used in the different models.

	Value
L	0.040 m
A	9.8741×10^{-3} m^2
h_c	12 W $\cdot$ m $^{-2}\cdot$ K^{-1}
$\dot{q}''_e$	25×10^3 W $\cdot$ m^{-2}
MC	0.101 kg$_{water}$ $\cdot$ kg$^{-1}_{wood}$
T_∞	295 K
ρ^0_w	482.14 kg$\cdot$m^{-3}
c_{p_w}	2600 J$\cdot$kg^{-1}K^{-1}
k_w	0.15 W $\cdot$ m $^{-1}\cdot$ K^{-1}
φ^0_{gas}	0.58
$\alpha = \varepsilon$	1

Table 4.1: Parameters common to all models.

4.3.6 Model Validation

Since the solution to the models was obtained using a bespoke computer program, it was decided to test the validity of the results before comparing them with each other. For this, the models were benchmarked against the work of several researchers, namely those that had used similar models in their work. This posed some difficulties, because the only data available was

Reaction	Parameter	Complete Model (Model 1)	No Pressure (Model 2)	Final Density (Model 3)	Final Density No Pressure (Model 4)	Heat of Reaction $kJ \cdot kg^{-1}$
$Wood \rightarrow Gas$	A_1 (s^{-1})	1.4345×10^4	1.4345×10^4	–	–	-418
	E_1 ($J \cdot mol^{-1}$)	8.86×10^4	8.86×10^4	–	–	
$Wood \rightarrow Tar$	A_2 (s^{-1})	4.125×10^6	4.125×10^6	–	–	-418
	E_2 ($J \cdot mol^{-1}$)	1.127×10^5	1.127×10^5	–	–	
$Wood \rightarrow Char$	A_3 (s^{-1})	7.3767×10^5	7.3767×10^5	–	–	-418
	E_3 ($J \cdot mol^{-1}$)	1.065×10^5	1.065×10^5	–	–	
$Tar \rightarrow Gas$	A_4 (s^{-1})	4.28×10^6	–	–	–	42
	E_4 ($J \cdot mol^{-1}$)	1.08×10^5	–	–	–	
$Tar \rightarrow Char$	A_5 (s^{-1})	1.0×10^6	–	–	–	42
	E_5 ($J \cdot mol^{-1}$)	1.08×10^5	–	–	–	
$Wood \rightarrow Gas + Char$	A_{global} (s^{-1})	–	–	2.4683×10^6	2.4683×10^6	-418
	E_{global} ($J \cdot mol^{-1}$)	–	–	1.065×10^5	1.065×10^5	
$Moisture \rightarrow Vapor$	A_{wat} (s^{-1})	5.13×10^6	5.13×10^6	5.13×10^6	5.13×10^6	-2257
	E_{wat} ($J \cdot mol^{-1}$)	7.0×10^4	7.0×10^4	7.0×10^4	7.0×10^4	

Table 4.2: Kinetic Parameters.

that which was published, and it never proved to be fully complete in terms of all the parameters used in the simulations or in the results presented. Prior to that, the models were tested for grid independency.

Model 1 was compared with the results presented by Di Blasi (Di Blasi 1993*a*). Good agreement was obtained with the temperature profiles, with the greatest error being of 18.5 % at 750 s, although at shorter times the error is less than 6.5 % (Figure 4.3). Good agreement was also obtained in the wood densities, although at longer times (750 s) the pyrolysis front in the present results is delayed by about 5 mm (Figure 4.4). This also explains the greater divergences in the temperatures, as they are located at the same place where the devolatilization reaction is taking place. Less agreement was obtained in the other species mass concentrations, although this does not seem to be very significant in terms of the temperature results. The worst results were the values for the gas pressure, where there was a discrepancy of 3 orders of magnitude, but the overall behaviour was qualitatively similar. However, it must be said that the values obtained in this work agree in a better manner with measured and calculated values reported in the literature (Tinney 1965, Lee et al. 1976, Fredlund 1988, Yuen et al. 2007).

The model presented by Bamford, Crank & Malan (Bamford et al. 1946) was also tested (Figures 4.5 and 4.6). The model takes into account the mass concentration of the volatile part of wood, but the model used in the trial was not a final-density type, but the complete model without pressure. Good agreement was obtained in the temperature profiles (error less than 5 %) and in the mass concentrations (error less than 14 % for times shorter than 540 s, and greater at longer times).

The model was also validated with that developed by Kung (Kung 1972). The temperature profiles did not give good results. A reason for the disagreement is that Kung's model, by working with non-dimensional parameters, gives results that are non-physical (i.e. the surface temperature is up to seven times the ambient temperature, which is equivalent to 2100 K). Better concurrence is obtained with the mass concentrations, but with poorer results at greater times. Other models tested were those by Kansa et al (Kansa et al. 1977), Chan et al (Chan et al. 1985) and Fredlund (Fredlund 1993).

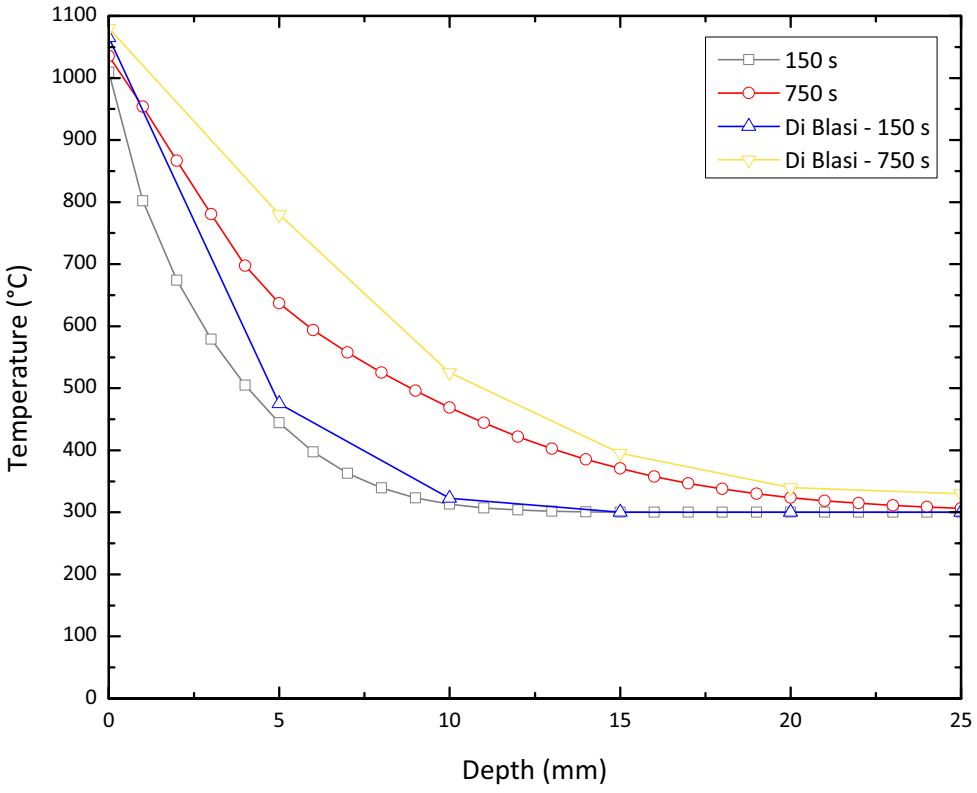

Figure 4.3: Comparison of temperature profiles with results by Di Blasi (Di Blasi 1993*a*). The agreement becomes worse for greater times: 6.5 % at 150 s and 18.5 % at 750 s.

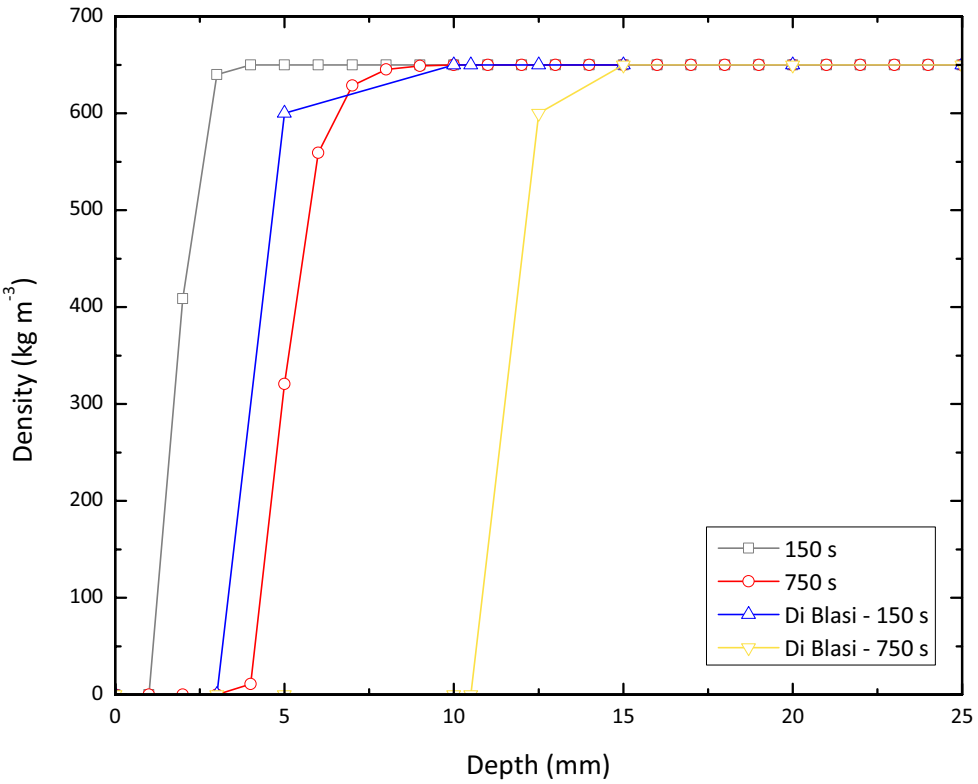

Figure 4.4: Comparison of wood densities with results by Di Blasi (Di Blasi 1993*a*).

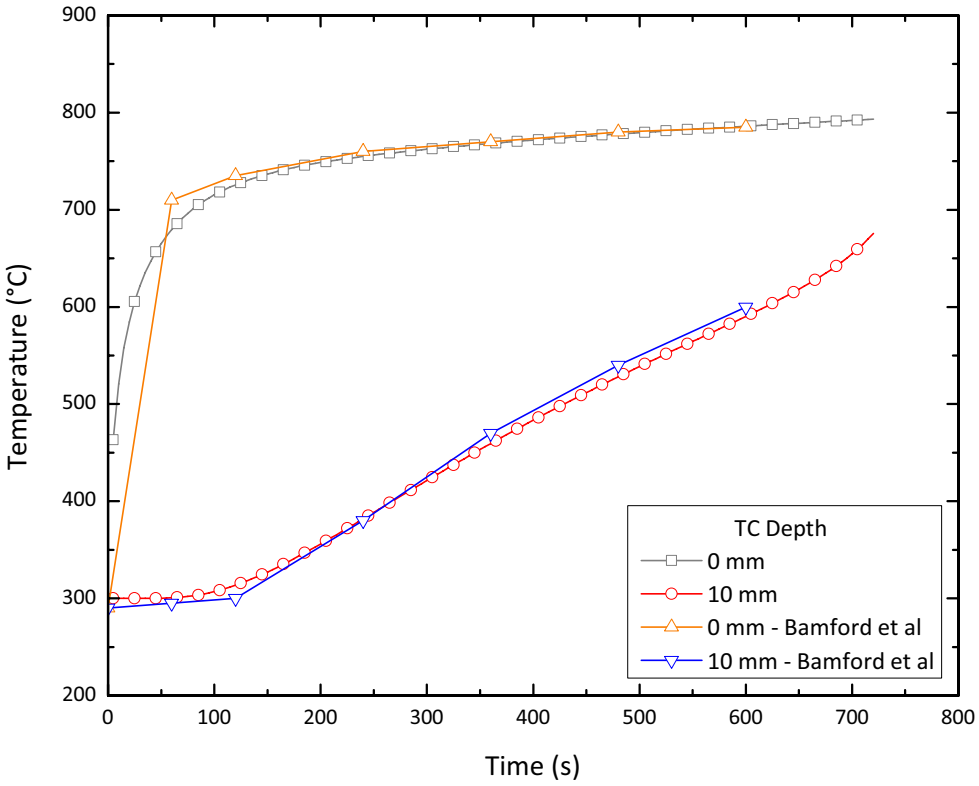

Figure 4.5: Comparison of temperature profiles with results by Bamford et al. (Bamford et al. 1946). The error is less than 5 %.

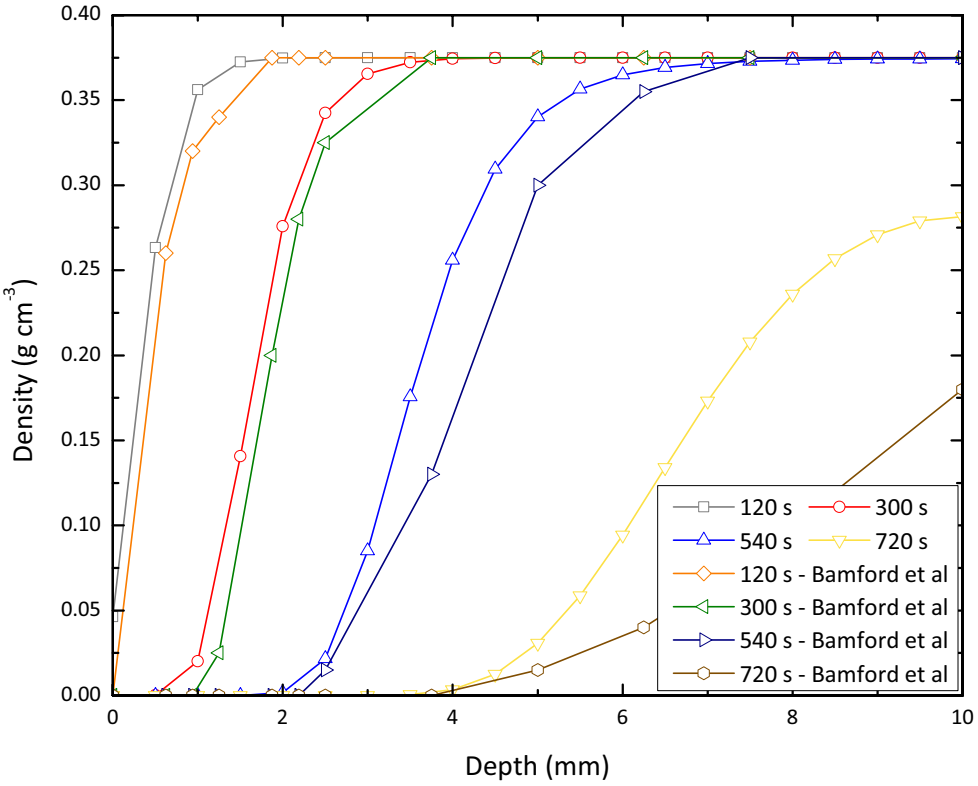

Figure 4.6: Comparison of wood densities with results by Bamford et al. (Bamford et al. 1946). The agreement is good but at longer times divergences occur.

Chapter 5

Numerical Results

This chapter will present the results of the different models described in Chapter 4. First, an analysis of the different terms in the energy conservation equation of each model will be presented. By analyzing the particular contribution of each term to the solution it will be possible to determine which of these terms must be included in a simplified model. A comparison of the results of all the models will then be carried out, which will show the level of accuracy of each model when compared to Model 1, the most detailed model, and thus the choice of the best simplified model to predict temperature profiles will be made. Then, using the simplified model a prediction of the temperature profiles will be shown. A comparison with the experimental measurements and the inert heating solution as presented in Chapter 3 will also be shown and discussed. All the numerical results in this chapter correspond to an imposed heat flux of 25 $kW \cdot m^{-2}$, except when explicitly mentioned.

5.1 Magnitude of Terms in the Energy Conservation Equation

The magnitude of the terms making up the energy equation of Model 1 has been analyzed. The procedure was simple: the contribution of each term into the final solution (i.e. the net heat flow) was calculated for every differential volume, and the energy flow as a function of sample depth was plotted for various times, as can be seen in Figures 5.1, 5.2 and 5.3. Thus, it can be determined how much each term in the right hand side of Equation 4.37 adds to the rise in sensible energy (left hand side in the equation) at each point in the sample. Equation 4.37 is shown again with the different terms labelled for convenience:

$$\frac{\partial}{\partial t}\left[\underbrace{\rho_w\, h_w + \rho_c\, h_c + \rho_{wat}\, h_{wat}}_{1} + \underbrace{\varphi_{gas}\left(\rho_{vap}\, h_{vap} + \sum_i \rho_{g_i}\, h_{g_i}\right)}_{2}\right] =$$

$$\overbrace{\frac{\partial}{\partial x}\left(k_{net}\frac{\partial T}{\partial x}\right)}^{3} + \overbrace{\dot{\omega}_{wat}\cdot\Delta h_{fg}}^{4} + \overbrace{\sum_{i=1}^{5}\dot{\omega}_i\cdot\Delta h_i}^{5} - \overbrace{\frac{\partial}{\partial x}\left(\sum_i \dot{m}''_{g_i}\cdot h_{g_i}\right)}^{6}.$$

Term 1 corresponds to the rise in sensible energy for the solid (non-gaseous material), and term 2 is the rise in sensible energy in the gases. On the right hand side of the equation, term 3 represents the heat transferred by conduction, term 4 the heat of moisture evaporation, the terms labelled 5 correspond to the heats of the various reactions included, and finally term 6 represents the heat losses by convection of volatile gases. Each of these terms has been plotted independently in Figures 5.1, 5.2 and 5.3, and with some terms missing (depending on the simplifications) in Figures 5.6, 5.7 and 5.8.

As the wood begins to heat up, the controlling phenomenon is heat diffusion into the solid, where the term accounting for conduction is the main contributor to the rise in sensible heat (see Figure 5.1). This continues to be the case until the beginning of moisture evaporation, where the endothermic latent heat of moisture evaporation and the convective losses begin to have an important effect (cf. Figure 5.2). At that point (10 s after the beginning of the exposure), the surface temperature is almost 500 K, and the moisture begins to evaporate in the interior parts of the sample. After 60 s of exposure, the moisture evaporation front is at about 2 mm from the surface, and the surface temperature is above 600 K. Pyrolysis reactions begin to take place in the surface, having the same endothermic effect. Wood conversion is low at this instant, and will be completed at about 400 s of exposure, where the remaining wood density is zero. At this time, the pyrolysis heat of reaction at the surface is zero.

The temperatures at which the maximum moisture evaporation rate and the maximum pyrolysis rate occur descend as the fronts go to the interior of the specimen. This is explained because closer to the surface the effect of heat diffusion is more important, making the rise in sensible energy at the surface about 14 times greater than when the moisture front is at 4 mm from the surface and almost 80 times greater than when it is at 10 mm from the surface (see Figures 5.2 and 5.3). The maximum value for both the evaporation and pyrolysis rates corresponds

to the maximum mass loss rate for moisture and wood, respectively, which is explained because the heats of reaction include the mass loss rate term (i.e. the time derivative of the mass concentration).

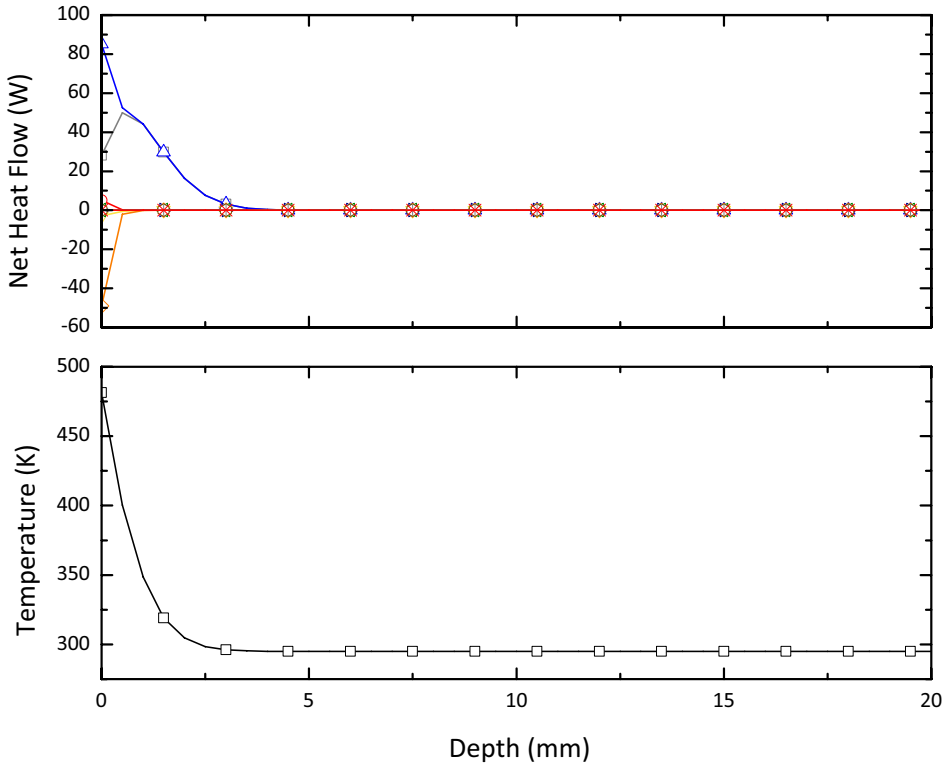

Figure 5.1: Model 1 (competing reactions; pressure). Magnitude of terms of the energy equation at 10 s of exposure. For convenience, only the first 20 mm of the sample are shown. Heat conduction is the main effect, although moisture evaporation begins to have a greater magnitude at the surface of the sample, where the temperature is close to 500 K. There is also a slight increase in the gas sensible heat which will become negligible at later stages. "□": Solid Sensible Heat; "○": Gas Sensible Heat; "△": Conduction; "▽": Convection; "◇": Moisture Latent Heat; "◁": Heat of Reaction #1 (Wood → Gas); "▷": Heat of Reaction #2 (Wood → Tar); "⬡": Heat of Reaction #3 (Wood → Char); "+": Heat of Reaction #4 (Tar → Gas); "×": Heat of Reaction #5 (Tar → Char).

In general, the magnitude of each of the terms in the energy equation decreases with depth. The magnitude of the heat of moisture evaporation and the combined heats of the pyrolysis reactions are similar for all depths. The moisture and the pyrolysis fronts become more separated as they proceed into the sample, confirming the same experimental observation (see Chapter 3). Finally, the convective losses are more important for the pyrolysis reaction than for the moisture evaporation process, because the converted mass is greater in the former case.

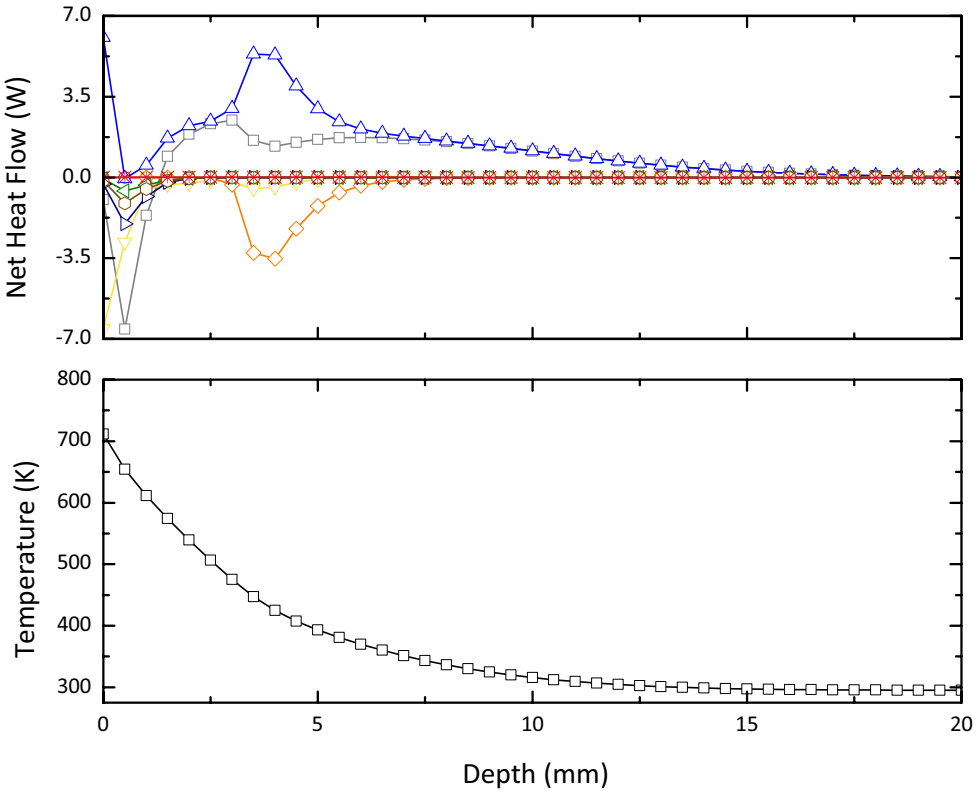

Figure 5.2: Model 1 (competing reactions; pressure). Magnitude of terms of the energy equation at 250 s of exposure. For convenience, only the first 20 mm of the sample are shown. At a surface temperature of 700 K approximately, the pyrolysis front has progressed into the inner parts of the sample. The endothermic effect of the pyrolysis reactions, added to the heat losses by convection, make the solid sensible heat become negative. Secondary Tar reactions are negligible. "□": Solid Sensible Heat; "○": Gas Sensible Heat; "△": Conduction; "▽": Convection; "◇": Moisture Latent Heat; "◁": Heat of Reaction #1 (Wood → Gas); "▷": Heat of Reaction #2 (Wood → Tar); "⬡": Heat of Reaction #3 (Wood → Char); "+": Heat of Reaction #4 (Tar → Gas); "×": Heat of Reaction #5 (Tar → Char).

In terms of the gas pressures, the values are higher than the measured data (Tinney 1965, Lee et al. 1976, Fredlund 1988). Another divergence with the previous experimental work is that no clear difference in the pressure can be observed for the moisture evaporation and the pyrolysis reactions. The maximum pressure is attained ahead of the moisture evaporation front (see Figure 5.4).

The maximum mass loss rate is attained at 120 s, about 500 s earlier than the actual measured value for a heat flux of 25 kW·m^{-2} (see Figure 5.15 in the next section for a comparison of the numerical and experimental results for the mass loss rate, although the model used is a simplified version of Model 4). At this time, the surface is close to attaining total conversion

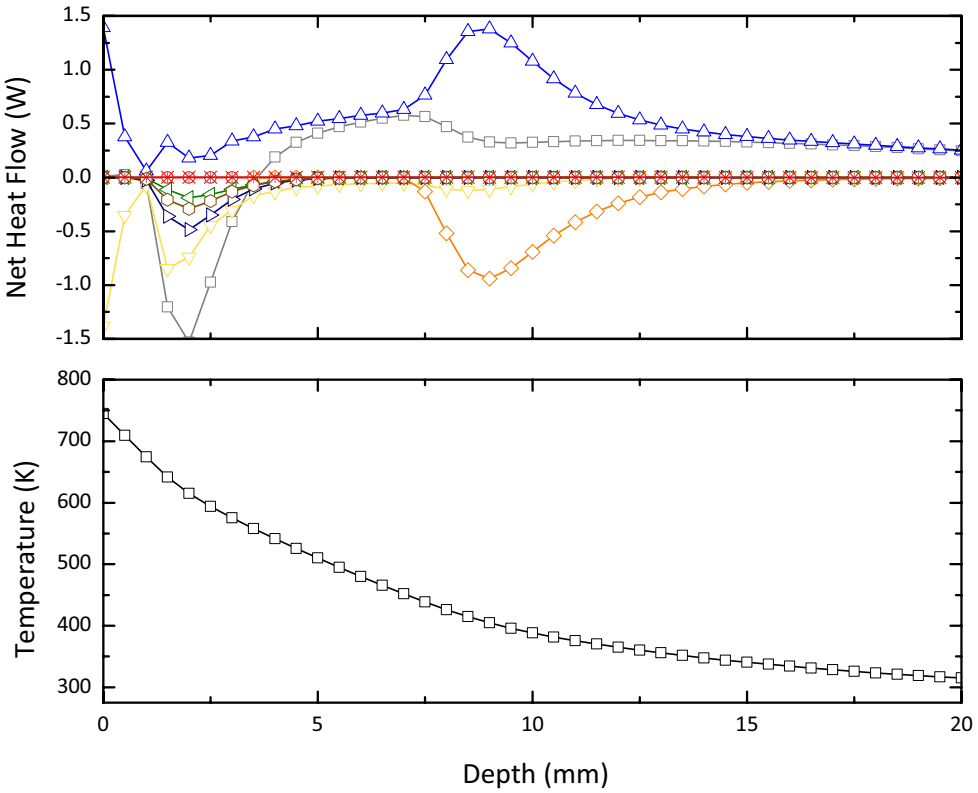

Figure 5.3: Model 1 (competing reactions; pressure). Magnitude of terms of the energy equation at 1000 s of exposure. For convenience, only the first 20 mm of the sample are shown. As the reactions progress to the interior of the wood block, the magnitude of the heating decreases (cf. Figures 5.1 and 5.2). The surface of the sample has reached conditions that can be termed as steady state, as the rise in the solid sensible heat is close to zero. "□": Solid Sensible Heat; "○": Gas Sensible Heat; "△": Conduction; "▽": Convection; "◇": Moisture Latent Heat; "◁": Heat of Reaction #1 (Wood → Gas); "▷": Heat of Reaction #2 (Wood → Tar); "⬡": Heat of Reaction #3 (Wood → Char); "+": Heat of Reaction #4 (Tar → Gas); "×": Heat of Reaction #5 (Tar → Char).

to char (Figure 5.5), which agrees with the statement by Roberts (Roberts 1971), indicating that the maximum mass loss occurs before the char layer at the surface has achieved a finite thickness (i.e. non-zero thickness).

Important conclusions are drawn from observing the graphs in Figures 5.1 to 5.3. It is clear that the gas sensible heat term is insignificant, being several orders of magnitude lower than the solid sensible heat term. This agrees with the conclusions of Kung and Atreya (Kung 1972, Atreya 1983). In terms of the chemical kinetics, the moisture evaporation term and the primary reactions are important, but secondary reactions do not have a significant effect in the final results. This is dependent, however, on the particular parameters used for those

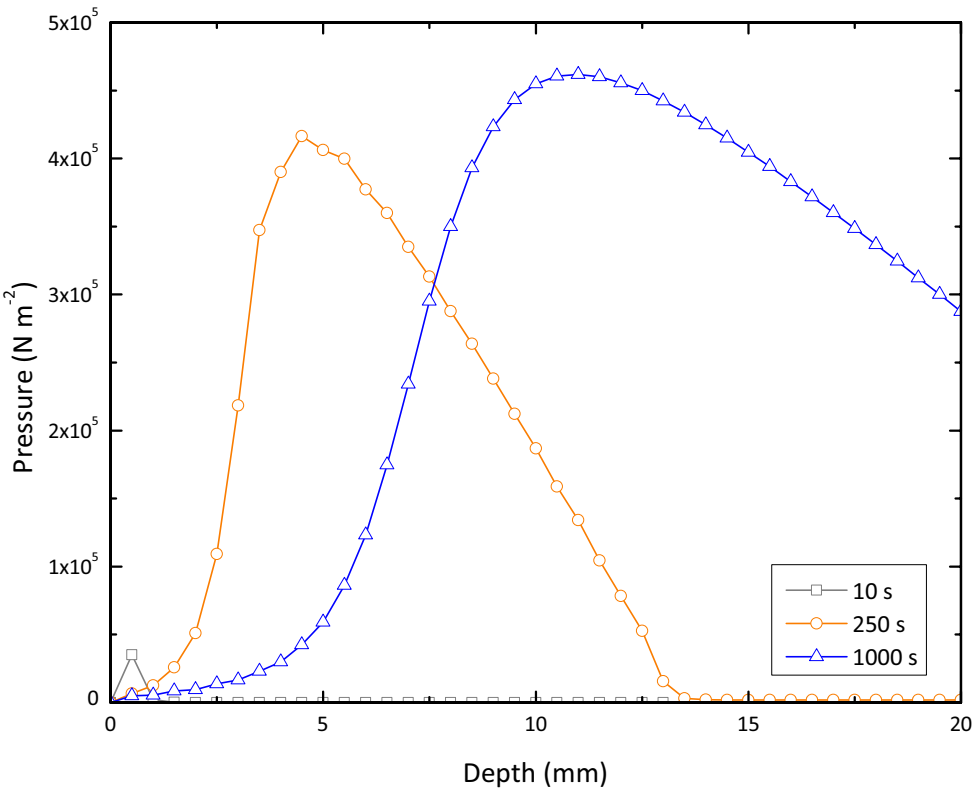

Figure 5.4: Model 1 (competing reactions; pressure). Gas phase pressures for 10, 600 and 1000 seconds of exposure. For convenience, only the first 20 mm of the sample are shown. Although the magnitude of the terms in the energy equation decreases as the exposure progresses, the pressures rise as the fronts move to the interior of the wood specimen, with the peak pressures occurring before the moisture evaporation front.

reactions, so a further analysis is required. In any case, the fact that the pyrolysis reaction has a low endothermic heat of reaction makes the process relatively insensitive to changes in the chemical modelling, unlike the moisture evaporation process, which has a higher latent heat. Convection is of the same order of magnitude as the other relevant terms, so these graphs suggest that it should be included in the final simplified model.

When the magnitude of the terms is plotted for Models 2, 3 and 4, similar conclusions are obtained: the significant terms are the primary reactions (the combined effect of the 3 primary reactions is quite comparable to that of the single reaction, something to be expected since the kinetic parameters utilised were equivalent) and moisture evaporation. For all the models, the fronts are at a similar position, indicating that the kinetic schemes are equivalent (Figures 5.6, 5.7 and 5.8).

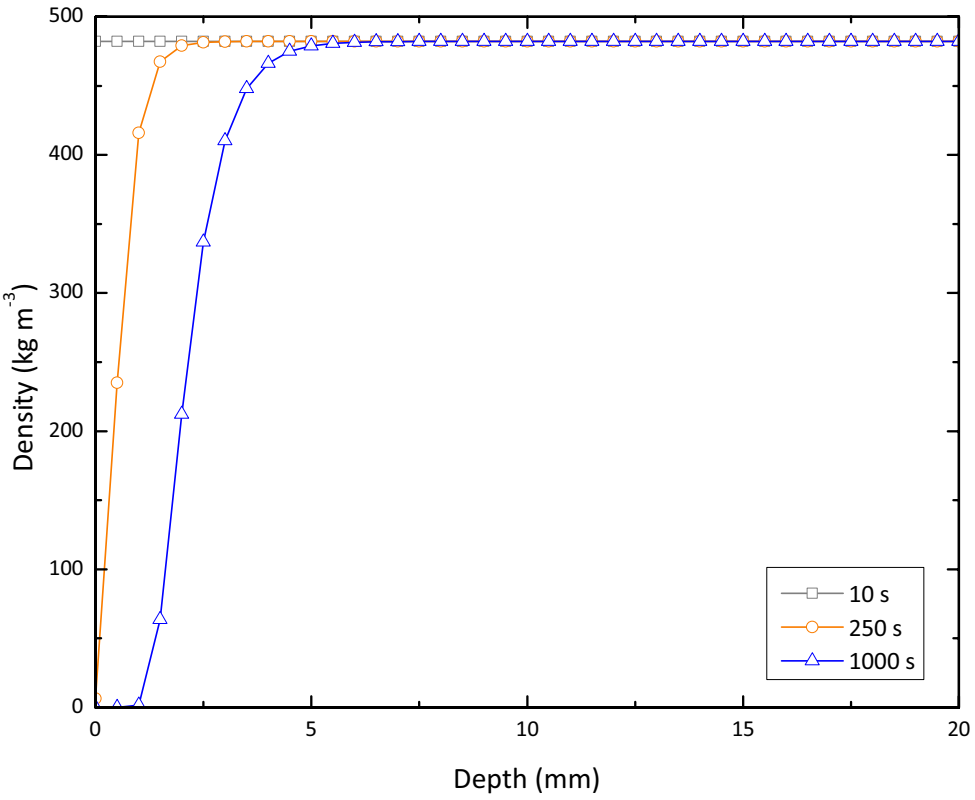

Figure 5.5: Model 1 (competing reactions; pressure). Wood mass concentrations for 10, 600 and 1000 seconds of exposure. For convenience, only the first 20 mm of the sample are shown. The effect of moisture evaporation is not seen here as this graph only presents the mass concentration of dry wood.

There is some divergence on the convective term, however. The models including gas-phase pressure (Models 1 and 3) have higher convective losses close to the surface, which are caused by higher velocities as calculated by the Darcy expression. In the interior of the sample, all models show similar magnitudes for the convective losses. The values for the rest of the terms are in agreement, indicating that the effect of the convective losses is not important. The fact that the solid sensible heat behaves in a similar way for all the models is a further proof that a detailed modelling of the chemistry of the pyrolysis process is not as important in terms of the temperature predictions.

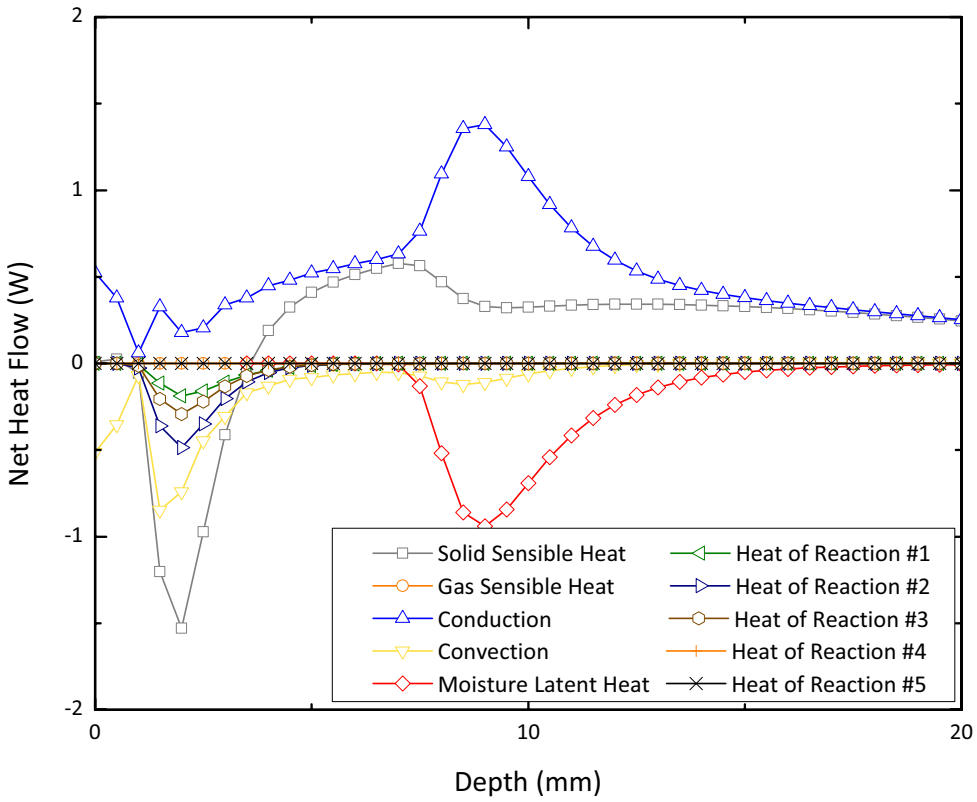

Figure 5.6: Model 2 (competing reactions; no pressure). Magnitude of terms of the energy equation at 1000 s. For convenience, only the first 20 mm of the sample are shown. This model shows similar results to Model 1.

5.2 Model Comparison

When the temperature results of all four models are compared with each other, similar results are obtained (this is to be expected, given the equivalent kinetic parameters). These results confirm the insensitivity of the temperature histories to the kinetic modelling of the devolatilization process.

At deeper sections of the wood specimen, the divergences are not important, but at shallower positions the differences are greater (Figure 5.9). At a depth of 5 mm, the model with no pressure (Model 2) gives slightly higher temperatures, which is explained by the fact that the term of convective losses is lower than that of the complete model. This simplification, however, only presents an error of less than 2 % (15 K) at 1500 s. This observation is in agreement with other publications (Di Blasi 1996), where the temperature profiles predicted by both types of

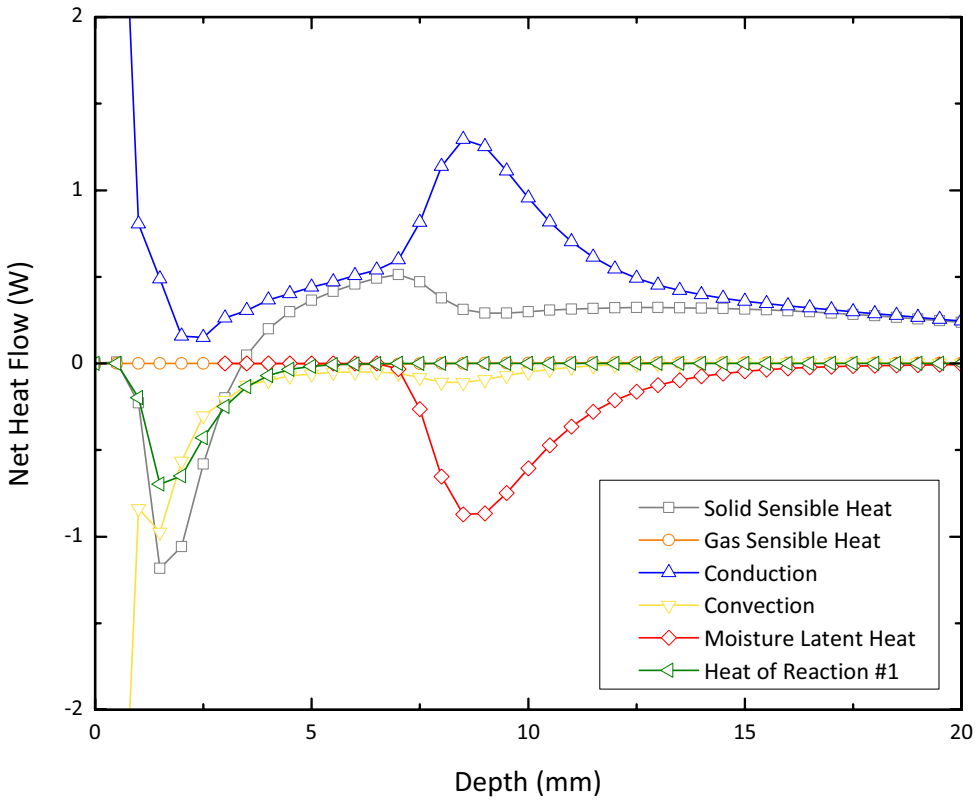

Figure 5.7: Model 3 (final char density; pressure). Magnitude of terms of the energy equation at 1000 s. For convenience, only the first 20 mm of the sample are shown. The convective term is greater than that of Model 1 because this model does not consider any Tar secondary reactions.

models are similar. The final density model (Model 3) yields slightly lower results, but within a 3 % difference at 1500 s. Again this is explained by differences in the convective losses: in this case the term for the final density model is 8.5 times greater than the complete model (at the surface of the specimen and at 1500 s), which happens because this model does not take into account the secondary reactions which in turn make the pressure build-up around 8 % higher than the non-simplified model. The temperature results for the final density model with no pressure (Model 4) lie between those for Model 1 and Model 2.

The results therefore show two things: when carrying out in-depth temperature predictions in pyrolyzing wood, there is no need to use a complex kinetic scheme to describe the pyrolysis reactions or to model the pressure build up within the solid matrix. Thus, a model like Model 4, which only includes the moisture evaporation, a one-step global reaction with a prescribed final char density, and losses by convection, is accurate enough for this purpose.

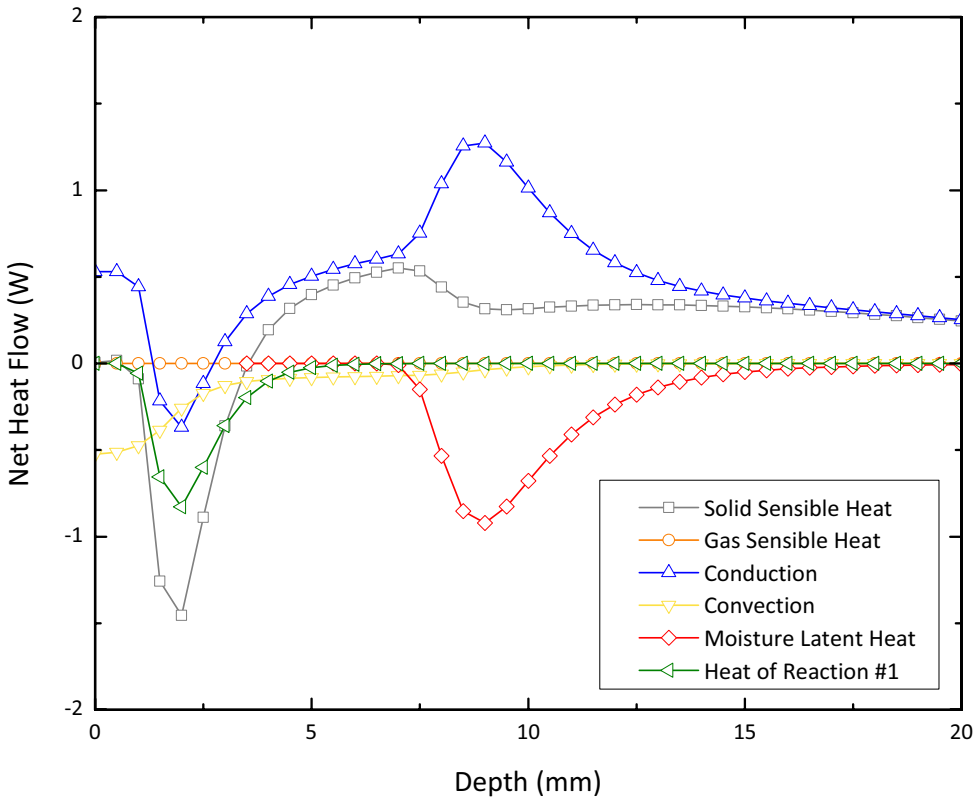

Figure 5.8: Model 4 (final char density; no pressure). Magnitude of terms of the energy equation at 1000 s. For convenience, only the first 20 mm of the sample are shown. The magnitude of the Heat of Reaction #1 is equivalent to the sum of all the magnitudes for reactions #1 to #5 in Model 1.

Returning to the significance of the convective losses term for in-depth temperature predictions, the results for Model 4, with and without the inclusion of the convective term are presented in Figure 5.10. From the figure it can be seen that the convective term has almost no relevance at all in the temperature results.

These results are an indication that the models with greater complexity do not necessarily add more in terms of accuracy for the particular problem which is being dealt with in this investigation. Comparison of models with and without the presence of moisture do show a delay in the heating while the moisture is being evaporated (the model with moisture reaches a temperature of 400 K 80 s later than the one with no moisture, and by the time the moisture model reaches that temperature, the dry model has a temperature of 434 K, at 5 mm depth), with both temperature curves showing closer agreement after the evaporation process, as would be expected. Therefore, not including the presence of moisture could make the temperature predictions in-

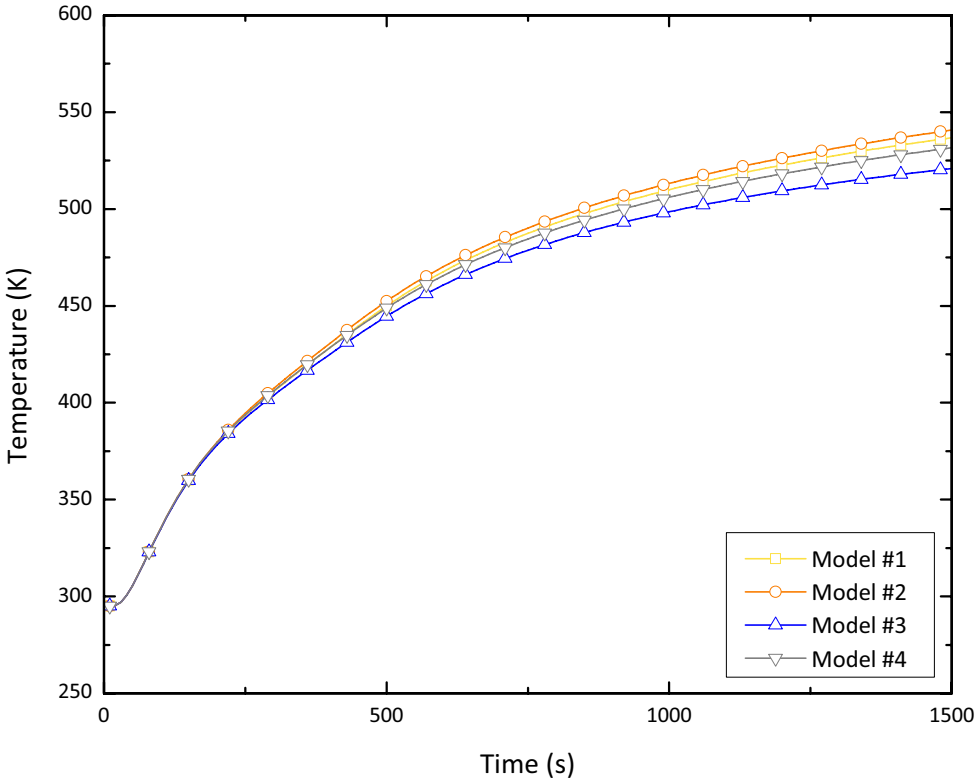

Figure 5.9: Temperature histories as predicted by Models 1 to 4, for a 5 mm deep thermocouple, 25 kW·m^{-2} imposed heat flux. Divergences begin to occur after moisture evaporation, because this process was modelled in the same way in all models, showing that even though the pressure rise is important and the convective losses show differences, these do not affect the temperatures.

accurate, especially considering the glass transition of lignin and the low-temperature failure of metallic connectors (see Chapter 1). Also, the marked change in the heating rate observed in the temperature profile tests cannot be neglected, so it is concluded that this phenomenon must be modelled. As was observed before, the temperature results appear to be insensible to the kinetic schemes employed, because of the low heats of reaction. But a comparison of models including and not including the pyrolysis reactions shows a difference of almost 10% (50 K) at 1500 s and a depth of 5 mm.

In conclusion, the best model that still has a similar accuracy to Model 1 is Model 4, with the extra simplification of not considering the convective losses. Thus, the model includes the heat of moisture evaporation, the heat of pyrolysis and uses a one step, final char density kinetic scheme.

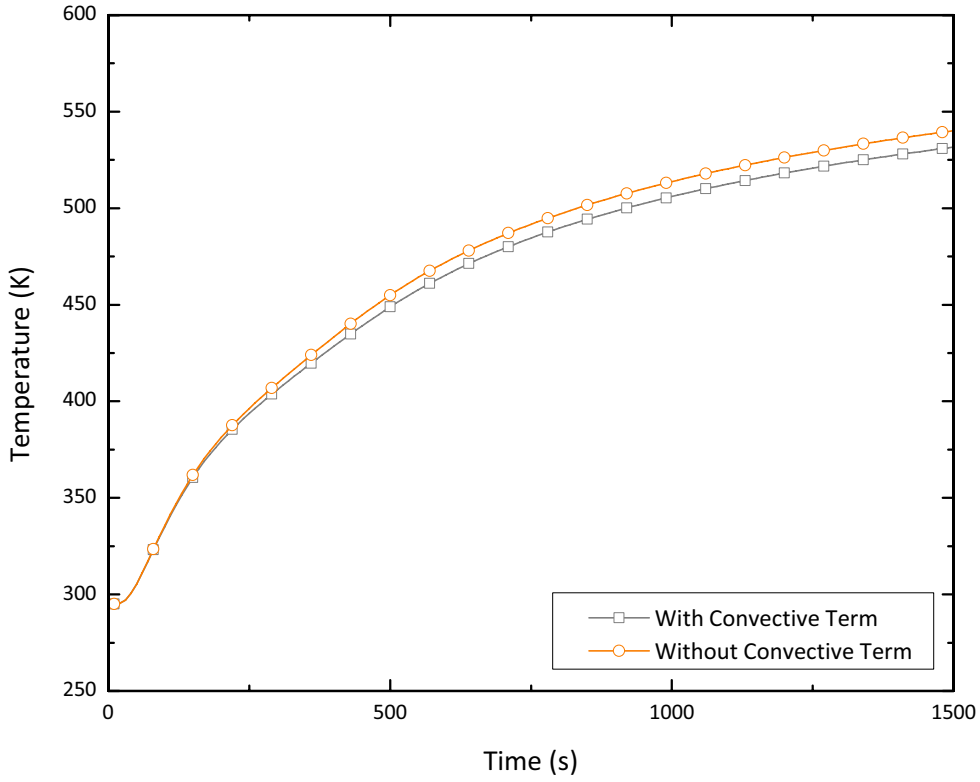

Figure 5.10: Model 4 (final char density; no pressure). Comparison of results with and without the convective term, 5 mm deep thermocouple, 25 kW·m^{-2} imposed heat flux.

5.2.1 Moving Boundary

The results of Model 5 agree well with those produced by the rest of the models which assume volumetric decomposition reactions of wood. This is a further proof that only the moisture evaporation and the devolatilization reaction need to be considered. However, some adjustment of the properties had to be done in order to fit the results to the other models. More specifically, the char conductivity was increased by 20%. Not much effort was dedicated to this model, as it was just intended to prove the quality of the results provided by this type of approach. Even though the problem was solved using simple programming, the results agreed satisfactorily, becoming an interesting alternative to solve the pyrolysis problem.

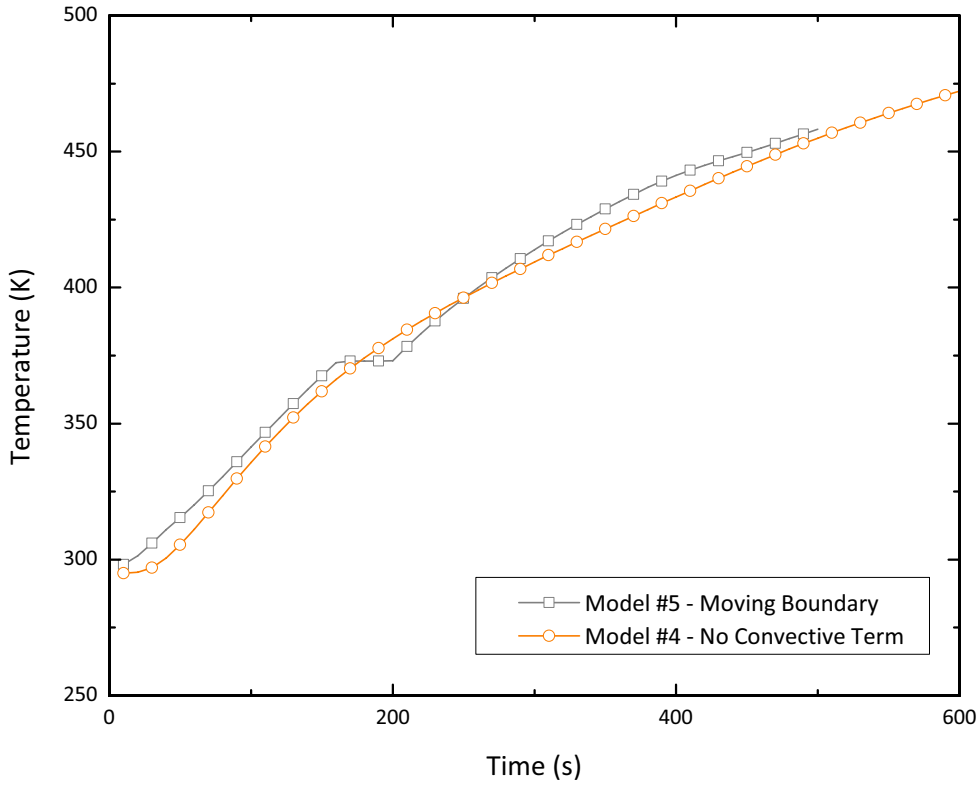

Figure 5.11: Comparison of temperature histories at 5 mm deep thermocouple and 25 kW·m^{-2} imposed heat flux for Model 4 and Model 5 (moving boundary model). The effect of moisture evaporation is clearly observed in the moving boundary model, while the volumetric reaction model does not show a marked change of gradient.

5.3 Prediction of Temperature Profiles

It was decided to carry out the comparison with the experimental measurements once the simplified model was identified, which implies less computational effort. One major difficulty in working with wood, as has been stated previously, is its inhomogeneity. Therefore, when trying to compare predicted results with measured data, it could happen that some model parameters are tailored to fit the data. This could lead to having to adjust the models for every case which is being simulated, which does not lie in the objectives of this study. Because of the variability in the imposed heat fluxes and thermocouple depths, the procedure followed was to compare the results for a given heat flux and depth, in this case 25 kW·m^{-2} and 5 mm, and then observe how well the adjusted model worked for the rest of the cases. The only model utilized was the simplified version of Model 4.

In terms of accuracy, the results are bounded by the experimental measurements on one side and by the results given by the solution to the inert heating problem, constituting the least accurate temperature prediction, which does not account for any physical or chemical changes in the wood matrix. The challenge is, then, to obtain results as close as possible to the most accurate bound, without compromising much on the simplicity of the model.

Preliminarily, the models did not agree with the experimental results. This was done using the calculated parameters for the thermal conductivity, specific heat and density of the samples, while the values for the kinetic parameters were taken from the literature (see Section 4.3, Model Parameters). The initial inert behaviour was closely predicted (because of the calculated parameters), but two main events were not accounted for by the model: the slowing down in the heating rate caused by the moisture evaporation and the increase in the heating rate immediately after the moisture has been evaporated. The temperature results behaved like a diffusion controlled heating process, with no clear effects of the moisture evaporation or the chemical reactions.

Two reasons explain some of these disagreements. The first one is that the value originally used for the activation energy for the moisture evaporation reaction, 87900 J·mol^{-1} (Chan et al. 1985) makes the reaction to set off at temperatures of about 450 K, almost 100 K higher than the observed temperature. The second reason is the lack of an exothermic effect or an increase in the heat flux received by the sample, accounting for the rise in the temperature growth rate. An exothermic reaction could be caused by secondary pyrolysis reactions, but their effect is weakly exothermic (Di Blasi 2007), so another source of heat must be found. This could be oxidation reactions at the char surface or even flaming (although it was not observed at the heat flux level being analyzed). Finally, the heat flowing into the inner portions of the specimen could be increased because of surface recession or cracking, where the incident heat can penetrate into the solid through the cracks (Roberts 1971).

The solution to the first of the problems seemed obvious. The results improved for an activation energy of 70000 J·mol^{-1}. However, a clear "plateau" in the temperature vs. time graphs was not observed in the vicinity of 373 K, even though the value for the latent heat of vaporization used was that for liquid water at 1 atmosphere, and not the one recommended for bound moisture in wood (moisture contents below the fibre saturation point), which depends on the moisture content and is lower than the nominal value (Siau 1984, Alves & Figueiredo 1989, Bilbao et al. 1996).

The aforementioned exothermic effect was not considered in the models, so a different procedure was employed in order to give a quantitative estimation of this effect. The incident heat flux was increased during the simulations in order to match the temperature histories of the 5 mm depth thermocouple. A similar approach was conducted by Atreya (Atreya 1983). So if this increased net heat flux (incident heat flux minus the surface losses by radiation and convection) is compared against the original net heat flux in time, an estimation of the heating effect can be obtained.

The incident heat flux was increased by a quadratic function of time, growing from 150 s until 600 s, where the value was left constant again (the experimental observations show that the exothermic effect is weakened somewhere around 600 s of exposure). Considering this, the extra net heating effect at the surface of the sample has been estimated to be of about 1.3 $kW \cdot m^{-2}$ (see Figure 5.12). An estimation of the extra imposed heat flux using the thermocouple values is presented in Appendix E, and the results agree with the value presented above.

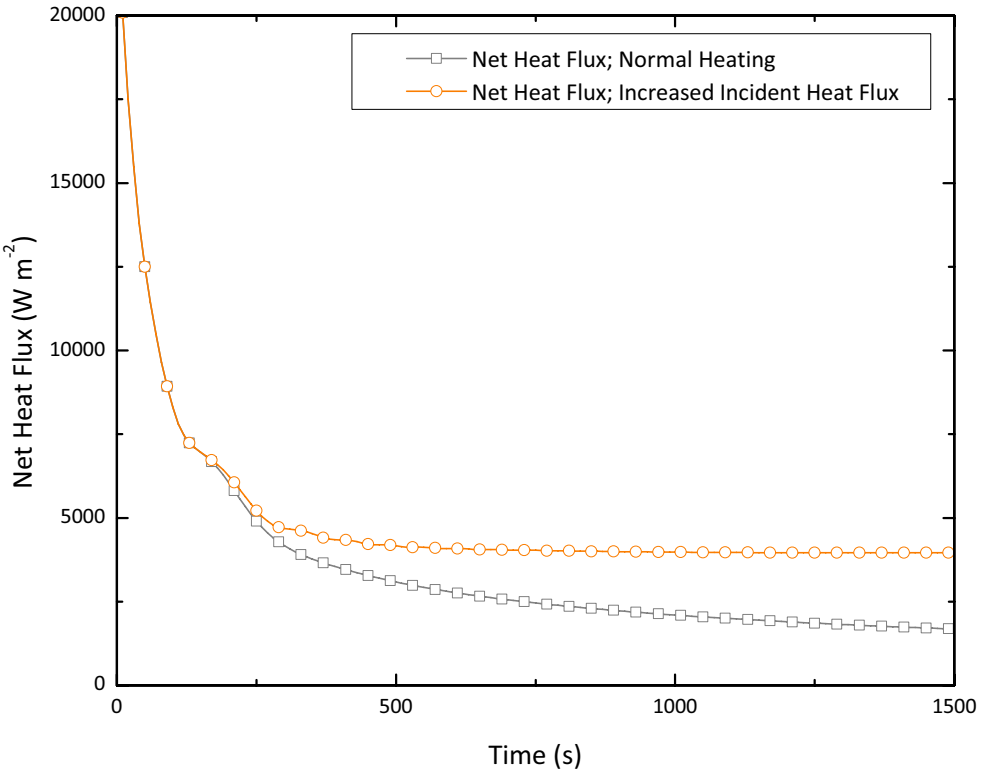

Figure 5.12: Simplified version of Model 4 (no convection). Difference in the net heat flux at the sample surface between the normal, fixed imposed heat flux and the increased imposed heat flux. The extra heating effect was taken as the average of the differences between both net heat fluxes.

The temperatures predicted by the model are presented in Figure 5.13. Also shown in the figure are the results of the inert heating solution. As has been shown in Chapter 3, the initial heating of wood is inert. The model departs from the inert heating solution at the same instant than the experimental data, indicating that the moisture evaporation phenomenon is correctly modelled. However, the figure shows that the incident heat flux should have grown faster, and that it should have stopped its growth before it was actually stopped. But given that this was just a simple exercise conducted to obtain a qualitative sense of the phenomenon, it was decided not to make any further adjustments. Nevertheless the results do give a reasonable approximation, and indicate that the exothermic phenomenon needs to be included in the modelling of wood pyrolysis for the purpose of temperature predictions. When comparing for deeper positions (Figure 5.14), the agreement is poorer but the qualitative behaviour is still predicted, but the worse agreement indicates that the exothermic effect does not only correspond to a surface phenomenon.

Mass loss results are also in qualitative agreement. The peak mass loss rate is not reproduced in terms of magnitude, but it is attained at a similar time. The graph in Figure 5.15 indicates that although there is agreement in the temperature predictions at that time, there is some process that is not modelled which produces an extra mass loss. The modelling of char oxidation could be the cause for this discrepancy, but also moisture evaporation could not be taken into account for the deeper positions, because there is a delay of about 30 K at 600 s between the predicted and measured temperatures at 10 mm.

Worse agreement is obtained when comparing the experimental measurements with other heat fluxes (Figures 5.16 to 5.19). This indicates that the exothermic process could have some degree of dependency on the incident heat flux. Greater divergences are observed for the 60 $kW{\cdot}m^{-2}$ case, and these are attributed to flaming. In the lower end of the heat flux range, the behaviour was more closely followed, although at 10 $kW{\cdot}m^{-2}$ there is a slowing down in the heating rate that is not properly predicted by the model. An explanation for this is the variability observed in the measurements at this level of radiant energy, as was discussed in Chapter 3. No comparison was made between the model predictions and the parallel heating tests.

These previous results indicate that the model should be fitted for each experimental condition in order to have a more accurate prediction, but as was previously mentioned, this procedure was expressly avoided in this research. The cause of the inaccuracies is probably a poor modelling of the exothermic effect, as the initial inert behaviour is correctly represented. This

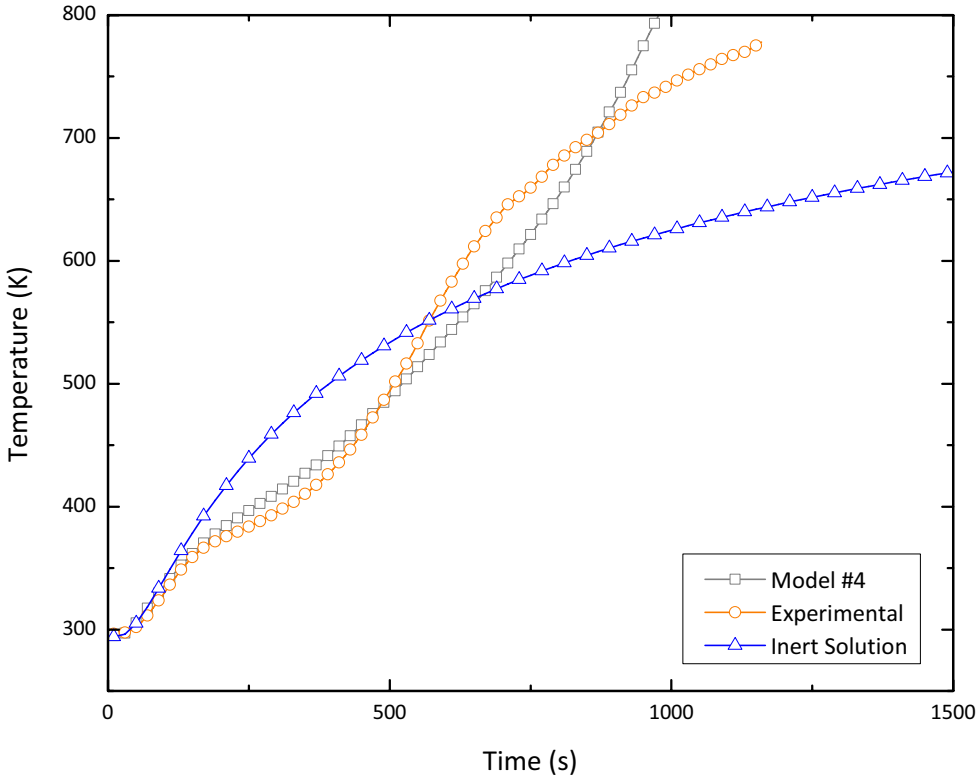

Figure 5.13: Temperature vs. time graphs for model prediction, experimental measurements and inert solution, 25 kW·m^{-2}, 5 mm. The inert solution shows no change in behaviour, while Model #4 shows a decrease in the heating rate caused by moisture evaporation and later an increase in the gradient caused by the extra imposed heat flux. The extra imposed heat flux should have been more intense and lasted less time, as can be seen from the experimental data.

means that in terms of virgin wood thermophysical properties, the values are correct (they were taken from the literature and the inert heating period of the experiments), and the divergences begin to occur close to the point of moisture evaporation. In terms of this latter effect, the behaviour is correctly modelled, although some disagreements are observed, especially for the lower incident heat fluxes.

Sensitivity analyses were performed, and the results were found to be insensitive to changes in the moisture content (40% higher MC), to a higher latent heat of moisture vaporization (20% higher latent heat), to a higher virgin wood thermal conductivity (10% increase in the conductivity), to a lower char thermal conductivity (a 20% lower value) and finally to a lower wood specific heat (10% lower).

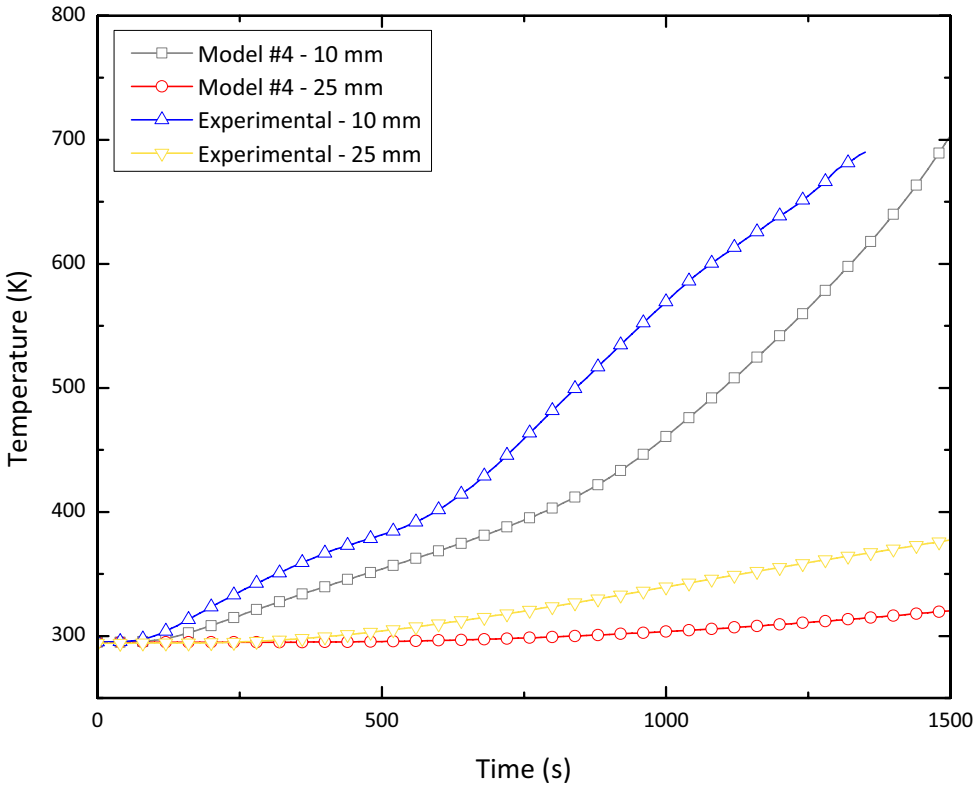

Figure 5.14: Temperature vs. time graphs for model predictions and experimental measurements, 25 kW·m^{-2}, 10 and 25 mm. There is worse agreement, indicating that the extra imposed heat flux should not only correspond to a surface process.

5.4 Concluding Remarks

The results from the modelling process show that the magnitude of the terms decreases with time, as the sample gets hotter and the net imposed heat flux diminishes and as the fronts move to the inner sections of the wood specimen and loose intensity. They agree with the experimental observations that the charring front moves slower than the moisture evaporation front, as they become more separated as the exposure progresses. In terms of gas-phase pressures, the calculated values are higher than the reported measured values, and the obtained profiles do not clearly show the distinct effects of the moisture evaporation and devolatilization processes. Mass loss rates show a similar behaviour, with the modelled values showing the attainment of an asymptotic rate for longer times, although the magnitude of the mass loss rates differs from the experimental values. However, the model agrees with the statement that the maximum mass loss rate will occur before the char layer has developed at the surface of the sample.

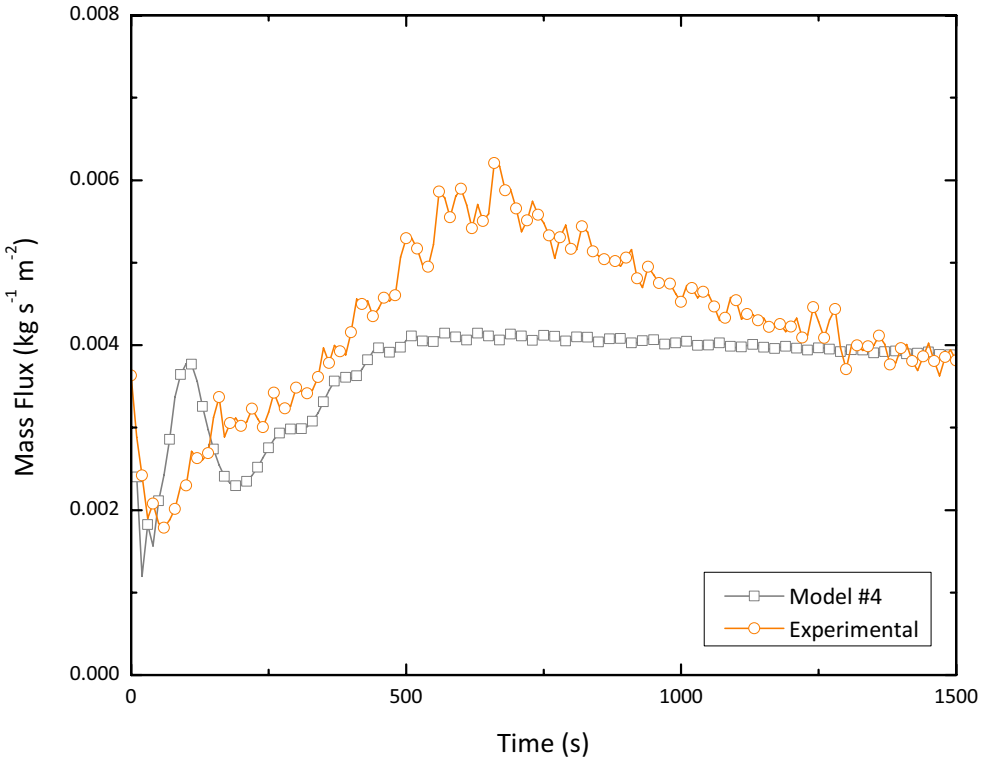

Figure 5.15: Mass flux for model predictions and experimental measurements, 25 kW·m^{-2}. The peak mass loss time is predicted by the model, but the its magnitude is 33% lower.

The main goal of this research is to identify a simple model that accurately predicts temperature profiles in timber exposed to fire-like situations. For this purpose, 4 models have been developed, each one incorporating different degrees of simplifications. It has been shown that several terms included in wood pyrolysis models can de discarded for the problem of the prediction of in-depth temperature profiles. Decomposition kinetics does not need to be accurately modelled, as the wood behaviour in terms of temperature seems to be insensible to more complicated kinetic schemes. This validates models that use a global, one-step reaction to represent pyrolysis. Not using competing reactions would also imply the impossibility to model the pressure build up inside the porous matrix, which has been concluded as not being relevant for the results. The contribution of the gas phases to the sensible heat is negligible, as well as the contribution of the convective term. Thus, all gas-phase processes need not be modelled.

In terms of comparison with the experimental results, the models give good results during the inert heating stage, independently of the incident heat flux. Divergences between the predicted and the measured results commence with the moisture evaporation process, although in general,

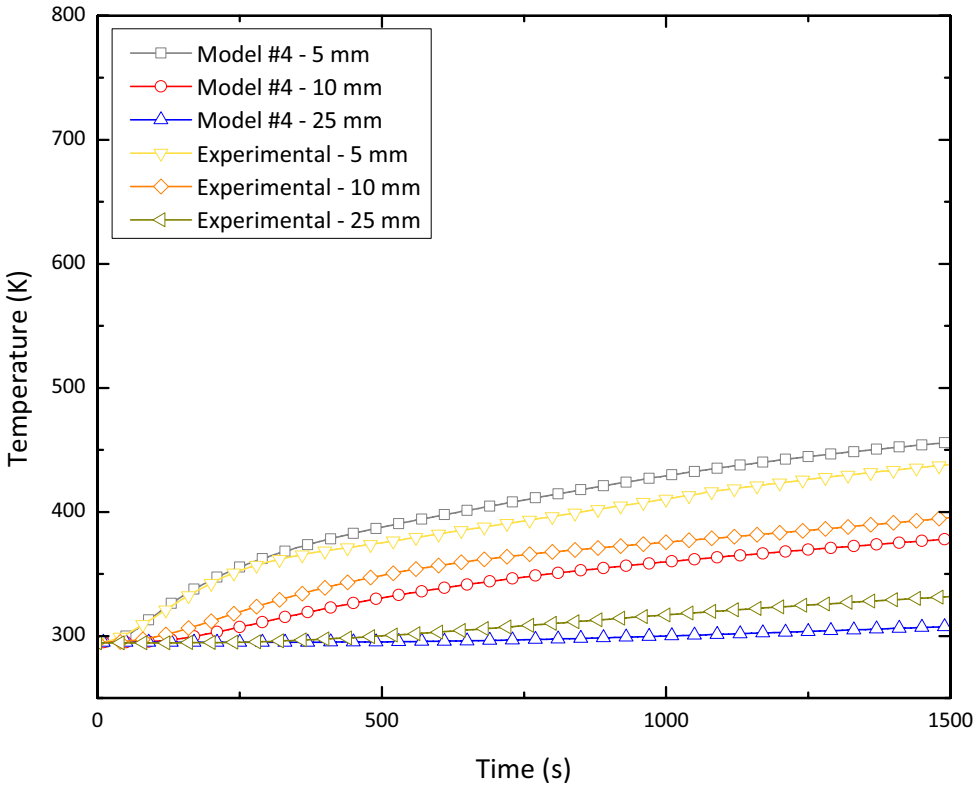

Figure 5.16: Temperature vs. time graphs for model predictions and experimental measurements, 10 kW·m^{-2}, 5, 10 and 25 mm. There is close agreement, although due to the time scales for this heat flux intensity, only low temperature processes were modelled.

and for the higher heat fluxes, it shows a reasonable agreement. The exothermic effect observed at temperatures above the moisture evaporation process, which was not modelled in this present work, accounts for the greater discrepancies observed in later times. To estimate the order of magnitude of this effect, the incident heat flux was incremented in time, and a greater agreement with the experimental data has been achieved. The exothermic effect has been estimated to be of an order of magnitude of 1.0 - 2.0 kW·m^{-2}. Even though the nature of this effect has not been clearly defined in this present work, it is concluded that it does not only correspond to a surface phenomenon, and it is very likely that this effect is caused by exothermic oxidation reactions (although it can also be generated by surface recession), and that this is an important effect that should be incorporated in any model that is used for the prediction of temperature profiles in wood elements. The final model was not found to be sensible to changes in parameters such as moisture content, virgin wood and char thermal conductivity and latent heat of moisture evaporation.

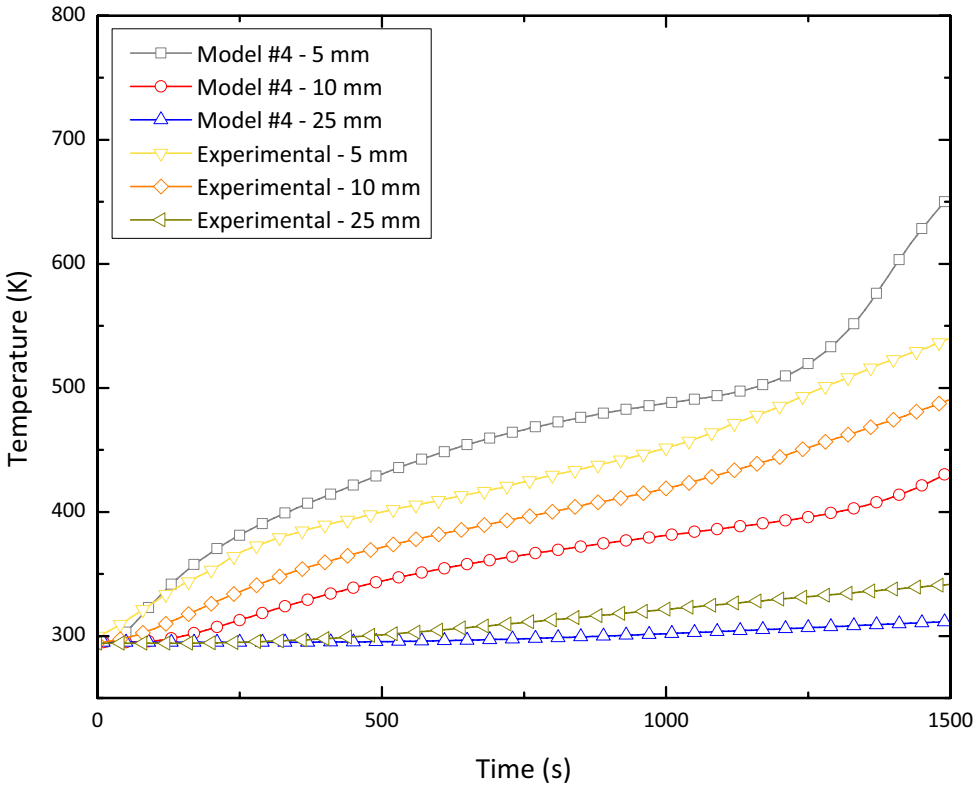

Figure 5.17: Temperature vs. time graphs for model predictions and experimental measurements, 18 kW·m^{-2}, 5, 10 and 25 mm. The "jump" in the temperatures, which marks the onset of the exothermic reactions, is not modelled properly, giving an indication on the nature of the exothermic effect, which probably is due to oxidation reactions.

Thus, a model to perform temperature profile predictions needs only to incorporate the solid sensible heat, conduction, the heat of the pyrolysis reaction, the heat of moisture evaporation and the aforementioned exothermic effect. This model is essentially the one proposed by Bamford et al in the late 1940s (Bamford et al. 1946, Crank & Nicolson 1947), but with extra source terms accounting for the different endo and exothermic reactions.

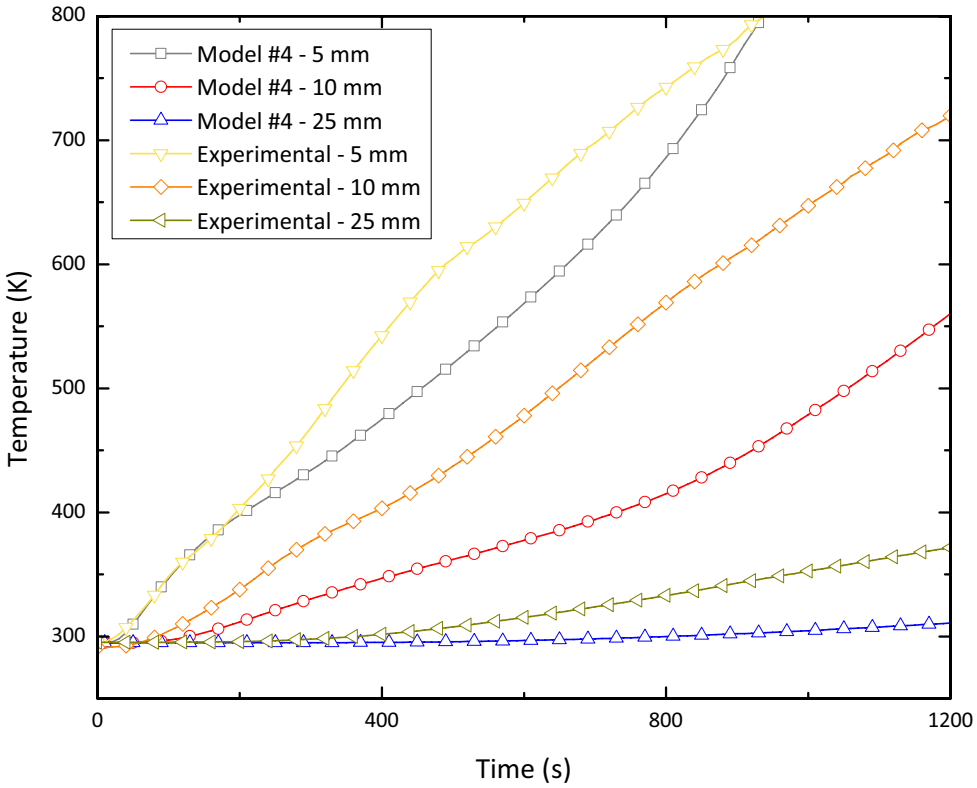

Figure 5.18: Temperature vs. time graphs for model predictions and experimental measurements, 40 kW·m^{-2}, 5, 10 and 25 mm. These results confirm that the exothermic effect does not have a long duration.

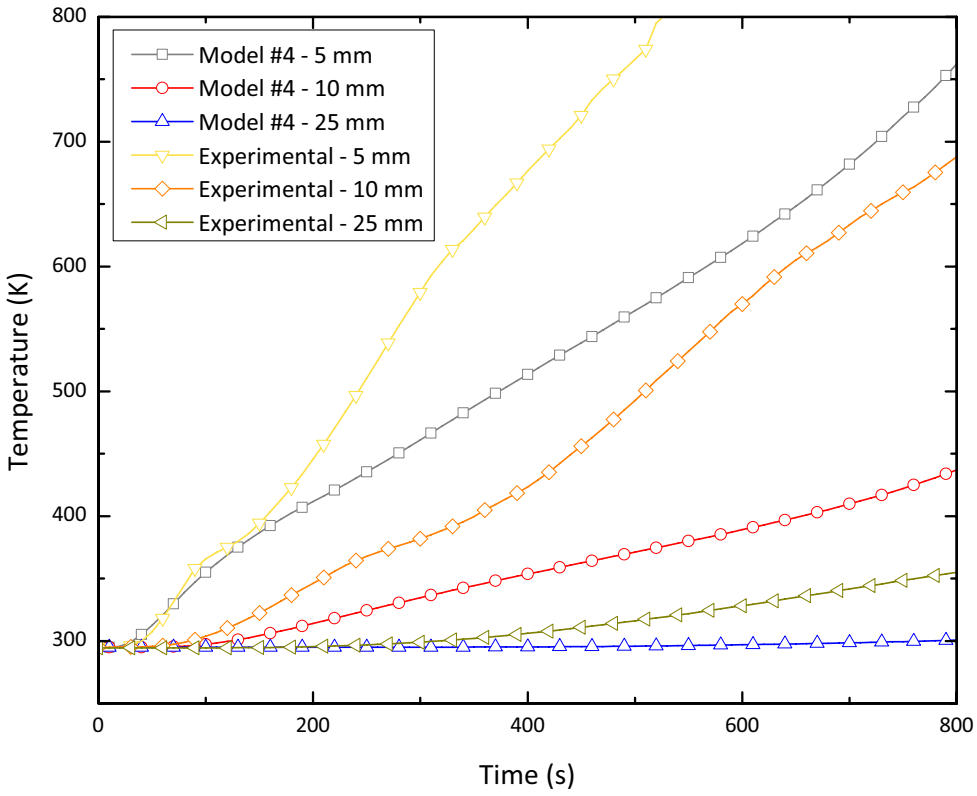

Figure 5.19: Temperature vs. time graphs for model predictions and experimental measurements, 60 kW·m^{-2}, 5, 10 and 25 mm. The greater divergences in this case are attributed to flaming combustion.

Chapter 6

General Summary and Conclusions

Modern timber construction techniques rely on methods that differ from the traditional methods and have increased productivity and cost effectiveness, thus making timber structures a popular construction method. Unfortunately some of these techniques present poorer behaviour in fires, especially some types of metallic connectors which are widely used, like truss plates. Normal prescriptive design methods assign low fire resistances for these structures, but the development of performance based design calls for a more detailed calculation of the fire behaviour of timber structures. These improved design methods require, among other things, an accurate knowledge of the temperature distributions encountered in the exposed timber element, to be input in the structural behaviour model.

Several models exist for this purpose. They range from simple empirical formulae, as used in some building standards to the solution of the energy, mass and momentum conservation equations in the timber element as part of the modelling of wood pyrolysis. Most of the empirical temperature profile models have been validated using fire resistance furnace tests, where a critical feature in the results of any thermal model, the boundary conditions, have not been clearly defined. The number of tests is generally low, which adds to the lack of repeatability between different furnaces and to the fact that there is only one thermal exposure level for this kind of tests.

Temperature profile tests carried out under fixed imposed heat fluxes presents advantages over that made using fire resistance furnaces. Boundary conditions are well defined, and a higher repeatability can be achieved. Given the smaller scale of the samples, the number of tests that can be performed is higher, and the specimens can be exposed to varied levels of imposed heat fluxes. Testing under these types of conditions has been carried out for several decades, but

the data is not readily available, and the individual studies have not been broad in terms of the range of heat fluxes to which the samples were exposed and the in-depth measurement points.

Comprehensive models have various degrees of complexity, incorporating different terms into the conservation equations. There is no agreement about the use of different terms for different applications (like the design of timber structures), and many of these modelled processes need accurately measured parameters. Because of the iterative nature of the design process, simplicity is a critical feature of any model for the prediction of in-depth temperature profiles used in structural applications, so the need to identify a simple and accurate model becomes relevant under this scope.

Some of these models have been validated with experimental temperature profile results, but in general there is only good agreement in the initial heating stages. In general, the models start to diverge from the experimental data for longer times and greater depths, which constitutes a disadvantage in terms of structural design, where the response of the structure should be modelled for long periods of time. Another drawback is that the comparisons are only presented for a narrow range of heating conditions.

With this motivation, a series of temperature profile tests were carried out under a wide range of imposed heat fluxes. The temperatures were measured at depths ranging from 5 mm to 40 mm from the exposed surface. Boundary conditions were clearly defined, allowing for a proper input for pyrolysis models. These tests constitute one of the broadest sets of data available, and show good repeatability, something unusual for an inhomogeneous material as wood.

The experimental results show that wood pyrolysis reactions begin at a heat flux close to 10 $kW \cdot m^{-2}$, where the behaviour is close to the inert heating case. Higher heat fluxes differ in a greater extent from the inert heating solution, but in all cases a moisture evaporation front and a charring front can be observed at the sides of the sample. The speeds of the moisture front at different heat fluxes converge to a final value for long exposure times. A similar behaviour is observed for the mass loss results, where the peak mass loss rates grow as the heat flux increases, but all heat fluxes reach a common asymptotic value. This indicates that for a constant heat flux wood attains heating conditions that are close to steady state and are independent of the incident heat flux.

A scaling of the experimental results showed that initially, the heating process of wood, independently of the imposed heat flux, is inert. The departure from the inert heating is caused by

the process of moisture evaporation, which constitutes a heat sink. The build-up of the char layer and the pyrolysis and combustion reactions make the behaviour to depart more strongly from the inert solution. The scaling method, based on the solution of a semi-infinite solid approximation, can be used to estimate the thermophysical properties of virgin wood, but its validity is greater only at early heating stages.

Observation of the moisture front speed and the measured temperatures when the moisture front reaches a given depth reveals two distinct behaviours. Low heat fluxes (i.e. ≤ 25 kW·m^{-2}) show lower speeds and higher measured temperatures than the higher intensities, indicating that moisture movement is faster than the heating rate. An interest result for modelling purposes, the Moisture Delay Time shows that the effect of the moisture evaporation process can be properly modelled as a heat sink, as the scaling shows that it mostly depends on the imposed heat flux.

It has also been shown that the heating conditions attained during the experimental tests can be treated as one-dimensional, which validates assumptions of this type when modelling the pyrolysis of wood.

An analysis of different modelling approaches has been conducted, placing more emphasis on the energy conservation equation. Resulting from this analysis, five models with different degrees of assumptions and numerical strategies were developed and solved, four incorporating volumetric reactions and the last one being of the moving boundary type. The analysis of the relative magnitude of each of the terms in the energy equation, and the comparison of the volumetric models between themselves has proven that for the purpose of predicting in-depth temperature profiles all the gas phase terms do not need to be present in the simplified model, including the pressure build up and the heat losses by convection of the pyrolysis gases. It has also been found that the temperature predictions are insensitive to the reaction schemes, thus validating the use of simple one-step reactions.

The comparison of the results of the simplified version of Model 4 (with no heat losses by convection) with the experimental data has shown good agreement only until after the process of moisture evaporation, where an exothermic effect that was not included in the models plays a relevant role in the temperature rise. This exothermic behaviour is probably caused by char oxidation reactions or by surface recession and cracking. This effect, whose magnitude has been estimated to be of 1.0 - 2.0 kW·m^{-2}, must be included in any model used in the design of timber structures.

Temperature predictions that include the exothermic effect show better agreement, but worse results are obtained for deeper positions and different incident heat fluxes (the model was calibrated for an external heat flux of 25 $kW \cdot m^{-2}$ and a depth of 5 mm, expressly avoiding the adjustment of the model for each particular condition). This indicates that the exothermic effect is not only a surface phenomenon, and that it could have some dependency on the incident heat flux.

Thus, a simplified model for the prediction of temperature profiles in timber elements exposed to fires must incorporate in the energy equation: the solid sensible heat, conduction, the heat of the pyrolysis reaction, the heat of moisture evaporation and the exothermic effect. The mass conservation equation can include three species, virgin wood, moisture and char, and the reaction schemes used can be simple one-step reactions that will not decrease the accuracy of the temperature predictions.

6.1 Future Work

The phenomenon of wood pyrolysis and combustion is not completely understood, and more detail is needed in some aspects in order to perform accurate temperature profile predictions in the context of structural timber design. The exothermic behaviour of wood must be properly identified and modelled; the relevance of this effect in the temperature profiles has been demonstrated in this thesis. As has been previously mentioned, the nature of this phenomenon is not clear, although it is likely to be caused by char oxidation reactions and is a volumetric event.

The next step must be the verification of the results presented in this work to other types of wood. This will indicate whether the chosen values for the kinetic parameters and thermophysical constants can be extended to other cases, or if there is a need for adjustment to particular cases.

The process of moisture migration and evaporation, important at the early heating stages, has been show to have two behaviours, dependent on the external heat flux. The precise external heat flux separating both patterns was not identified, and its dependence on initial moisture content and wood species should be studied. The kinetic modelling of this process should also be investigated in more detail, and also other effects that could prove to be important, like

the observed divergences in the behaviour of the shallower positions, which might indicate a surface effect.

In the quest of simple tools for the prediction of temperature profiles, integral models appear as a valid alternative, although for reasons previously explained it was decided not to work with them in the course of this research project. Their validity should be tested, using the experimental results of this thesis. Moving boundary models should also be studied in more detail, as they also constitute a good alternative.

Finally, an interesting expansion of this work would be the incorporation of metallic connectors in the thermal models, although this probably implies an expansion into two dimensional modelling. This would allow modelling the performance of the joint, which constitutes an important aspect for the structural design of timber structures in fires.

Bibliography

Agarwal, P., Genetti, W. & Lee, Y. (1986), 'Coupled Drying and Devolatilization of Wet Coal in Fluidized Beds', *Chemical Engineering Science* **41**(9), 2373–2383.

Alves, S. & Figueiredo, J. (1989), 'A Model for Pyrolysis of Wet Wood', *Chemical Engineering Science* **44**(12), 2861–2869.

Antal, M. & Varhegyi, G. (1995), 'Cellulose Pyrolysis Kinetics: The Current State of Knowledge', *Industrial & Engineering Chemistry Research* **34**, 703–717.

Atreya, A. (1983), Pyrolysis, Ignition and Fire Spread on Horizontal Surfaces of Wood, PhD thesis, Harvard University.

Atreya, A. (1998), 'Ignition of Fires', *Philosophical Transactions Royal Society London* **A 356**, 2787–2813.

Atreya, A. & Baum, H. (2002), 'A Model of Opposed-Flow Flame Spread Over Charring Materials', *Proceedings of the Combustion Institute* **29**, 227–236.

Atreya, A. & Wichman, I. (1989), 'Heat and Mass Transfer During Piloted Ignition of Cellulosic Solids', *Journal of Heat Transfer* **111**, 719–725.

Babrauskas, V. & Williamson, R. (1978), 'The Historical Basis of Fire Resistance Testing - Part II', *Fire Technology* **14**(4), 304–316.

Bamford, C., Crank, J. & Malan, D. (1946), 'The Combustion of Wood. Part 1', *Proc. Cambridge Philosophical Society* **42**, 166–182.

Baum, H. & Atreya, A. (2007), 'A Model of Transport of Fuel Gases in a Charring Solid and Its Application to Opposed-Flow Flame Spread', *Proceedings of the Combustion Institute* **31**, 2633–2641.

Beck, J. (1962), 'Thermocouple Temperature Disturbances in Low Conductivity Materials', *Transactions of the ASME Journal of Heat Transfer* pp. 124–132.

Bejan, A. (1997), *Advanced Engineering Thermodynamics*, John Wiley & Sons.

Benichou, N. & Sultan, M. (2000), 'Fire Resistance Performance of Lightweight Wood-Framed Assemblies', *Fire Technology*.

Benkoussas, B., Consalvi, J., Porterie, B., Sardoy, N. & Loraud, J. (2007), 'Modelling Thermal Degradation of Woody Fuel Particles', *International Journal of Thermal Sciences* **46**, 319–327.

Bilbao, R., Mastral, J., Ceamanos, J. & Aldea, M. (1996), 'Modelling of the Pyrolysis of Wet Wood', *Journal of Analytical and Applied Pyrolysis* **36**, 81–97.

Blackshear, P. & Kanury, A. (1965), 'Heat and Mass Transfer To, From, and Within Cellulosic Solids Burning in Air', *Proceedings of the Combustion Institute* **10**, 911–923.

Boonmee, N. & Quintiere, J. (2005), 'Glowing Ignition of Wood: The Onset of Surface Combustion', *Proceedings of the Combustion Institute* **30**, 2303–2310.

Bryden, K., Ragland, K. & Rutland, C. (2002), 'Modeling Thermally Thick Pyrolysis of Wood', *Biomass and Bioenergy* **22**, 41–53.

Buchanan, A. (2000), 'Fire Performance of Timber Construction', *Prog. Struct. Engng Mater.* **2**, 278–289.

Buchanan, A. (2002), *Structural Design for Fire Safety*, John Wiley & Sons.

Carling, O. (1989), Fire Resistance of Joint Details in Loadbearing Timber Construction - A Literature Survey, Technical Report BRANZ Study Report SR 18, Building Research Association of New Zealand.

Carslaw, H. & Jaeger, J. (1959), *Conduction of Heat in Solids*, Oxford University Press.

CEN (2004), 'Eurocode 5, Design of Timber Structures, Part 1-2, EN 1995-1-2'.

Chan, W., Kelbon, M. & Krieger, B. (1985), 'Modelling and Experimental Verification of Physical and Chemical Processes During Pyrolysis of a Large Biomass Particle', *Fuel* **64**, 1505–1513.

Childs, P., Greenwood, J. & Long, C. (2000), 'Review of Temperature Measurement', *Review of Scientific Instruments* **71**, 2959–2978.

Clancy, P. (2001), 'Advances in Modelling Heat Transfer Through Wood Framed Walls', *Fire and Materials* **25**, 241–254.

Clancy, P. & Young, S. (2004), 'Full Scale Experiments for Evaluating Theoretical Fire Wall Models', *Fire and Materials* **28**, 431–458.

Crank, J. (1984), *Free and Moving Boundary Problems*, Oxford University Press.

Crank, J. & Nicolson, P. (1947), 'A Practical Solution for Numerical Evaluation of Solutions of Partial Differential Equations of the Heat-Conduction Type', *Proceedings of the Cambridge Philosophical Society* **43**, 50–67.

Di Blasi, C. (1993*a*), 'Analysis of Convection and Secondary Reaction Effects Within Porous Solid Fuels Undergoing Pyrolysis', *Combustion Science and Technology* **90**, 315–340.

Di Blasi, C. (1993*b*), 'Modeling and Simulation of Combustion Processes of Charring and Non-Charring Solid Fuels', *Progress in Energy and Combustion Science* **19**, 71–104.

Di Blasi, C. (1996), 'Influences of Model Assumptions on the Predictions of Cellulose Pyrolysis in the Heat Transfer Controlled Regime', *Fuel* **75**, 58–66.

Di Blasi, C. (2007), 'Modeling Chemical and Physical Processes of Wood and Biomass Pyrolysis', *Progress in Energy and Combustion Science* p. (in press).

Dietenberger, M. (2006), 'Using a Quasi-Heat-Pulse Method to Determine Heat and Moisture Transfer Properties for Porous Orthotropic Wood Products or Cellular Solid Materials', *Journal of Thermal Analysis and Calorimetry* **83**, 97–106.

Do, M. & Springer, G. (1983), 'Mass Loss of and Temperature Distribution in Southern Pine and Douglas Fir in the Range 100 to 800° C', *Journal of Fire Sciences* **1**, 271–284.

Drysdale, D. (1998), *An Introduction to Fire Dynamics*, 2nd edn, John Wiley & Sons, New York.

Filipczak, R., Crowley, S. & Lyon, R. (2005), 'Heat Release Rate Measurements of Thin Samples in the OSU Apparatus and the Cone Calorimeter', *Fire Safety Journal* **40**, 628–645.

Foliente, G. (2000), History of Timber Construction, *in* 'Wood Structures: A Global Forum on the Treatment, Conservation, and Repair of Cultural Heritage, ASTM STP 1351', American Society for Testing and Materials, pp. 3–22.

FPL (1999), Wood Handbook - Wood as an Engineering Material, Technical Report FPL-GTR-113, USDA Forest Service, Forest Products Laboratory.

Frangi, A. & Fontana, M. (2003), 'Charring Rates and Temperature Profiles of Wood Sections', *Fire and Materials* **27**, 91–102.

Fredlund, B. (1988), A Model for Heat and Mass Transfer in Timber Structures During Fire, PhD thesis, Lund University.

Fredlund, B. (1993), 'Modelling of Heat and Mass Transfer in Wood Structures During Fire', *Fire Safety Journal* **20**, 39–69.

Fuentes, A. (2007), 'Personal Communication'.

Galgano, A. & Di Blasi, C. (2004), 'Modeling the Propagation of Drying and Decomposition Fronts in Wood', *Combustion and Flame* **139**, 16–27.

Gerhards, C. (1982), 'Effect of Moisture Content and Temperature on the Mechanical Properties of Wood: an Analysis of Immediate Effects', *Wood and Fiber* **14**, 4–36.

Hadvig, S. (1981), *Charring of Wood in Building Fires*, Technical University of Denmark, Lyngby, Denmark.

Herzog, T., Natterer, J., Schweitzer, R., Volz, M. & Winter, W. (2004), *Timber Construction Manual*, Birkhauser.

Incropera, F. & DeWitt, D. (2002), *Fundamentals of Heat and Mass Transfer*, John Wiley & Sons.

Ingberg, S. & Mitchell, N. (1941), Fire Tests of Wood- and Metal- Framed Partitions, Technical report, National Bureau of Standards.

Irvine, G. (1984), 'The Glass Transitions of Lignin and Hemicellulose and their Measurement by Differential Thermal Analysis', *Tappi Journal* **67**, 118–121.

ISO (1993), 'ISO 5660-1:1993 Fire Tests Reaction to Fire Part 1: Rate of Heat Release from Building Products (Cone Calorimeter Method)', International Organization for Standardization.

ISO (1999), 'ISO 834-1:1999 Fire Resistance Tests Elements of Building Construction Part 1: General Requirements', International Organization for Standardization.

Janssens, M. (1991), Fundamental Thermophysical Characteristics of Wood and their Role in Enclosure Fire Growth, PhD thesis, University of Gent.

Janssens, M. & White, R. (1994), 'Short Communication: Temperature Profiles in Wood Members Exposed to Fire', *Fire and Materials* **18**, 263–265.

Kansa, E., Perlee, H. & Chaiken, R. (1977), 'Mathematical Model of Wood Pyrolysis Including Internal Forced Convection', *Combustion and Flame* **29**, 311–324.

Kanury, A. (1972), 'Ignition of Cellulosic Solids – A Review', *Fire Research Abstracts and Reviews* **14**(1), 24–52.

Kanury, A. (1987), 'On the Craft of Modeling in Engineering Science', *Fire Safety Journal* **12**, 65–74.

Kashiwagi, T., Ohlemiller, T. & Werner, K. (1987), 'Effects of External Radiant Flux and Ambient Oxygen Concentration on Nonflaming Gasification Rates and Evolved Products of White Pine', *Combustion and Flame* **69**, 331–345.

Kidd, C. & Nelson, C. (1995), How the Schmidt-Boelter Gage Really Works, *in* '41st International Instrumentation Symposium', pp. 347–368.

Klingsch, W., Tavakkol-Khah, M., Wesche, J. & Kersken-Bradley, M. (1993), Temperaturentwicklung in Brandbeanspruchten Holzquerschnitten, Technical report, Bergische Universitat Wuppertal.

Kocaefe, D., Younsi, R., Poncsak, S. & Kocaefe, Y. (2006), 'Comparison of Different Models for the High-Temperature Heat-Treatment of Wood', *International Journal of Thermal Sciences* **46**, 707–716.

Kollmann, F. & Cote, W. (1968), *Principles of Wood Science and Technology*, George Allan & Unwin Ltd.

Koufopanos, C., Papayannakos, N., Maschio, G. & Lucchesi, A. (1991), 'Modelling of the Pyrolysis of Biomass Particles. Studies on Kinetics, Thermal and Heat Transfer Effects.', *The Canadian Journal of Chemical Engineering* **69**, 907–915.

Kung, H. (1972), 'A Mathematical Model of Wood Pyrolysis', *Combustion and Flame* **18**, 185–195.

Kuo, J. & Hsi, C. (2005), 'Pyrolysis and Ignition of Single Wooden Spheres Heated in High-Temperature Streams of Air', *Combustion and Flame* **142**, 401–412.

Kuo, K. (2005), *Principles of Combustion*, John Wiley & Sons.

Lau, P. & Barrett, J. (1994), 'Factors Affecting Reliability of Light-Framing Wood Members Exposed to Fire - A Critical Review', *Fire and Materials* **18**, 339–349.

Lee, C., Chaiken, R. & Singer, J. (1976), 'Charring Pyrolysis of Wood in Fires by Laser Simulation', *Proceedings of the Combustion Institute* **16**, 1459–1470.

Liden, A., Berruti, F. & Scott, D. (1988), 'A Kinetic Model for the Production of Liquids From the Flash Pyrolysis of Biomass', *Chemical Engineering Communications* **65**, 207–221.

Long, R., Torero, J., Quintiere, J. & Fernandez-Pello, C. (2000), Scale and Transport Considerations on Piloted Ignition of PMMA, *in* 'Fire Safety Science, Proceedings 6th International Symposium', Poitiers, France, pp. 567–578.

Luikov, A. (1975), 'Systems of Differential Equations of Heat and Mass Transfer in Capillary-Porous Bodies (Review)', *International Journal of Heat and Mass Transfer* **18**, 1–14.

Majesko, G., Brady, W. & Burley, N. (1985), 'Introduction to Type N Thermocouples', *Plant Engineering* **39**, 88–90.

Martin, S. (1965), 'Diffusion-Controlled Ignition of Cellulosic Materials by Intense Radiant Energy', *Proceedings of the Combustion Institute* **10**, 877–896.

Melaaen, M. (1996), 'Numerical Analysis of Heat and Mass Transfer in Drying and Pyrolysis of Porous Media', *Numerical Heat Transfer, Part A* **29**, 331–355.

Mikkola, E. (1990), Charring of Wood, Technical report, VTT Research Report.

Mikkola, E. (1992), Charring of Wood Based Materials, *in* 'Fire Safety Science, Proceedings 3rd International Symposium', Edinburgh, UK, pp. 547–556.

Moghtaderi, B. (2006), 'The State-of-the-Art in Pyrolysis Modelling of Lignocellulosic Solid Fuels', *Fire and Materials* **30**, 1–34.

Montgomery, D. (2001), *Design and Analysis of Experiments*, John Wiley & Sons.

Moraes, P. (2003), Influence De La Temperature Sur Les Assemblages Bois, PhD thesis, Universite Henri Poincaré, Nancy 1.

Moraes, P., Rogaume, Y., Bocquet, J. & Triboulot, P. (2005), 'Influence of Temperature on the Embedding Strength', *Holz als Roh- und Werkstoff* **63**, 297–302.

Moran, M. & Shapiro, H. (1998), *Fundamentals of Engineering Thermodynamics*, John Wiley & Sons.

Motevalli, V., Chen, Y., Gallagher, G. & Sheppard, D. (1992), Measurement of Horizontal Flame Spread on Charring and Non-Charring Material Using the LIFT Apparatus, *in* 'Fire and Materials International Conference', pp. 23–32.

Nield, D. & Bejan, A. (1992), *Convection in Porous Media*, Springer-Verlag.

Noren, J. (1996), 'Load-Bearing Capacity of Nailed Joints Exposed to Fire', *Fire and Materials* **20**, 133–143.

Ostman, B. (1985), 'Wood Tensile Strength at Temperatures and Moisture Contents Simulating Fire Conditions', *Wood Science and Technology* **19**, 103–116.

Panton, R. & Rittmann, J. (1971), 'Pyrolysis of a Slab of Porous Material', *Proceedings of the Combustion Institute* **13**, 881–891.

Parker, W. (1985), Prediction of the Heat Release Rate of Wood, *in* 'Fire Safety Science, Proceedings 1st International Symposium', Maryland, USA, pp. 207–216.

Poon, L. (2003), Literature Review on the Contribution of Fire Resistant Timber Construction to Heat Release Rate, Technical report, Warrington Fire Research Report.

Rammer, D. (2001), Effect of Moisture Content on Nail Bearing Strength, Technical Report FPL-RP-591, US Forest Products Laboratory Research Paper.

Rammer, D. & Winistorfer, S. (2001), 'Effect of Moisture Content on Dowel Bearing Strength', *Wood and Fiber Science* **33**(1), 126–139.

Rein, G. (2007), 'Personal Communication'.

Reszka, P. & Torero, J. (2008), 'In-depth Temperature Measurements in Wood Exposed to Intense Radiant Energy', *Experimental Thermal and Fluid Science* **32**, 1405–1411.

Roberts, A. (1971), 'Problems Associated with the Theoretical Analysis of the Burning of Wood', *Proceedings of the Combustion Institute* **13**, 893–903.

Roberts, A. & Clough, G. (1963), 'Thermal Decomposition of Wood in an Inert Atmosphere', *Proceedings of the Combustion Institute* **9**, 158–166.

Saastamoinen, J. & Richard, J. (1996), 'Simultaneous Drying and Pyrolysis of Solid Fuel Particles', *Combustion and Flame* **106**, 288–300.

Schaffer, E. (1967), Charring Rate of Selected Woods - Transverse to Grain, Technical Report FPL 69, US Forest Service Research Paper.

Schaffer, E. (1973), 'Effect of Pyrolytic Temperatures on the Longitudinal Strength of Dry Douglas-Fir', *Journal of Testing and Evaluation* **1**, 319–329.

Schaffer, E. (1984), Structural Fire Design: Wood, Technical report, US Forest Service Research Paper.

Schaffer, E. (1988), 'How Well Do Wood Trusses Really Perform During a Fire?', *Fire Journal* pp. 57–62.

Schober, K. (2000), Numerical Simulation of Contact Problems - Traditional Timber Joints Under Monotonous Loading, Technical report, University of Dortmund.

Shen, D., Fang, M., Luo, Z. & Cen, K. (2006), 'Modeling Pyrolysis of Wet Wood Under External Heat Flux', *Fire Safety Journal*.

Shrestha, D., Cramer, S. & White, R. (1994), 'Time-Temperature Profile Across a Lumber Section Exposed to Pyrolytic Temperatures', *Fire and Materials* **18**, 211–220.

Siau, J. (1984), *Transport Processes in Wood*, Springer-Verlag.

Siegel, R. & Howell, J. (2002), *Thermal Radiation Heat Transfer*, Taylor & Francis.

Simms, D. (1962), 'Damage to Cellulosic Solids by Thermal Radiation', *Combustion and Flame* **6**, 303–318.

Singh, B. & Kaviany, M. (1994), 'Effect of Solid Conductivity on Radiative Heat Transfer in Packed Beds', *International Journal of Heat and Mass Transfer* **37**, 2579–2583.

Spearpoint, M. (1999), Predicting the Ignition and Burning Rate of Wood in the Cone Calorimeter Using an Integral Model, Master's thesis, University of Maryland.

Spearpoint, M. & Quintiere, J. (2000), 'Predicting the Burning of Wood Using an Integral Model', *Combustion and Flame* **123**, 308–324.

Spearpoint, M. & Quintiere, J. (2001), 'Predicting the Piloted Ignition of Wood in the Cone Calorimeter Using an Integral Model - Effect of Species, Grain Orientation and Heat Flux', *Fire Safety Journal* **36**, 391–415.

Staggs, J. (2003), 'Heat and Mass Transport in Developing Chars', *Polymer Degradation and Stability* **82**, 297–307.

Suuberg, E., Milosavljevic, I. & Lilly, W. (1994), The Behavior of Charring Materials in Simulated Fire Environments, Technical Report NIST GCR 94-645, NIST Internal Report.

Takeda, H. & Mehaffey, J. (1998), 'WALL2D: A Model for Predicting Heat Transfer Through Wood-Stud Walls Exposed to Fire', *Fire and Materials* **22**, 133–140.

Tamanini, F. (1976*a*), A Numerical Model for One-Dimensional Heat Conduction with Pyrolysis in A Slab of Finite Thickness, Technical Report FMRC Serial No. 21011.7, Factory Mutual Research Corporation.

Tamanini, F. (1976*b*), 'A Study of the Extinguishment of Vertical Wood Slabs in Self-Sustained Burning by Water Spray Application', *Combustion Science and Technology* **14**, 1–15.

Taylor, J. (1997), *An Introduction to Error Analysis*, University Science Books.

Thurner, F. & Mann, U. (1981), 'Kinetic Investigation of Wood Pyrolysis', *Industrial & Engineering Chemistry Process Design and Development* **20**, 482–488.

Tinney, E. (1965), 'The Combustion of Wooden Dowels in Heated Air', *Proceedings of the Combustion Institute* **10**, 925–930.

Tran, C. & White, R. (1992), 'Burning Rate of Solid Wood Measured in a Heat Release Rate Calorimeter', *Fire and Materials* **16**, 197–206.

Tsantaridis, L. & Ostman, B. (1998), 'Charring of Protected Wood Studs', *Fire and Materials* **22**, 55–60.

Van Wylen, G. & Sonntag, R. (1978), *Fundamentals of Classical Thermodynamics*, John Wiley & Sons.

Vovelle, C., Akrich, R. & Delfau, J. (1984), 'Thermal Degradation of Solid Materials Under a Variable Radiant Heat Flux', *Proceedings of the Combustion Institute* **20**, 1647–1654.

Weatherford, W. & Sheppard, D. (1965), 'Basic Studies of the Mechanism of Ignition of Cellulosic Materials', *Proceedings of the Combustion Institute* **10**, 897–910.

White, R. (1988), Charring Rates of Different Wood Species, PhD thesis, University of Wisconsin-Madison.

White, R. (2002), Analytical Methods for Determining Fire Resistance of Timber Members, *in* 'SFPE Handbook of Fire Protection Engineering', Society of Fire Protection Engineers, pp. 4–257–4–273.

White, R. & Cramer, S. (1994), Improving the Fire Endurance of Wood Truss Systems, *in* 'Proceedings of Pacific Timer Engineering Conference', Timber Research Development and Advisory Council, pp. 582–589.

White, R. & Schaffer, E. (1981), 'Transient Moisture Gradient in Fire-Exposed Wood Slab', *Wood and Fiber Science* **13**(1), 17–38.

White, R., Cramer, S. & Shrestha, D. (1993), Fire Endurance Model for a Metal-Plate-Connected Wood Truss, Technical Report FPL-RP-522, US Forest Service Research Paper.

Williams, C. (1953), Damage Initiation in Organic Materials Exposed to High-Intensity Thermal Radiation, PhD thesis, Massachusetts Institute of Technology.

Yang, L., Chen, X., Zhou, X. & Fan, W. (2002), 'A Modified Model of Pyrolysis for Charring Materials in Fire', *International Journal of Engineering Science* **40**, 1011–1021.

Yang, L., Chen, X., Zhou, X. & Fan, W. (2003), 'The Pyrolysis and Ignition of Charring Materials Under an External Heat Flux', *Combustion and Flame* **133**, 407–413.

Yoshizawa, Y. & Kubota, H. (1982), 'Experimental Study on Gas-Phase Ignition of Cellulose Under Thermal Radiation', *Proceedings of the Combustion Institute* **19**, 787–795.

Young, S. & Clancy, P. (2001*a*), 'Compression Mechanical Properties of Wood at Temperatures Simulating Fire Conditions', *Fire and Materials* **25**, 83–93.

Young, S. & Clancy, P. (2001*b*), 'Structural Modelling of Light-Timber Framed Walls in Fire', *Fire Safety Journal* **36**, 241–268.

Yuen, R., Yeoh, G., de Vahl Davis, G. & Leonardi, E. (2007), 'Modelling the Pyrolysis of Wet Wood I. Three-Dimensional formulation and Analysis', *International Journal of Heat and Mass Transfer*.

Appendix A

Quantification of Thermal Boundary Conditions

A.1 Convective Losses: Front Surface

Measurements have been carried out of the air velocities in the Cone Calorimeter enclosure with the extraction fan at normal operating velocity (flow rate of 24 L·s^{-1}), and no measurable velocity was obtained around the sample (the measurements were carried out with both rotating vane and hot wire anemometers with the heater switched off), which means that in this case convection is natural. An estimation of the convective coefficient was carried out for increasing values of the surface temperature, using a correlation by Churchill and Chu (for a vertical plate, as reported by Incropera and De Witt (Incropera & DeWitt 2002)):

$$\overline{Nu}_L = 0.68 + \frac{0.670 \cdot Ra_L^{1/4}}{\left[1 + (0.492/Pr)^{9/16}\right]^{4/9}} \qquad 0 < Ra_L < 10^9 \tag{A.1}$$

Figure A.1 shows the calculated values for the convective coefficient as a function of the surface temperature. Further measurements with the heater on (at a temperature of 873 K) were carried out, and they indicated speeds of 1.4 m · s $^{-1}$ around the sample. This results in a laminar flow, with an average convective coefficient of 12.7 W · m $^{-2}$· K^{-1}, which is slightly higher than the previous value.

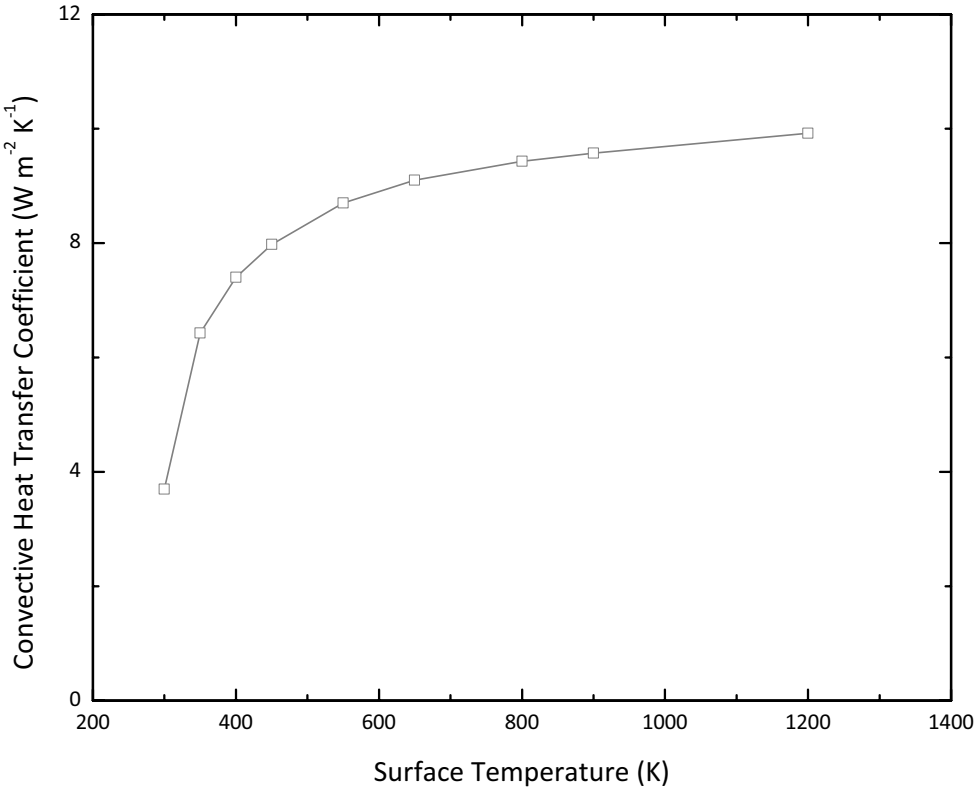

Figure A.1: Calculated convective coefficient as a function of the surface temperature.

A.2 Convective Losses: Back Surface

The aluminium block attached to the back of the specimen is assumed to behave like a fin. Steady state conduction (an assumption deemed valid due to the slower heating at the back and because the Biot number for the block is low, see Sample Preparation in Section 2.3) and convective losses as the boundary condition at the end of the block are assumed for this extended surface. Then, an equivalent convective coefficient is calculated such that the energy lost at the back end of the specimen is equal to that lost with the presence of the aluminium block attached to its back. The solution for the steady state conduction of extended surfaces is readily available in standard heat transfer books (Incropera & DeWitt 2002) and will not be presented here. For a back temperature of 323 K (50°C), and a calculated natural convection coefficient of 5.4 W $\cdot$ m $^{-2}\cdot$ K^{-1}, the heat dissipated is estimated at $\dot{q}_{Al}$ = 3.2 W. Then, taking

$$h_{eq} = \frac{\dot{q}_{Al}}{A_S \cdot (T - T_\infty)} \tag{A.2}$$

The equivalent convective coefficient, h_{eq}, can be obtained; its calculated value is 11.87 W· m $^{-2}$· K^{-1}.

A.3 Total Convective Coefficient

Surface heat losses are generated by convection and radiation. Following a common linearization of the radiative losses (Incropera & DeWitt 2002), the total losses can be expressed as a function of the temperature difference between the surface and the surroundings by incorporating a total convective coefficient. The linearization takes the following form:

$$\sigma \epsilon \left(T_s^4 - T_\infty^4\right) = \sigma \epsilon \left(T_s^2 + T_\infty^2\right) \left(T_s - T_\infty\right) \left(T_s + T_\infty\right). \tag{A.3}$$

The radiative component of the total convective coefficient corresponds to:

$$h_{rad} = \sigma \epsilon \left(T_s^2 + T_\infty^2\right) \left(T_s - T_\infty\right). \tag{A.4}$$

Taking a value for the emissivity equal to 1, h_{rad} will grow as a function of the surface temperature, as shown in Figure A.2:

Since this procedure is done only for the inert heating solution, a constant value for the radiative component has been assumed to be of 23 W·m^{-2}· K^{-1}, which added to the convective component (described previously) gives a total convective coefficient of 35 W·m^{-2}· K^{-1}.

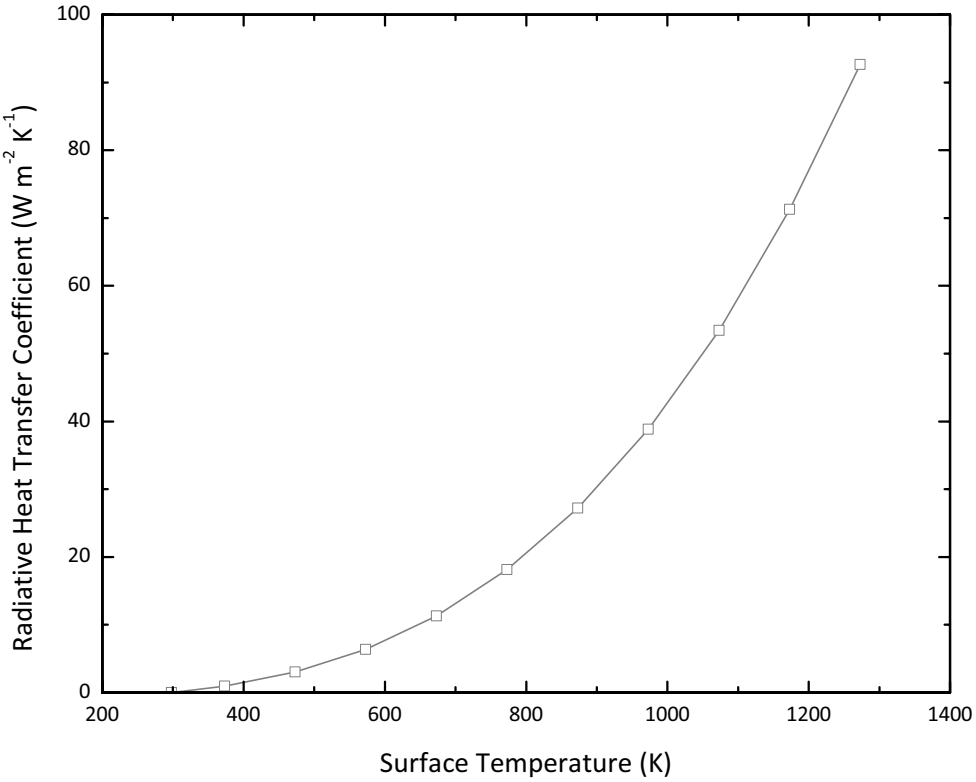

Figure A.2: Calculated radiative heat transfer coefficient as a function of the surface temperature.

Appendix B

Further Experimental Results

B.1 Thermocouple readings

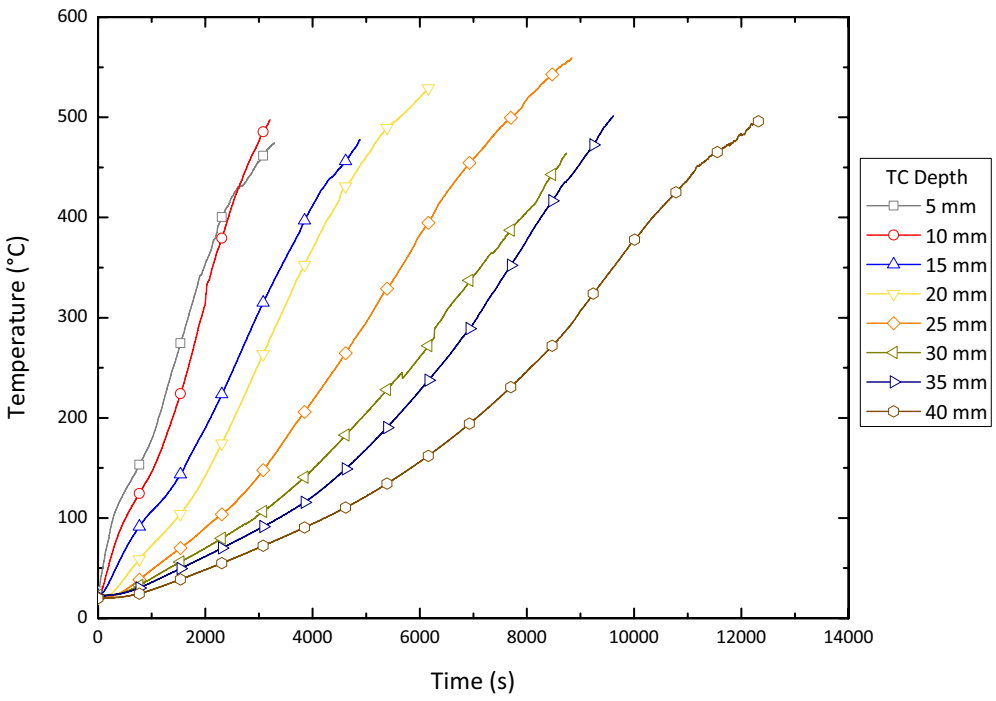

Figure B.1: Averaged temperature histories for 18 kW·m^{-2}, perpendicular heating.

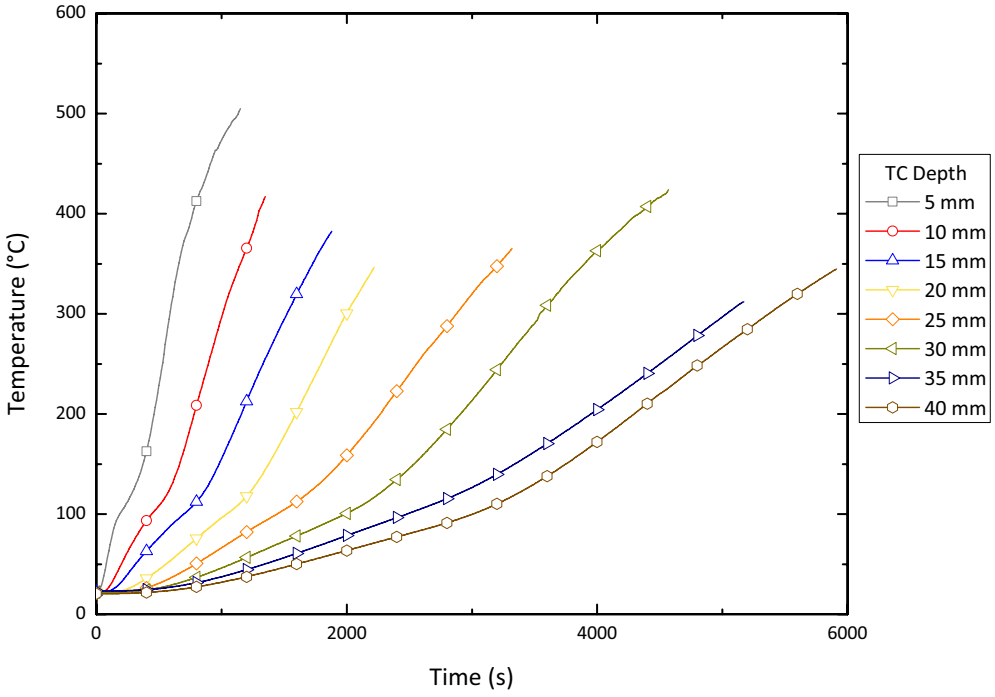

Figure B.2: Averaged temperature histories for 25 kW·m^{-2}, perpendicular heating.

B.2 Movement of Moisture Evaporation and Pyrolysis Fronts

The following figures show the individual thermocouple readings when the average temperature is either 373 K or 573 K, values that correspond to the passing of the moisture evaporation and pyrolysis fronts, respectively. According to their position with respect to the central point of the sample, the thermocouples are labelled left, right or centre.

B.3 Visual Observations: Parallel Heating Test

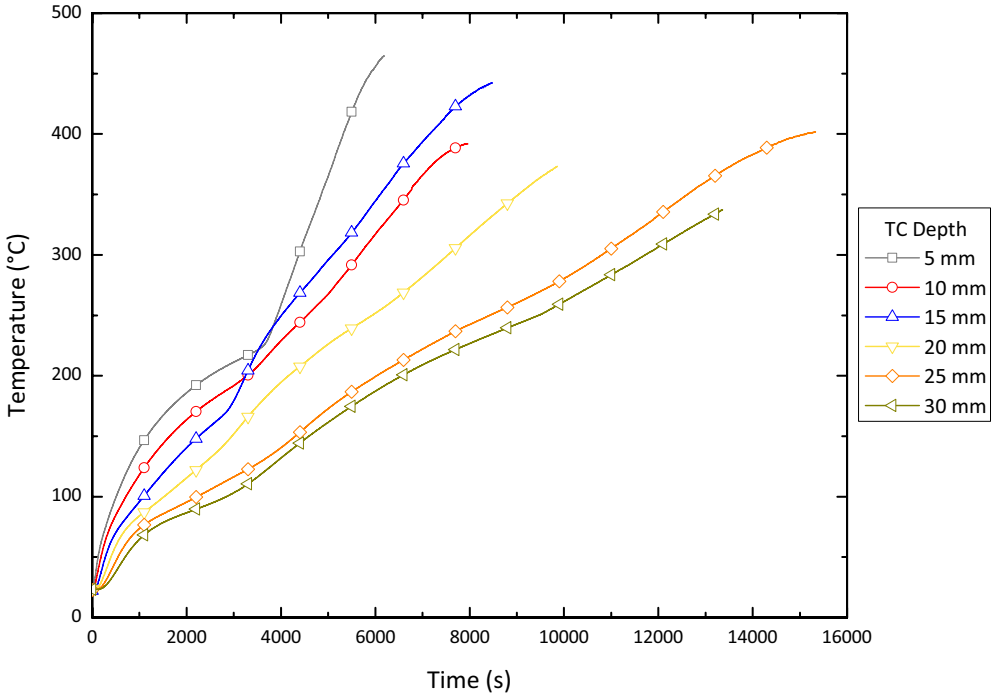

Figure B.3: Averaged temperature histories for 10 kW·m^{-2}, parallel heating.

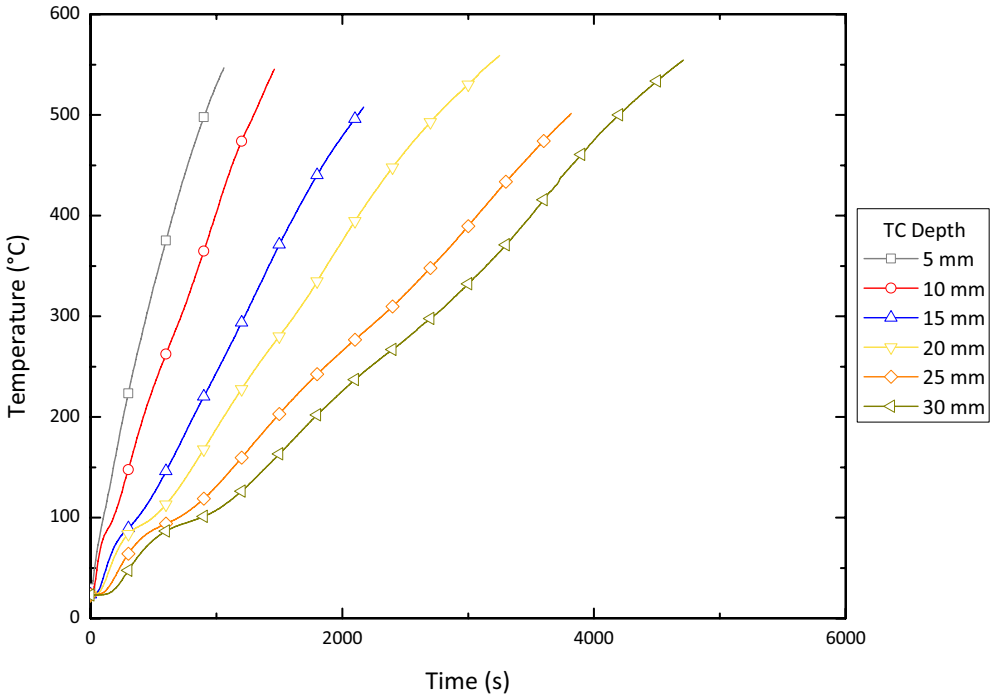

Figure B.4: Averaged temperature histories for 60 kW·m^{-2}, parallel heating.

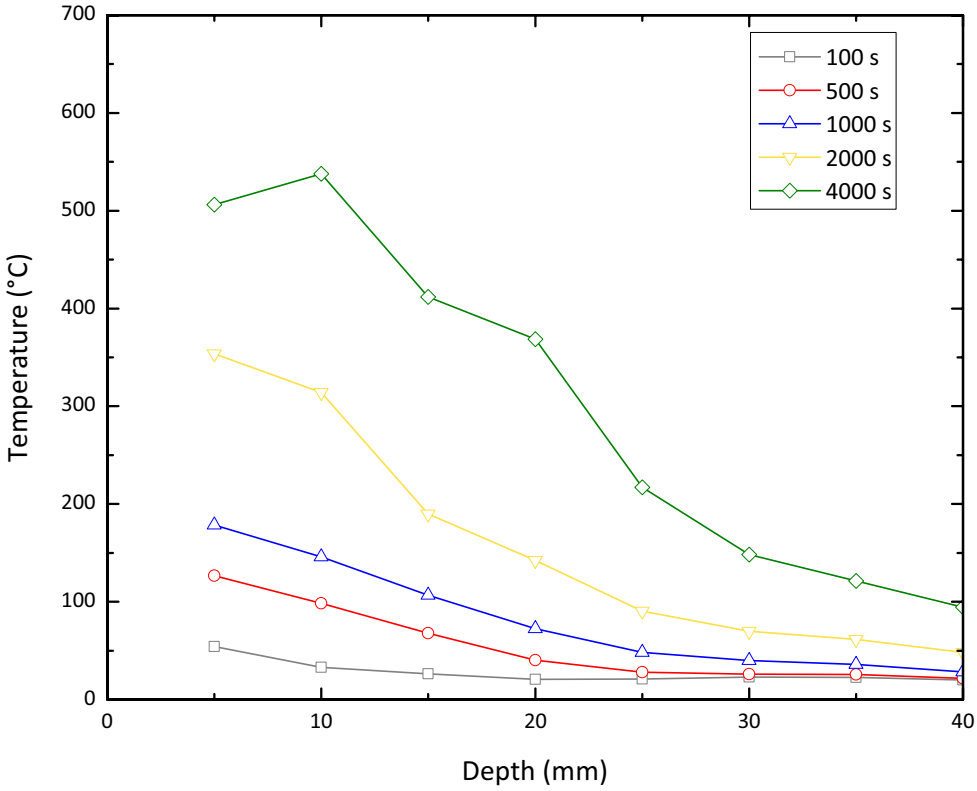

Figure B.5: Averaged temperature profiles for 18 kW·m^{-2}, perpendicular heating.

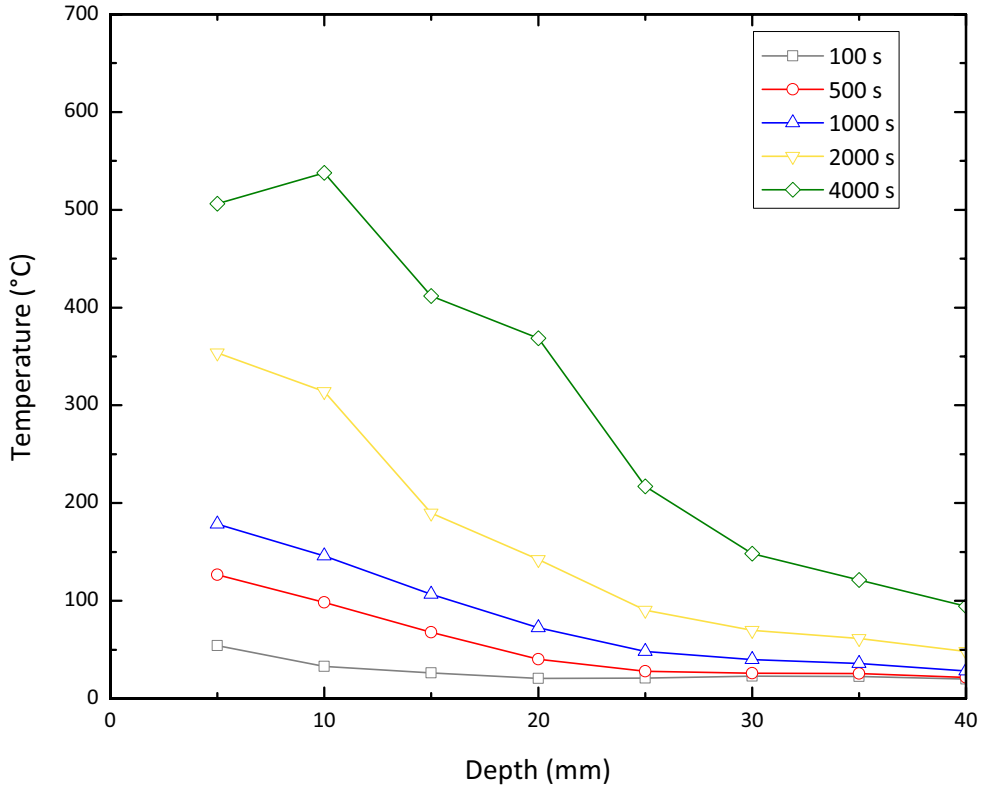

Figure B.6: Averaged temperature profiles for 25 kW·m^{-2}, perpendicular heating.

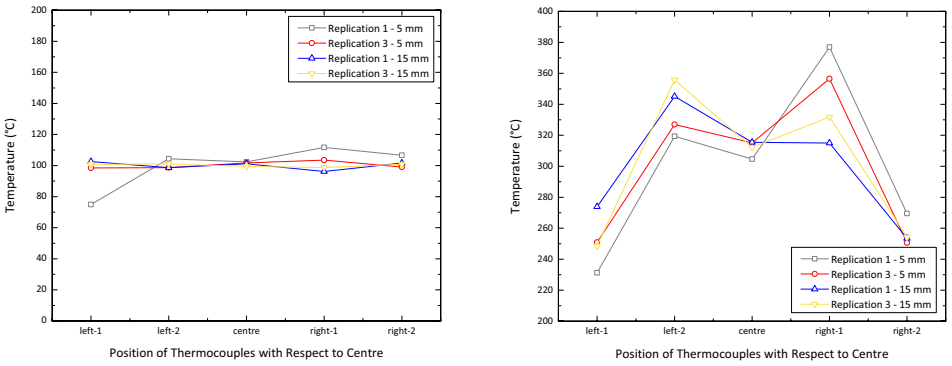

(a) *373 K Average*

(b) *573 K Average*

Figure B.7: Individual thermocouple readings for the instants when the averages mark 373 K and 573 K. 10 kW·m^{-2}, perpendicular heating.

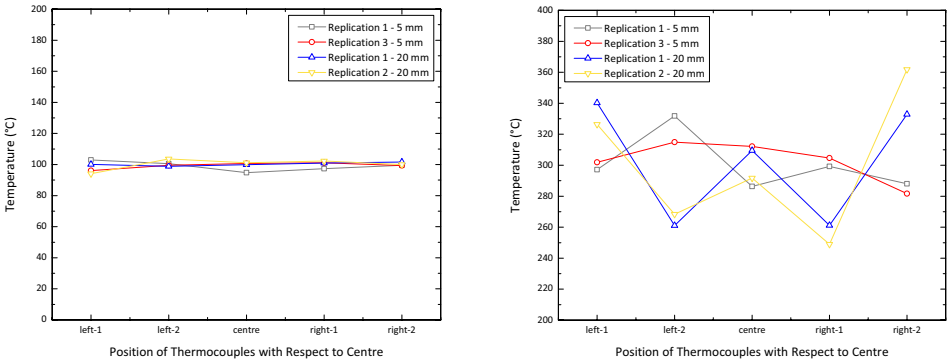

(a) *373 K Average* (b) *573 K Average*

Figure B.8: Individual thermocouple readings for the instants when the averages mark 373 K and 573 K. 25 kW·m^{-2}, perpendicular heating.

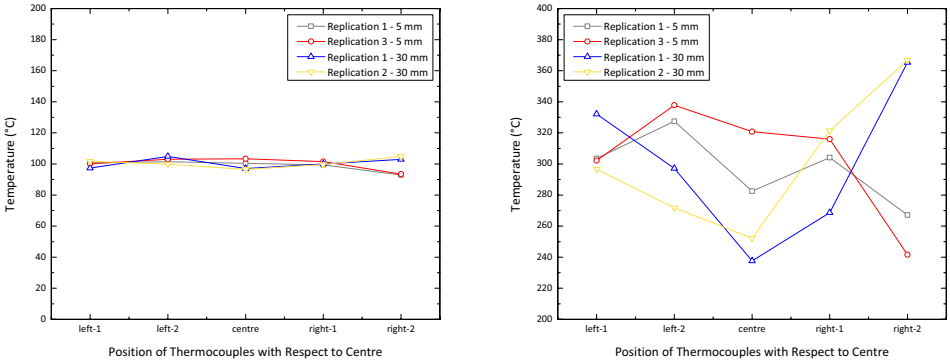

(a) *373 K Average* (b) *573 K Average*

Figure B.9: Individual thermocouple readings for the instants when the averages mark 373 K and 573 K. 60 kW·m^{-2}, perpendicular heating.

(a) *60 s* (b) *360 s* (c) *660 s*

(d) *960 s* (e) *1260 s* (f) *1560 s*

(g) *1860 s* (h) *2160 s* (i) *2460 s*

(j) *2760 s* (k) *3060 s* (l) *3360 s*

Figure B.10: 60 kW·m^{-2}, parallel heating. Charring and surface oxidation fronts evolution in time. Note the insulating effect of the sample holder, which accelerates the reactions at the bottom of the specimen and the absence of the moisture evaporation front, due to a lower diffusivity in the transverse direction (perpendicular to the grain).

Appendix C

Thermocouple Correction

The presence of the thermocouples will generate a temperature disturbance in the wood, due to the fact that the thermal conductivity of wood is several orders of magnitude lower than that of the thermocouple wires (Beck 1962). The disturbance was estimated by calculating the temperature rise in a one-dimensional inert solid and comparing it to the temperature rise in the same solid but with the thermocouple inserted (see a schematic representation in Figure C.1). In order to cover all the range of disturbances, they were calculated using both wood and char thermophysical properties. This was done for all the incident heat fluxes that were used in this work.

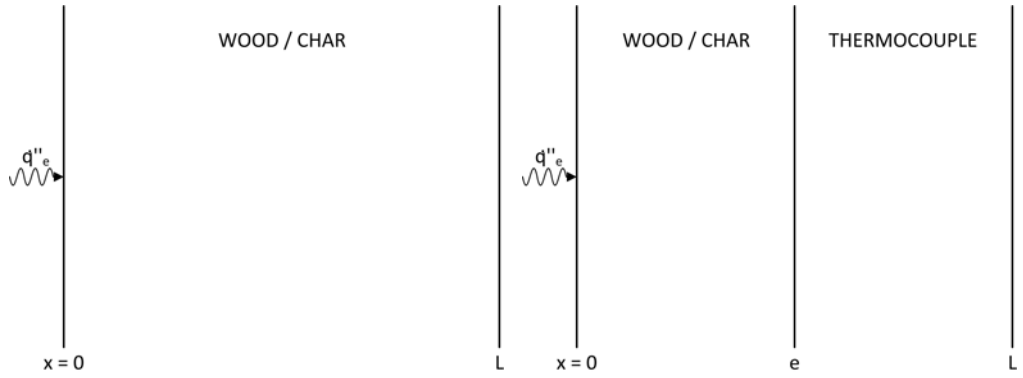

(a) *No thermocouple* (b) *With embedded thermocouple*

Figure C.1: Schematic representation of the two modelled cases.

The temperature rise for the undisturbed solid is given by the following equation:

$$\rho\, c_p \frac{\partial T}{\partial t} = k \frac{\partial^2 T}{\partial t^2}. \tag{C.1}$$

When the thermocouple is embedded, a system of two equations must be solved,

$$\begin{aligned} \rho\, c_p \frac{\partial T}{\partial t} &= k \frac{\partial^2 T}{\partial t^2},\ x < e; \\ (\rho\, c_p)_{tc} \frac{\partial T}{\partial t} &= k_{tc} \frac{\partial^2 T}{\partial t^2},\ x \geq e. \end{aligned} \tag{C.2}$$

These equations were solved using finite difference techniques. The temperature correction, according to Beck, is the convolution integral of the time derivative of the temperature disturbance multiplied by the net incident heat flux:

$$T_{tip}(t) - T_{tip,\,undist.}(t) = \frac{r_{tc}\, k_{tc}}{k^2} \int_0^t \dot{q}''_{net}(\lambda) \frac{\partial \phi_{tip}(t-\lambda)}{\partial t} d\lambda. \tag{C.3}$$

The temperature disturbance is defined as

$$\phi_{tip} = \frac{k^2}{k_{tc}} \frac{(T_{tip} - T_{undisturbed})}{\dot{q}''_e\, r_{tc}}. \tag{C.4}$$

The maximum temperature differences calculated using this method are shown in Figure 3.37.

Appendix D

Error Estimation

This appendix will detail the development of the expression to estimate the error in the measured incident heat flux, as discussed in Section 3.5. The equations presented in Chapter 3 are repeated here for convenience. The incident heat flux, as measured by the radiometer, was defined as,

$$\dot{q_e}'' = \epsilon_h \cdot F \cdot \sigma \left(T_h^4 - T_\infty^4 \right), \tag{D.1}$$

F is a "view factor",

$$F = \frac{F_{m-h}}{1 - F_{h-h}\left(1 - \epsilon_h\right)}. \tag{D.2}$$

The proper view factors F_{m-h} and F_{h-h} are a function of the normal distance between the meter surface and the base of the cone (L_2) and the distance between the centre of the radiometer and the edge of the heater, r_r (see Figure 3.36). The error in the incident heat flux can be expressed as (Atreya 1983):

$$d\dot{q_e}'' = \left| \frac{\partial \dot{q_e}''}{\partial L_2} \right| dL_2 + \left| \frac{\partial \dot{q_e}''}{\partial r_r} \right| dr_r + \left| \frac{\partial \dot{q_e}''}{\partial T_h} \right| dT_h, \tag{D.3}$$

The view factors are expressed as functions of the geometric dimensions of the heater - radiometer system. F_{h-h}, however, does not need to be differentiated, because it corresponds to the view factor for the radiative exchange of the heater with itself, and this does not depend on the placement of the radiometer. F_{m-h} is expressed as

$$F_{m-h} = 1 - F_{m-3} - F_{m-5}, \tag{D.4}$$

with

$$F_{m-3} = \frac{1}{2}\left(1 + \frac{(L_1+L_2)^2 + r_3^2}{r_m^2} - \sqrt{\left(1 + \frac{(L_1+L_2)^2 + r_3^2}{r_m^2}\right)^2 - 4\left(\frac{r_3}{r_m}\right)^2}\right), \tag{D.5}$$

$$F_{m-5} = 1 - \frac{1}{2}\left(1 + \frac{L_1^2 + r_r^2}{r_m^2} - \sqrt{\left(1 + \frac{L_1^2 + r_r^2}{r_m^2}\right)^2 - 4\left(\frac{r_r}{r_m}\right)^2}\right). \tag{D.6}$$

Differentiating Equation D.1 with respect to L_2, r_r and T_h yields the expression already presented in Section 3.5:

$$\frac{d\dot{q}_e''}{\dot{q}_e''} = f_1(L_2, r_r)\frac{dL_2}{L_2} + f_2(L_2, r_r)\frac{dr_r}{r_r} + f_3(T_h)\frac{dT_h}{T_h}, \tag{D.7}$$

with

$$f_1 = \frac{L_2\,(L_1+L_2)}{r_m^2 \cdot F_{m-h}}\left[\left(1 + \frac{(L_1+L_2)^2 + r_3^2}{r_m^2}\right)^2 \frac{1}{\sqrt{\left(1 + \frac{(L_1+L_2)^2+r_3^2}{r_m^2}\right)^2 - 4\left(\frac{r_3}{r_m}\right)^2}} - 1\right], \tag{D.8}$$

$$f_2 = \frac{r_r^2}{r_m^2 \cdot F_{m-h}}\left[1 - \frac{1}{\sqrt{\left(1 + \frac{L_1^2+r_r^2}{r_m^2}\right)^2 - 4\left(\frac{r_r}{r_m}\right)^2}}\left\{\left(1 + \frac{L_1^2 + r_r^2}{r_m^2}\right) - 2\right\}\right]. \tag{D.9}$$

$$f_3 = \frac{T_h^4}{T_h^4 - T_\infty^4}. \tag{D.10}$$

Appendix E

Estimation of the Exothermic Effect

If the measured temperature rise at a depth of 5 mm is used to estimate the net energy received by a slab of wood at that depth, following

$$\dot{q}''_{net} = e\,\rho\,c_p\,\frac{\partial T}{\partial t}, \tag{E.1}$$

where the properties are those of wood, and e is taken as 2.5 mm, the evolution of the net heat flux reveals the effect of the moisture evaporation at shallower depths and shows a peak at about 550 s (see Figure E.1). The magnitude of the net heat flux is similar to the previously calculated value. But the calculated value is the difference between the increased and the normal incident heat fluxes, so the baseline net heat flux should be subtracted from the peak in the graph. If we consider this baseline to be the maximum value before the commencing of the moisture evaporation process (about 2.0 kW·m^{-2}), then the value of the extra net heat flux due to exothermic effects is of a similar value as that obtained previously (note that the previously calculated value was calculated at the surface of the specimen, so some of it will be consumed in the regions shallower than 5 mm).

It is interesting to note that this maximum value of the net transferred heat flux into the shallowest thermocouple roughly coincides with the peak measured mass loss, which occurs in the vicinity of 600 s. This would suggest that the two events are somehow linked. It indicates that the peak mass loss rate will correspond to the time when exothermic reactions take place in the first 5 mm of the sample. At the same time, moisture evaporation is taking place at a depth of 10 mm, so it is concluded that the greatest mass loss rate is generated only by wood which is located in the shallowest 10 mm of the wood surface.

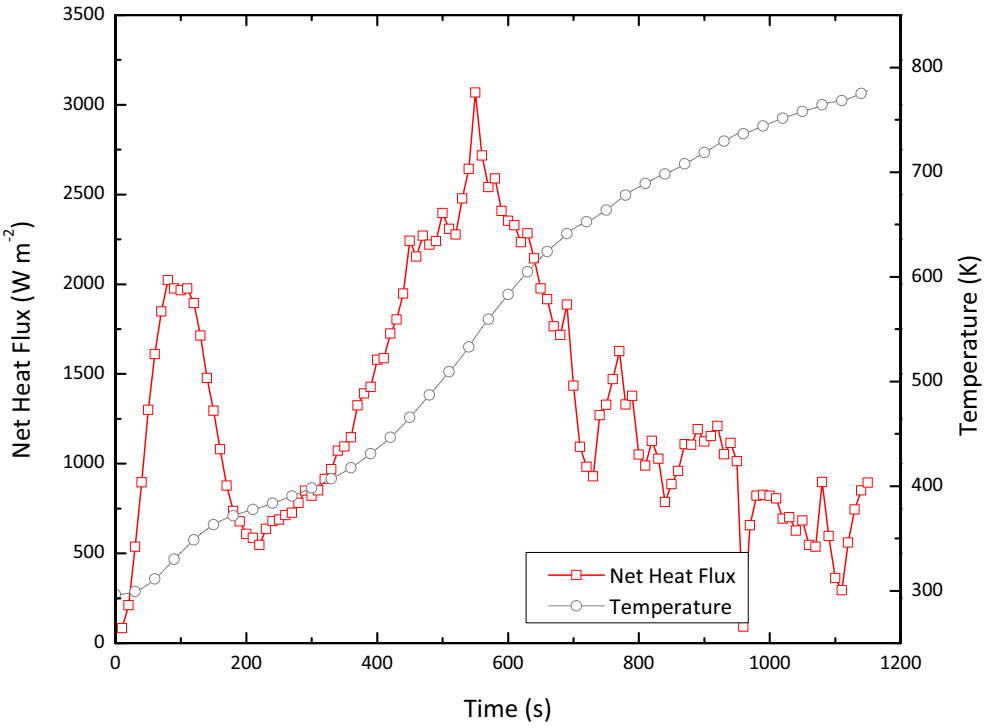

Figure E.1: Net heat flux at a depth of 5 mm, 25 kW·m^{-2}, taken from measured values of temperature.